Order Number 9107051

A search for very high-energy gamma rays from Cygnus X-3

Sinnis, Constantine, Ph.D.

University of Hawaii, 1990

U·M·I
300 N. Zeeb Rd.
Ann Arbor, MI 48106

A SEARCH FOR VERY HIGH ENERGY GAMMA RAYS FROM CYGNUS X–3

A DISSERTATION SUBMITTED TO THE GRADUATE DIVISION OF THE UNIVERSITY OF HAWAII IN PARTIAL FULFILLMENT OF THE REQUIREMENTS FOR THE DEGREE OF

DOCTOR OF PHILOSOPHY

IN PHYSICS

AUGUST 1990

by
Constantine Sinnis

Dissertation Committee:
John G. Learned, Chairman
Chuck Hayes
Sandip Pakvasa
Fred Harris
Len Cowie

To my parents,

Acknowledgments

My path to this point was not that of least action. As such, thanking everyone who deserves credit is an impossible task. But there are some people, whose help it would be a crime to ignore.

I must first thank Sau Lan Wu for providing me with the opportunity to work with the some of the finest experimental physicists in the world; and I would like to thank those physicists, all members of the ALEPH collaboration, for teaching me the art of modern electronic detectors.

This dissertation would not have been possible if not for the hard work and dedication of those who have gone before me. The builders of the Haleakala Gamma Ray Telescope: Bob Morse, Andy Szentgyorgi, Jim Gaidos, Frank Loeffler, and Chuck Wilson, deserve the highest praise for a job well done.

To the rest of the Haleakala collaboration: Pat Slane, Glenn Sembroski, John Jennings, Robert Austin, John Finley, Dan Weeks, Linda Kelly, and Jacob Hudson, who have kept the telescope running through the years, thank you.

I must also thank Leo Resvanis for being himself.

There are two people, who have been with me for many years, Almus Kenter and Ugo Camerini. From my first days at Wisconsin (when I met them both), to the troubled times in northern Germany, when Ugo set me towards a desolate volcano in the Pacific, to the long nights at the top of that

volcano, and the beautiful days under the seas and on the beaches of Maui with Almus, they have been a constant source of inspiration and insight.

The final thanks are of course saved for John Learned, who has not only given me the intellectual freedom to pursue my dreams, but has been a friend, and stood by me through both, bad times, and the much more numerous good times. The drive through the Australian outback will be long remembered. Thank you John.

This work was supported in part by the United States Department of Energy, contract **DE-AC03-83ER40103**

Abstract

Cygnus X–3 is an x-ray binary system approximately $10kpc$ away from the earth, lying in the plane of the galactic disc. Since the observation of intense radio jets emanating from the system, it has continued to confound experimentalists and theorists alike. In certain models of γ-ray production Cygnus X–3 could supply the power necessary to sustain the high energy ($E > 10^{17}eV$) galactic cosmic ray population against leakage (Hillas 1984a). By any model, the experimental results indicate that it is the most intense source of high energy cosmic rays observed. This thesis represents an attempt to verify the previous observations, and elucidate the nature of the γ-ray emission.

Taking a conservative viewpoint we set an upper limit to the time averaged flux from Cygnus X–3 of $5.8 \times 10^{-11}\gamma' s cm^{-2} s^{-1}$ above $300GeV$. However there is evidence, of low statistical significance (2σ), that Cygnus X–3 is a sporadic emitter of γ-rays, with a measured flux of $(3.3 \pm 0.7) \times 10^{-10}\gamma' s cm^{-2} s^{-1}$, and a duty cycle of 6% (consistent with previous observations); though it appears that this emission is not correlated with the $4.8hr$ x-ray period (in contradiction to previous observations). We also see no evidence of the reported $12.59ms$ pulsations, and note that the published world data is now consistent with this hypothesis at the 2% level.

Table of Contents

Acknowledgements iv

Abstract vi

List of Tables xii

List of Figures xiii

1 Introduction 1

2 Cosmic Rays and Their Acceleration 4

2.1 Introduction 4

2.2 Background on Cosmic Rays 5

2.2.1 The Energy Spectrum 5

2.2.2 Chemical and Isotopic Composition 7

2.2.3 Cosmic Ray Anisotropy 11

2.3 Acceleration Mechanisms 14

2.3.1 The Fermi Mechanism 14

2.3.2 Shock Acceleration 18
2.3.3 Pulsar Acceleration Mechanisms 28
2.3.4 Acceleration in Compact Binary Systems 38

3 Cygnus X–3: Observations and Models **51**

3.1 Introduction 51
3.2 Radio Observations of Cygnus X–3 52
3.3 Infra-Red Observations 54
3.4 X-Ray Observations 55
3.4.1 Periodic Phenomena 55
3.4.2 Non-Periodic Phenomena 65
3.4.3 X-Ray Models 67
3.5 Gamma Ray Data: MeV 80
3.6 VHE and UHE Gamma Ray Data 83
3.6.1 VHE Observations 83
3.6.2 UHE Observations 86
3.7 Underground Muons 91
3.8 Summary 94

4 The Extensive Air Shower and its Detection by the Atmospheric Čerenkov Technique **96**

4.1 Introduction 96
4.2 The Electromagnetic Cascade 98

4.3 The Nuclear Cascade 103
4.4 Čerenkov Radiation 104
4.5 Monte Carlo Study 110
4.5.1 Spatial Distribution of Čerenkov Photons 111
4.5.2 Angular Distribution of Čerenkov Photons 114
4.5.3 Temporal Distribution of Čerenkov Photons 117
4.5.4 The Telescope 120
4.5.5 Procedure 123

5 The Haleakala Gamma Ray Telescope and its Calibration 126
5.1 Introduction 126
5.2 Physical Description 127
5.3 Electronics and Data Acquisition 130
5.3.1 Timing Circuitry 130
5.3.2 Pulse Height Measurement 133
5.3.3 Latches 134
5.3.4 The Camerini Ambush 134
5.4 Data Acquisition 138
5.4.1 Event Time Determination 139
5.5 Calibration Procedures 139
5.5.1 Timing Calibration 140
5.5.2 ADC Calibration 146
5.6 Stability of Calibrations 148

6 Search for an Excess I: Technique **153**

6.1 Introduction 153

6.2 Physical Operation 154

6.3 Event Selection 155

6.3.1 Choice of Multiplicity Cut 155

6.3.2 Elimination of Contaminated Data 156

6.4 Zenith Angle Dependence of Trigger Rate 157

6.4.1 The Assumptions 158

6.4.2 Method 159

6.4.3 The Result 163

6.4.4 Determination of λt_0 164

6.4.5 Determination of γ' 168

6.4.6 Run Selection 172

6.4.7 Check on the Choice of γ' 175

6.5 Analysis Technique 182

6.5.1 The Expected Number of Events 182

6.5.2 The Error in the Expected Number of Events 182

7 Search for an Excess II: Results **186**

7.1 Introduction 186

7.2 1986 Data Set 187

7.2.1 Results of Burst Search 189

7.2.2 Results of D.C. Analysis 191

7.2.3 Search for Emission Pulsed at X-Ray Period 200
7.3 1989 Data Set 208
7.3.1 Modifications to the Telescope 208
7.3.2 Burst Search 215
7.3.3 D.C. Results from 1989 215
7.3.4 Summary of 1989 Results 218

8 Search for a Pulsar in Cygnus X–3 **219**
8.1 Introduction 219
8.2 1986 Data Base 220
8.2.1 Search for 12.59ms Pulsar 220
8.2.2 Search for Pulsar of Arbitrary Period 225
8.3 1989 Data Set 227
8.4 Conclusion 231

9 Conclusions **234**

Bibliography **238**

List of Tables

3.1 Ephemeris for Cygnus X–3. (from van der Klis and Bonnet-Bidaud 1988) 60

5.1 Pedestal subtracted ADC counts for various input pulse heights135

6.1 Extinction Curve at Mauna Kea 164

6.2 Average Measured Spectral Indices by Aperture and Grouping. All sources, multiplicity cut of 9 hits in 5 ns. 168

7.1 List of runs used in analysis of 1986 data. 188

7.2 Results of 1986 D.C. analysis. 191

7.3 Runs and excess between day 217 and 250 (1986). 198

7.4 List of Cygnus runs used in 1989 analysis. 214

7.5 Results of 1989 D.C. analysis. 217

8.1 Top 20 powers from FFT of two 720 second intervals 232

8.2 Top 20 powers from FFT of 900 second interval in run 1647 . 233

List of Figures

2.1 Energy Spectrum of Cosmic Rays (from Hillas 1984) 6

2.2 Comparison of Solar Elemental Abundances and Elemental Observed in Cosmic Rays. (from Simpson 1983) 9

2.3 Phase of Rayleigh vector with respect to 24-hour sidereal period versus energy for cosmic rays. (from Hillas 1984) 12

2.4 Amplitude of first harmonic versus energy. (from Hillas 1984) 13

2.5 Fermi acceleration of a charged particle reflecting off of magnetic irregularity. 16

2.6 A shock front viewed in its rest frame. 21

2.7 Particle crossing a shock front viewed in rest frame of upstream scatterers. 23

2.8 Variation with time of the momentum, p, of a proton accelerated by a SN I shock, evolving in a medium of density $s \times 10^{-3} cm^{-3}$ without cloud evaporation. Full line: injection at the beginning of the blast wave phase. Dotted line: injection at the beginning of the Sedov, (adiabatic), phase. (Lagage and Cesarsky 1983). 27

2.9 Pulsar and its Magnetosphere. (from Goldreich and Julian 1969) 32

2.10 Magnetospheric gap at pulsar pole. (from Ruderman and Sutherland 1975) 37

2.11 Outer Gap in magnetosphere. (from Cheng and Ruderman (1986a) 39

2.12 Compact Binary system. Top: Roche Lobe overflow, Bottom: Stellar Wind. (From Shakura and Sunyaev (1973) 41

2.13 Accretion onto a neutron star. (From Ghosh and Lamb (1978) 46

3.1 Radio flux versus time for September 1972 outburst. (from Bonnet-Bidaud and Chardin 1988) 53

3.2 Light curve of Cygnus X–3 in the energy band 1.5-15 KeV recorded by EXOSAT MEDA. Bin size is 40s. (from Willingale 1985) 56

3.3 Flux history at 3-12 KeV of Cygnus X–3, in 10 day averages, from *Vela 5B* satellite. Arrows mark the giant radio outburst of 1972 September, and the 1973 *SAS-2* and 1975 *COS B* gamma ray observations. (from Priedhorsky and Terrel 1986.) 57

3.4 Flux in the energy band 1.5-15 KeV folded using ephemeris of van der Klis and Bonnet-Bidaud 1981a. (from Willingale 1985) 59

3.5 Depth of modulation as a function of energy. (from Molnar and Mauche 1986) 63

3.6 RMS fluctuations versus orbital phase (from van der Klis and Bonnet-Bidaud 1982) 66

3.7 Ratio of modulated to unmodulated x-ray flux versus unmodulated x-ray flux. See text for explanation of curves. (from van der Klis and Bonnet-Bidaud 1981b) 68

3.8 Normal Cygnus x-ray light curve superposed on actual light curve for two different source intensities. (a) low intensity. (b) high intensity (from van der Klis and Bonnet-Bidaud 1982) . . 69

3.9 Energy spectrum of Cygnus X–3, in x-ray high state and in x-ray low state. Note average kT is lower for x-ray high state. (from White and Holt 1982) 70

3.10 The Cocoon Model of Cygnus X–3. (from Milgrom 1976) . . . 74

3.11 Light curve of 4U 1822-37 with fit from ADC model. (from White and Holt 1982) 76

3.12 ADC model, with bulge. Top: cross section, Bottom: top view. (from White and Holt 1982) 77
3.13 Light curve of Cygnus X–3 with best fit from ADC model. (from White and Holt 1982) 78
3.14 Gamma ray maps of Cygnus region: (left) During state of high x-ray activity. (right) During state of low x-ray activity. (from Li and Wu 1989) 82
3.15 Energy spectrum of Cygnus X–3 from radio to EeV. (adapted from Hermsen et. al. 1987) 95

4.1 Geometry for Čerenkov radiation 107
4.2 Distribution of photon density on the ground: (a) normally incident $320GeV$ photon primary, (b) normally incident $1TeV$ proton primary. A $600m \times 600m$ area of ground is shown, with $50m$ grid spacing. 112
4.3 Radial distribution of photon density on the ground: (a) normally incident $600GeV$ photon primary, (b) normally incident $2TeV$ proton primary. 113
4.4 Radial distribution of photon densities for various cuts on angle from vertical. Curves are for $< 1/2, < 3/4, < 1, < 2, < 4, <$ 6 degrees and for all photons. (a) $600GeV$ photon primary, (b) $2TeV$ proton primary. 115

4.5 Scatter plot of photon angle versus radial distance from shower core. (a) $600GeV$ photon primary, (b) $2TeV$ proton primary. . 116
4.6 Arrival time distribution of Čerenkov photons as a function of radial distance from core for a $600GeV$ photon primary. 118
4.7 Arrival time distribution of Čerenkov photons as a function of distance from core for a $2TeV$ proton primary. From Suda 1989.119
4.8 Surviving fraction of photons from: atmosphere, filters, and PMT's 122
4.9 Effective trigger area versus incident primary energy for: (a) photon primaries, and (b) proton primaries. 125

5.1 The Haleakala Gamma Ray Telescope. (From Szentgyorgi 1986)128
5.2 Schematic of mirror and 'can'. (From Szentgyorgi 1986) 129
5.3 Schematic of data acquisition electronics. (From Slane 1988) . 131
5.4 ADC Gain curves for 4 channels (from pulser run). Pedestal subtracted ADC values versus input pulse height in millivolts . 136
5.5 Gain of each channel. ADC counts/mV vs. channel number . 137
5.6 Trigger slewing. Shown are uncalibrated timing distributions for channel 3. (a). multiplicity 10, (b). multiplicity 12, (c). multiplicity 15, and (d). multiplicity 18 141

5.7 ADC slewing. Shown are uncalibrated timing distributions for channel 3, for an event multiplicity 10. (a). ADC range 0-200, (b). ADC range 200-300, (c). ADC range 300-400, and (d). ADC range 400-600 143
5.8 Timing histogram for channel 3 145
5.9 Uncalibrated TDC distribution for channel 3 ($ADC > 500$). (a). event multiplicity 17, (b). event multiplicity 18 147
5.10 Pedestal histogram for channel 3 149
5.11 One PE histogram for channel 3 150
5.12 The stability of the calibrations. Shown are the calibration constants vs. day number in the year. a. channel 1 b. channel 12 c. channel 21 152

6.1 Geometry of change in distance to shower maximum with zenith angle. $< n_{r.l.} >$ is the average number of radiation lengths to shower maximum for a proton primary of energy E_0. The quotes in the expression denote that the units are wrong, this should be converted to a thickness of material, gcm^{-2}, for the equality to be strict. 162
6.2 Rate as a function of zenith angle, theoretical formula. $\gamma' = 2.2$, $\lambda t_0 = .1$ to 1.0 in steps of .1 165
6.3 Extinction Curve at Mauna Kea: from Beland et al 166

6.4 Distribution of γ. All data, multiplicity cut of 9 in 5. a.) A Aperture b.) B Aperture 170
6.5 Distribution of γ. All Cygnus data, multiplicity cut of 12 in 5. a.) A Aperture b.) B Aperture 171
6.6 Zenith angle fit and data from a good run (no. 816). (a) A aperture (probability 98%), (b) B aperture (51%) 173
6.7 Zenith angle fit and data froma rejected run (no. 851). (a) A aperture probability (0.8%), (b) B aperture (5.0%) 174
6.8 Fit residuals vs. zenith angle. (a) $\gamma' = 1.8$ A aperture, (b) $\gamma' = 1.8$ B aperture, (c) $\gamma' = 2.0$ A aperture, and (d) $\gamma' = 2.0$ B aperture 176
6.9 Fit residuals vs. zenith angle. (a) $\gamma' = 2.2$ A aperture, (b) $\gamma' = 2.2$ B aperture 177
6.10 Fit residuals vs. zenith angle. (a) $\gamma' = 2.4$ A aperture, (b) $\gamma' = 2.4$ B aperture, (c) $\gamma' = 2.6$ A aperture, and (d) $\gamma' = 2.6$ B aperture 178
6.11 Distribution of fit residuals. (a) $\gamma' = 1.8$ A aperture, (b) $\gamma' = 1.8$ B aperture, (c) $\gamma' = 2.0$ A aperture, and (d) $\gamma' = 2.0$ B aperture 179
6.12 Distribution of fit residuals. (a) $\gamma' = 2.2$ A aperture, (b) $\gamma' = 2.2$ B aperture 180

6.13 Distributrion of fit residuals. (a) $\gamma' = 2.4$ A aperture, (b) $\gamma' = 2.4$ B aperture, (c) $\gamma' = 2.6$ A aperture, and (d) $\gamma' = 2.6$ B aperture 181

6.14 Time development of fit error (straight line) and normal error (curve) over a run. 184

6.15 Histogram of ratio of fit error to normal error at end of each run. For all Cygnus runs 185

7.1 Distribution of excesses. Smooth curve is result of a Gaussian fit to the distribution. Parameters given are from HFITGA. . 190

7.2 Integrated excess versus interval number. A aperture 192

7.3 Integrated excess versus interval number. B aperture 193

7.4 Integrated excess versus interval number. A+B aperture . . . 194

7.5 Excess versus γ' used in fitting procedure. See above for definition of units. 197

7.6 Excess by run versus day number in year (1986). 199

7.7 Radio flux from Cygnus X–3 vs. day number (1986). Waltmann 1989 201

7.8 Expected number of events vs. orbital phase, day 217-250. (VdK 1988 quadratic ephemeris). (a) ON Source, (b) OFF Source 203

7.9 Excess number of events (corrected for D.C. excess and phase coverage) vs. orbital phase, day 217-250. (VdK 1988 quadratic ephemeris). (a) ON Source, (b) OFF Source 204

7.10 Expected number of events vs. orbital phase, all data. (a) ON Source, (b) OFF Source 206

7.11 Excess number of events (corrected for D.C. excess and phase coverage) vs. orbital phase, all data. (a) ON Source, (b) OFF Source 207

7.12 1989 Radio outburst from Cygnus X–3. 11 cm. Adapted from Johnston 1989. 209

7.13 Random trigger rate versus multiplicity demanded in $5ns$ window. 211

7.14 Distribution of γ'. All 1989 Cygnus runs. Multiplicity cut of 12 hits in $5ns$. a.) A Aperture b.) B Aperture 212

7.15 Rate as a function of zenith angle from run 1647. Curve is fitted function and points are data. Multiplicity cut of 12 hits in $5ns$. (a) A Aperture, (b) B Aperture 213

7.16 Distribution of excesses over $900s$ intervals. 1989 data. 216

8.1 Pulsar ephemeris as given by Durham collaboration. (from Brazier et. al. 1989) 221

8.2 Distribution of Rayleigh powers observed from test of the Durham hypothesis. 1986 dataset. (a) On source, (b) OFF source 226

8.3 Distribution of power observed from FFT. Data from run 855. (a) On source, (b) OFF source 228

8.4 Distribution of power observed from FFT. Data from run 869. (a) On source, (b) OFF source 229

8.5 Distribution of power observed from FFT. Data from run 1647. (a) On source, (b) OFF source 230

9.1 Flux from Cygnus X–3 versus Energy. *H* denotes the measurements from this thesis. (adapted from Halzen 1986) 235

Chapter 1

Introduction

Since their discovery in the 1920's, the origin of cosmic rays has remained a mystery. Though a unified view of the production, acceleration and propagation of cosmic rays still eludes us, a consistent model is emerging. Cosmic rays with energies below $10^{15}eV$ are accelerated at the shock fronts of supernovae remnants. Above $10^{15}eV$, where the spectrum steepens, compact objects such as pulsars, X–ray binaries, and black holes are thought to be responsible for the bulk of cosmic rays. And at the highest detected energies, above $10^{19}eV$, an extragalactic origin is preferred.

While shock acceleration is generally accepted, having a solid theoretical basis and direct experimental verification, the acceleration of particles to cosmic ray energies by compact objects is not as well established. Theoretically, no commonly accepted self consistent mechanism exists for accelerating cosmic rays in these environments. While observations of optical synchrotron radiation within the Crab nebula imply the existence of TeV electrons within

the nebula, direct measurements of higher energy radiation from pulsars and evolved binaries has proven elusive. Detection of such sources of energetic particles would not only help solve the cosmic ray riddle, but would aid in the theoretical understanding of these complex systems.

Since the galaxy is pervaded by a magnetic field, only neutral particles retain their directionality. To find the sources of cosmic rays we must find the sources of neutral particles. The only two stable neutral particles provided by nature are the photon and the neutrino. Though much more abundant, the neutrino is notoriously difficult to detect (due to its very small cross section with normal matter) and attention has turned to the photon.

The atmospheric Čerenkov technique provides a cheap and efficient method for the detection of incoming cosmic rays. When a cosmic ray enters the earth's atmosphere it dissipates its energy via interactions with the nuclei, creating a shower of relativistic particles, both charged and neutral. The charged particles, if travelling faster than the speed of light in air, emit Čerenkov radiation. It is this radiation that we detect. With this technique it is possible to obtain large collection areas ($\sim 10,000m^2$) with small telescopes ($\sim 10m^2$ mirror area), and sensitivity to incoming particles with energies as low as a few hundred GeV.

Early applications of this technique and air shower detectors, sensitive to much higher energy radiation, were encouraging. Beginning with the first observation of Cygnus X–3 by the Crimean Astrophysical Observatory in the

early 1970's (Stepanian et. al. 1975), and culminating with the detection of underground muons from Cygnus by SUDAN (Marshak et. al. 1985) and NUSEX (Battistoni et. al. 1985), it appeared that a major source of high energy cosmic rays had been discovered. The results indicated a flat spectrum ($\sim E^{-1}$ integral flux) and a luminosity sufficient to replenish (against leakage) the galactic cosmic rays above $10^{17}eV$ (Hillas 1984a).

"... a number of authors have pointed out that it [Cygnus X–3] may be one of the major (or possibly the only) source(s) of cosmic rays active in our galaxy at the present time." (Watson 1984).

In 1985 the Haleakala Air Čerenkov Telescope was commissioned. With a low energy threshold (300 GeV) and simultaneous monitoring of the background (the first ACT to implement this) we possessed the capability to verify this claim. This thesis represents an analysis of over 130 hours of high quality data taken on Cygnus X–3 in 1986 and in 1989 (when the source was undergoing a large radio outburst).

The bulk of the analysis is devoted to a search for an excess in the cosmic ray rate from the direction of Cygnus X–3: steady state (D.C. emission), in the form of bursts (of $\sim 15min$ duration), or correlated to the well known x-ray period ($4.79hr$) of the system. We devote the final chapter to a search for high frequency pulsations from Cygnus, the detection of which would point to a rapidly spinning neutron star as the ultimate energy source of the system.

Chapter 2

Cosmic Rays and Their Acceleration

2.1 Introduction

In this chapter we will first review the observations of cosmic rays, concerning ourselves primarily with the energy spectrum, the chemical and isotopic composition, and the anisotropy of cosmic rays. For historical background on the field see Hillas (1972) or Wolfendale (1963). For a more modern overview see Wefel (1988). We then discuss various acceleration schemes, starting with the Fermi process, moving into shock acceleration from supernova remnants, pulsar acceleration mechanisms, and acceleration in compact binary systems.

2.2 Background on Cosmic Rays

2.2.1 The Energy Spectrum

The differential cosmic ray spectrum is shown in Figure 2.1 (from Hillas 1984). At energies above $\sim 1GeV$ the cosmic ray spectrum is well described by a power law; $J(E) \propto E^{-\alpha}$, with $\alpha = 2.6$. Below this energy the effects of the solar magnetosphere make interpretation of the data difficult. At roughly $10^{15}eV$, the knee, the spectrum steepens, $\alpha = 3.1$, but remains a power law. At the highest energies, above $10^{19}eV$, a flattening of the spectrum is observed.

Of particular interest is the region around the knee. Unfortunately measurements are difficult in this region (the extensive air showers are very weak at these low energies and are therefore dominated by fluctuations) and the detailed structure of the spectrum is as yet unclear. There are two theories to explain the steepening of the spectrum:

1 The knee is a rigidity dependant feature of cosmic ray confinement in the galaxy. Then one would observe the knee at a different energy for each species. One does observe that the escape length of cosmic rays decreases with energy, $\lambda \propto E^{-(.3-.6)}$ (Cesarsky 1980), however the sharpness of the knee would seem to indicate that the galaxy becomes suddenly transparent to cosmic rays with energies above $10^{15}eV$.

2 There are two acceleration mechanisms, one operating at the lower

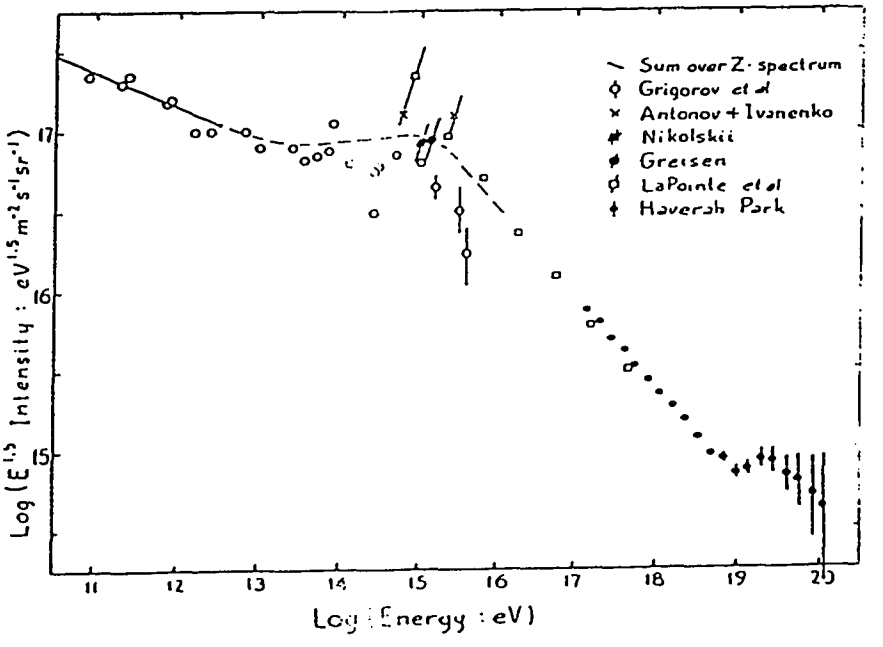

Figure 2.1 Energy Spectrum of Cosmic Rays (from Hillas 1984)

energies and another at the higher energies. If this were the case one would expect some structure around the knee, there being no reason for a smooth transition in intensity from one mechanism to the next. An abrupt change in composition at the knee, would strongly favor this hypothesis.

At energies above $10^{19}eV$ interactions with the $3K$ background photons leads to a degradation of the primary energy and one would expect the spectrum to fall off even faster in this region. The observed flattening of the spectrum is most likely due to photon pile-up from higher energy cosmic rays interacting with the $3K$ background, though it could also indicate that the acceleration site is within the our local cluster of galaxies.

2.2.2 Chemical and Isotopic Composition

Cosmic rays provide us with our only sample of galactic matter. Clues to their origin might be found by comparing the relative elemental abundances in cosmic rays to solar neighborhood abundances, see Figure 2.2 (Simpson 1983). (See Lund 1986 for a review of elemental and isotopic composition) There is almost no Li, Be, or B in the solar neighborhood, and relative deficits of the elements just before Fe. These deficiencies have been filled in by spallation of the heavier cosmic rays, interacting with the H and He in the ISM, as they travel through the galaxy. The abundances of Li and B relative to C, N, and O, along with production cross sections, have been

used to estimate the average amount of material traversed by cosmic rays, $6g\ cm^{-2}$ (Garcia-Munoz 1977). Once propagation effects are accounted for there is good agreement between solar and cosmic ray abundances, with a few notable exceptions. The relative abundance of ^{12}C in cosmic rays is twice its solar system value, the $^{22}Ne/^{20}Ne$ ratio is three times as great in cosmic rays, the $^{25,26}Mg/^{24}Mg$ ratio and the $^{29,30}Si/^{28}Si$ ratio are 1.7 times greater in cosmic rays, and finally ^{26}Al is overabundant in cosmic rays. The cosmic ray composition is well described by a solar composition plus a 2% admixture of Wolf-Rayet ejecta. A Wolf-Rayet star is a massive star, $30 - 120 M_{\odot}$, with large stellar winds that eventually strip away the surface layers and expose a highly evolved core. The composition of this core closely matches the observed anomolies in the cosmic ray composition.

Information is also available on isotopic composition. By measuring the relative amounts of radioactive and stable daughter nuclei, produced by spallation, one can estimate the age of cosmic rays. Using the observed ratio of ^{10}Be to ^{9}Be and some standard assumptions (sources uniformly distributed, leaky box model of confinement and escape length independent of time and energy) Garcia-Munoz et. al. derive an average density of traversed material of $.18 atoms/cc$. This implies an age of roughly 17 million years (Garcia-Munoz 1977, see also Wiedenbeck 1983) for the low energy cosmic rays.

This value for the average density of the material traversed is about one order of magnitude smaller than the average density of the ISM. Originally

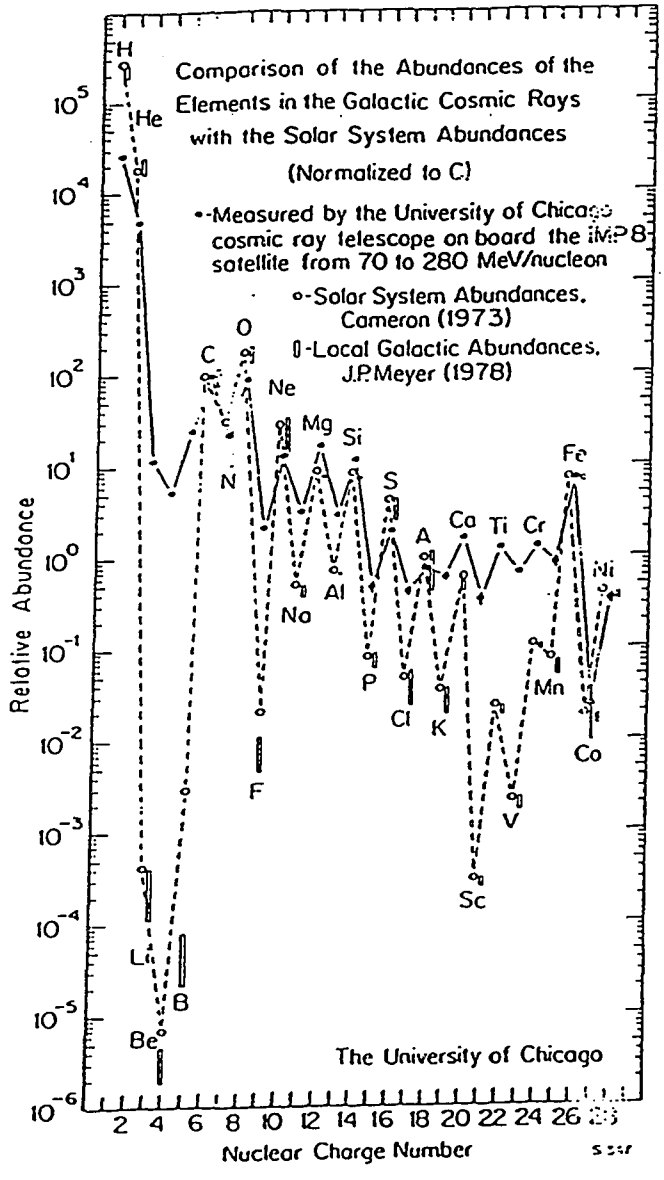

Figure 2.2 Comparison of Solar Elemental Abundances and Elemental Observed in Cosmic Rays. (from Simpson 1983)

this was taken to indicate that cosmic rays spend most of their time in the halo surrounding our galaxy. However recent experimental evidence indicates that the interstellar medium (ISM) has three components: a hot rarefied component ($10^{-2.5} atoms/cc$, $10^{5.8} K$) occupying $70 - 80\%$ of the volume of the galaxy, a warm component ($.25 atoms/cc$, $8000 K$) occupying $15 - 30\%$ of the volume, and a cold dense component ($40 atoms/cc$, $80 K$) occupying $2 - 5\%$ of the galaxy (McCray and Snow 1979 and McKee and Ostriker 1977). This leaves open the possibility that cosmic rays remain within the disc of the galaxy, confined to the hot rarefied regions of the ISM.

Of particular interest are any changes in composition near the knee of the spectrum. An abrupt change in composition at the knee would rule out the possibility that the knee is a feature of the confinement mechanism, and point to the presence of another acceleration mechanism coming into play. Recently Friedenreich et. al. (1989), at the University of Maryland, have studied the elemental composition at $10^{15} eV$. Unfortunately their conclusions are dependent on the model chosen for high energy interactions (where no accelerator data exist). If one simply extrapolates present accelerator data to these energies, then a heavy (heavier than He) composition is preferred. If proton collisions become more inelastic at high energies then their data is consistent with a pure H beam.

2.2.3 Cosmic Ray Anisotropy

When looking for anisotropies in the arrival directions of cosmic rays one performs a Rayleigh test (Scargle 1982 and see chapter 8) at the 24 hour sidereal period. Using the right ascension of the incoming particles as the 'phase', and grouping all events with the same declination together, one looks at the amplitude and phase of the resultant Rayleigh vector. Figure 2.3 shows the phases reported by 5 different experiments as a function of energy (from Hillas 1984). There is good agreement between the various experiments. Figure 2.4 (Hillas 1984) shows the amplitude of the first harmonic as a function of energy.

The fact that the amplitude of the anisotropy changes at the knee of the spectrum is supportive of the knee being a rigidity dependent feature. If the knee is a feature of a two-component model (two different acceleration mechanisms) then the change in anisotropy would imply that high energy cosmic rays originate from point sources.

More recently, as the statistics have improved, people have taken small slices of declination and analyzed them separately. Analysis from Chacaltaya, Haverah Park, Sydney, and Yakutsk strongly favor a galactic origin for cosmic rays with energy between $10^{14} - 10^{19} eV$ while particles of higher energy seem to point towards the Virgo cluster (Wdowczyk 1986 and Watson 1984).

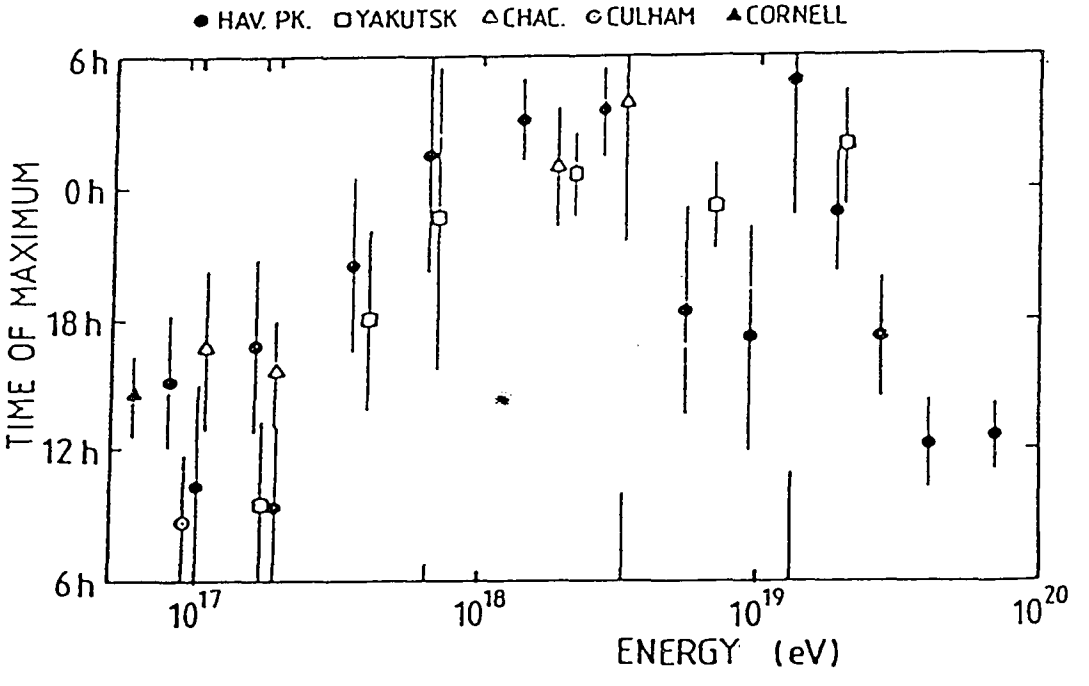

Figure 2.3 Phase of Rayleigh vector with respect to 24-hour sidereal period versus energy for cosmic rays. (from Hillas 1984)

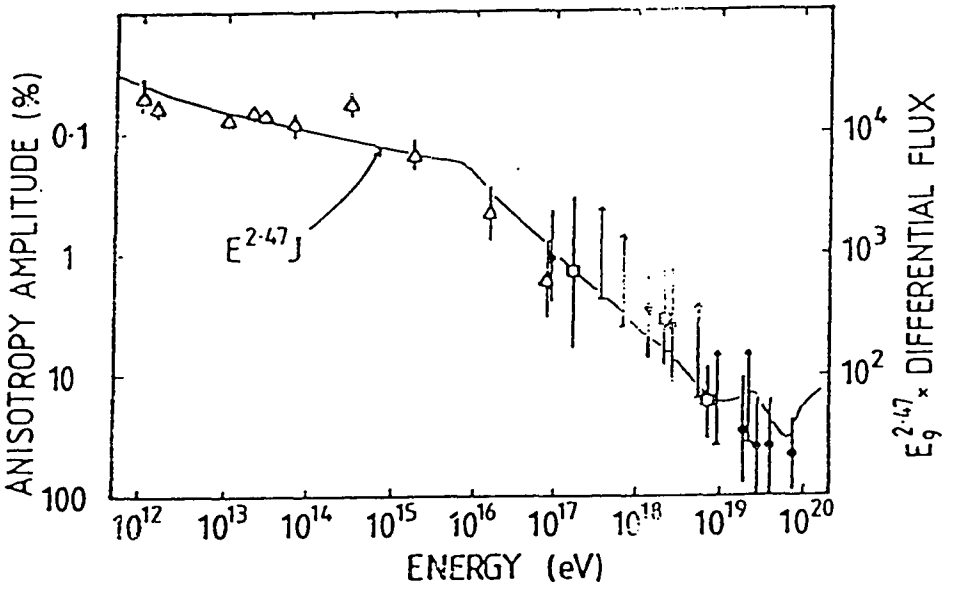

Figure 2.4 Amplitude of first harmonic versus energy. (from Hillas 1984)

2.3 Acceleration Mechanisms

2.3.1 The Fermi Mechanism

Enrico Fermi was the first to propose a mechanism capable of accelerating particles to cosmic ray energies (Fermi 1949). In his model charged particles are magnetically reflected by moving interstellar clouds. If the collisions are elastic, the incoming and outgoing particle energies are equal in the rest frame of the cloud. A simple Lorentz transformation gives the energy gain/loss per reflection. If the cloud is moving with velocity β_c, and the particle has energy E_{in} in the rest frame of the ISM then (primed quantities refer to the rest frame of the cloud):

$$E'_{out} = E'_{in} \tag{2.1}$$

$$E'_{out} = \gamma'(E_{out} - \vec{\beta}_c \cdot \vec{p}_{out}) \tag{2.2}$$

$$E'_{in} = \gamma'(E_{in} - \vec{\beta}_c \cdot \vec{p}_{in}) \tag{2.3}$$

$$E_{out} = E_{in}\left(\frac{1 - \vec{\beta}_c \cdot \vec{\beta}_{in}}{1 - \vec{\beta}_c \cdot \vec{\beta}_{out}}\right) \tag{2.4}$$

See Figure 2.5 for the definition of the quantities. If the cloud is moving towards/away (from) the particle, there is a net energy gain/loss. Since oncoming collisions are more frequent than following collisions, over a long period of time there will be a net gain in energy.

Given a characteristic escape time and an average time between collisions one can calculate the resulting particle spectrum. To make the calculation

more transparent, without appreciably altering the results, we make the following approximations: the particle velocity is c, the cloud is non-relativistic, and only normal collisions occur. The relative probability of an oncoming collision is $P_+ = .5(\beta_p + \beta_c)/\beta_p$ and of a following collision $P_- = .5(\beta_p - \beta_c)/\beta_p$. Therefore the average energy gain per collision, $< \Delta E >$, is:

$$\begin{aligned} \Delta E &= E_{out} - E_{in} && (2.5) \\ &= E_{in}\left(\frac{\vec{\beta}_c \cdot (\vec{\beta}_{out} - \vec{\beta}_{in})}{1 - \vec{\beta}_c \cdot \vec{\beta}_{out}}\right) && (2.6) \\ < \Delta E > &= \Delta E \times (P_+ - P_-) && (2.7) \\ &\approx E\beta_c^2 && (2.8) \end{aligned}$$

So that $E = \exp \beta_c^2 N$ where N is the number of collisions suffered by the particle. With $\tau =$ *mean time between collisions* and $N = t/\tau$ we have:

$$E(t) = E_0 \exp^{\beta_c^2 t/\tau} \qquad (2.9)$$

If the system possesses a characteristic loss time T then the particle fraction surviving to a time t is $N(t) = \exp^{-t/T} dt/T$. Solving eq. 2.9 for t:

$$\begin{aligned} t &= \frac{\tau}{\beta_c^2} \ln(E/E_0) && (2.10) \\ dt &= \frac{\tau}{\beta_c^2 E} dE && (2.11) \end{aligned}$$

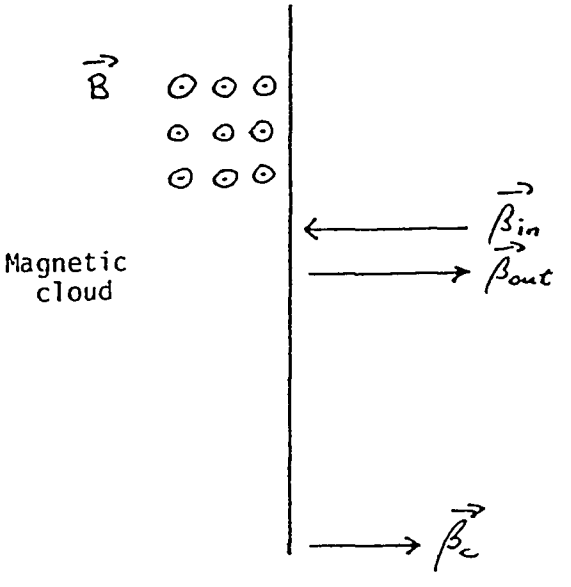

Figure 2.5 Fermi acceleration of a charged particle reflecting off of magnetic irregularity.

Substituting for t leads to the following energy spectrum:

$$N(E) = \exp^{\frac{-\tau}{\beta_c^2 T}\ln(E/E_0)} \frac{\tau}{T\beta_c^2 E} dE \tag{2.12}$$

$$= \left(\frac{E}{E_0}\right)^{-(1+\tau/\beta_c^2 T)} \frac{\tau}{\beta_c^2 T E_0} \tag{2.13}$$

And we have a power law spectrum with spectral index $\alpha = 1 + \tau/\beta_c^2 T$. For this to be equal to the measured spectral index of 2.6 would require a special relationship between the mean time between collisions and the time spent in the accelerating region, $\tau = 1.6\beta_c^2 T$. There does not appear to be any reason why this should be so.

Apart from the arbitrariness of the spectral index the Fermi mechanism has some other problems. As Fermi himself recognized ionization losses dominate energy gains for low energy particles. One needs a separate mechanism for injecting relativistic particles into the accelerating region. For protons $E_{inj} \sim 200MeV$, for heavier nuclei the injection energies are even greater, and for electrons ionization losses always beat energy gain. Fermi proposed magnetically active stars as the sight of the initial acceleration. However ionization loses suffered by the particles as they travel from the site of initial acceleration to the final accelerating region, imply the need for enormous amounts of injection energy (more then is present in the cosmic rays themselves). We will discuss the modern solution to this problem below.

The most serious problem with the Fermi mechanism is the rate of energy gain. For typical cloud velocities, $\beta_c = 10^{-4}$, a particle would have to

undergo 10^8 collisions to increase it's energy by a factor of e. We now know that hydromagnetic turbulence in the ISM, such as Alfven waves, is largely responsible for the scattering of cosmic rays, the measured density of clouds being too small to accelerate the particles within 20 million years. The acceleration rate is then dependent on the spectrum and density of interstellar turbulence. Present measurements of the interstellar turbulence indicate that Fermi's original proposal is untenable as it stands.

2.3.2 Shock Acceleration

In Fermi's theory the energy gain is second order in the β of the scattering center. One order of β comes from the actual scattering process (Lorentz transformation to rest frame of cloud), the other from the stochastic nature of the process (more oncoming than following collisions). A simple way to speed up the Fermi process is to make it non-stochastic, i.e. all collisions are oncoming. Then the energy gain is linear in the β of the scattering centers. This occurs when a particle is trapped between two converging magnetic mirrors. Shock waves from supernova remnants have been proposed as a likely sight of this type of acceleration, known as a first order Fermi process. Let us examine the situation in some detail.

There are three important ingredients to shock acceleration. First is the injection mechanism, here we face the same difficulty as Fermi's theory, ionization losses beat energy gains for non-relativistic particles. Next is the

process by which particles gain energy. The process is similar to Fermi's original mechanism. A particle gains energy upon reflection from scattering centers on both sides of the shock front. The last ingredient is the creation of sufficient turbulence to reflect particles across the shock front many times. We will begin with a brief discussion of shocks, then derive the energy gain per shock crossing. We will then be in a position to derive the spectrum of particles based solely on the shock parameters. After a brief discussion of the generation of upstream turbulence we will discuss the injection problem.

Astrophysical Shocks

A shock wave can be viewed as a moving discontinuity in the thermodynamic variables of a system of matter and fields. When the particles in the plasma are frozen to the field lines, and the plasma has infinite conductivity, it is possible for the shock to propagate without particle collisions (the fields mediating the shock), a so-called collisionless shock. By applying the basic conservation laws; energy, momentum, and mass across the shock front one arrives at the shock 'jump' conditions (Katz 1987).

$$\rho_1 u_1 = \rho_0 u_0 \tag{2.14}$$

$$P_1 + \rho_1 u_1^2 = P_0 + \rho_0 u_0^2 \tag{2.15}$$

$$U_1 + \frac{P_1}{\rho_1} + \frac{1}{2}u_1^2 = U_0 + \frac{P_0}{\rho_0} + \frac{1}{2}u_0^2 \tag{2.16}$$

Where ρ_0 is the downstream density, u_0 the downstream fluid velocity, P_0

the downstream pressure, and U_0 the downstream internal energy density. ρ_1, u_1, P_1, and U_1 are the corresponding upstream quantities. Figure 2.6 shows the situation in the rest frame of the shock. If the fluid is an ideal gas we can use the jump conditions to arrive at the result that no shock can compress matter by more than a factor of $\chi_{max} = (\gamma + 1)/(\gamma - 1)$, where $\gamma = c_p/c_v$ is the ratio of specific heats of the fluid. For a monatomic gas $\gamma = 5/3$ and $\chi_{max} = 4$. This relation will be important when we want to calculate the energy spectrum of particles produced by a collisionless shock.

There are two stages in the life of a supernova shock wave. A blast phase, with $u_s \sim 10^9(E_{51}/M_e)^{1/2} cm/s$, which lasts until the shock has swept up the mass ejected from the star. And an adiabatic phase, with $u_s \sim 4 \times 10^{10} t_{yr}^{-3/5} cm/s$, which ends when the shock velocity is equal to the speed of sound (Lagage and Cesarsky 1983). For a typical Type II SN, with an energy release of $5 \times 10^{51} ergs$ and $5M_\odot$ of ejected matter, the blast phase lasts for roughly $5700 yrs$ and the adiabatic phase for a million years. For a typical Type I SN, $M_e = .5M\odot$, and $E = 5 \times 10^{50} ergs$, the timescales are $1200 yrs$ and $4.8 \times 10^5 yrs$.

The Acceleration

To derive the energy gain of a particle per shock crossing we use the same approach used for the Fermi mechanism above. Taking eq. 2.4 and replacing E_{out} with E_{k+1}, E_{in} with E_k (where E_k is the particle energy after the k^{th}

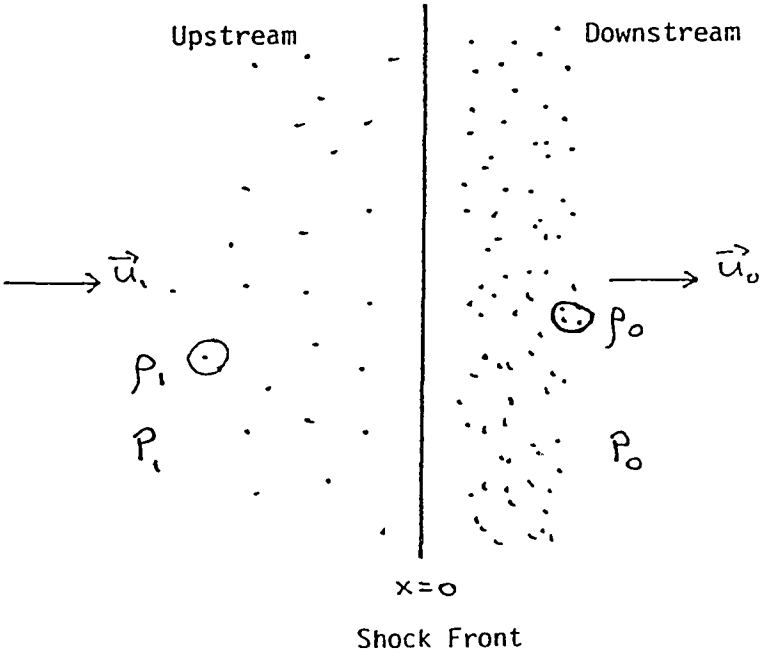

Figure 2.6 A shock front viewed in its rest frame.

crossing), and β_c (the cloud velocity) with $u_1 - u_0$ (the difference in velocity of the upstream and downstream scatterers) we have:

$$E_{k+1} = E_k \left(\frac{1 + v_{k1}(u_1 - u_0)\cos\theta_{k1}}{1 - v_{k0}(u_1 - u_0)\cos\theta_{k0}} \right) \tag{2.17}$$

See Figure 2.7 for a definition of the variables.

For a relativistic particle, $v_k = c$, and after l crossings of the shock we have:

$$\ln\left(\frac{E_l}{E_0}\right) = l\left\{\left\langle \ln\left(1 + \frac{u_1 - u_0}{c}\cos\theta_{k1}\right)\right\rangle - \left\langle \ln\left(1 - \frac{u_1 - u_0}{c}\cos\theta_{k0}\right)\right\rangle\right\} \tag{2.18}$$

$$\approx l\left\{\left\langle \frac{u_1 - u_0}{c}\cos\theta_{k1}\right\rangle + \left\langle \frac{u_1 - u_0}{c}\cos\theta_{k0}\right\rangle\right\} \tag{2.19}$$

We have expanded the ln under the assumption that $(u_1 - u_0) \ll c$, (i.e. the shock is moving non-relativistically with respect to the ISM) and the angle brackets denote a weighted average over crossing angles, θ_k (for an isotropic particle distribution the weight is simply the projected area, $\cos\theta d(\cos\theta)d\phi$). Performing the average leads to:

$$\ln\left(\frac{E_l}{E_0}\right) = \frac{4}{3} l \frac{u_1 - u_0}{c} \tag{2.20}$$

To proceed further we need to know the probability that a particle cross the shock l times. By demanding a time-independent solution to the diffusion equation Bell (1978) finds that the probability of escape is $\eta = 4u_0/v$, where

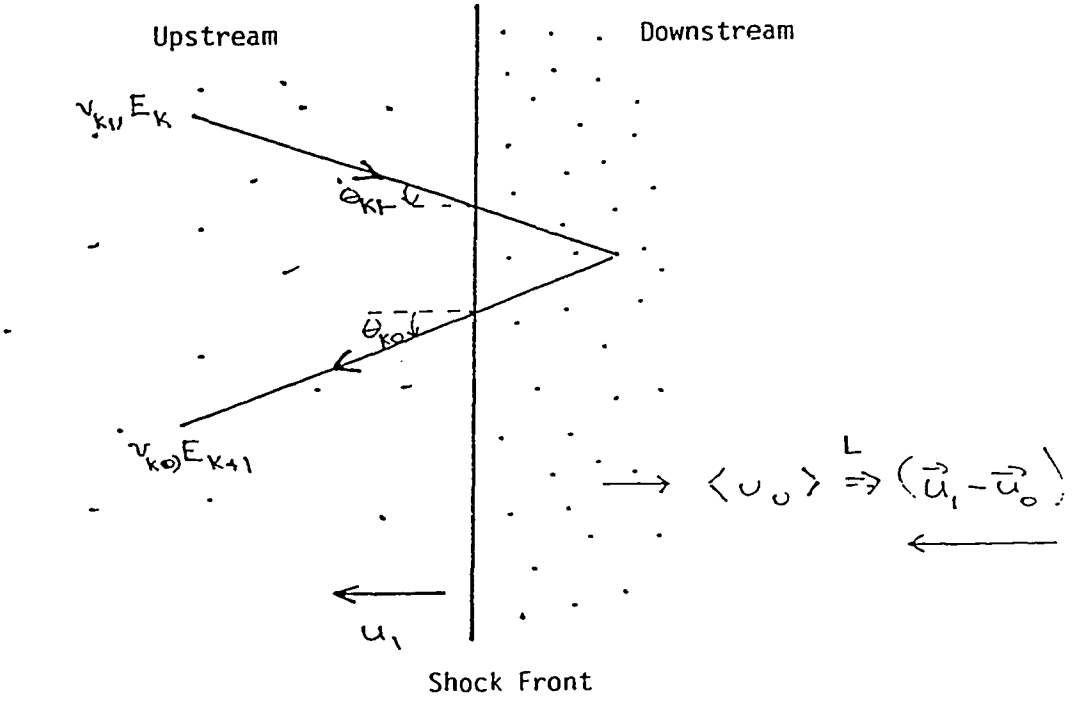

Figure 2.7 Particle crossing a shock front viewed in rest frame of upstream scatterers.

$v \approx c$ is the particle velocity, and u_0 the mean velocity of the downstream scatterers. Then the probability for a particle to survive at least l crossings is $P_l = (1 - 4u_0/c)^l$. Taking the natural log, expanding ($\ln P_l \approx -l4u_0/c$), and solving eq. 2.20 for l:

$$l = \frac{3}{4}\frac{c}{u_1 - u_0}\ln\left(\frac{E_l}{E_0}\right) \tag{2.21}$$

Substituting for l in the escape probability leads to:

$$\ln P_l = -\frac{3u_0}{u_1 - u_0}\ln\left(\frac{E_l}{E_0}\right) \tag{2.22}$$

$$P_l = \left(\frac{E_l}{E_0}\right)^{-\mu} \tag{2.23}$$

$$\mu = \frac{3u_0}{u_1 - u_0} \tag{2.24}$$

Leading to the following energy spectrum:

$$\frac{dN(E)}{dE} \propto \frac{dP}{dE} \tag{2.25}$$

$$\propto E^{-\mu'} \tag{2.26}$$

$$\mu' = \frac{2u_0 + u_1}{u_1 - u_0} \tag{2.27}$$

Using the jump conditions we can rewrite this in terms of the compression ratio of the shock $\chi = u_1/u_0$ resulting in $\mu' = (\chi + 2)/(\chi - 1)$. With $\chi = 4$, the strongest shocks, we arrive at a spectral index of 2.0 as compared to the

experimental value of 2.6. The difference can be ascribed to leakage from the galaxy.

Maximum Energy Attainable

The maximum energy to which a particle can be accelerated by a SNR depends both on the lifetime of the shock and on the presence of sufficient upstream turbulence to scatter the particle. The ISM does not possess sufficient turbulence to scatter particles with momentum above roughly $1GeV$. Therefore we must look to the cosmic rays themselves, either ambient or created by the shock, to generate the necessary turbulence.

Charged particles travelling faster than the Alfven speed, $v_a = B/\sqrt{4\pi\rho}$, will be resonantly scattered by Alfven waves whose wavelength is of the order of the Larmor radius of the particle, $r_L = pc/ZeB$ (Blandford and Eichler 1987). These particles will also generate Alfven waves of the same wavelength. This leads to the possibility that the particles are capable of confining themselves. In the quasi-linear theory, the diffusion coefficient is given by $D \sim 4/(3\pi) \times (r_L v)/\mathcal{F}$, where $\mathcal{F}(p)d(\log p)$ is the ratio of the magnetic energy density in waves, to the total magnetic energy density, $B^2/8\pi$. Once the diffusion length becomes comparable to the radius of the shock the particle will escape from the accelerating region. Lagage and Cesarsky (1983) arrive at an absolute upper limit to the energy by assuming $\mathcal{F} = 1$, its maximum value, everywhere. They find that by the time the shock has

dissipated, the highest energy particles have $E_{max} = 10^5 Z B_{-6} GeV/n$, where B_{-6} is the magnetic field strength in $\mu Gauss$ (see Figure 2.8). By matching the wave energy, $\mathcal{F}$, linearly from its value at the shock to its value in the ISM they obtain a diffusion length that is dependent on position (increasing linearly as one moves away from the shock). In this more realistic treatment they find the maximum energy to be one order of magnitude lower, $E_{max} = 10^4 Z B_{-6} GeV/n$

Injection

The problem of injection of particles of sufficient energy, $> 200 MeV$, into the accelerating region is still unsolved. If the preacceleration is to take place elsewhere, i.e. in Wolf-Rayet stars, one must demand a prodigious energy input in order to overcome ionization losses as the particles traverse the ISM. A much more satisfactory solution would be to generate the particles locally from the thermal bath. To see if this is feasible requires the solution of the full nonlinear shock problem. Blandford and Eichler (1987) have made some progress in this area. They claim '... that when the mean free path increases with energy, a strong shock always puts much of its energy into very energetic particles.' Since the more energetic particles are more mobile (having a larger diffusion length) they cross the shock front more often than the less energetic particles. Each time a particle crosses the shock front it gains energy. So as long as the diffusion length grows with particle energy,

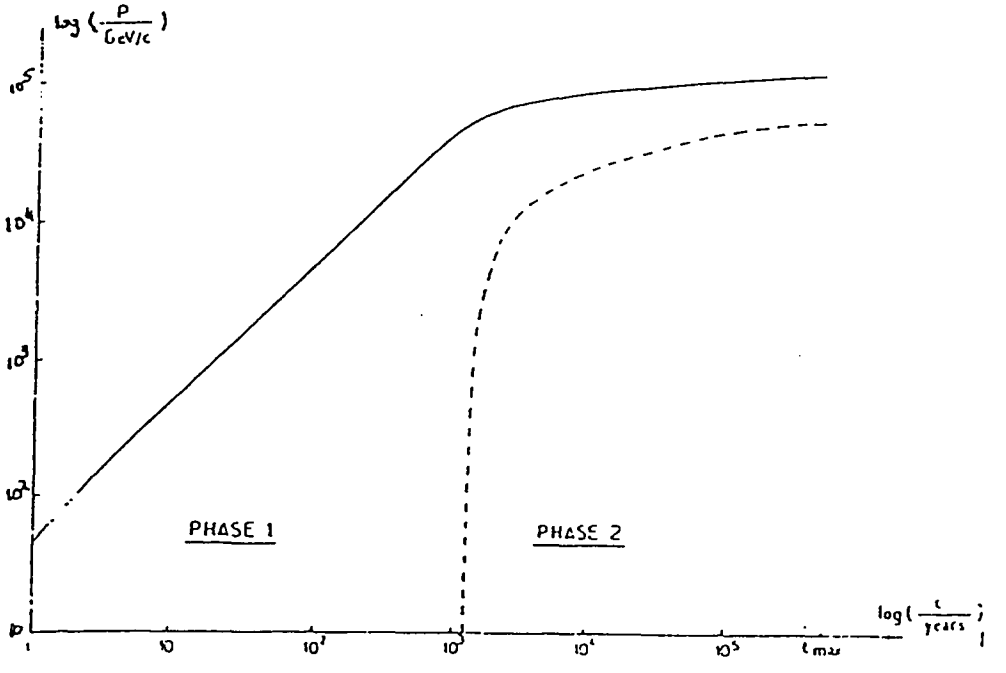

Figure 2.8 Variation with time of the momentum, p, of a proton accelerated by a SN I shock, evolving in a medium of density $s \times 10^{-3} cm^{-3}$ without cloud evaporation. Full line: injection at the beginning of the blast wave phase. Dotted line: injection at the beginning of the Sedov, (adiabatic), phase. (Lagage and Cesarsky 1983).

the shock will preferentially put its energy into high energy particles. As the shock propagates through the ISM it selects out the suprathermal particles from the bath (possibly in the hot, rarefied regions of the ISM and in the stellar winds of Wolf-Rayet stars) and accelerates them to high energies.

2.3.3 Pulsar Acceleration Mechanisms

We have seen above that shock acceleration mechanisms have difficulty in accounting for the higher energy cosmic rays, above $10^{14}eV$, and they certainly can not account for the highest energy cosmic rays. Pulsars have strong magnetic fields, $\sim 10^{12}Gauss$ and high spin rates, $\omega \sim 100rads/s$. So from dimensional arguments we could expect potentials of the order of $\Phi \sim \omega R^2 B/c \sim 10^{18}(B/B_{12})(\omega/\omega_{100})V$. Where B/B_{12} is the surface magnetic field in units of $10^{12}Gauss$, and ω/ω_{100} is the angular velocity in units of $100rads/s$. Any model of pulsar acceleration must localize this potential drop and show how particles can escape to infinity.

Because of their strong surface gravity it was first believed that pulsars would be surrounded by a vacuum. In this case the full potential of $10^{18}eV$ would be available, either from direct electrostatic acceleration, or from R.F. acceleration (Ostriker and Gunn 1969a, 1969b). In the latter case energies of $10^{21}eV$ are possible for young pulsars. We will see below that because of the large induced electric fields near the stellar surface, the pulsar can not be surrounded by a vacuum. Goldreich and Julian (1969) showed that a pulsar is surrounded by a charge separated plasma, known as the pulsar

magnetosphere. In this case only a small fraction of the potential drop is available for particle acceleration, and the phase coherence necessary for R.F. acceleration is destroyed by the presence of the plasma (Arons 1981).

There is no completely satisfactory model of a pulsar magnetosphere. All of the models discussed below have difficulties which we will point out as we proceed. Be this as it may, we know from observations of the Crab nebula that pulsars do accelerate particles to high energies ($\sim 1TeV$ in the Crab). To date all observations of pulsars have been of 'low' energy photons, mainly synchrotron radiation from the charged particles. A direct observation of the highest energy particles would bring us a long way in understanding the basic workings of the pulsar mechanism.

Pulsar Magnetospheres

For a complete discussion of pulsar magnetospheres see Michel (1982). Here we will derive what has become the standard model of pulsar magnetospheres first put forward by Goldreich and Julian (1969). It is assumed that the supernova blast wave has swept up all matter in its path. The neutron star is surrounded by a vacuum out to a distance D, the present radius of the shock front. Using the assumption of a spinning, uniformly magnetized sphere of infinite conductivity, we derive the electric and magnetic fields everywhere. We find that the electric field at the surface is more than sufficient to remove electrons and possibly ions from the stellar surface and therefore our vacuum

model can not be correct.

We begin by assuming a uniformly magnetized neutron star whose rotation axis is aligned with the magnetic axis, say the $\hat{z}$ direction. The interior magnetic field is given by, $\vec{B}^{(in)} = B_0\hat{z}$, and the exterior field is purely dipolar. If the interior has infinite conductivity, we can immediately write down the electric field inside the star, $\vec{E}^{(in)} = -((\vec{\Omega}\times\vec{r})/c)\times\vec{B}^{(in)}$. Using the continuity of the tangential component of $\vec{E}$ across a boundary we find that just outside the stellar surface $E_\theta^{(out)} = -(\Omega B_0 R_*/c)\sin\theta\cos\theta = \frac{\partial}{\partial\theta}[(\Omega B_0 R_*/c)P_2(\cos\theta)]$. Where P_2 is the Legendre polynomial with $l = 2$ and R_* is the radius of the neutron star, $\sim 10^6 cm$. Using $\nabla^2\Phi = 0$ outside the star and the above boundary condition at the surface we can solve Laplace's equation outside the star:

$$\Phi(r,\theta) = -\frac{\Omega B_0}{c}\frac{R_*^5}{r^3}P_2(\cos\theta) \tag{2.28}$$

We now have the electric field everywhere. Since the magnetic field is strong ($\sim 10^{12} Gauss$), charged particles are constrained to the magnetic field lines. We find the component of the electric field parallel to the magnetic field at the surface, $\vec{E}\cdot\vec{B}/|\vec{B}| \sim -(\Omega B_0 R_*/c)\cos^3\theta$. Comparing the resulting electric force to the gravitational force, $F_E/F_G = (e\Omega B_0 R_*^3)/(GMmc) \sim 10^{12}/(10^9)$, for an electron/(proton), we see that electrons will stream from the poles and ions from the equatorial regions (opposite for an anti-aligned rotator). The demarcation line being where $\Phi(R,\theta) = 0$ (i.e. $\cos\theta = \sqrt{1/3}$).

Goldreich and Julian now make the assumption that particles are pulled from the surface to ensure that $\vec{E}\cdot\vec{B} = 0$ near the surface; a charge separated plasma of infinite conductivity surrounds the star. Infinite conductivity leads to the tying of magnetic field lines and charged particles, so the field lines can no longer co-rotate with the star beyond a radius $R_l = c/\Omega$, known as the light cylinder. Within this radius both particles and field lines co-rotate with the star and a corotating magnetosphere is established. The electric field can now be found from $\vec{E} = -((\vec{\Omega}\times\vec{r})/c)\times\vec{B}$, and the magnetospheric charge density from:

$$\rho = \vec{\nabla}\cdot\vec{E}/4\pi \tag{2.29}$$

$$= \frac{\vec{\Omega}\cdot\vec{B}}{2\pi}\frac{1}{1-(\Omega r/c)^2\sin^2\theta} \tag{2.30}$$

$$= 7\times10^{-2}B_z/P\ cm^{-3} \tag{2.31}$$

The last line is valid for regions close to the star , (i.e. $\Omega r\sin\theta/c \ll 1$).

There are two field lines of interest: the last closed field line, and the field line along which the potential is zero (i.e. no potential difference between stellar surface and the ISM). Using Figure 2.9 as a guide we find the last closed field line. Along any dipolar field line $\sin^2\theta/r$ is constant, therefore $\sin^2\theta_{cap} = R_*/R_l = R_*\Omega/c$. Particles can only escape along open field lines so θ_{cap} defines the region within which particles can escape from the surface to infinity, this region is known as the polar cap.

The field line along which the potential is zero is called the critical field

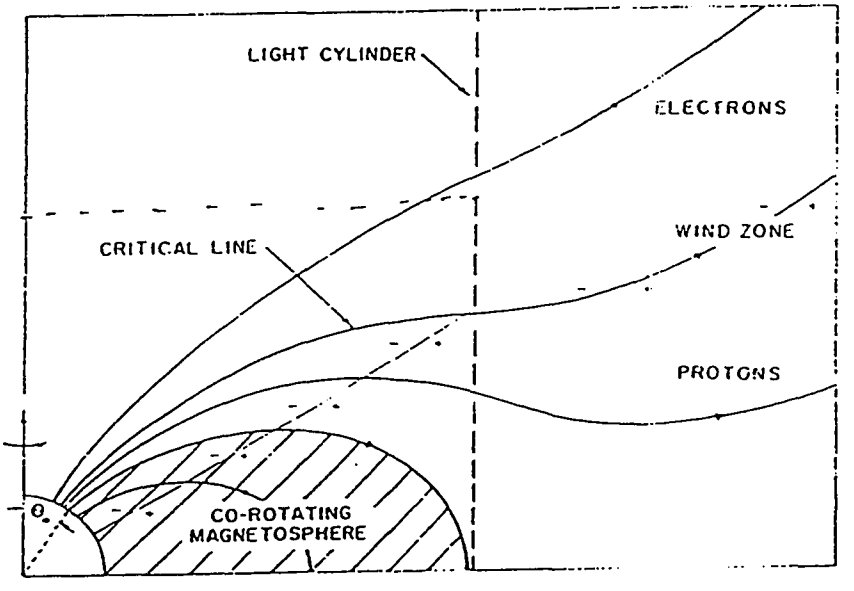

Figure 2.9. Pulsar and its Magnetosphere. (from Goldreich and Julian 1969)

line, and it presents us with our first difficulty. Using the potential derived above we see that this field line ($\cos\theta = \sqrt{1/3}$) lies deep in the region of closed magnetic field lines. We must close the electrical circuit in order to conserve charge. Goldreich and Julian do this by demanding that the polar cap consists of two regions, one from which negative charges flow, and one from which positive charges flow. The critical field line is found by demanding that the two currents are equal. This is just the field line that crosses the light cylinder parallel to the equator. Though the current closure problem has been solved we now demand that positive charges stream out through a region of the magnetosphere that is negatively charged, a point noted by the authors.

Acceleration of Charges in the Standard Model

Since particles can only escape along open field lines the full potential from pole to equator is not available for acceleration. In the Goldreich Julian model only the potential difference from the pole to the edge of the cap is available. Using the vacuum potential derived above we find that:

$$\Delta\Phi_{max} = \Phi(\cos 0) - \Phi(\cos\theta_{cap}) \tag{2.32}$$

$$= \frac{\Omega B_0 R^2}{3c}[P_2(1) - P_2(1 - \Omega R/2c)] \tag{2.33}$$

$$= \frac{1}{2}\left(\frac{\Omega R}{c}\right)^2 B_0 R \tag{2.34}$$

$$= 6 \times 10^{12} R_6^3 B_{12}/P^2 \; eV \tag{2.35}$$

Since $\vec{E} \cdot \vec{B} = 0$ in the light cylinder all of the acceleration takes place far from the star in regions of reduced magnetic field. Using the period of the Crab pulsar we find a maximum energy of $10^{15}\ eV$, more than sufficient to explain the optical synchrotron radiation emanating from the nebula. The fastest young pulsars, with $P = .001s$ and $B = 10^{12}G$, could in principle accelerate particles to $6 \times 10^{18}\ eV$. However, Goldreich and Julian give no solution for the fields in the boundary zone and it is unclear if these potentials are actually realized.

Modifications of the Standard Model

One of the major shortcomings of the standard model is that it does not predict pulsations. One might think that a misalignment between rotation axis and magnetic axis would solve this deficiency. In fact the problem is deeper. In the standard model acceleration takes place well beyond the light cylinder, in the boundary zone where $\vec{E} \cdot \vec{B} \neq 0$. To obtain coherent emission in the form of pulses we must bring the acceleration region inside the light cylinder, where we have corotation with the neutron star. Then a misalignment between spin and magnetic axes will lead to the observation of pulses.

What is needed is a region where there is a nonzero component of the electric field parallel to the magnetic field. Since particles emitted by the neutron star insure that $\vec{E} \cdot \vec{B} = 0$, a lack of these particles would result in

an accelerating region within the light cylinder. The first such model was put forth by Sturrock (1971) and later modified by Ruderman and Sutherland (1975).

In high magnetic fields, where the Larmor radius is comparable to the classical electron radius ($H \sim m^2c^3/e\hbar \sim 4 \times 10^{13} Gauss$), atoms become needle shaped, with their axis aligned with the magnetic field. This results in a large electric quadrupole moment and strong interatomic attraction (Zeldovich 1983). This attraction leads a large binding energy, making the availability of positive ions questionable. The current from the surface depends on the temperature of the surface, the electric field above the surface, and the binding energy of the material. Initial estimates of the binding energy, $\sim 14 KeV$ (Ruderman and Sutherland 1975), lead to the belief that no positive ions would be available (except in very young pulsars with high surface temperatures and a He layer on their surface). More recent estimates place the binding energy at a few KeV and the availability of ions is unclear.

Ruderman and Sutherland assumed that while electrons are freely emitted from the star, positive ions are bound to the surface. In an anti-aligned rotator the polar caps would normally be a source of positive charges acting to cancel any component of the electric field parallel to the magnetic field. They found that the unavailability of such charges causes the magnetosphere to pull away from the surface leaving a gap where $\vec{E} \cdot \vec{B} \neq 0$. The electric field at the pole is normal to the surface and given by $E_p = 2\Omega B_0 h/c$, where

h is the gap height, and the potential across the gap is $\Delta V = \Omega B h^2/c$. As positive charge streams out along the open field lines the gap grows (since the surface can not provide the replacement charge). The gap size is limited by a positron electron avalanche that is started by any photon which enters the gap. If $E_\gamma B_\perp \geq 10^{18} G \cdot eV$ then the reaction $\gamma + B \rightarrow e^+ + e^- + B$ becomes possible. The electrons stream towards the surface and the positrons follow the field lines towards the top of the gap. Since the field lines are curved the electrons and positrons emit curvature radiation in the form of high energy photons, $E_\gamma \approx \gamma^3 \hbar c/\rho$. These photons do not follow the magnetic field lines and therefore can pair create in the strong magnetic field (photons travelling parallel to the magnetic field can not pair create). These pairs emit more curvature radiation and the process continues leading to an avalanche discharge which stops the growth of the gap. Ruderman and Sutherland derive an equilibrium gap height of roughly $1000cm$ (Figure 2.10).

While the above model can explain many features of pulsars it is totally inadequate in explaining high energy particle production. The strong magnetic fields near the poles lead to a degradation of photon energies and the most energetic photons which escape have frequencies $\nu_{max} = 2 \times 10^9 P^{-67/28} Hz$.

To explain the higher energy radiation Cheng and Ruderman (1986) proposed that gaps could form in the outer magnetosphere. Bypassing the issue of how such gaps would form they claim that the only stable gap would be along the last closed field line with one end at the null surface and the other

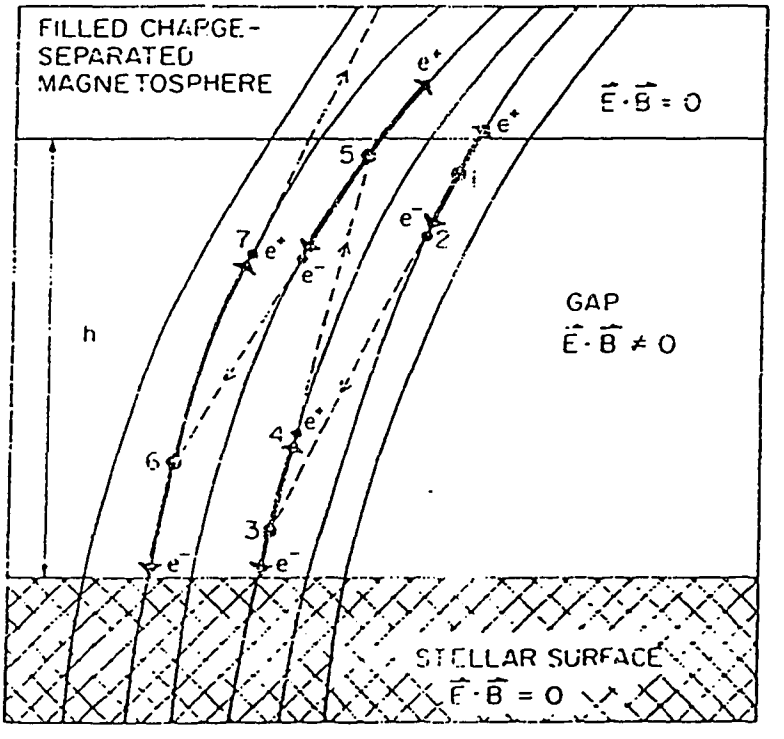

Figure 2.10 Magnetospheric gap at pulsar pole. (from Ruderman and Sutherland 1975)

end at the light cylinder (see Figure 2.11), though the exact location of the ends are in doubt. Since the gap is far away from the surface the magnetic field is greatly reduced and the above mechanism, $\gamma + B \rightarrow e^+ + e^- + B$, is not capable of limiting the length of the gap. Instead they propose $2\gamma \rightarrow e^+ + e^-$, as a source of e^+e^- pairs. The C.M. energy of the photons must be greater than $E_{\gamma 1}E_{\gamma 2} \geq m_e^2 \sim .25TeV^2$ for this process to occur. So one needs GeV photons to interact with the ambient X-rays and TeV photons to interact with the optical or infrared photons. Making many assumptions and some very crude approximations, they estimate the total available potential along such a gap to be $\Delta V \sim 1.3 \times 10^{14}/P\ Volts$. This potential can only be fully realized by protons and nuclei; curvature radiation and inverse Compton scattering limits the energy of electrons accelerated within the gap to roughly $10^{13}eV$. This is the maximum energy gamma rays which escape to infinity. The actual energy might be considerably lower, depending on the material beyond the outer gap.

2.3.4 Acceleration in Compact Binary Systems

If a neutron star is a member of a close binary system, matter can be transferred from the 'normal' star onto the neutron star. This can occur either via a stellar wind or Roche lobe overflow (see Figure 2.12). The latter occurs when the companion star has evolved to such a stage that its radius is greater than the radius of the Roche lobe, and matter flows through the first Lagrange point. If mass transfer takes place via Roche lobe overflow,

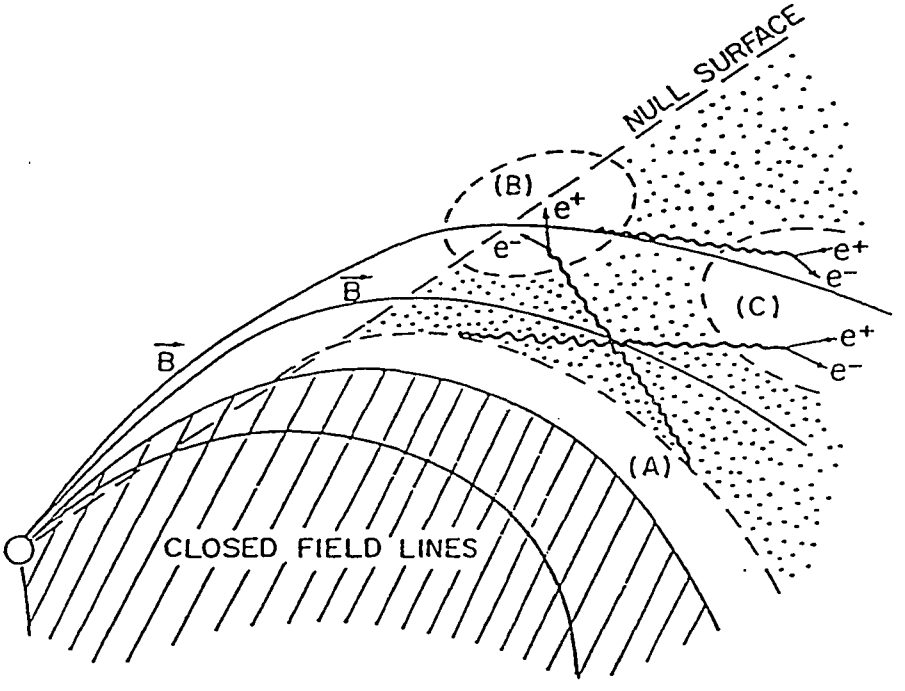

Figure 2.11 Outer Gap in magnetosphere. (from Cheng and Ruderman (1986a)

the material will have a significant amount of angular momentum. Since the material can thermalize much quicker than it can shed angular momentum, it will form a disc as it spirals onto the neutron star. In the case of a stellar wind the material might not possess sufficient angular momentum to form an accretion disc. Stellar winds typically transfer $10^{-7} - 10^{-6} M_{\odot}/yr$, while rates of roughly, $3 \times 10^{-4} - 3 \times 10^{-8} M_{\odot}/yr$ are possible via Roche overflow.

To date two proposals have been put forward for particle acceleration in such systems. One involves acceleration at a standing shock, expected to form near the poles of the neutron star, the other dynamo action by a differentially rotating accretion disc.

Spherical Accretion

We first take a look at the flow of material from the normal star to the neutron star surface. After the material passes through the first Lagrange point its trajectory is determined by gravitational forces. The matter free falls into the neutron star until the magnetic field becomes strong enough to dominate the motion. This occurs at the Alfven radius, where the magnetic energy density is equal to the kinetic energy density.

$$B^2(r)/8\pi = 4\pi\rho(r)v^2(r) \tag{2.36}$$

For spherical accretion the Alfven radius is readily calculable. For a dipolar field, $B(r) = 10^{30} B_{12} R_6^3/r^3$, and for material in free fall, $v(r) =$

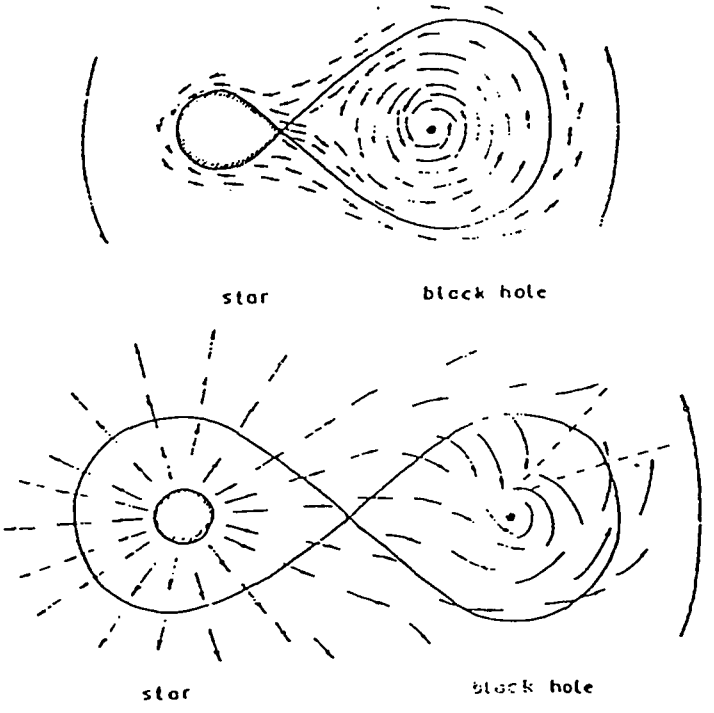

Figure 2.12 Compact Binary system. Top: Roche Lobe overflow, Bottom: Stellar Wind. (From Shakura and Sunyaev (1973)

$\sqrt{(2GM/r)}$. If matter doesn't accumulate anywhere (except at the surface) then $\dot{M}(r) = constant = 4\pi r^2 v(r)\rho(r)$, so $\rho(r) = \dot{M}/(4\pi v(r) r^2)$. Solving for r in eq. 2.36:

$$R_A = 3.2 \times 10^8 \dot{M}_{17}^{-2/7} \mu_{30}^{4/7} (M/M_\odot)^{-1/7} cm \qquad (2.37)$$

Where $\mu_{30} = B_{12} R_6^3$ is the magnetic moment of the neutron star in units of $10^{30} G\ cm^3$ and $\dot{M}_{17}$ is the mass transfer rate in units of $10^{17} g\ s^{-1}$.

Within the Alfven radius the particle trajectories are determined by the magnetic field. Charged particles are forced to corotate with the neutron star and are funneled onto the star's polar regions.

When the matter strikes the stellar surface the kinetic energy is transformed into heat and radiated away. If all of the kinetic energy is so transformed the resultant luminosity will be, $L = (1/2)\dot{M} v_{ff}^2 = G\dot{M}M/R$ With this relation between luminosity and the rate of mass transfer we find:

$$R_A = 3.5 \times 10^8 L_{37}^{-2/7} \mu_{30}^{4/7} (M/M_\odot)^{1/7} R_6^{-2/7} cm \qquad (2.38)$$

Since there is a limit to the accretion driven luminosity, the value of R_A can not vary by more than a few orders of magnitude.

Eddington Limiting Luminosity

Since the radiation force on a proton is less than that on the electron by a factor of $(m_e/m_p)^2$, radiation pressure acts mainly on electrons. The electrostatic force between electrons and protons forces the protons to follow the electrons. Since the proton mass is much greater than the electron mass we can find the maximum accretion rate by balancing the gravitational force on a proton with the radiation force on an electron. We assume steady state, spherical accretion of ionized hydrogen. The force on an electron is given by the energy flux times the Thompson cross section, so at a distance r from the surface (the source of the luminosity) $F_{rad} = L\sigma_T/(4\pi r^2 c)$. Equating this with the gravitational force on the proton gives us the maximum stable luminosity, the Eddington limit.

$$\frac{L_{Edd}\sigma_T}{4\pi r^2 c} = \frac{GMm_p}{r^2} \tag{2.39}$$

$$L_{Edd} = \frac{4\pi c}{\sigma_T} GMm_p \tag{2.40}$$

$$= 1.3 \times 10^{38} \frac{M}{M_\odot} \, ergs/s \tag{2.41}$$

With this relation, and eq, 2.38 we see that the Alfven radius can be no closer to the star than:

$$R_A \geq 1.7 \times 10^8 B_{12}^{4/7} R^{10/7} (M/M_\odot)^{8/7} \tag{2.42}$$

We will see below that extracting the maximum voltage drop across an accretion disc requires bringing the Alfven radius as close to the stellar surface as possible. Consequently one requires small magnetic fields, $B \ll 10^{12}G$, to attain the highest possible energies. This is just the opposite of what we found in the case of pulsar acceleration.

Systems with Discs

For a system with an accretion disc the dynamics are much more complicated. Here one must balance the magnetic stress with the viscous stress on the accreting matter. Viscosity in a disc (and consequently the transport of angular momentum) is poorly understood. Normal molecular viscosity is orders of magnitude too small to account for the observed accretion rates. It is believed that turbulence and magnetic stress are the main arbiters of angular momentum transport within the disc. Shakura and Sunyaev (1973) handled the case of accretion onto a black hole (no stellar magnetic field). They found that magnetic stresses contribute an amount $(H_r \times H_\phi)/8\pi$ to the viscous stress tensor and turbulence an amount $\sim \rho v_t v_s$, where ρ is the density of the disc, v_t is the turbulent velocity, and v_s is the speed of sound in the plasma. This can be rewritten as:

$$w_{r\phi} \sim \rho v_s^2 \left(\frac{v_t}{v_s} + \frac{H^2}{4\pi\rho v_s^2} \right) \tag{2.43}$$

$$= \alpha \rho v_s^2 \tag{2.44}$$

All of our ignorance (i.e. magnetic field amplification and turbulence in discs) has been parameterized by the quantity α. Shakura and Sunyaev show that on very general principles $\alpha \lesssim 1$. In fact one generally assumes $\alpha = 1$.

Gosh and Lamb (1978, 1979a, and 1979b) extended the above model to include the magnetic coupling between the disc and a magnetized neutron star. They find that there is a thin boundary layer at $R_0 \approx .41 R_A$, of thickness $.03 R_0$, where the plasma leaves the plane of the disc and follows the field lines onto the poles. This is followed by a broad transition region, where the rotation is Keplerian but magnetic coupling to the star is still important (see Figure 2.13). Beyond the transition region the stellar field is completely screened.

Shock Acceleration

As the material follows the magnetic field lines and flows onto the polar cap it forms an accretion column. Within this column it is possible, though by no means definite, that a shock will form (Frank et. al. 1985). We know that a shock mediated by collisions is not possible since the mean free path of the particles, $\lambda \gtrsim 5 \times 10^9 cm$ (Frank p147), is much larger than any other length scale around. There is still the possibility of forming a collisionless shock. For the case of a neutron star accreting near the Eddington limit radiation pressure becomes an important mediator of the shock. At low accretion rates the shock would be located near the stellar surface. An increase in the

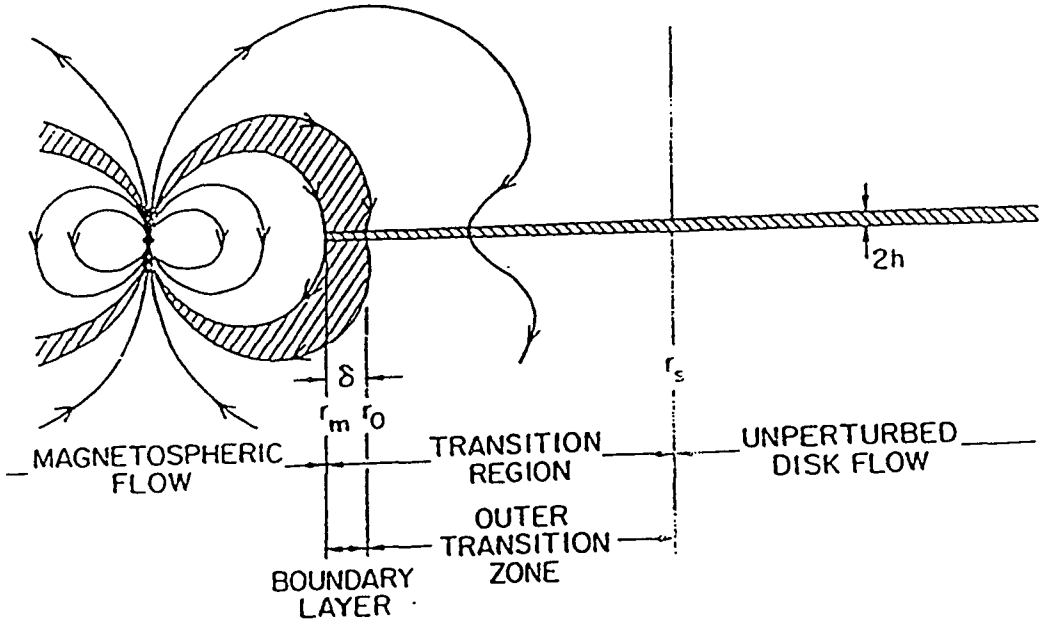

Figure 2.13 Accretion onto a neutron star. (From Ghosh and Lamb (1978)

accretion rate tends to elevate the location of the shock, though the exact dependence of accretion rate and shock height is poorly understood.

If a shock does form there is the possibility of first order Fermi acceleration at the shock. Eichler and Verstrand (1985) were the first to suggest this as a source of high energy particles in accreting systems. In the case of acceleration by supernova shock waves we found that the maximum energy attainable was dependent purely on the shock radius and the amount of turbulence. Here, because of the strong magnetic fields, we must worry about synchrotron losses. By balancing energy gain with radiation losses Eichler and Verstrand find for the maximum energy:

$$\gamma_{max} = \beta_s \left[\left(\frac{3}{2\pi\zeta} \right) \frac{Rm}{Z^2 r_e m_e} \right]^{1/3} \tag{2.45}$$

where ζ is the mean free path of the particles in units of the Larmor radius ($\zeta \sim 1$), R is the radius of the shock, r_e is the classical electron radius, and β_s is the shock velocity in the frame of the upstream scatterers, $\beta_s = v_{ff} = \sqrt{(2GM/R)}$. For shocks formed near the stellar surface ($R \sim 10^6 cm$ and $\beta_s \sim c/2$) proton energies of $10^7 GeV$ are possible.

If the accretion is from a stellar wind, there will be a shock at the Alfven radius, $R_A \sim 10^8 cm$. Now the shock velocity is just the velocity of the stellar wind. If the wind is relativistic we can take $\beta_s \sim c$, and proton energies of $\sim 10^8 GeV$ are possible.

In this model the protons form a beam which interacts with surrounding

material, either in the accretion disc or the companion star (the so called 'beam dump' model). The proton proton collisions create pions which subsequently decay to photons, muons, electrons, and neutrinos. To be an effective source of gamma rays the dump material should be at least one interaction length thick, any less and not many photons will be created, and no thicker than one radiation length (so that gamma rays can escape without being reabsorbed). If the model is correct one should see gamma rays when the beam grazes the companion star or the accretion disc. If the accretion disc is optically thin, one should observe γ-rays when a clump of matter in the disc intercepts the beam. One therefore expects only short bursts of gamma rays from these sources. If one where to detect neutrinos the situation would be more advantageous, in that any thickness of material greater than an interaction length will do, since neutrinos will always be able to escape from the dump.

Since the proton beam originates at the polar cap, it will sweep through the observers line of sight at the rotational period of the neutron star. Therefore this model predicts that any gamma ray or neutrino signal should be periodic, with the rotational period of the neutron star.

Unipolar Inductors

A rotating, conducting disc immersed in a magnetic field develops an *EMF* between the rotation axis and the disc edge. In a Keplerian accretion disc

(beyond the Alfven radius) the differential rotation will set up a potential drop between the inner and outer edges of the disc. This model was originally proposed as a model for AGNs, $10^8 M_\odot$ black hole surrounded by an accretion disc, by Lovelace (1976). Chanmugam and Brecher (1985) where the first to adopt this model to accreting neutron stars.

For a disc of infinite conductivity,

$$E(r) = (1/c)\vec{v}(r) \times \vec{B}(r)$$

. For a Keplerian disc, $v_\phi(r) = \sqrt{GM/r}$, the radial electric field is, $E_r(r) = (1/c)\sqrt{GM}r^{-1/2}B_z(r)$, and the potential drop across the disc is then:

$$V = \int_{r_1}^{r_2} E_r(r)dr \tag{2.46}$$

$$= \sqrt{GM}/c \int_{r_1}^{r_2} B_z(r)dr/\sqrt{r} \tag{2.47}$$

The magnetic field in the disc is not the normal dipolar field associated with the neutron star. That field is mostly shielded by the portion of the disc within the Alfven radius and matter flowing to the poles. The disc field is generated by dynamo action within the disc, following Lovelace (1976) we take $B_z(r) = B_z(r_1)\sqrt{r_1/r}$. The potential drop is then given by:

$$V = \frac{\sqrt{GM}}{c} \int_{r_1}^{r_2} \frac{B_z(r)}{\sqrt{r}} dr \tag{2.48}$$

$$= \frac{\sqrt{GM}}{c} \sqrt{r_1} B_z(r_1) \ln(r_2/r_1) \tag{2.49}$$

Taking the inner radius to be the Alfven radius and the magnetic field at the inner radius to be that given by the neutron star's dipolar field, $B_z(r_1) = B_0(R/r_1)^3$ (Chanmugan and Breecher 1985), the resulting potential is:

$$V = 3.8 \times 10^{32} M_{33.3}^{1/2} B_{12} R_6^3 r_1^{-5/2} \ln(r_2/r_1) \quad (2.50)$$

$$= 2.6 \times 10^14 B_{12}^{-3/7} L_{38}^{5/7} R_6^{-4/7} M_{33.3}^{1/7} Volts \quad (2.51)$$

$$\leq 2 \times 10^{17} Volts \quad (2.52)$$

Where the last inequality comes from associating the inner edge of the disc with the surface of the neutron star, corresponding to a surface field $B = 1.3 \times 10^8 G$.

As with the shock acceleration model outlined above, gamma rays and neutrinos would be produced by interaction of the accelerated protons with the surrounding material. In this model it is difficult to imagine (though Chanmugan and Beecher discuss the possibility) that any signal would be pulsed at the rotational period of the neutron star.

Chapter 3

Cygnus X–3: Observations and Models

3.1 Introduction

First discovered as an X-ray source in 1966 (Giacconi et. al. 1967), it was a huge radio outburst in 1972 that brought Cygnus X–3 to everyone's attention. With the 1983 report of $10^{15}eV$ particles coming from Cygnus X–3, it became one of the most studied objects in the sky. It soon became accepted that this was indeed a bizarre and poorly understood object which might very well be a significant source of high energy cosmic rays. With the reporting of underground muon signals from Cygnus it also became a focal point for particle theorists. Lack of convincing modern confirmation and contradictions among various experiments have cast doubts on the original claims. However, the recent reports by two groups of EeV ($10^{18}eV$) radiation from Cygnus, keep the controversy brewing. In this chapter we will review the

observations of Cygnus X–3 from radio wavelengths to the highest energies particles.

3.2 Radio Observations of Cygnus X–3

In a 1971-1972 radio survey of known x-ray sources Braes and Miley (1972) discovered the radio counterpart of Cygnus X–3. Though a weak radio source it was the strongest counterpart of the known x-ray sources (excluding supernova remnants). Later that year Gregory (1972) (and Hjellming and Balick 1972) observed a large flaring event where Cygnus became one of the strongest radio sources in the sky ($\sim 20Jy$). Based on the temporal evolution of the radio spectrum (see Figure 3.1), time of maximum flux increases with decreasing frequency, the flare was interpreted as synchrotron radiation from an expanding cloud of relativistic electrons. As the cloud expands its density decreases and it becomes transparent to progressively lower frequencies (Van der Laan 1966).

Subsequently there have been many large radio flares (Johnston et. al. 1986), the last two occurring in 1989. VLBI observations during the times of the flares showed an evolving structure similar to the jets observed in SS433. Though the two jets were not individually resolved a linear expansion rate of $0.6c$[1] (Geldzahler et. al. 1983 and Spencer et. al. 1986) was measured,

[1]The inferred expansion velocity is dependent on the distance to Cygnus. Unfortunately this is not very well known. Dickey (1983), using the absorption of $21cm$ radiation during the October 1982 outburst, inferred a lower limit of $11.6 \times (\pi_\odot/10kpc)kpc$, where $\pi_\odot$ is the distance from the sun to the galactic center. Recent estimates place the galactic center $(8.5 \pm 1)kpc$ away (Binney and Tremaine 1987). For the above velocity and for the remainder of this thesis we assume a distance to Cygnus X–3 of $10kpc$.

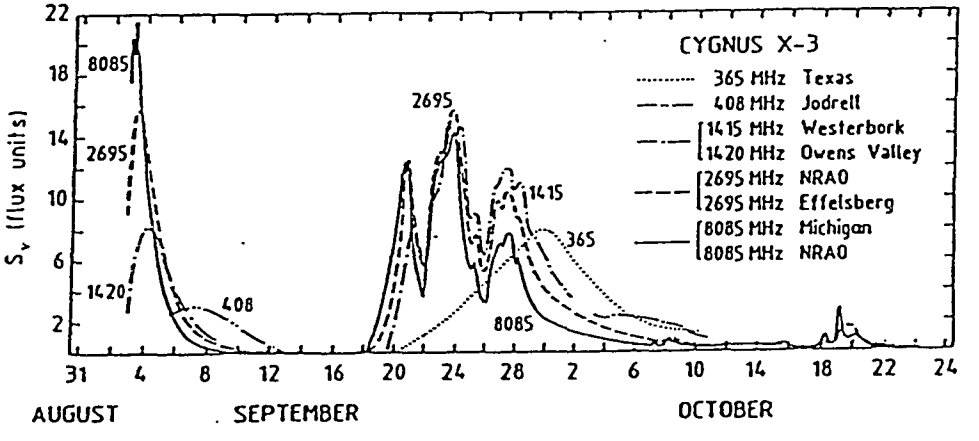

Figure 3.1 Radio flux versus time for September 1972 outburst. (from Bonnet-Bidaud and Chardin 1988)

and assuming a two jet morphology, one arrives at an expansion velocity of $\sim 0.3c$, very similar to that of SS433, $(0.26 \pm 0.3)c$. More recent VLBI surveys have resolved a double radio source straddling the compact core of Cygnus (Strom et. al. 1988), thus confirming the two jet hypothesis.

In addition to the flaring activity, there is also quiescent radio emission from Cygnus X–3. The low level radio activity seems to be composed of a superposition of flares similar in structure to the large flares, differing only in their strength (Molnar 1985). There is some evidence (of low statistical significance) that these small flares occur with a preferential period of 4.95 hours (Molnar 1985, and Molnar et. al. 1988b), though no such periodicity has been seen in the larger ($> 50mJy$) flares (Johnston et. al. 1986).

3.3 Infra-Red Observations

In a series of IR observations, some simultaneous with radio and x-ray observations (Becklin et. al. 1974, Mason et. al. 1976, and Mason et. al. 1986), it was found that the IR radiation was also modulated at the $4.8hr$ x-ray period though with much less modulation (10%).

As with the radio data, a large number of flares were observed, some with intensities over twice the quiescent level. Their fast rise time suggests that they originate close to the binary system (the inner part of any radio jet). Mason et. al. (1986) suggest that the flares originate from hot blobs of plasma being ejected from the system, and as they expand, cool, and become

optically thin, become the low level radio flares observed by Molnar (1985).

3.4 X-Ray Observations

Figure 3.2 shows a continuous 30.6 hour observation of Cygnus X–3 taken with the EXOSAT MEDA detector between July 3 and 4, 1983 (Willingale, et. al. 1985). There are 3 striking features:

1 There is a periodic modulation, but no extinction usually associated with an eclipse, of the x-ray intensity.

2 There are large cycle to cycle variations in the flux.

3 There is significant structure on short timescales.

Examination of Figure 3.3 reveals the presence of much larger long term intensity fluctuations which can persist over many cycles. In this section we will review the known x-ray properties of Cygnus X–3. Starting with periodic behavior and then covering random changes in the x-ray behavior of Cygnus.

3.4.1 Periodic Phenomena

4.8 Hour Period

The only irrefutable period in Cygnus X–3 is the 4.79 hour modulation in the x-ray intensity first observed by Parsignault (Parsignault, et. al., 1972). The most recent ephemeris (van der Klis and Bonnet-Bidaud 1988) is given in

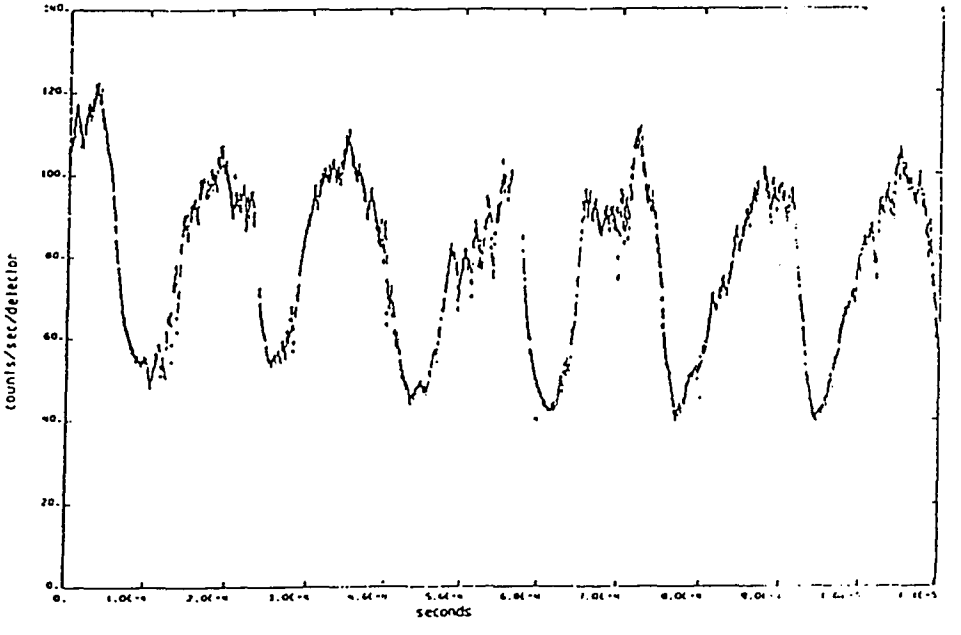

Figure 3.2 Light curve of Cygnus X–3 in the energy band 1.5-15 KeV recorded by EXOSAT MEDA. Bin size is 40s. (from Willingale 1985)

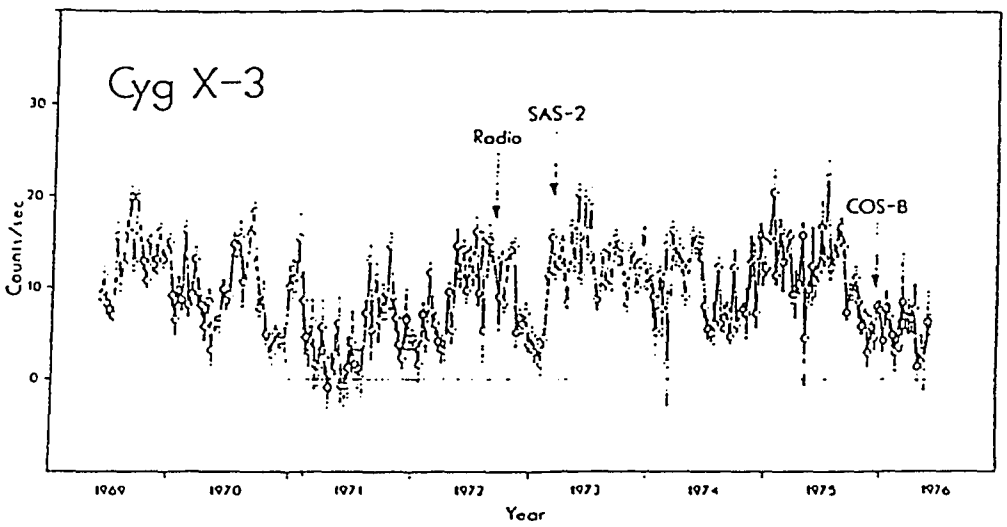

Figure 3.3 Flux history at 3-12 KeV of Cygnus X–3, in 10 day averages, from *Vela 5B* satellite. Arrows mark the giant radio outburst of 1972 September, and the 1973 *SAS-2* and 1975 *COS B* gamma ray observations. (from Priedhorsky and Terrel 1986.)

Table 3.1 (in all subsequent analysis the quadratic ephemeris from this table is used). The light curve is seen to be slightly asymmetric (Figure 3.4), with a gradual rise followed by a steep decline. Despite fluctuations in the arrival time of x-ray minimum, and cycle to cycle changes in the shape of the light curve, averaged over several cycles the light curve is found to be extremely stable. This long term stability, over a span of nearly twenty years, has led to the conclusion that this period is due to orbital motion. For a circular orbit Kepler's third law gives the orbital separation as $a = 10^{11}(M/M_{\odot})^{1/3}cm$.

The first secular change in this period, detected in 1977 by COS-B (Manzo, et. al., 1978), was measured to be $\dot{P} = (2.83 \pm .67) \times 10^{-9} ss^{-1}$. Subsequent observations have confirmed the existence of a period derivative, though the measured value has steadily decreased: $\dot{P} = (1.78 \pm 0.40) \times 10^{-9} ss^{-1}$ (Elsner, et. al. 1980), $\dot{P} = (1.18 \pm 0.14) \times 10^{-9} ss^{-1}$ (van der Klis and Bonnet-Bidaud 1981a), and $\dot{P} = (0.904 \pm 0.048) \times 10^{-9} ss^{-1}$ (van der Klis and Bonnet-Bidaud 1988). In the last analysis, using data taken between 1970 and 1985, van der Klis and Bonnet-Bidaud find evidence for a secular change in the period derivative, $\ddot{P} = (-0.16 \pm 0.04) \times 10^{-9} yr^{-1}$. If confirmed, this would shed light the nature of the system.

The three most natural explanations for an increasing period are:

1 Conservative mass transfer within the system.

2 Mass loss from the system.

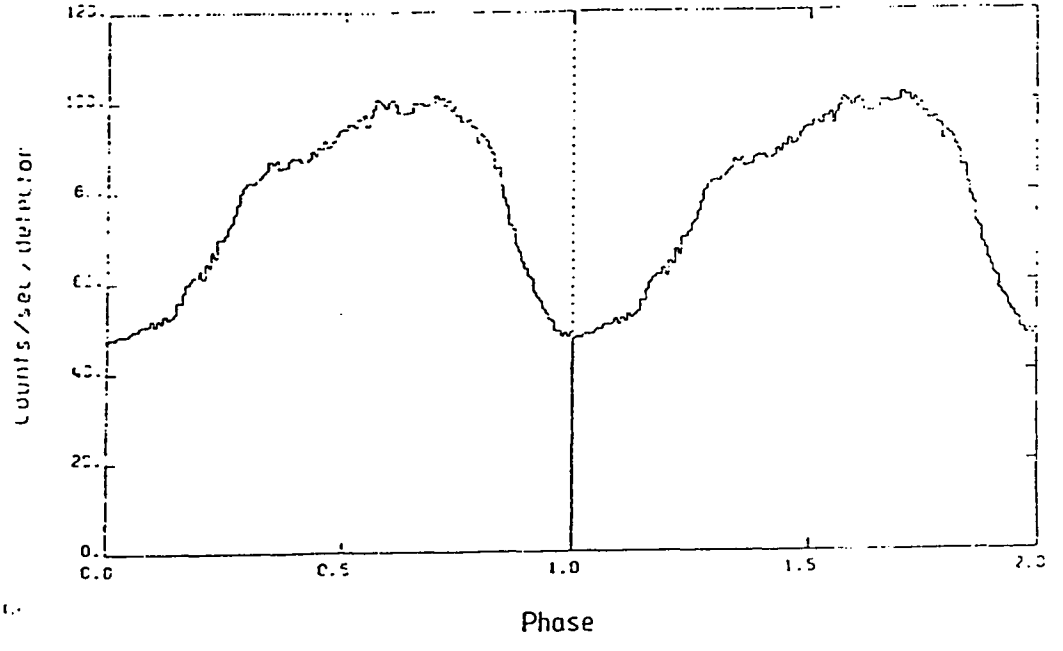

Figure 3.4 Flux in the energy band 1.5-15 KeV folded using ephemeris of van der Klis and Bonnet-Bidaud 1981a. (from Willingale 1985)

Linear ephemeris:

$T_n = T_0 + Pn$
T_0 = HJD 2 440 949.881 25 ± 0.00049
P = 0.199 686 274 ± 0.000 000 030 d $\mathrm{Cov}(T_0, P) = -1.3\ 10^{-11}$ d^2

Parabolic ephemeris:

$T_n = T_0 + P_0 n + cn^2$, where $\mathrm{Cov}(T_0, P_0) = -1.3\ 10^{-10}$ d^2
$c = P_0\dot{P}/2$ $\mathrm{Cov}(T_0, c) = 3.9\ 10^{-15}$ d^2
T_0 = HJD 2 440 949.896 22 ± 0.000 94 $\mathrm{Cov}(P_0, c) = -7.1\ 10^{-19}$ d^2
P_0 = 0.199 683 54 ± 0.000 000 15 d $\dot{P} = (0.904 \pm 0.048)\ 10^{-9}$
$c = (9.03 \pm 0.48)\ 10^{-11}$ d $\dot{P}/P_0 = (1.6 \pm 0.1)\ 10^{-6}$ yr^{-1}

Cubic ephemeris:

$T_n = T_0 + P_0 n + c_0 n^2 + dn^3$, where $\mathrm{Cov}(T_0, P_0) = -6.2\ 10^{-10}$ d^2
$c_0 = P_0\dot{P}_0/2$ and $\mathrm{Cov}(T_0, c_0) = 4.4\ 10^{-14}$ d^2
$d \approx P_0^2\ddot{P}/6$ $\mathrm{Cov}(T_0, d) = -9.0\ 10^{-19}$ d^2
T_0 = HJD 2 440 949.9013 ± 0.0016 $\mathrm{Cov}(P_0, c_0) = -4.9\ 10^{-22}$ d^2
P_0 = 0.199 681 96 ± 0.000 000 42 d $\mathrm{Cov}(P_0, d) = 1.0\ 10^{-26}$ d^2
$c_0 = (2.18 \pm 0.32)\ 10^{-10}$ d $\mathrm{Cov}(c_0, d) = -8.5\ 10^{-31}$ d^2
$d = (-2.89 \pm 0.72)\ 10^{-15}$ d $\dot{P}_0 = (2.18 \pm 0.32)\ 10^{-9}$
$\ddot{P} = (-0.16 \pm 0.04)\ 10^{-9}$ yr^{-1}

Table 3.1 Ephemeris for Cygnus X–3. (from van der Klis and Bonnet-Bidaud 1988)

3 The period is not really changing; we are seeing apsidal precession in an eccentric orbit.

For conservative mass transfer in a circular system, $\dot{P}/P = 3(1/M_x - 1/M_c)\dot{M}_{acc}$ (Bonnet-Bidaud and Chardin 1988). If we assume that the x-ray luminosity is due to accretion then $\dot{M}_{acc} = 10^{-8} M_\odot yr^{-1}$. With $M_x = M_\odot$ we obtain $M_c = .03 M_\odot$ for the companion mass. Originally this was thought to be unreasonably small, however there is some recent evidence which points to a very small companion mass, $.0004 M_\odot < M_c < .05 M_\odot$, (Molnar 1988a).

If there is mass loss from the system, $\dot{P}/P \approx \dot{M}/M$, implying $\dot{M} \sim 10^{-6} M_\odot yr^{-1}$. This is the same order of mass loss as needed to explain the x-ray modulation in stellar wind models (Pringle 1974 and Davidsen and Ostriker 1974).

For a system with an eccentric orbit the shape of the light curve should change in unison with the changing period (Elsner et. al. 1980 and Ghosh et. al. 1981), and one also expects the period derivative to change. Interpreting $\ddot{P}$ as apsidal motion, van der Klis and Bonnet-Bidaud (1988) find an apsidal period of $27^{+4}_{-3} yrs$ and an eccentricity of 0.25. Over a 15 year observing period, over half of the apsidal period, there should have been significant changes in the asymmetry of the light curve; it has remained steadfastly constant.

One of the more informative aspects of the light curve is its behavior as a function of photon energy. After correcting for the effects of scattering

from interstellar grains [2] it is found that the depth of modulation, defined as $(S_{max} - S_{min})/S_{max}$ ($S = counts/sec$), falls steadily from .75 at $1KeV$ to nearly 0 at $50KeV$ (Figure 3.5). The glitch between $6 - 7KeV$ is due to K-shell ionization of iron in the environment of Cygnus X–3.

Other Periodicities

There have been many other periodicities reported, though none have been confirmed. Molteni et. al. (1980) reported a $34.1day$ period in the x-ray intensity with a modulation of $\sim$ 50%. On the basis of what he believed to be evidence for a Doppler shift of the $4.8hr$ period, though the data fits nearly as well to no Doppler shift (see Figure 2 of Molteni et. al. 1980), he interpreted the $34.1day$ modulation to be an orbital period and the $4.8hr$ period to be the rotational period of the compact x-ray source [3].

Holt et. al. (1976) reported a $16.7day$ period with an amplitude of 18%. In a later observation (Holt et. al. 1979) they failed to confirm this period, though they did claim evidence for a $33.0day$ period.

In long term observations (1969-1979) with the *Vela 5B* satellite, none of

[2]The original light curve showed no change in modulation depth with energy out to $10KeV$. However, scattering of x-rays from interstellar grains ($\sim .1\mu m$ size) produces an x-ray halo around the source (Mauche and Gorenstein 1986). Since the x-rays in the halo have been scattered, their arrival times at earth have been delayed with respect to the unscattered x-rays. The time delay is dependent on energy, $t_d = 16(E/1KeV)^{-2}(D/8Kpc)(a/.1\mu m)^{-2}$ (where a is the grain size) (Molnar and Mauche 1986), so that x-rays with energy less than $6KeV$ have been scattered uniformly over the $4.8hr$ phase.

[3]If one believes that there is an accretion disc in the system, then the stability of the $4.8hr$ period rules out the possibility of it being a rotational period.

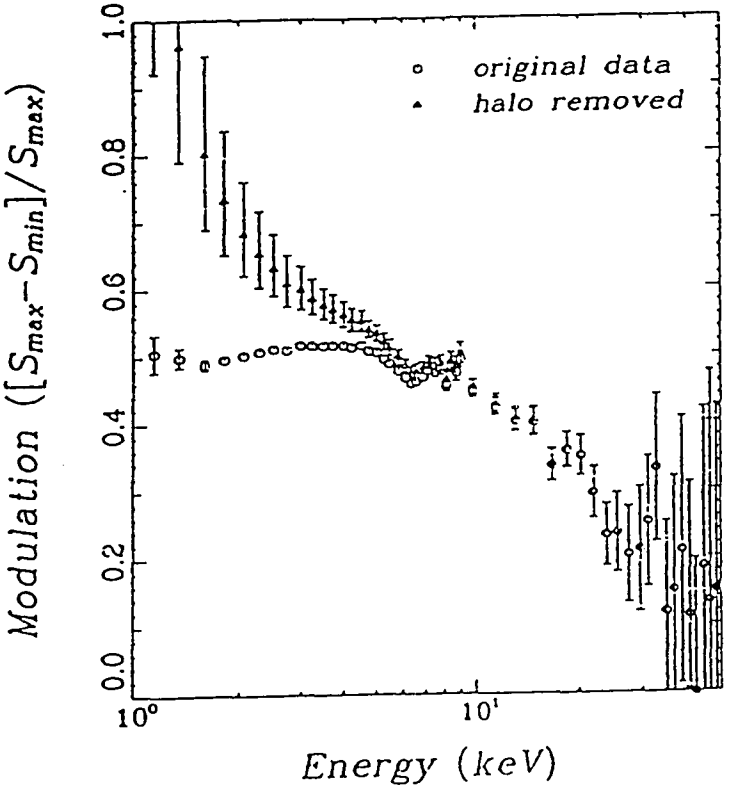

Figure 3.5 Depth of modulation as a function of energy. (from Molnar and Mauche 1986)

the above periodicities where observed (Priedhorsky and Terrel 1986).

Finally, van der Klis and Bonnet-Bidaud (1981b) collected a data set with evidence for an $18.7day$ periodic modulation in the arrival time of x-ray minimum. They attributed this to apsidal motion and derived an eccentricity of 0.03. Due to double aliasing of the $4.8hr$ period Priedhorsky and Terrel could not conduct a search for this period.

QPOs in Cygnus

In an analysis of EXOSAT data taken between October 1983 and May 1984, van der Klis and Jansen (1985) observed transient, quasi-periodic oscillations. The oscillations had quasi-periods between $50s$ and $1500s$ and lasted for 5 to 40 oscillation cycles. The amplitude of the oscillations was between 5 and 20% of the $1 - 10KeV$ flux and occurred only between orbital phases 0.0 and 0.75. If these are real there almost certainly must be an accretion disc in the system. van der Klis and Bonnet-Bidaud interpret these QPOs as arising from blobs of material projecting out of the plane of the disc, at radii between 5 and 50% of the radius of a Roche lobe filling accretion disc, occulting the compact x-ray source.

3.4.2 Non-Periodic Phenomena

Cycle to Cycle Variations

A glance at Figure 3.2 shows that there is large variability in the behavior of Cygnus X–3 from one cycle to the next as well as within one cycle. There is a roughly 10% variability on a timescale of a few 1000 seconds (Parsignault et. al. 1972, van der Klis and Bonnet-Bidaud 1982, and Willingale et. al. 1985)

Within an orbital cycle it is found that fluctuations occur preferentially between phases 0.2 to 0.3 and 0.5 to 0.6, see Figure 3.6, (van der Klis and Bonnet-Bidaud 1982 and Willingale et. al. 1985). The absence of fluctuations near phase 0.0 is taken as an indication of an eclipse of the central x-ray source at this orbital phase.

Long Term Variability

Use Figure 3.3 as a guide. There is a roughly 200% variability in the x-ray intensity over timescales of hours to days (Parsignault et. al. 1977). The variability occurs mainly in the low energy x-rays ($< 20KeV$).

Correlated with this change in x-ray flux are: the depth of modulation, the symmetry of the light curve, and the mean kT of the spectrum. As the intensity of the source increases the depth of modulation increases (Figure 3.7), the light curve becomes more symmetric (Figure 3.8), and the average kT decreases (Figure 3.9). The two curves in Figure 3.7 represent two different behaviors for the opacity as a function of intensity (van der Klis and

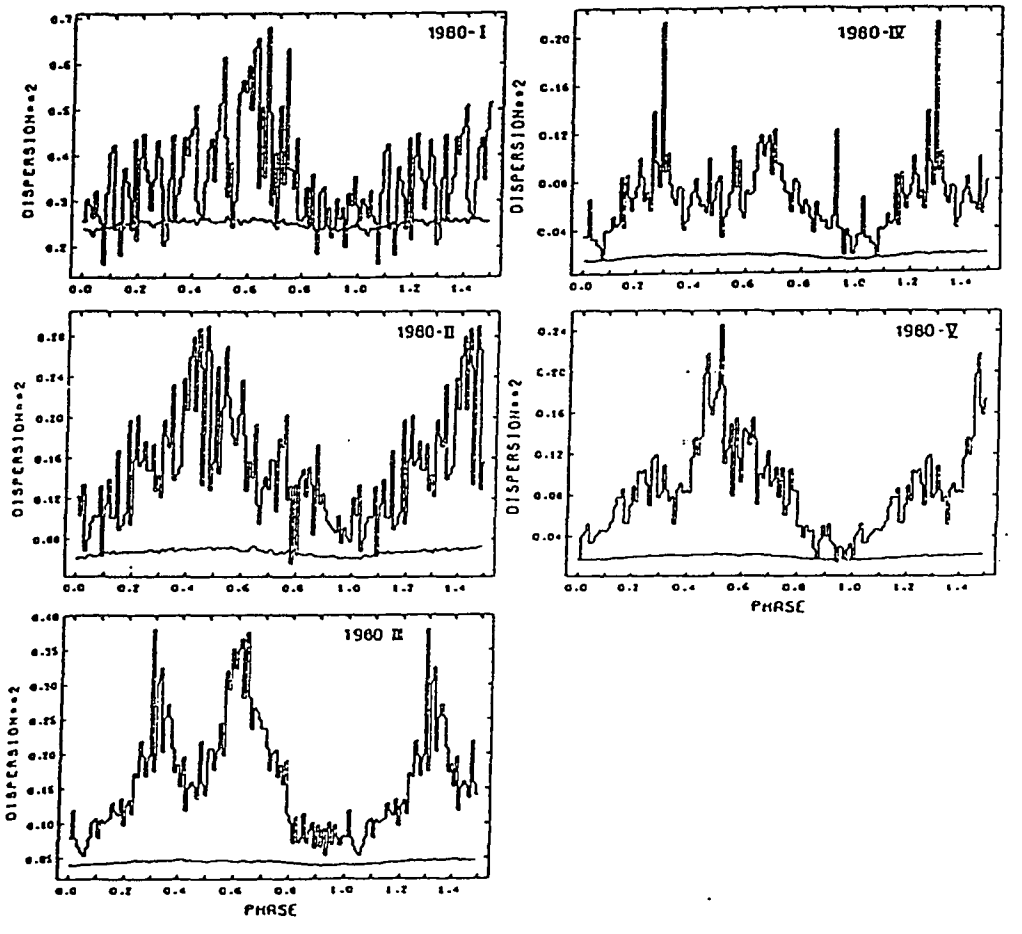

Figure 3.6 RMS fluctuations versus orbital phase (from van der Klis and Bonnet-Bidaud 1982)

Bonnet-Bidaud 1981b, Leach et. al. 1975, and Parsignault et. al. 1977). The dotted curve is what one would expect if the opacity increased with increasing flux, and the dashed curve if the opacity decreased with increasing intensity. As the x-ray intensity increases, the degree of ionization of the surrounding plasma increases. When the ionization is complete, bound-bound and bound-free contributions to the opacity are eliminated and Compton scattering (or Thompson scattering) dominates the opacity. This causes the opacity to decrease rapidly with increasing temperature (Clayton 1983). As the opacity decreases, scattering becomes less important and the underlying eclipse (which is symmetric) becomes more pronounced, so the light curve is more symmetric and deeper.

3.4.3 X-Ray Models

The most prominent feature of the x-ray light curve is the modulation with the absence of complete extinction normally associated with an eclipse. To accommodate this feature it is necessary to extend the x-ray source. This is done by placing scattering material around the compact object. The models described below differ in their placement and structure of the scattering material. As we will see there are problems with all of the models, though the accretion disc corona (ADC) model comes closest to matching the observations (though we should also mention that it has the largest number of free parameters).

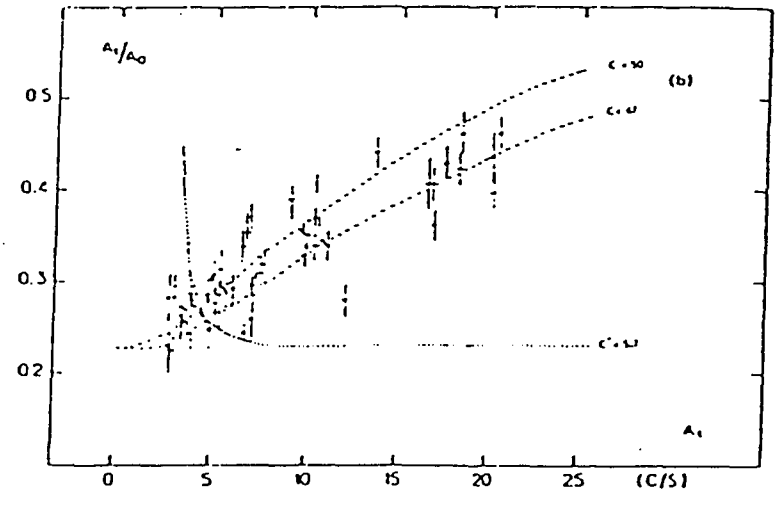

Figure 3.7 Ratio of modulated to unmodulated x-ray flux versus unmodulated x-ray flux. See text for explanation of curves. (from van der Klis and Bonnet-Bidaud 1981b)

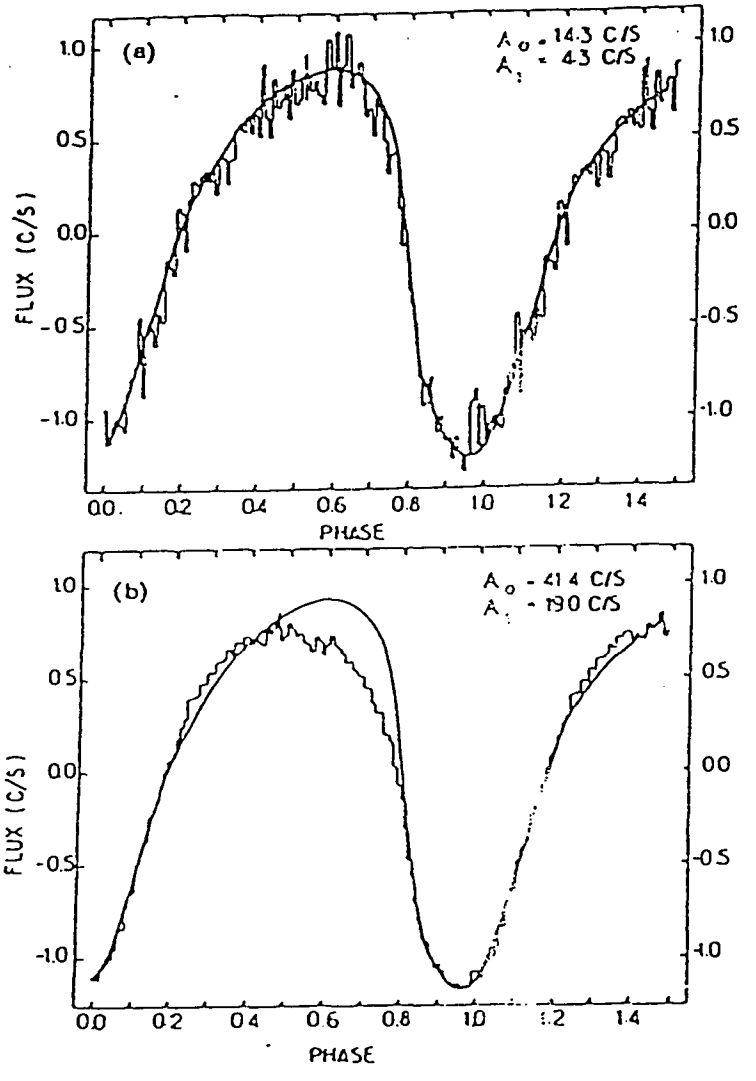

Figure 3.8 Normal Cygnus x-ray light curve superposed on actual light curve for two different source intensities. (a) low intensity. (b) high intensity (from van der Klis and Bonnet-Bidaud 1982)

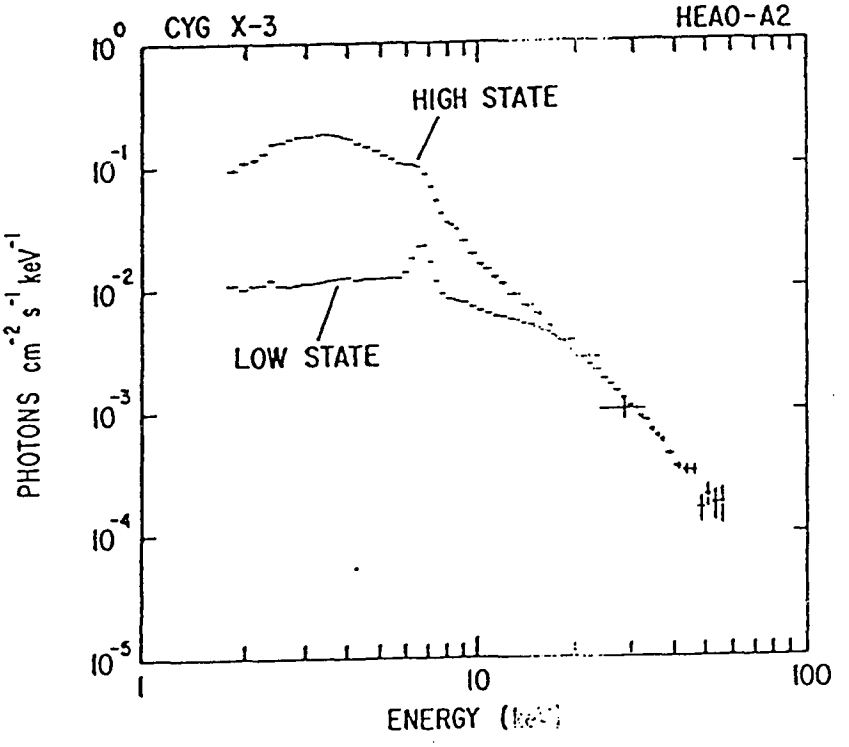

Figure 39. Energy spectrum of Cygnus X–3, in x-ray high state and in x-ray low state. Note average kT is lower for x-ray high state. (from White and Holt 1982)

Because of the short orbital period, we know that the companion star must be fairly dense to avoid tidal disruption. In general one has the following relation between orbital period and density, $\rho \geq 98G^{-1}P^{-2}$ (Faulkner et. al. 1972). Using the main sequence relation $R/R_{\odot} \approx M/M_{\odot}$, we can set an upper limit of $0.5M_{\odot}$ for the companion mass. So the companion is either a main sequence dwarf or a degenerate star.

Stellar Wind Model

This model is due to Pringle (1974) and Davidsen and Ostriker (1974). Cygnus X–3 is a compact object (neutron star, black hole, or white dwarf) in a binary system with a main sequence red dwarf companion. The companion is losing mass via a stellar wind. The orbit is so inclined to our line of sight that no eclipse occurs. However, as the objects orbit each other the amount of wind material along the line of sight (from x-ray source to earth) changes, thus leading to the observed modulation.

There are two independent uses for the wind in this model. It is used to transfer mass to the compact object and create the observed x-ray luminosity. The necessary mass transfer rates are $10^{-6}M_{\odot}yr^{-1}$ for a white dwarf and $5 \times 10^{-9}M_{\odot}yr^{-1}$ for a neutron star. Of course much more mass is lost than is transferred.

The stellar wind must also modulate x-ray flux and therefore must have a certain optical depth. Assuming that electron scattering is the main contributor to the opacity it is possible to derive the column density of the wind,

$N \approx 10^{13}(M/M_\odot)^{-1/2}L_{38}^{1/2}T_6^{3/8}cm^{-3}$ (Pringle 1974). If the wind velocity is assumed to be the escape velocity from the system one can derive the rate of mass loss from the system. $\dot{M} = 4\pi a^2 N m_p v_{esc}$, where $a = 10^{11}(M/M_\odot)^{1/3}cm$ is the binary separation, m_p is the proton mass (we are assuming that the wind is comprised mostly of protons), and $v_{esc} \approx 6 \times 10^7 cm/s$ is the escape velocity of the system (the value quoted is the escape velocity from the sun). Then the rate of mass loss from the system is $\dot{M} \approx 2 \times 10^{-6} M_\odot yr^{-1}$; in good agreement with the above estimate based on the x-ray luminosity.

As we saw above this is roughly the mass loss rate needed to explain the observed increase in orbital period. Note that the orbital period derivative was not observed at the time that these models were put forward.

This model predicts that the low energy cutoff (dependent on the column density between x-ray source and observer) should be phase dependent. It also predicts no change in the depth of modulation with increasing x-ray energy. Both of these predictions are wrong.

Cocoon Model

In the cocoon model there is a distant, thin shell surrounding the binary system (see Figure 3.10). The companion star casts a moving shadow on the shell as it moves in its orbit. Assuming that the shaded portion does not contribute to the x-ray flux, one can derive the expected amplitude of

modulation (Milgrom 1976).

There are three requirements for this scenario to work: 1.) The shell must not trap x-rays, ($\tau \sim 1$), 2.) The recombination time in the shell must be much less than the orbital period (so the shadow is ionized to a lesser degree than the rest of the shell), and 3.) Changes in the shell must propagate much slower than ωR, so that the shadow will not be in equilibrium with the rest of the shell.

By adjusting the inclination angle of the orbit and θ_0, the angular size of the shadow, one can duplicate the approximate shape of the light curve. Note also that if the shell is near or beyond the light cylinder the light curve will become asymmetric, a fast rise followed by a more gradual fall off.

This model correctly predicts the close correlation between the IR light curve and the x-ray light curve, as well as the reduced modulation of the IR light curve. However, it also predicts that the higher energy x-rays should have a greater modulation (since the higher energy x-rays are scattered less, they should have a light curve more like the underlying eclipse). This is in direct contradiction to the results mentioned above (Figure 3.5).

Accretion Disc Corona Model

This model was originally proposed to explain the light curve of 4U 1822-37 (White et. al. 1975), a low mass x-ray binary system, and later modified,

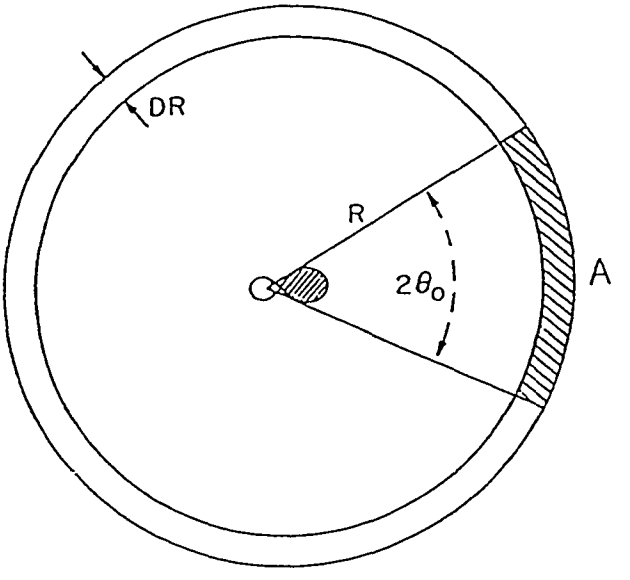

Figure 3.10 The Cocoon Model of Cygnus X–3. (from Milgrom 1976)

with the addition of bulges on the outer edge of the accretion disc, by (White and Holt 1976).

In this model the compact x-ray source possesses an accretion disc. Due to heating of the disc by the x-ray source, material is evaporated from the disc and a corona is formed around the compact object. The radius of the corona is less than the binary separation and less than the disc radius, though it may be bigger than the companion radius. The corona is optically thick and is the extended x-ray source seen by a distant observer. By adjusting the radius of the corona, the radius of the companion, and the inclination angle of the binary system White et. al. (1975) obtained partial eclipses of the ADC by the companion to match the observed dips in the light curve of 4U 1822-37 (Figure 3.11).

In addition to the observed dip in the light curve of 4U 1822-37 there is also smooth, broad modulation similar to the light curve of Cygnus X-3. These arise from partial occultations of the ADC by bulges on the outer edge of the disc. These bulges form where the accretion stream meets the disc (Lubow and Shu 1975). Figure 3.12 gives a picture of the model and Figure 3.13 the light curve for Cygnus, the solid line is the ADC model with the same bulge profile as found from fitting the light curve of 4U 1822 and a best fit inclination angle of orbit, radius of companion, and radius of accretion disc (with values as indicated on the figure).

Though this model originally predicted an energy independent light curve, Molnar (1985), by allowing the density in the bulge to vary with height above

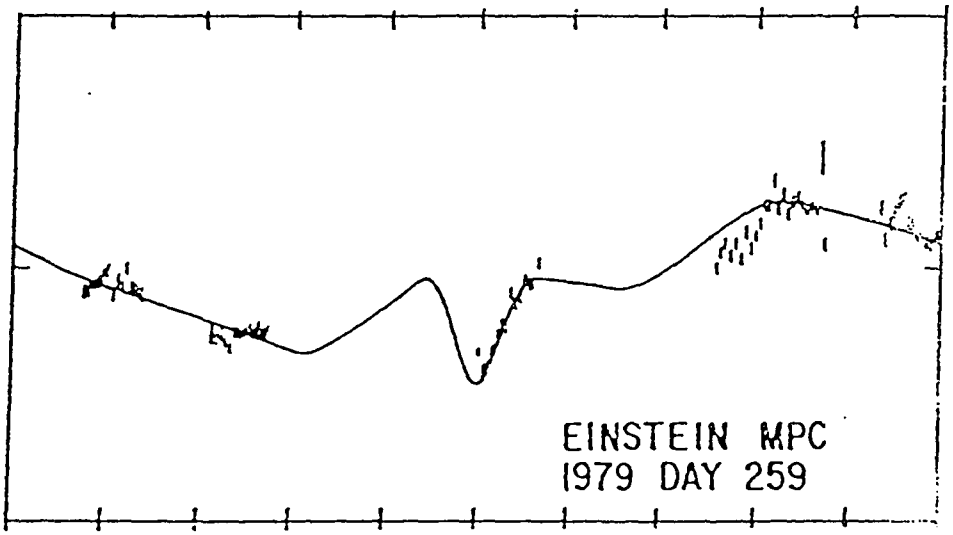

Figure 3.11 Light curve of 4U 1822-37 with fit from ADC model. (from White and Holt 1982)

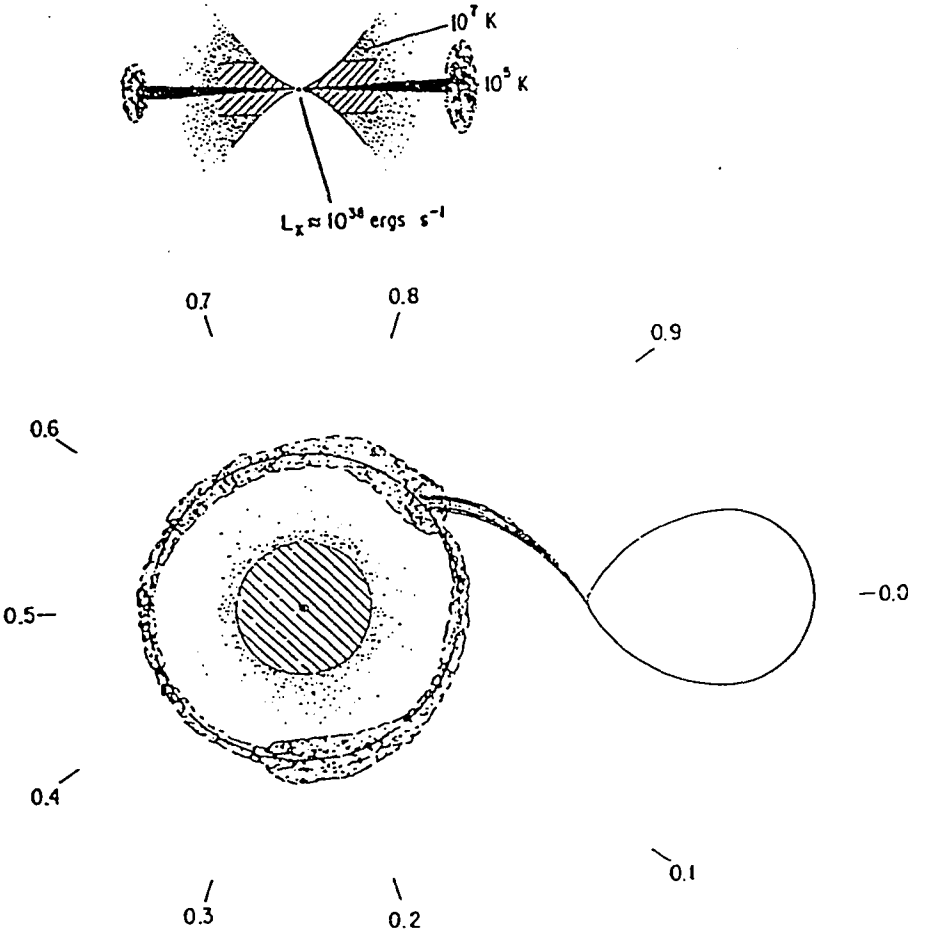

Figure 3.12 ADC model, with bulge. Top: cross section, Bottom: top view. (from White and Holt 1982)

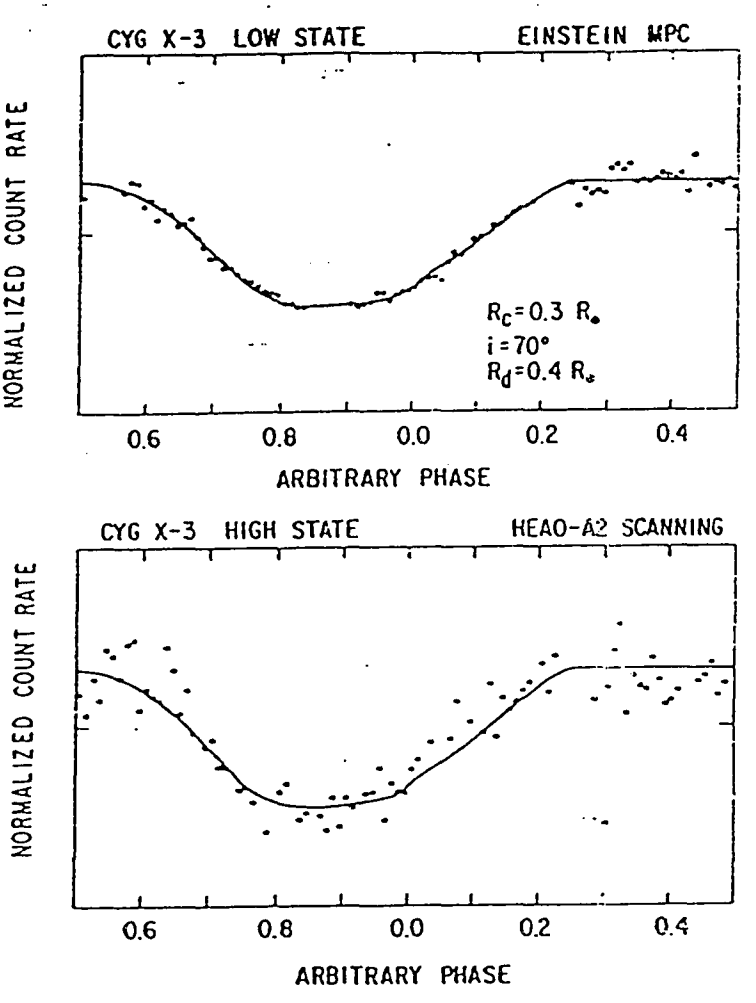

Figure 3.13 Light curve of Cygnus X–3 with best fit from ADC model. (from White and Holt 1982)

the disc, was able to reproduce the observed energy dependence.

The main motivation for this model is the growing belief that Cygnus is a member of the class of low mass x-ray binaries (LMXRBs), systems very similar to cataclysmic variables, except that the white dwarf is replaced by a neutron star. Both types of systems are characterized by short orbital periods, though while there are probably thousands of CV's in the galaxy there are at most 100 LMXRBs. Their rarity is probably due to the very special (and not understood) circumstances that must have prevailed for the low mass companion not to have been ejected from the system during the collapse of the neutron star. The detection of QPOs in Cygnus by van der Klis (see above) makes this interpretation almost inescapable.

There is however one unsolved problem with this scenario, the increasing orbital period. As we saw above Cygnus' companion must have a low mass, and might possibly be degenerate. For a red dwarf to fill its Roche lobe the following condition must be satisfied, $(\dot{P}/P)_{orb} = (\dot{M}/M)_{rd}$ (van der Klis and Bonnet-Bidaud 1985). This means that the period must be decreasing. In a system with an increasing orbital period the red dwarf can not remain in contact with the Roche lobe. So mass transfer must proceed via a different mechanism. One possibility is that x-ray heating of the companion star by the compact object leads to an evaporative wind (Tavani, Ruderman, and Shaham 1989) which drives the mass transfer. Another possibility is that a high energy proton beam emanating from the neutron star evaporates the

surface layers of the companion (leading to a stellar wind), and the resulting neutrinos, produced by the proton-proton collisions, deposit energy deep in the core of the companion star (Gaisser and Stecker 1986). The deposited energy causes the companion star to expand, in order to maintain hydrostatic equilibrium, and possibly fill its Roche lobe.

3.5 Gamma Ray Data: MeV

The observational situation in the gamma ray data is rather confused. The historical record shows a pattern of detection followed by lack of detection, though the situation has become more clear.

The first reported detection of Cygnus X–3 in the gamma ray regime was in a 1972 balloon flight by Gulper et. al. (1978). They reported a flux of $(2.0 \pm 0.8) \times 10^{-4} cm^{-2} s^{-1}$ above $40 MeV$, modulated with the $4.79 hr$ x-ray period (though roughly 180 degrees out of phase with the x-ray light curve). In the same year, in another balloon flight, McKechnie et. al. (1976) saw no gamma ray signal from Cygnus and put an upper limit (95% confidence level) of $6.5 \times 10^{-6} cm^{-2} s^{-1}$ above $70 MeV$. Two years later Gulper et. al. made another balloon flight and also failed to observe any gamma ray emission from Cygnus.

In an analysis of *SAS-2* data Lamb et. al. (1977) reported a flux level

$(4.4 \pm 1.1) \times 10^{-6} cm^{-2} s^{-1}$ above $35 MeV$. The $4.79 hr$ modulation was apparent in their data, though the light curve was in phase with the x-ray light curve.

Subsequently the *COS-B* satellite (Hermsen et. al. 1987), with 300 days of data taken between 1975 November and 1982 February, failed to detect any gamma ray emission from Cygnus X–3. They set upper limits to the flux of $7.5 \times 10^{-7} cm^{-2} s^{-1}$, almost an order of magnitude lower than the flux levels reported by *SAS-2*. They examined the background in the Cygnus region much more carefully than was possible by *SAS-2* and found that there is enhanced emission from the general region around Cygnus, but there was no evidence for a point source. They attributed the positive detection of *SAS-2* to this background emission, though *SAS-2* rejects this hypothesis and claims that time variability of the source is to blame (Fichtel et. al. 1987), though they found no evidence for variability in their dataset.

In a reanalysis of *COS-B* data, Li and Wu (1989) find that there is indeed gamma ray emission from Cygnus X–3 and that it is anti-correlated with the x-ray flux. The gamma ray source is brightest during the x-ray 'low' state, and below detection threshold at times of 'high' x-ray state (Figure 3.14). However, they fail to find any modulation at the $4.79 hr$ period. They report a flux of $(1.3 \pm 0.6) \times 10^{-6} cm^{-2} s^{-1}$ above $100 MeV$. They explain the anti-correlation by postulating absorption of gamma rays by the more plentiful x-rays ($\gamma\gamma \rightarrow e^+e^-$).

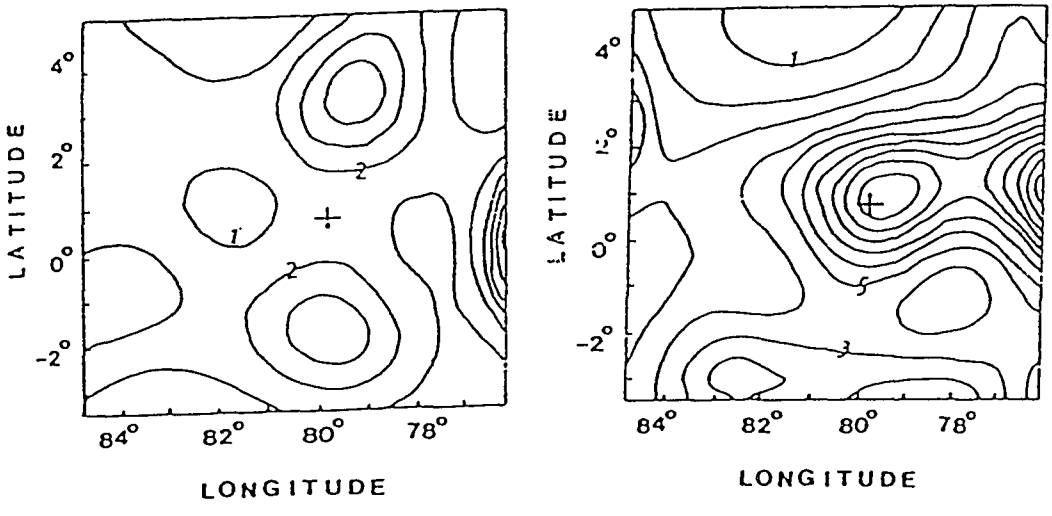

Figure 3.14 Gamma ray maps of Cygnus region: (left) During state of high x-ray activity. (right) During state of low x-ray activity. (from Li and Wu 1989)

3.6 VHE and UHE Gamma Ray Data

The observations of Cygnus X–3 in the high energy regime, $E > 10^{11} eV$, are even more enigmatic than the lower energy observations described above. There have many observations, albeit of rather low statistical significance, of Cygnus and we will not discuss them all. The interested reader is referred to Bonnet-Bidaud and Chardin (1988) for an excellent, though somewhat skeptical, review of the situation. Here we will merely highlight the important observations.

3.6.1 VHE Observations

Cygnus X–3 was first observed in the $10^{12} eV$ range by Stepanian et. al. (1975) (see also Vladimirsky et. al. 1973). In data collected during 1972, using the air Čerenkov technique, they failed to observe any D.C. emission from Cygnus, $flux(E > 2 \times 10^{12}) < 1.1 \times 10^{-10} cm^{-2} s^{-1}$. However, they did observe a significant burst, at 20% of the background, on 1972 September 8 and 9 in one of their two detectors, $flux = 2 \times 10^{-10} cm^{-2} s^{-1}$. Though the chance probability was rather low, $\sim 10^{-5}$ after trials, they failed to observe the outburst in their second detector. They attributed this to the higher energy threshold (by a factor of 1.8) of this detector. From this hypothesis they postulated that the energy spectrum of Cygnus must be steeper than that of the cosmic ray background and tentatively assigned a spectral index of 3.2 or greater. As we will see this is in disagreement with later measurements.

When they folded the data at the $4.79hr$ period, using the ephemeris of Canizares, et. al. (1973), they found evidence for emission at phases $.300 \pm .025$ and $.900 \pm .025$, corresponding to phases $.190 \pm .025$ and $.790 \pm .025$, with the ephemeris of van der Klis and Bonnet-Bidaud (1981).

This result was first confirmed by Neshpor (1979). They observed Cygnus from 1972 to 1977, with an energy threshold of $2 \times 10^{12} eV$. Folding the data at periods near the x-ray period (the x-ray ephemeris was not very well known at the time), and scanning in period space, they found the highest χ^2 value at a period of $(.199683 \pm .000001) days$. Extrapolating the latest ephemeris (van der Klis and Bonnet-Bidaud 1988) back predicts, P(1972 Jan 0)=.1996838714 days, and P(1977 Jan 0)=.1996855215 days, in good agreement with their value. Using this value for the period, and no period derivative (it had yet to be observed), they saw significant emission at phases, $\phi = .157 - .212$ (5.4 σ), and $\phi = .768 - .823$ (3.0 σ). With corresponding flux levels of $1.8 \times 10^{-10} cm^{-2} s^{-1}$ and $9.0 \times 10^{-11} cm^{-2} s^{-1}$ respectively.

Further confirmation came from the Whipple collaboration (Danaher et. al. 1981). In data taken between 1980 April through June, they observed phased emission at $\phi = 0.70 \pm .05$ at a flux level of $1.5 \times 10^{-10} cm^{-2} s^{-1}$ at $E > 2 \times 10^{12} eV$. Though they failed to observe any emission at $\phi = .30$. The same group, using a then new imaging detector, saw further evidence for pulsed emission in one of two data runs in 1983. In a run from 1983 October 29 to November 11, they observed a 4.4σ excess at $\phi = .58 - .67$ (corresponding

to a flux of $(5.1 \pm 1.1) \times 10^{-10} cm^{-2} s^{-1}$). During the second data run, 1983 November 28 to December 7, they failed to observe any emission (Cawley et. al. 1985).

The Durham collaboration (Dothwaite et. al. 1983) claimed confirmation of the above signal, with data taken between 1981 July and October ($E_{th} \sim 1.3 TeV$). This 'confirmation' is rather weak, only 2.4σ, and the data has been rebinned, though the signal was observed between phase .625-.655.

At roughly the same time, 1981 August 29 to September 6, Lamb et. al. (1982), with an energy threshold of $500 GeV$ observed a 4.4σ excess between phases .5 and .7, much wider than previous measurements.

In 1985 the Durham collaboration (Chadwick et. al. 1985) reported evidence for a pulsar in Cygnus X–3. During one 7-minute burst at orbital phase .625, they observed a pulsed signal with a chance probability of .3% at a period of $12.5908 \pm .0003 ms$. After correlating the change in pulsed fraction to the rate excess and re-examining the rest of their data, where they found two more significant intervals, they arrived at an overall chance probability of 4×10^{-7}, a virtual certainty. If confirmed this would represent the first unambiguous pulsar to be observed at these energies, and as such is one of the more important discoveries in the field of gamma ray astronomy.

Since the initial report there has been no independent confirmation of the signal. The same group (Brazier et. al. 1990) continues to see evidence for the pulsar. However, no other group has seen any evidence for such a signal.

The Whipple collaboration in analysis of all of their data taken between 1983 and 1986 saw no evidence for the reported pulsar (O'Flaherty et. al. 1990 and Fegan et. al. 1987). The Haleakala group analyzed a 60 second burst (with 80% S/B) concurrent with a radio outburst (October 1985) for the reported pulsar but failed to observe it (Resvanis et. al. 1987). In a more thorough analysis of their entire 1985 data base they found no evidence for the pulsar (Szentgyorgi 1986). Finally, the Gulmarg group observed two episodes of significant rate excesses on 1988 October 14 and 16 (3.5σ each), occurring at orbital phase 0.60 ± 0.01. A period search for the $12.59ms$ pulsar failed to reveal anything.

While any one of the above null detections can not rule out the observation by the Durham group, taken together they make a very strong case against the original observation. As we will see a search of the 1986 data set of the Haleakala collaboration also fails to detect any significant signal at $12.59ms$.

3.6.2 UHE Observations

The first report of ultra high energy (UHE) radiation from Cygnus X–3 came from the Kiel air shower array (Samorski and Stamm 1983a). In an analysis of data taken between 1976 March 18 and 1980 January 7, they observed a D.C. excess (4.4σ significance) from the direction of Cygnus X–3, placing the flux above $2 \times 10^{15} eV$ at $(7.4 \pm 3.2) \times 10^{-14} cm^{-2} s^{-1}$. When folded at the $4.79hr$ period using the ephemeris of Parsignault et. al. (1976), they observed 13 events when they expected 1.44 between orbital phases .2 and .3

(Poisson probability 5×10^{-8}). They observed no events with energy above $2 \times 10^{16} eV$ (expect a few), taken as evidence for a cutoff in the spectrum, or at the least a steepening of the spectrum above this energy. They also found that the excess prevails even when their phase bins are only 1.1 minute wide (Samorski and Stamm 1983b), implying incredible long term stability for the system. Contrary to expectations they found the average muon content of the showers coming from the direction of Cygnus to be similar to that of the background showers. Since the only mechanism for generating muons in photon showers is by photo-production off of nuclei (direct pair production is negligible due to large muon mass), one expects a muon content less than 10% of that observed in background showers. They observed a muon content of roughly 80% of the background.

This result was confirmed by the Leeds group (Lloyd-Evans et. al. 1983). In analysis of their data, taken between 1979 and 1984, there was strong $(3.5 - 4\sigma)$ evidence for pulsed emission at $\phi = .25$ (threshold energy $3 \times 10^{15} eV$) from 1979 through 1981, flux= $(1.5 \pm 0.3) \times 10^{-14} cm^{-2} s^{-1}$. From 1982 to 1984 no signal was apparent. In 1984 they commissioned another array with a lower energy threshold, $5 \times 10^{14} eV$. Using this array there was evidence for a low level signal near phases 0.63 and 0.27 (all phases by van der Klis and Bonnet-Bidaud 1981) (Lambert et. al. 1985), though with low statistical significance ($\sim 2\%$).

The Fly's Eye group (Baltrusaitis et. al. 1985), with an energy threshold

of $10^{15}eV$, observed a 3.5σ excess at phase 0.2-0.3, corresponding to a flux of $(3.2 \pm 1.2) \times 10^{-13}cm^{-2}s^{-1}$ in their 1983 data set, and saw nothing in their 1984 data set (flux upper limit $2.0 \times 10^{-13}cm^{-2}s^{-1}$). Data taken during 1985 June, July, and August folded at the $4.79hr$ period (van der Klis 1981 ephemeris), showed evidence for emission (3.9σ) between phases 0.65 and 0.70, with a corresponding flux of $(4.5 \pm 1.2) \times 10^{-13}cm^{-2}s^{-1}$ above $10^{14}eV$ (Baltrusaitis et. al. 1987a). They also took a small (14.3 hrs) sample of data at the time of the 1985 October radio outburst (Baltrusailtis et. al. 1987b). The radio outburst peaked on October 11 (20 Jy) and had fallen to $\sim 1-2Jy$ by October 17 (Johnston 1985). Fly's Eye had data on October 17, 18, and 19. They saw no evidence of bursts or D.C. emission, setting a flux limit of $\sim 2 \times 10^{-13}cm^{-2}s^{-1}$.

In analysis of data taken between 1981 and 1984 the Akeno group (Kifune et. al. 1986), observed significant emission (3σ), in a broad region around phase 0.6 (van der Klis 1981 ephemeris). The corresponding flux is $(1.1 \pm 0.4) \times 10^{-14}cm^{-2}s^{-1}$ above $10^{15}eV$. In contrast to the original Kiel signal this result was obtained only after selecting muon poor events.

The Haverah Park array GREX (Eames, P.J., et. al. 1987, and Bloomer et. al. 1980) reported on data taken between 1986 March and 1988 September. With an energy threshold of $5 \times 10^{14}eV$ they set a flux limit of $7.1 \times 10^{-14}cm^{-2}s^{-1}$ for D.C. emission. During the sample of data which overlaps with the data presented in this thesis, their most significant excess occurred

between 1986 August 30 and 31.

The Cygnus array (Dingus et. al. 1988) operating between 1986 April 2 and 1987 May 3, with an energy threshold of $5 \times 10^{13} eV$, see no evidence for D.C. emission and set a flux limit of $1.5 \times 10^{-13} cm^{-2} s^{-1}$ for all showers, and $7.6 \times 10^{-14} cm^{-2} s^{-1}$ for muon poor showers. They did observe a 45 day interval with significant emission beginning on 1986 April 17, with a corresponding flux of $(8.2 \pm 2.0) \times 10^{-13} cm^{-2} s^{-1}$.

The 1989 Radio Flares

As stated above Cygnus X–3 underwent two large flaring events (20 Jy) in 1989 (the first peaking on June 3, the second on July 21). A few groups have contemporary data, none have reported a significant excess during this time. Both the Cygnus array, with an energy threshold of $10^{14} eV$ (Haines et. al. 1990), and the Utah-Michigan array (Ciampa, D., et. al., 1990), with an energy threshold of $10^{14} eV$, report null results. The Utah-Michigan collaboration analyzed their data for emission at three different timescales, 1 day, 2.4 hrs, and 14.4 min. They report their most significant dates for each timescale: (1 day) July 24, (2.4 hr) May 31.6, (14.4 min) May 28.42. None of these are statistically significant (all less than 3σ before accounting for trials).

The Highest Energies

Long term studies of the highest energy cosmic rays, $E > 5 \times 10^{17} eV$, have yielded the first evidence for a point source of cosmic rays at these energies. The Fly's Eye group ($E_{th} = 5 \times 10^{17} eV$), have analyzed data taken between 1981 November and 1988 May. After constructing a sky map using all of their events they find that the most significant point in the entire sky is centered on Cygnus X–3 (Cassiday et. al. 1989), with a significance of 3.5σ. The inferred flux is $(2.0 \pm 0.6) \times 10^{-17} cm^{-2} s^{-1}$. They see a weak tendency for the events to be clustered around phase 0.0 (van der Klis 1989 cubic ephemeris).

This important result has been confirmed by the Akeno array (Teshima et. al. 1990). With an energy threshold of $5 \times 10^{17} eV$ they measure a flux of $(1.4 \pm .5) \times 10^{-17} cm^{-2} s^{-1}$, between 1984 September and 1989 July. They also find Cygnus to be the 'brightest' point in the entire sky.

Haverah Park (Lawrence et. al. 1990) has accumulated data in this energy range from 1974 January to 1988 July. They find no evidence for excess emission from Cygnus X–3 and set flux limits considerably below the positive fluxes reported above. For their entire data set they find, $flux(95\%cl) < 4 \times 10^{-18} cm^{-2} s^{-1}$, and for the time they overlapped with the Fly's Eye data set, $flux(95\%cl) < 5 \times 10^{-18} cm^{-2} s^{-1}$.

3.7 Underground Muons

In 1985 the NUSEX collaboration (Battistoni et. al. 1985), operating under an overburden of $6250 hg\ cm^{-2}$ of rock, reported evidence for a signal with the characteristic $4.79 hr$ period in their muon data from the direction of Cygnus X–3. The overburden gives them an energy threshold of roughly $5 TeV$ for single muons, and the excess (observed between orbital phases 0.7 and 0.8) yields a secondary flux of $(2.5 \pm 0.5) \times 10^{-12}$. They claim a rejection of the null hypothesis at the 5.3σ level. However, the signal was observed in a $10° \times 10°$ bin, much larger than their $\sim 1°$ angular resolution, and no account has been made for trials associated with this choice of bin size. The above analysis is based on data taken between 1982 June 1 and 1985 February 1. In an analysis of their more recent data (Aglietta et. al. 1990) it appears that the muon signal was not present for the time period 1985-1986 and then returned during the period 1987-1988 (at the same orbital phase and with the same angular cut as used in the original analysis). Though the significance of the original analysis may be criticized for not properly accounting for all trials, one can not say the same for the last analysis; the same angular bin size as used and moreover the excess appears in the same range of orbital phase.

The effect was simultaneously reported by the Soudan collaboration (Marshal et. al. 1985). With a muon threshold of $600 GeV$ (1800 mwe), and an angular resolution of 1.4° they observed a 4.2σ (84 ± 24 events) excess between phases 0.65 and 0.9. With a corresponding flux of $7.0 \times 10^{-11} cm^{-2} s^{-1}$.

Though the peak in their distribution (which is the value they quote) occurred at a declination 2.7° away from Cygnus X–3. The data was taken between 1981 September and 1983 November. Soudan also reported similar results with a more recent data set (Johns, et. al. 1990), though the significance of their results was not that high, and it was not clear if all data selection cuts remained identical.

The Frejus collaboration (Berger et. al. 1986), operating from 1984 February to 1986 January failed to observe any signal. With an energy threshold of $3TeV$ (for muons) they were able to place flux limits well below the fluxes reported in the above two experiments, $< 1.5 \times 10^{-12} cm^{-2} s^{-1}$ over all phases and even more stringent limits over the orbital phases reported above.

The IMB detector (Bionta et. al. 1987) (at 1570 m.w.e. and a muon energy threshold of $2GeV$) in an analysis of data taken between 1982 September and 1984 April, set an upper limit to the flux from Cygnus X–3 of $flux < 6.9 \times 10^{-11} cm^{-2} s^{-1}$ (90% c.l.) for all of their data. For their large zenith angle data (4600 m.w.e., similar to that of NUSEX) they set an upper limit of $flux < 5.1 \times 10^{-12} cm^{-2} s^{-1}$. In an analysis of data taken within 2 weeks of a radio burst, they found a significant enhancement (4.2σ) between phases 0.50 and 0.65, during one of three such data sets (1983 September 11 to October 8), with a corresponding flux of $1.0 \times 10^{-9} cm^{-2} s^{-1}$ at 1800 m.w.e..

Similarly, Kamioka (Oyama et. al. 1986) failed to observe any excess muons from the direction of Cygnus X-3. At a muon energy above $760GeV$ they limit the flux to be less than $2.2 \times 10^{-12} cm^{-2} s^{-1}$. Their data was obtained between 1983 July and 1984 September.

Due to the strong zenith angle dependence of the NUSEX and Soudan results, neutrinos as primary particles are ruled out. The large fluxes reported seem to rule out the photon as the primary particle unless new interactions turn on at these energies enabling the copious production of muons. However the large angular spread of the NUSEX events would seem to rule out this scenario. Since the $4.79hr$ phase coherence is maintained, any scattering that might be invoked to explain the large angular spread, would have to take place locally (i.e. in the rock above the detectors). Given the known muon properties this is untenable. Numerous other particles have been proposed to explain these results: dilamda hyperons, photinos, glueballinos, and free massless gluons, none of which can fully explaion all of the experimental results (Berezinsky et. al. 1986).

It would seem as if a completely new type of particle is needed to explain this effect: but given the experimental constraints it is difficult to construct any particle that will fit the bill, see Bonnet-Bidaud and Chardin 1988 and Berezinsky 1986. Berezinsky et. al. come very close to establishing a 'no-go' theorem, the only out being that the 'cygnet' is a decay product of a

more massive parent particle; though even in this scenario the experimental window is small.

There is still a slim chance the result is a real one. However it now seems more likely that it is spurious and should be a warning to all concerned in periodic analysis: the proper accounting of statistical trials is paramount.

3.8 Summary

Cygnus X–3 has been observed across 24 orders of magnitude in energy (see Figure 3.15). At no frequency is its nature completely understood. From radio observations we know that Cygnus X–3 produces jets of relativistic particles, but the mechanism of jet production is not known. The x-ray observations give us the most reason for complacency, however as we have seen the categorization of Cygnus as a 'typical' low mass x-ray binary, is not valid. At higher energies, $10^{15}eV$ and above, initial reports suggested that emission occurred preferably at phases 0.2-0.3, while later measurements indicated that the emission occurs near phase 0.6. The TeV observations favor emission at phase 0.6. Taken together the observations seem to indicate a strong, highly variable source of comsic rays, though individually none of the observations are compelling. The lack of contemporary observations has placed the significance of the old observations in doubt, but new observations at the highest energies, $10^{18}eV$, continue to make Cygnus X–3 one of the more intriguing objects in the sky.

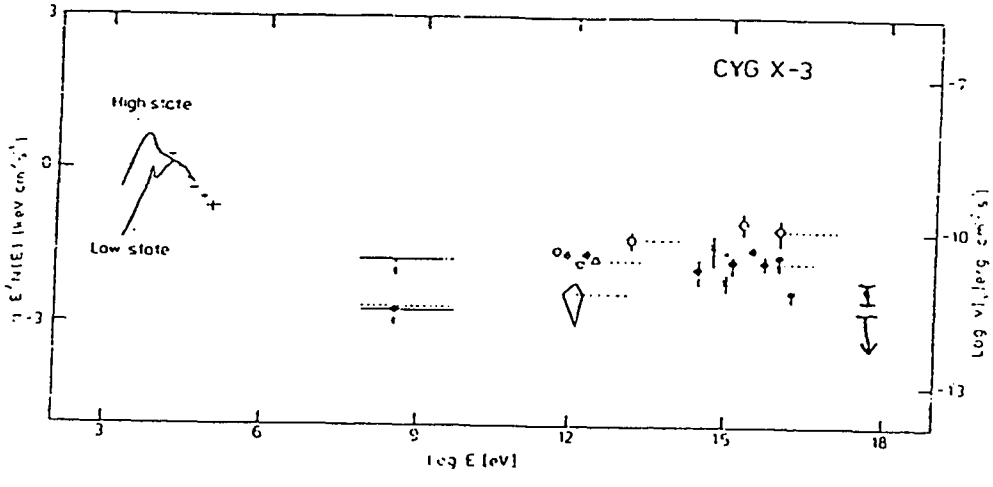

Figure 3.15 Energy spectrum of Cygnus X-3 from radio to EeV. (adapted from Hermsen et. al. 1987)

Chapter 4

The Extensive Air Shower and its Detection by the Atmospheric Čerenkov Technique

4.1 Introduction

In the late 1700's Augustus Coulomb observed a charged sphere, insulated from its surroundings, gradually lose its charge. It would take over a century, until Hess' historic balloon flights with a Wulf electroscope, for the extraterrestrial origin of this ionizing radiation to become clear. Origin established but nature still unknown, the 'cosmic' rays continued to intrigue and confuse scientists. In the 1930's, using coincidence techniques with Geiger-Mueller counters, Auger established correlations between cosmic ray particles separated by hundreds of meters. The Extensive Air Shower (EAS) was discovered. High energy particles, mainly protons with some mixture of heavier

nuclei and some photons (though this wouldn't be known for some time yet), were impinging upon the upper atmosphere and losing energy via the creation of secondary particles. These secondary particles lose energy in the same manner, and the process continues until the mean energy per electron becomes too small to create new photons and the energy of the shower is absorbed by the atmosphere (ionization losses). This picture leads naturally to power law growth of particle number within the shower, until the shower is quenched.

Every charged particle in the shower that has sufficient energy (so that its speed is greater then the local velocity of light) will cause the medium to emit coherent electromagnetic radiation - Čerenkov light. It is this radiation which the Atmospheric Čerenkov Technique (ACT) seeks to exploit. The atmosphere is an integral part of the detector. In this chapter we will explore the EAS and its accompanying Čerenkov signature. We will start with a brief overview of the electromagnetic and nuclear cascades, then discuss the nature of Čerenkov radiation. To proceed with the analysis of our telescope's response to extensive air showers we will use a Monte Carlo program which takes an incoming high energy primary and yields a Čerenkov footprint on the ground. We will then use a simple model of the Haleakala telescope to derive the effective area as a function of incident primary energy for photon and proton primaries.

4.2 The Electromagnetic Cascade

There are two types of primary particle that concern us, the proton and the photon. Whereas the photon, according to conventional wisdom, has only an electromagnetic cascade, the proton shower has a nuclear component as well. Using the field of a nucleus as a momentum sink, the photon can pair create, $\gamma \rightarrow e^+e^-$, forming the basis for an electromagnetic cascade. It is also possible for the photon to interact directly with the nucleus to form a nuclear cascade. However the cross section for this reaction is roughly 3 orders of magnitude smaller than the pair production cross section (Particle Data Book 1984). It has recently been proposed that at very high energies ($\geq 1PeV$) the QCD gluon structure function of the photon will begin to rear its head, increasing the photon-nucleon cross section, and giving the photon shower an appreciable nuclear component. We will stick with conventional wisdom and assume that a photon induced air shower has no nuclear component. Indeed these modifications would only be important in the higher energy showers detected by underground detectors and extensive air shower arrays.

In this section we will study the shower due to an incoming photon primary. Everything we say will apply equally well to the electromagnetic portion of the nuclear cascade.

When a high energy photon enters the earth's atmosphere it interacts with the atoms in the atmosphere and dissipates its energy via these interactions. There are a host of mechanisms available to the photon, the energy of the

photon deciding which mechanism will dominate. At energies of interest to us, $\sim 100GeV$, pair production is by far the dominant mechanism. Since the cross section for pair production is proportional to the inverse of the square of the mass of the produced particles, we need only consider production of electron-positron pairs. Once these pairs are produced they lose their energy predominantly via bremsstrahlung radiation (if their energy is above 80MeV). The radiated photon then goes on to pair produce once more.

The average distance that an electron travels before radiating away $1/e$ of its energy is called a radiation length. Though the electron emits photons of all frequencies it is the high energy photons, with roughly half of the electron's energy, that concern us. A radiation length is usually expressed in the more convenient units of gcm^{-2} (length $\times$ density). In air a radiation length is $36.7g/cm^2$, or about 300 meters at sea level. For photons the average distance travelled before creation of an electron positron pair is slightly greater, about 9/7 of a radiation length.

The process of bremsstrahlung followed by pair production continues until the electron energy falls below a critical energy, whereupon ionization losses begin to dominate over bremsstrahlung. In air this critical energy is about 80 MeV. Though photons at this energy will still create electron positron pairs, the electrons thus created will not create new photons, instead they will begin to ionize the air around them. In this manner the shower gets quenched, without new photons no increase in the total number of particles

is possible. The height at which the average electron energy falls below the critical energy is called shower maximum. This is the point in the shower's development at which the number of particles is a maximum.

With the simple model outlined above it is possible to derive some order of magnitude estimates for the distance to shower maximum (measured from the top of the atmosphere) and the number of particles present at shower maximum. At each radiation length there is a doubling in the number of particles present. If we let

n = the number of radiation lengths

$N(n)$ = the number of particles present at n radiation lengths

E_0 = the energy of the incoming primary particle

E_n = the energy per particle after n radiation lengths

E_c = the critical energy, 80MeV

Then:

$$E_n = E_0/e^n$$

setting E_n equal to the critical energy leads to

$$n(\text{to shower maximum}) = \ln(E_0/E_c)$$

for the number of radiation lengths to shower maximum. And since

$$N(n) = 2^n$$
$$N(\text{shower max}) \approx E_0/E_c$$

This is the total number of particles: photons, electrons, and positrons. A more interesting number is the number of charged particles present, since only they contribute to the Čerenkov light produced by the shower. If we assume that every photon is converted to an e^+e^- pair after traversing one radiation length, and every electron emits one bremsstrahlung photon after one radiation length, then the number of photons and electrons present in the shower after n radiation lengths is

$$N_\gamma(n) = N_e(n-1)$$
$$N_e(n) = N_e(n-1) + 2N_\gamma(n-1)$$

with

$$X(n) = N_e(n)/N_\gamma(n)$$

we obtain

$$X(n) = 1 + \frac{2}{X(n-1)}$$

This quickly (after $n = 4$) converges to $\lim_{n\to\infty} X(n) = 2.0$ Therefore the number of charged particles present at shower maximum is just $2/3 \times E_0/E_c$.

While the above estimate for the number of radiation lengths traversed to shower maximum is reasonable, the estimate on the number of particles present at shower maximum is rather poor. A more careful treatment, due to Carlson and Oppenheimer (Takagi 1964), based on the solution of the diffusion equations ($\frac{\partial N_e}{\partial t} = -AN_e + BN_\gamma$ and $\frac{\partial N_\gamma}{\partial t} = CN_e - DN_\gamma$ where t is the thickness of the atmosphere and the coefficients are linear operators that depend only on the energy) leads to the following results:

$$n(\max) = 1.01[\ln(\frac{E_0}{E_c}) - .5]$$
$$N_e(\max) = \frac{.137}{\sqrt{\ln(\frac{E_0}{E_c}) - .18}} \times \frac{E_0}{E_c}$$

The denominator is a slowly varying function of the incident energy. Taking $E_0 = 1\ TeV$ we get $\ln(E_0/E_c) \sim 10$. This gives us about 1 particle present at shower maximum for every 2 GeV of primary energy, a good approximation at all energies of concern to us.

The angular width of the e-m cascade is determined by multiple coulomb scattering. The mean scattering angle per radiation length is $< \theta^2 > \approx (E_s/p\beta c)^2$, where $E_s \approx \sqrt{4\pi/\alpha} m_e c^2 \approx 21\ MeV$. So at shower maximum, where the mean electron energies are near 80 MeV $< \theta^2_{ms} > \approx (2°)^2$. So to be sensitive to the entire shower, it is necessary to have an aperture at least

this large. We will return to this point when we give the results of the Monte Carlo analysis of EAS.

4.3 The Nuclear Cascade

For a high energy proton entering the atmosphere the first interaction is usually:

$$p + nucleus \rightarrow \pi'^{s} + nuclear\ fragments$$
$$\downarrow \rightarrow \begin{cases} \pi^0 \rightarrow 2\gamma \\ \pi^{\pm} \rightarrow \mu^{\pm} + \nu_{\mu} \\ or \\ \pi^{pm} + nucleus \rightarrow \pi'^{s} + nuclear\ fragments \end{cases}$$

The emitted pions form jets with an angular width determined by their transverse momentum. In a typical high energy interaction $< p_{\perp} > \approx 400\ MeV$. So a typical hadronic shower will have an angular spread of roughly $p_{\perp}/E_{\pi}$. The pion energy depends on the multiplicity of the event, which roughly scales like $(E_0/m_{\pi})^{1/4} (= 9.2$ for a $1\ TeV$ primary). If we assume that half of the primary energy is channeled into π production and the energy is shared equally among the daughter pions, then the angular spread of the nuclear cascade from a $1\ TeV$ primary should be roughly .4° at its conception. Any daughter pion which interacts with another air nucleus, having roughly an order of magnitude smaller energy, will form a subshower with multiplicity ~ 5 and an angular width of $\sim 2.3°$. So the shower spreads out as its energy is degraded.

The produced pions have an interaction length of $90 gcm^{-2}$, which corresponds to $750m$ (or $2.5\mu s$) at sea level. Since the neutral pion has a lifetime

of $10^{-16}s$ all $\pi^o s$ will decay into 2 photons, leading to an electromagnetic cascade. For charged pions, with a lifetime of $2.6 \times 10^{-8}s$, the situation is quite different. The probability for the $\pi^{\pm}$ to decay before interacting is $(1 - \exp^{-L(h)/\gamma c\tau})$, where $L(h) = 90/\rho_0 \exp^{-h/h_0}$ is the interaction length at a height h above sea level. Using $h_0 = 8.4\ km$ (the scale height of the atmosphere at sea level) and $\rho_0 = 1.22 \times 10^{-3}\ gcm^{-3}$, and setting the decay probability to $1/e$ we get $E_d \approx 13 \exp^{h/h_0}\ GeV$. Pions above this energy will interact before decaying and thereby feed energy back into the shower, while pions of lower energy will decay into muons which travel to the ground suffering only multiple scattering.

If not for the reinjection of energy into the shower via the high energy pions and assuming isospin invariance holds (i.e. all three species of pion produced in equal amounts), then we would expect 1/3 of the primary energy to be channeled into the electromagnetic cascade. Since it is the electrons from the the e-m shower that produce the bulk of the Čerenkov light a proton primary is expected to produce only 1/3 as much light as a γ primary of the same energy.

4.4 Čerenkov Radiation

When a charged particle travels through matter it tends to polarize the medium. The molecules which comprise the medium have a dipole moment:

separated positive and negative charges. So if a positive charge traverses the medium the dipoles will tend to align themselves such that the negative end is pointing towards the moving charge. Since the charge is in motion this becomes a rotation about an axis perpendicular to their dipole moment. A rotation is an acceleration and an accelerated charge radiates.

As the velocity of the passing charge increases the electric field perpendicular to its velocity increases ($E'_\perp = \gamma E_\perp$ where $E_\perp$ is the perpendicular electric field of the charge in its rest frame), while the electric field parallel to the direction of motion is unchanged. This means that the effect of the passing charge is felt farther away the greater its velocity (actually $b_{max} = \gamma v/\omega$ where ω is the orbital frequency of the electrons in the medium, v is the velocity of the passing charge, γ is the Lorentz factor of the charge, and b_{max} is the distance over which the charge acts).

As the maximum impact parameter (b_{max}) over which the charge makes itself felt increases, the effect of the polarization of the medium becomes important. Polarization of the medium tends to lower the value of the electric field due to the passing charge. This is known as the density effect and leads to a reduction in the energy loss of the particle from the value predicted by extrapolating the low energy formula, where the effect of the medium on the distant fields is ignored.

If the charge is travelling faster than the velocity of information transfer, the medium has no warning of the charges arrival. This has two important

consequences. First, it makes it possible for an electromagnetic 'shock' front to form. The radiation from a previous segment of the particles trajectory will arrive after the particle has passed. Therefore there exists a front along which electromagnetic waves from different segments of the track will have the same phase. The medium's response has become coherent (see Figure 4.1). The second result has to do with the spectrum of the emitted radiation. Since the particle is travelling faster than information, knowledge of its arrival is like a step function in time. Actually, to the extent that the electric field is perpendicular to the direction of motion it is a delta function in time. The frequency spectrum of the emitted radiation is simply the Fourier transform of the time development of the electric field. Since the transform of a delta function is a constant, independent of frequency, to the extent that the permittivity of the medium is constant, the spectrum is flat in frequency space.

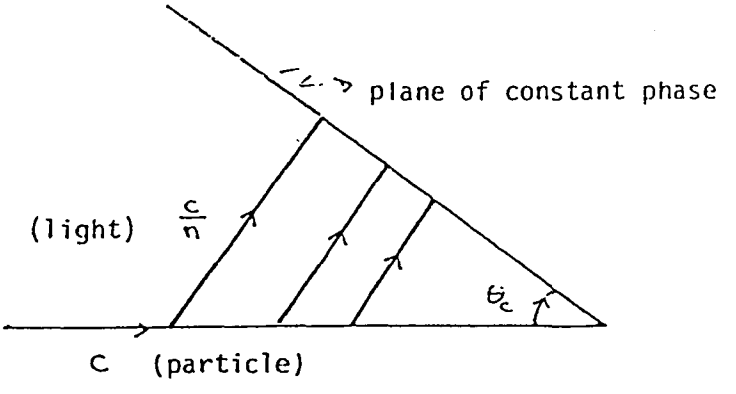

Figure 4.1 Geometry for Čerenkov radiation

Now let's work out, quantitatively, some important parameters of Čerenkov radiation. From Figure 4.1 it is clear that the emission angle of the radiation is just:

$$\cos\theta_c = ct/nvt = 1/\beta n(\omega)$$

If we demand that this angle be real, we obtain a threshold velocity

$$\beta \geq 1/n(\omega)$$

for the moving charge. This can be converted into a threshold energy. Since,

$$\begin{aligned} \beta &= \sqrt{\gamma^2 - 1}/\gamma \\ \Longrightarrow \gamma &\geq n/\sqrt{n^2 - 1} \end{aligned}$$

or

$$\begin{aligned} E_{th} &= \gamma_{th} m \\ &= \frac{n}{\sqrt{n^2 - 1}} m \end{aligned}$$

The only other quantity we need to know is the number of photons emitted per unit track length per frequency interval. From Jackson (1962):

$$\frac{dE}{dx} = \frac{(Ze)^2}{c^2} \int_{\epsilon(\omega) > \frac{1}{\beta^2}} \omega \left(1 - \frac{1}{\beta^2 \epsilon(\omega)}\right) d\omega$$

Since for a photon $E = \hbar\omega$, this translates to

$$\frac{dN_\gamma}{dx} = \frac{(Ze)^2}{\hbar c^2} \int_{\epsilon(\omega)>\frac{1}{\beta^2}} \left(1 - \frac{1}{\beta^2 \epsilon(\omega)}\right) d\omega$$

If $\epsilon(\omega) > 1/\beta^2$ and is constant for all frequencies within the range of interest ($\epsilon = n^2$) then, for a singly charged particle we have:

$$\begin{aligned} \frac{dN_\gamma}{dx} &= \frac{1}{137c} \sin^2\theta_c \Delta\omega \\ &= 50,000 \sin^2\theta_c \, photons/m \text{ in the visible band} \end{aligned}$$

We are now in a position to estimate the amount of Čerenkov light produced on the ground by a high energy cosmic ray. Assuming that all of the light originates from shower maximum, for an incident photon of 1 TeV we expect roughly 500 electrons at shower maximum. At shower maximum (an altitude of $8.0km$), the index of refraction is $n = 1 + 2.7 \times 10^{-4} \exp^{-8.0/8.4} \approx 1.0001$ where we have used the isothermal approximation to the atmosphere. The Čerenkov angle is then $\theta_c = \cos^{-1}(1/n) = .724°$ and the number of Čerenkov photons produced per particle per meter is $50,000 \times \sin^2(.724) = 8.0/part/m$. At shower maximum one radiation length is roughly $1km$, therefore we expect roughly $500 \times 8 \times 1000 = 4 \times 10^6$ Čerenkov photons on the ground. To obtain more information about the nature of these photons, (i.e. their spatial, temporal, and angular distributions), it is best to turn to a Monte Carlo approach.

4.5 Monte Carlo Study

Our goals in this section are twofold. First we will use the Monte Carlo to study the Čerenkov light from EAS in more detail than possible in the previous sections. We will generate some distributions (spatial, temporal, and angular) for the photons and look at differences in these between the two types of primaries. Then we will couple a simple model of our telescope to the Monte Carlo in order to better understand the response of the telescope to these showers. The goal will be to see how the sensitive area of the telescope changes with incoming primary energy, for both proton and photon primaries.

In the first part of the Monte Carlo, written by Todor Stanev of Bartol, a given primary is allowed to interact with a nucleus, and secondary particles are produced; the energy, number, and type of secondaries are random but the distributions from which these random sequences are drawn are derived from measured cross sections. The output of this program is a list of 'track segments'; for each segment we store the x-y position of the start of the segment, the direction cosines of the beginning of the segment, the height of the beginning and the end of the segment, the time at the beginning of the segment (relative to when the primary would have hit the ground if it hadn't interacted), the energy of the particle at the midpoint of the segment, the particle type, and the direction cosines at the end of the segment.

The next part of the program was written by a member of our collaboration, Glenn Sembroski of Purdue. Here we generate the Čerenkov light

associated with each segment and follow it to the ground. For each photon we save the wavelength, x-y coordinates, direction cosines, and time of arrival on the ground. The shear number of photons prohibits us from using all of this information and we must develop some form of sampling to reduce computation time.

4.5.1 Spatial Distribution of Čerenkov Photons

Figures 4.2a and 4.2b show the Čerenkov photon density on the ground from a $320GeV$ photon primary and a $1TeV$ proton primary respectively (Hillas 1987). One can see, the photon shower has a high degree of symmetry, with the incident photon trajectory being the symmetry axis. There is no such symmetry axis for the proton shower. Figures 4.3a and 4.3b are similar except that photon densities have been averaged over azimuth. They have been created by the author using the collaboration's Monte Carlo. The characteristic Čerenkov ring is evident in the photon shower and absent from the proton shower.

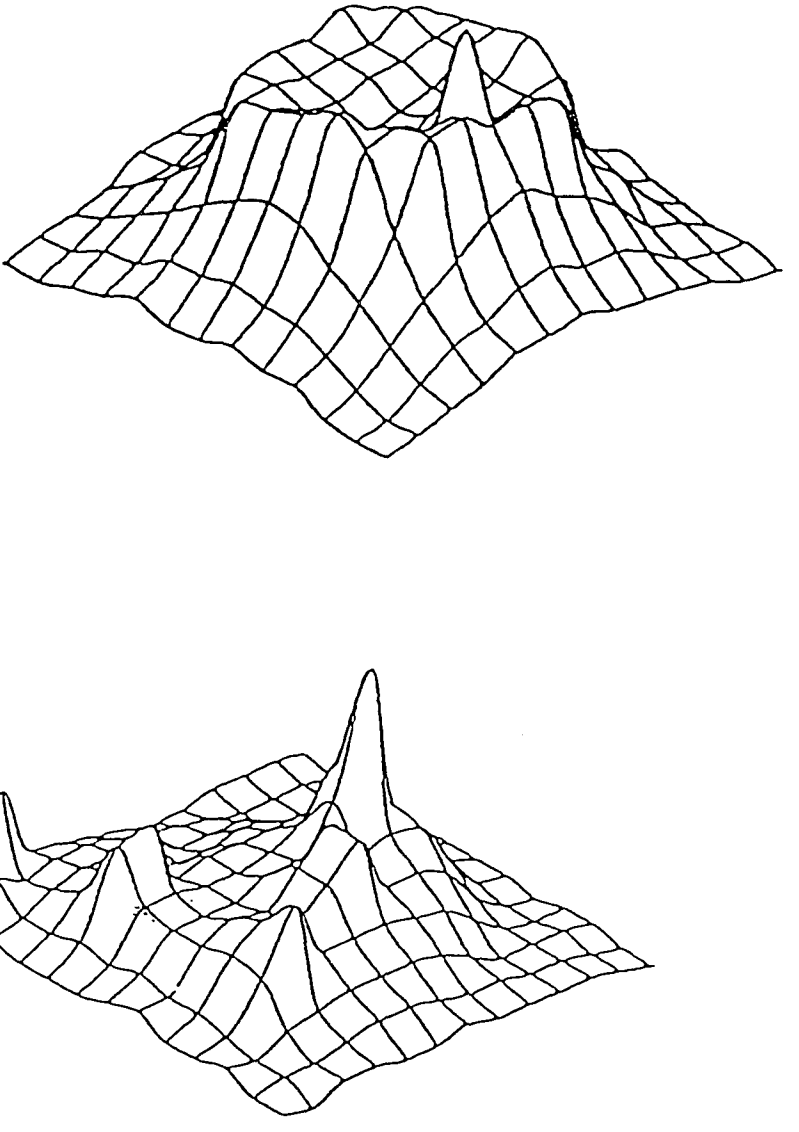

Figure 4.2 Distribution of photon density on the ground: (a) normally incident $320GeV$ photon primary, (b) normally incident $1TeV$ proton primary. A $600m \times 600m$ area of ground is shown, with $50m$ grid spacing.

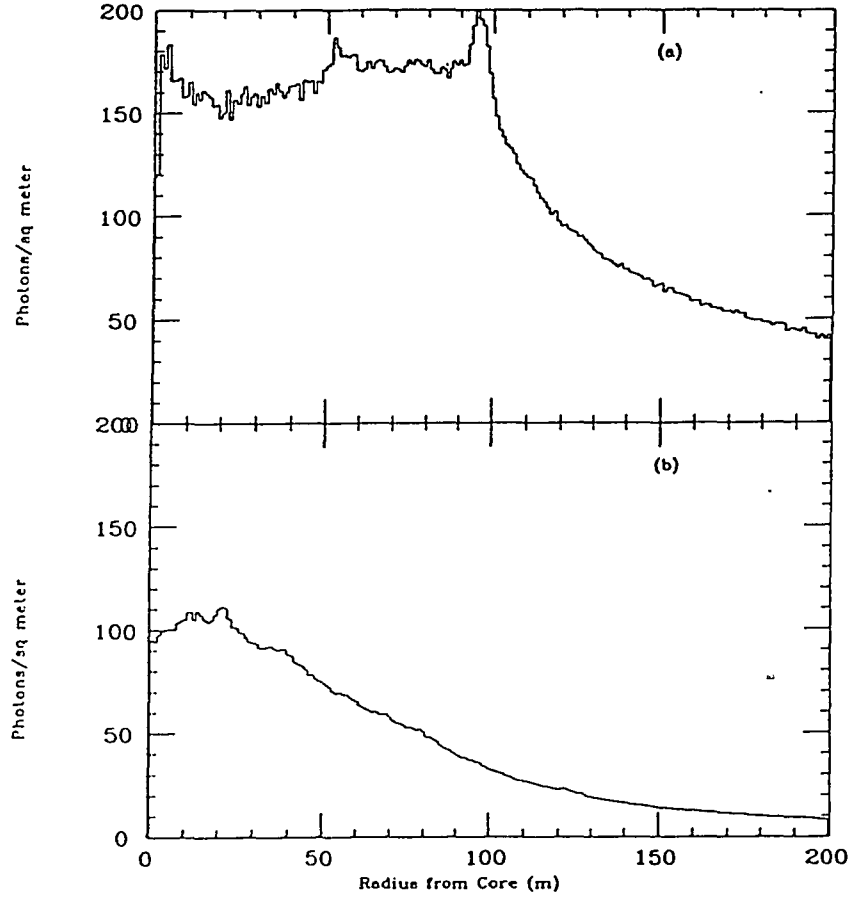

Figure 4.3 Radial distribution of photon density on the ground: (a) normally incident $600GeV$ photon primary, (b) normally incident $2TeV$ proton primary.

4.5.2 Angular Distribution of Čerenkov Photons

Figures 4.4a and 4.4b are similar to Figures 4.3a and 4.3b except that we have drawn different curves for different photon angles. We measure the angle from the vertical (incident primary direction) and plot photon densities versus radius for all photons with angles less than or equal to $(1/2)°, (3/4)°, 1°, 2°, 4°, 6°$, and all photons. In Figures 4.5a and 4.5b we show a scatter plot of photon angle versus radial distance from the shower core.

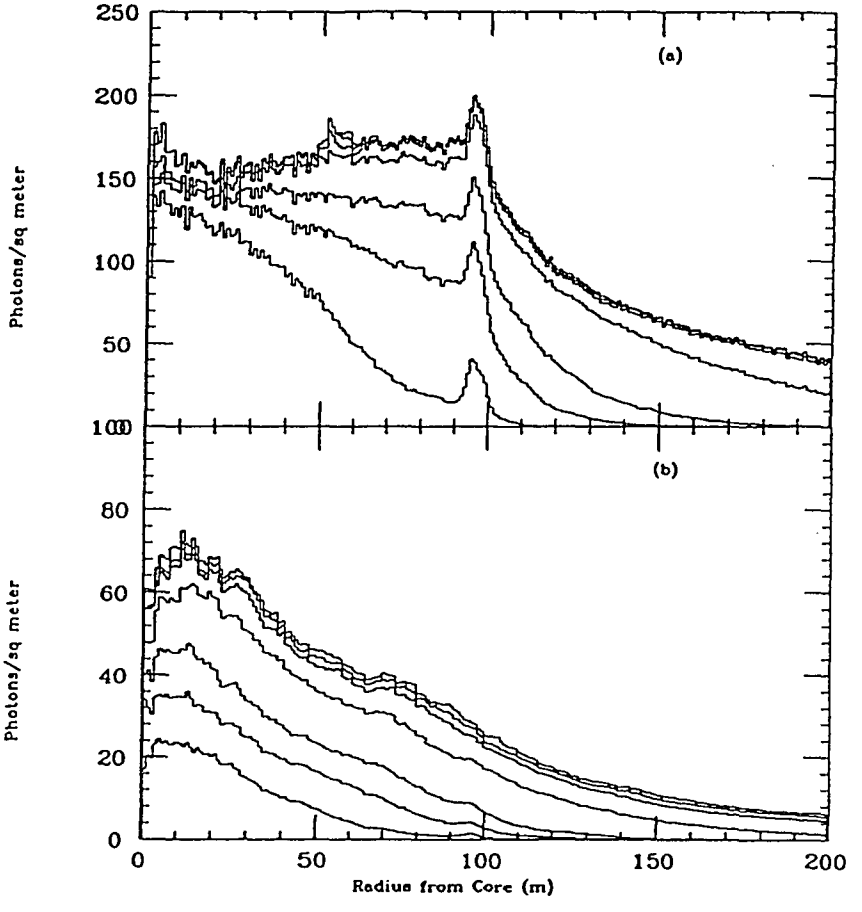

Figure 4.4 Radial distribution of photon densities for various cuts on angle from vertical. Curves are for $< 1/2, < 3/4, < 1, < 2, < 4, < 6$ degrees and for all photons. (a) $600GeV$ photon primary, (b) $2TeV$ proton primary.

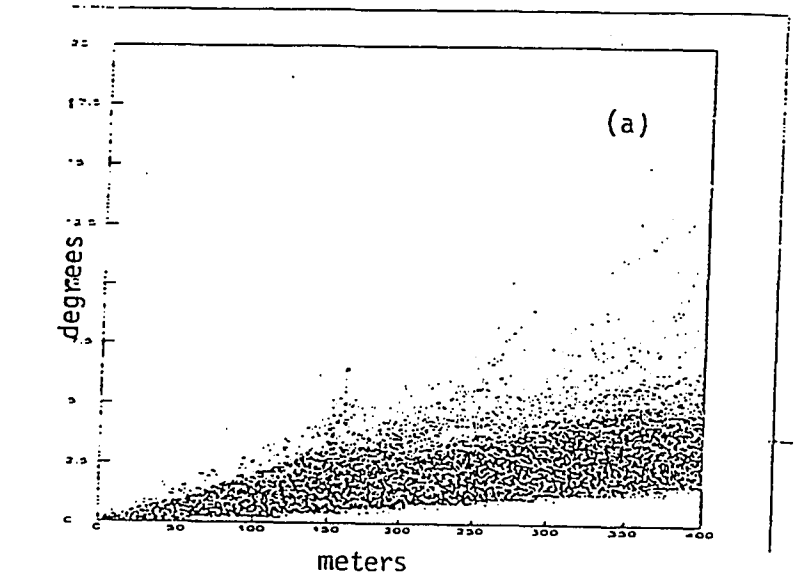

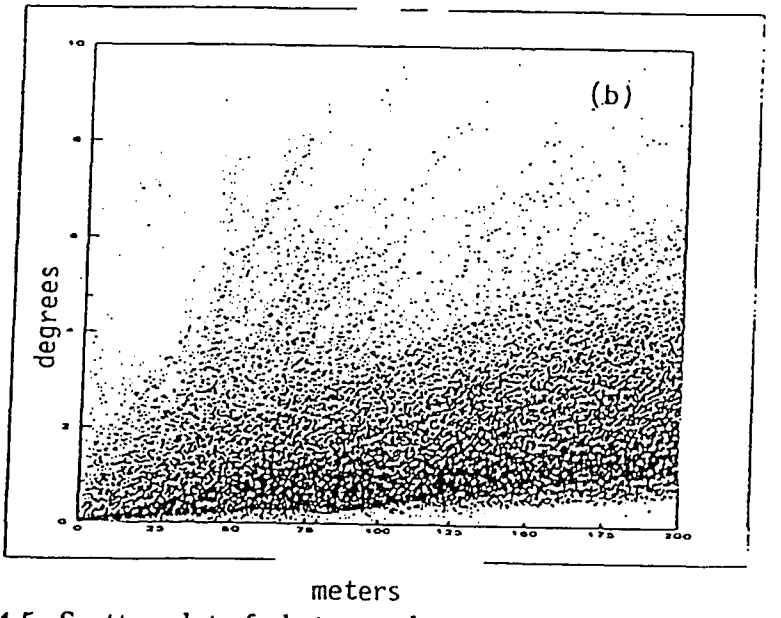

Figure 4.5 Scatter plot of photon angle versus radial distance from shower core. (a) $600GeV$ photon primary, (b) $2TeV$ proton primary.

4.5.3 Temporal Distribution of Čerenkov Photons

In Figure 4.6 we show the arrival time distribution of Čerenkov photons versus radial distance from the core for a photon primary. Since the shower core is not a good axis of symmetry for the proton shower it is inappropriate to average over azimuthal angle in this case. In Figure 4.7 we take a band around the x-axis and show the individual photon arrival times as a function of distance from the shower core (Suda 1989).

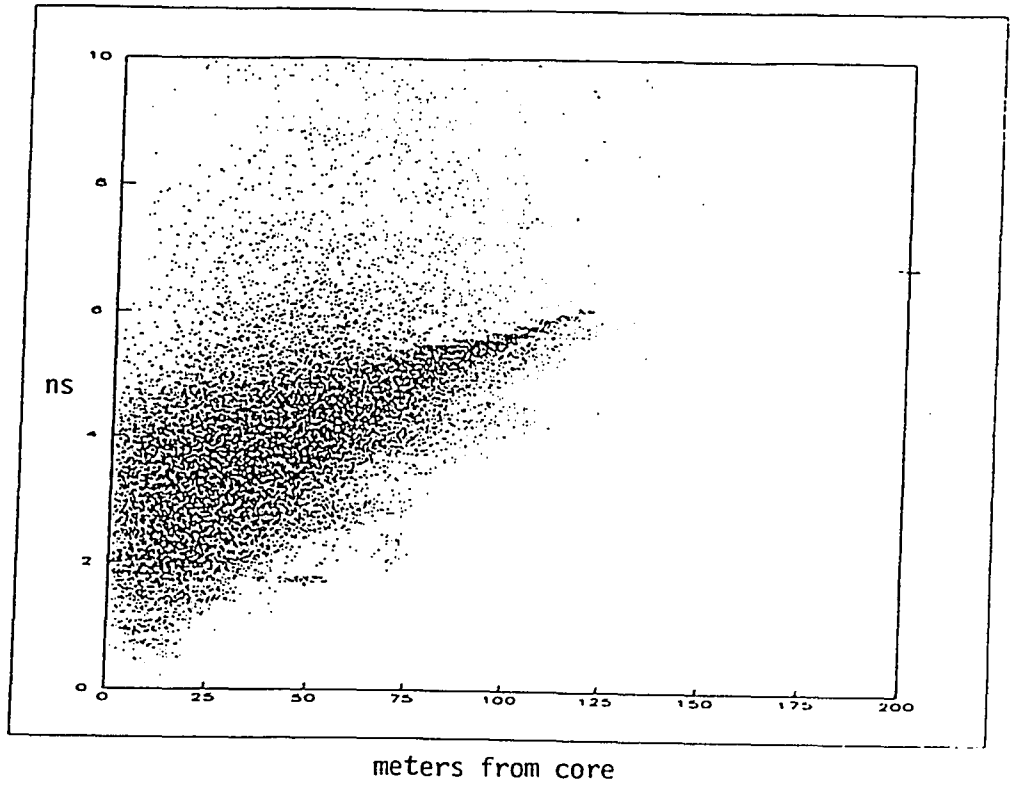

Figure 4.6 Arrival time distribution of Čerenkov photons as a function of radial distance from core for a $600GeV$ photon primary.

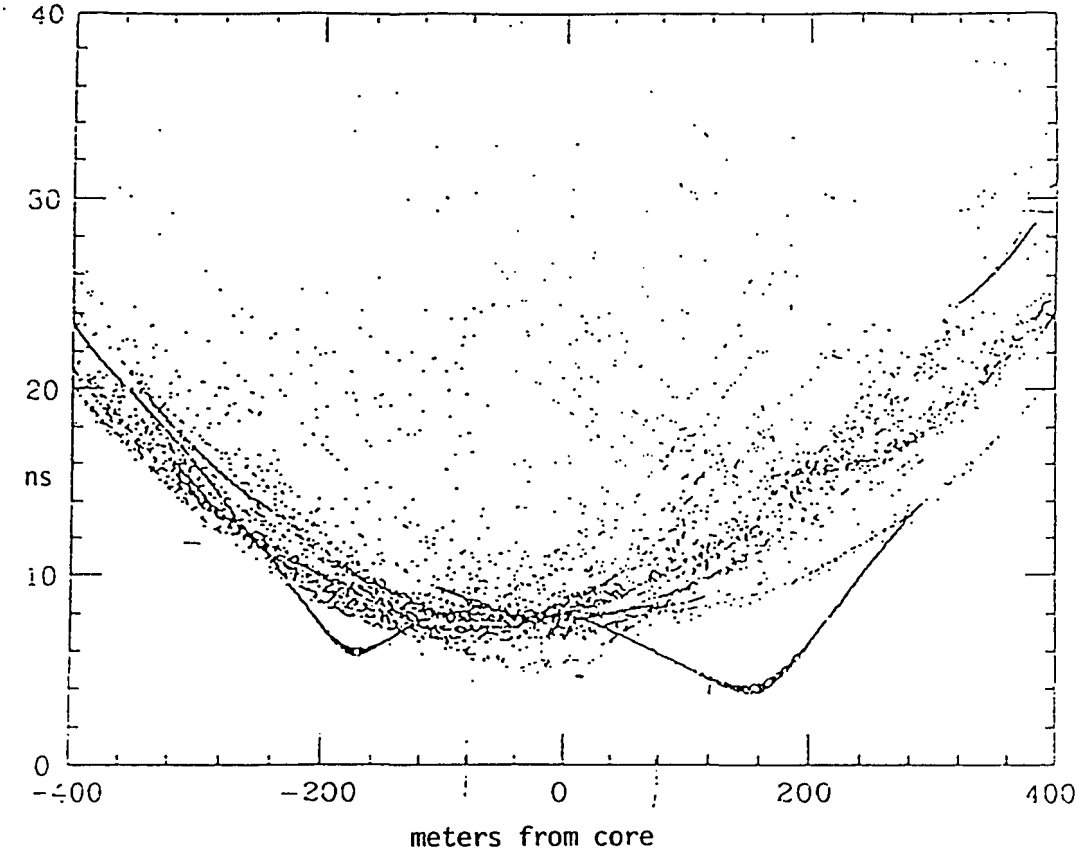

Figure 4.7 Arrival time distribution of Čerenkov photons as a function of distance from core for a $2TeV$ proton primary. From Suda 1989.

4.5.4 The Telescope

In the next chapter we will describe the physical characteristics of the telescope in detail. Here we take the telescope to consist of $10m^2$ of mirror area distributed over $16m^2$, with a $(3/4)^\circ$ aperture (full angle), and an efficiency (atmospheric response, PMT response, and filter response) of 5% (see Chapter 5 and Slane 1988).

We first construct an array on the ground $200 \times 200m^2$ on the ground. Each grid element is $1m^2$ and can store the arrival times of 20 photons. In order to mimic our telescope we impose the following criteria on the photons. First the direction of the photon must allow it fall within our aperture, and then the photon must make a PE in our electronics. Due to the frequency response of our filters and the PMTs the second criteria is wavelength dependent. In order to reduce running time we will only generate photons that would have passed all of these criteria.

We do this in the following manner. For a first pass we generate all photons and follow them through each component of the atmosphere and our telescope. In Figure 4.8 we show the efficiency of each component of our detector, as derived from the Monte Carlo. To obtain the effective efficiency we merely see what fraction of the incoming photons survived all of the wavelength dependent cuts. In this manner we obtain $eff = \#PE's/\#\gamma's = 884411/1.75 \times 10^7 = .05$. To reduce running time we will only generate 5% of the initial photons, but now we know that they will all be PEs if they pass

our angular and timing cuts. Note that we have not included the efficiency of the mirrors or our 'geometric efficiency' caused by the incomplete coverage by our phototubes. We will insert these later.

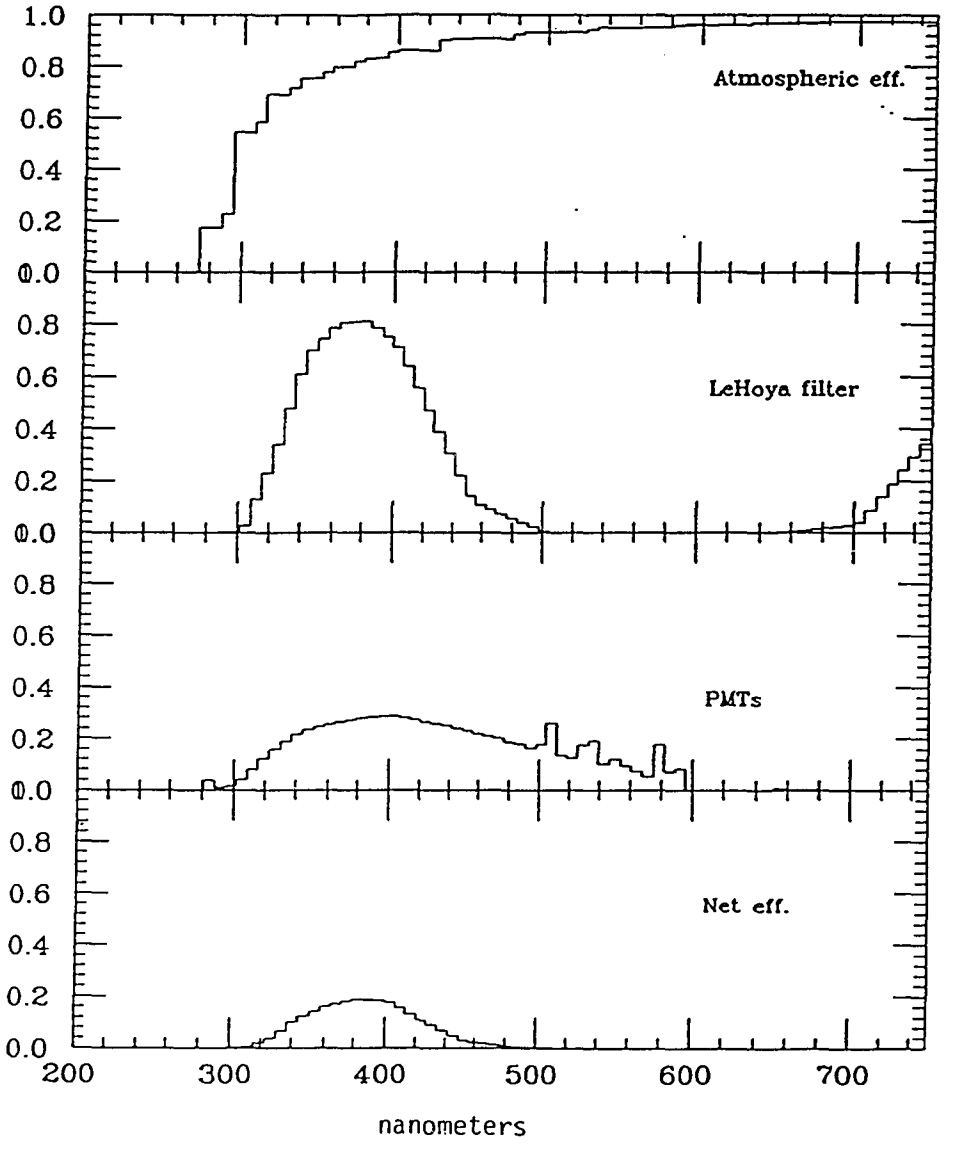

Figure 4.8 Surviving fraction of photons from: atmosphere, filters, and PMT's

4.5.5 Procedure

A gamma ray shower has a high degree of symmetry about the axis made by the incident particle's trajectory. In this case it is useful to examine photon density and arrival time distributions as a function of radius from the core of the shower. By making assumptions about our efficiency we can arrive at a critical radius at which the photon density is sufficient to trigger our telescope. Our trigger requirement for all of the following analysis will be 12 PE's within $5ns$. This technique will not work for proton induced showers and in fact is not very useful for photon showers when one wishes to observe the effects of shower to shower fluctuations .

To circumvent this problem we devise another technique for estimating the sensitive area of the telescope. We will consider our telescope to be comprised of 10 $1 \times 1m^2$ grid elements. We then move across the entire $400 \times 400m^2$ array area, examine the time structure of the photons resident there and determine if our telescope would have registered a trigger. Our sensitive area is just the fraction of times the telescope triggers, times the total area of the array, $1.6 \times 10^5 m^2$.

For a gamma-ray primary we take only showers that are along the axis of the telescope. We take 20 showers for each of the following energies: 30GeV, 300GeV, 600GeV, 1TeV, and 2TeV. We then plot the average area for each energy and the variance about this average. For the proton case we take 20 showers for each of the following energies: 300GeV, 1TeV, 3TeV, and 6Tev

(all at normal incidence).

Figures 4.9a and 4.9b show the derived area as a function of incident energy for photon and proton showers respectively. The error bars show the r.m.s. deviation in area as derived from the shower to shower fluctuations. Since we have three phototubes set back from the focal point of each aperture (see next chapter) we do not have complete coverage by the photocathode. Given the diameter of each phototube and the spot size for the distance from the focal point to the phototubes we estimate this geometric efficiency to be 75%. In addition to this the mirrors have been exposed to the elements for several years and their reflectivity has been degraded. We estimate their present reflectivity to be $\sim$ 65% (Slane 1988). These two losses have been incorporated into the detector Monte Carlo.

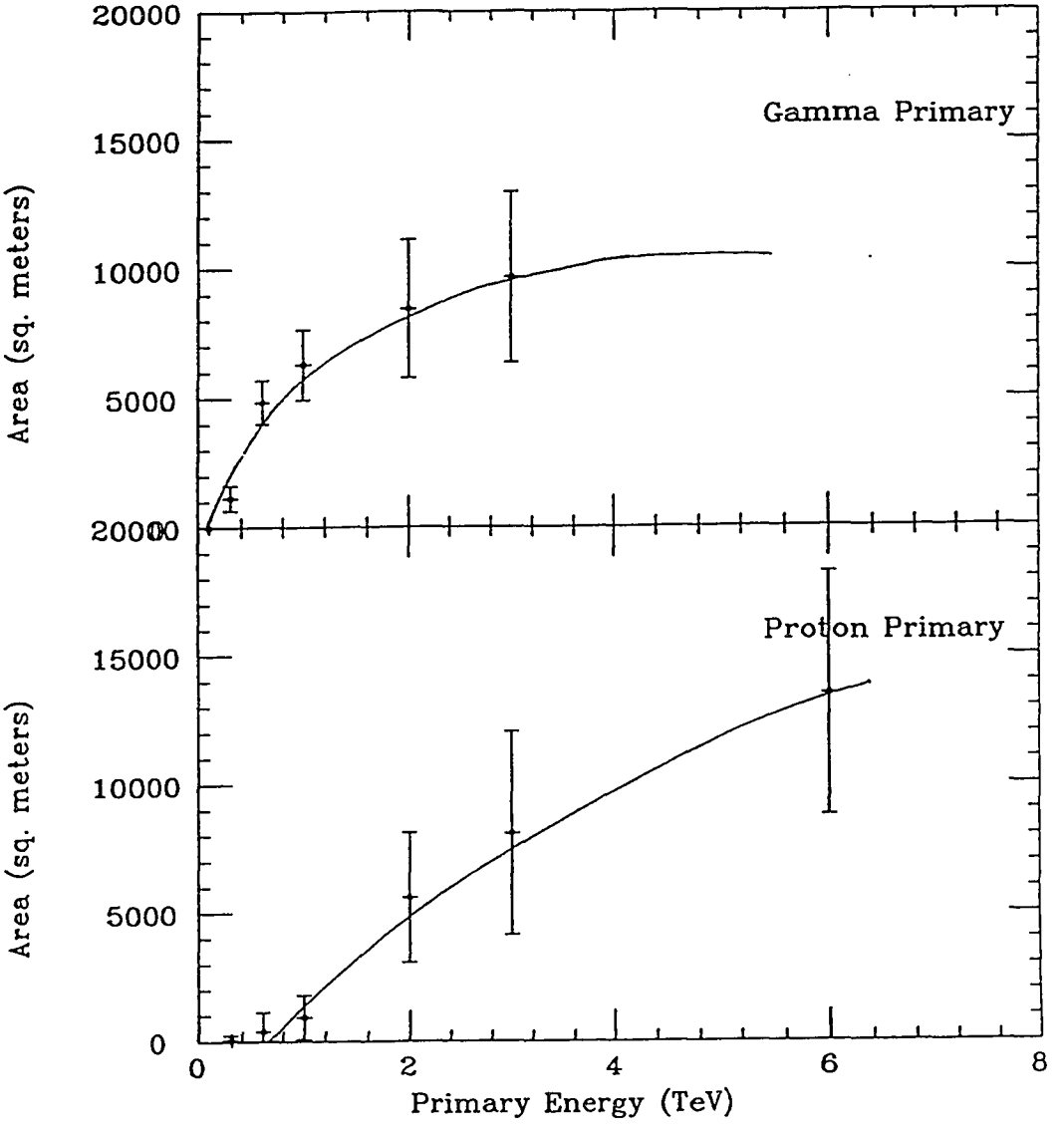

Figure 4.9 Effective trigger area versus incident primary energy for: (a) photon primaries, and (b) proton primaries.

Chapter 5

The Haleakala Gamma Ray Telescope and its Calibration

5.1 Introduction

In the previous chapter we saw that an extensive air shower gives rise to a pancake of Čerenkov light. Th pulse lasts for a few nanoseconds and contains roughly $100 photons/m^2$ contained within $\sim 4 mrad$. An air Čerenkov detector must be able to distinguish this signal from the night sky background, roughly $6 \times 10^{10} m^{-2} s^{-1} st^{-1}$. This is accomplished by utilizing fast phototubes and small apertures ($\sim 1°$) to look for many photons arriving within a few nanoseconds. By using the fastest available phototubes and state of the art electronics the Haleakala Telescope is able to reject the night sky background while discriminating at the one photoelectron level. This makes it possible for us to obtain the lowest possible energy threshold for a given mirror area. Here we describe the Haleakala Gamma Ray Telescope and the methods used to calibrate the electronics chain. For a more complete

physical description of the telescope see Szentgyorgi 1986.

5.2 Physical Description

The Haleakala Gamma Ray Telescope (HGRT) is located on the island of Maui in Hawaii (latitude $+20°42.6'$, longitude $-156°15.5'$). Situated near the summit of the Haleakala volcano, at an altitude of $2,900m$ above sea level, we are favored with excellent viewing conditions throughout most of the year. The telescope is an air Čerenkov detector consisting of six, $1.5m$ mirrors provided by the Utah Cosmic Ray Facility. The six mirrors are arranged in an equal time plane to within $\sim 0.25ns$. Located above each mirror is a cannister with two 3/4" apertures. The apertures are located so they receive light from two different regions of the sky separated by 3.6° in declination. This enables us to simultaneously monitor an 'off-source' region of the sky, which helps us track the behavior of both, the background cosmic ray flux and the ambient atmospheric conditions.

Behind each aperture are three phototubes, set slightly back from the focal plane of the mirrors. Due to the size of the mirrors, a single phototube placed at the focal point would have intolerably high singles rates. For this reason it was decided to share the light equally among three phototubes. This arrangement leads to complications with the optics as well as to a loss in efficiency. However, it allows us to have a large mirror area and single photo-electron discrimination, thus lowering our energy threshold.

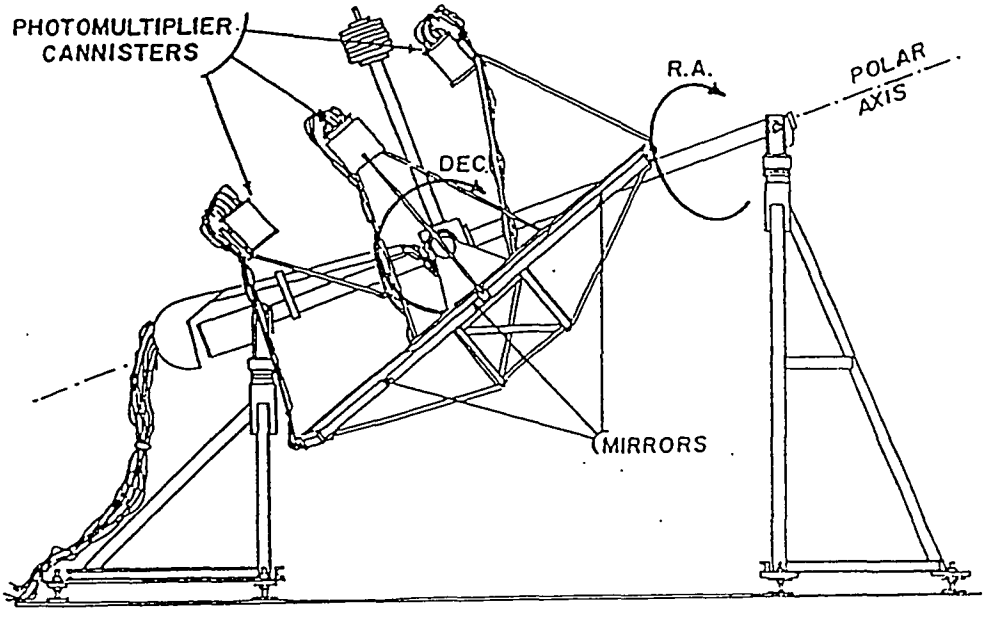

Figure 5.1 The Haleakala Gamma Ray Telescope. (From Szentgyorgi 1986)

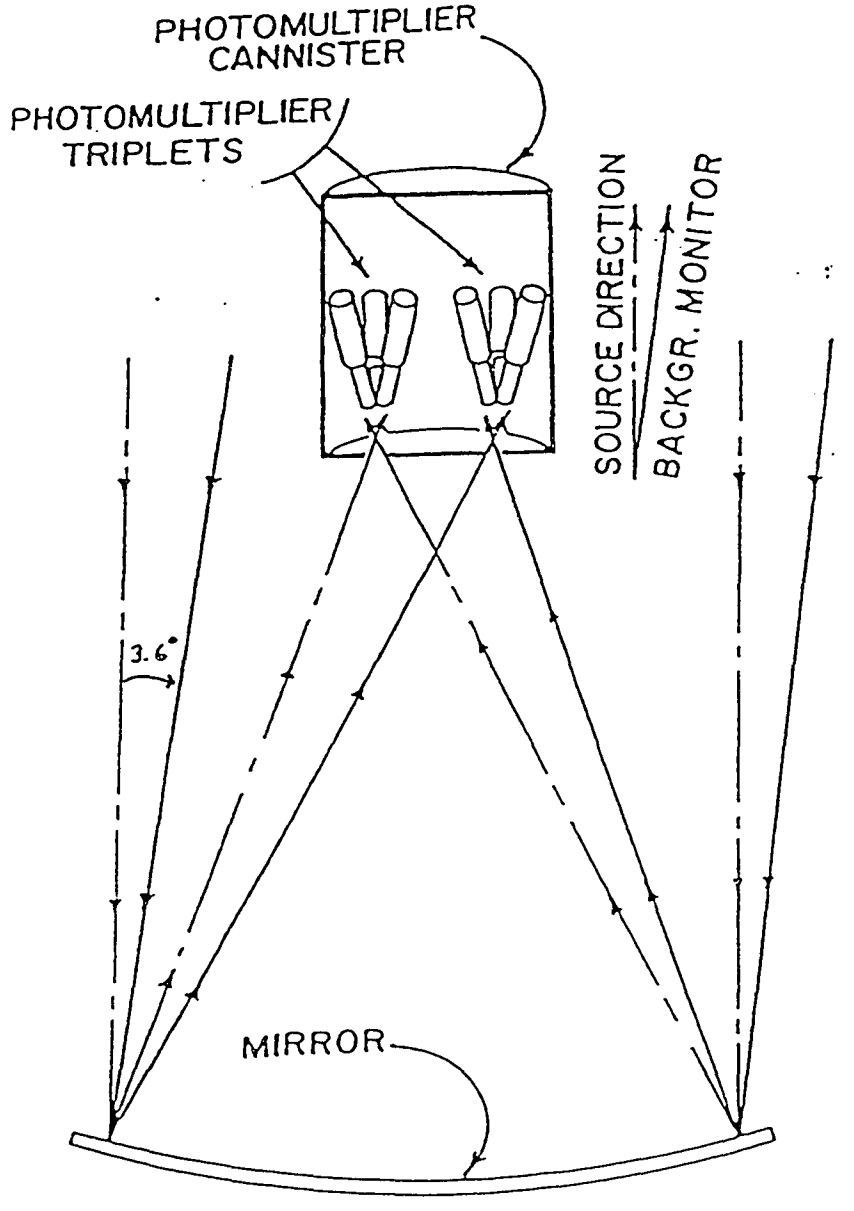

Figure 5.2 Schematic of mirror and 'can'. (From Szentgyorgi 1986)

The six mirrors are mounted on an equatorial mount. The main advantage of this system is the ease with which it allows one to track a source in the sky. Also, the off-source region does not change with time. The main disadvantage of this arrangement is that the off-source region has a different 'zenith angle' then the on-source region. In principle it is possible to correct for this effect (see next chapter), but differences in the response of the two apertures make this a difficult affair. To ensure the validity of the procedure the apertures are toggled every 720 seconds so that both apertures monitor the source region of the sky, as well as a background region.

5.3 Electronics and Data Acquisition

5.3.1 Timing Circuitry

From each phototube comes three cables, two signal cables and one cable to provide the high voltage to the phototube. The anode signal, used for timing information, from each phototube is amplified in the cannister before being sent into the 'counting house' via an RG-8U coaxial cable. The amplifiers have a rise time of $3ns$, a bandwidth of $1GHz$, and a gain of ~ 40. The dynode signal, which is used for pulse height determination, is sent directly to the counting house via an RG-58 cable.

Once inside the counting house the anode signal is sent to either a Lecroy 623 or 620 BL discriminator. Discriminator thresholds are set to 40mV, corresponding to a single photo-electron signal. Two outputs are taken from

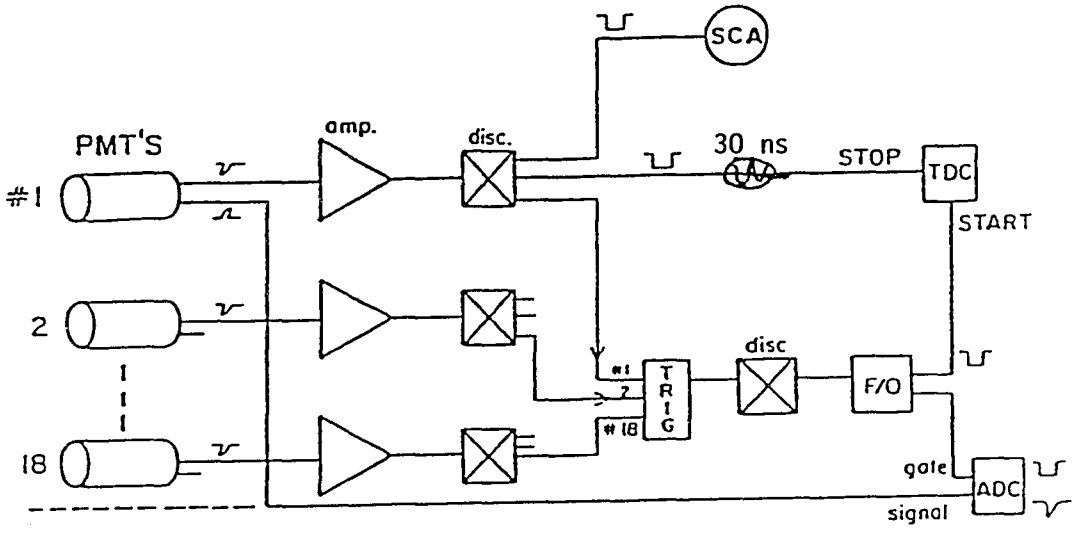

Figure 5.3 Schematic of data acquisition electronics. (From Slane 1988)

the discriminator, one goes into a logical fanout and the other to a Lecroy model 380A multiplicity logic unit. From the fanout three signals are taken, the first goes to a $33ns$ delay cable, then into the TDC stop, the second into a $33ns$ delay cable and then into a latch input, the last signal goes into a counter which is used to monitor the singles rate in the tube.

Trigger Logic

After discrimination the anode signal is input to a multiplicity logic unit. The output of this unit is set to $50\times$ (the number of input signals) mV. This signal goes to another discriminator whose threshold is set at $350mV$. Since the discriminated anode pulses have a duration of $\sim 7ns$, a trigger will be established if seven phototubes generate a signal above threshold ($40mV$) within $7ns$. Due to finite pulse rise times and some slop in the discriminators, this number (7 hits in $7ns$) is only a nominal value, in practice a temporally tight occurrence of 6 hits can generate a trigger, while a higher multiplicity event may have slightly looser timing.

The output from the trigger discriminator is fanned out to all of the TDC modules and acts as the start pulse for the TDCs. As explained above the stop pulse is given by the discriminated anode pulse after it has gone through the $33ns$ delay cable. The TDC time is then the time difference between the time when the MLU has an output greater then $350mV$ and when the delayed anode pulse reaches the TDC stop gate. This has two

important consequences for us. First, it means that all times are measured relative to the seventh phototube to receive a hit. For different events this is a different channel and therefore we must be careful not to overestimate the accuracy of our calibration, which is an average over all tubes being the seventh to fire. The other effect is called 'trigger slewing', this arises because higher multiplicity events generate a higher MLU output, therefore the MLU output reaches the discriminator threshold sooner. But since the time taken for the anode pulses to reach the TDC stop gate is unchanged the TDC value read out will be greater. Since all TDC values are changed by the same amount we use a 'sliding time window' when making offline cuts (to eliminate random light) and thereby circumvent this problem.

5.3.2 Pulse Height Measurement

The other signal from the PMTs, a sum of the last five dynode signals, is used for pulse height determination. After summing, the dynode signal is sent to the electronics house along a RG-58 cable. Once there, the signal is amplified and routed to a Lecroy 2282B ADC unit. The ADC is given a $70ns$ gate, generated by the trigger logic, and integrates the charge deposited on its front end capacitor over this gate interval.

In April of 1986 (about 2 months prior to the beginning of the Cygnus runs) a number of tests were performed on the telescope electronics. To test the linearity of the amplifiers and ADCs, pulses of various amplitudes were input to the RG-58 cables at the base of the canisters. The results of these

tests are given in Table 5.1.

From this we can construct gain curves for all of the channels, these are shown in Figure 5.4, the amplifiers and ADCs are seen to be linear over a wide range of input pulse heights ($40mV$ to $1012mV$) to better then 3%. The slopes of all of the gain curves are plotted in Figure 5.5 versus channel number. For the A aperture the mean of these slopes is $1.16 \pm .07 counts/mV$ and for the B aperture $1.17 \pm .04 counts/mV$. Aside from the phototubes themselves the gain of all channels is very similar.

5.3.3 Latches

Because the TDC stop signal is delayed by $33ns$ relative to the generation of a trigger, there exists the possibility that a phototube will be hit by random light before the trigger is established. Since the TDCs are single hit, timing information for this channel is lost. To aid in the reconstruction of such an event, 'latches' have been installed. A latch receives a $10ns$ long gate, centered around the trigger time, from the trigger logic. If the channel receives a hit above threshold during this time a 1 will be latched, if not a 0. In this manner we can obtain crude ($10ns$) timing information even for channels that receive early hits from random light.

5.3.4 The Camerini Ambush

In the course of running the experiment, we felt that we were receiving too many early hits and that the crude timing information obtained from the

Channel	40mV	80mV	160mV	320mV	640mV	1012mV
1	49	98	190	376	756	1140
2	51	101	196	386	775	1147
3	52	99	197	391	793	1234
4	48	96	186	369	745	1163
5	49	98	192	380	770	1196
6	45	88	171	341	690	1077
7	51	101	200	395	799	1243
8	42	84	163	323	654	1025
9	48	96	189	374	755	1166
10	56	110	213	419	846	1308
11	44	86	169	335	677	1053
12	50	100	195	386	781	1220
13	46	92	181	358	726	1133
14	51	101	197	391	794	1236
15	50	98	191	378	768	1209
16	49	98	189	375	759	1187
17	49	96	185	368	739	1156
18	50	97	188	370	747	1162
19	59	101	195	385	787	1207
20	50	90	172	342	698	1072
21	0	0	0	0	0	0
22	56	96	185	368	751	1153
23	55	98	192	381	776	1186
24	55	92	179	357	739	1123
25	57	98	191	379	779	1199
26	54	98	188	375	765	1183
27	53	95	183	365	749	1150
28	54	93	182	362	739	1138
29	55	100	195	385	790	1216
30	60	104	204	403	826	1268
31	52	91	180	360	735	1134
32	56	100	192	383	783	1205
33	54	99	191	379	778	1192
34	57	100	195	387	789	1203
35	55	98	190	376	771	1186
36	57	98	190	379	773	1180

Table 5.1 Pedestal subtracted ADC counts for various input pulse heights

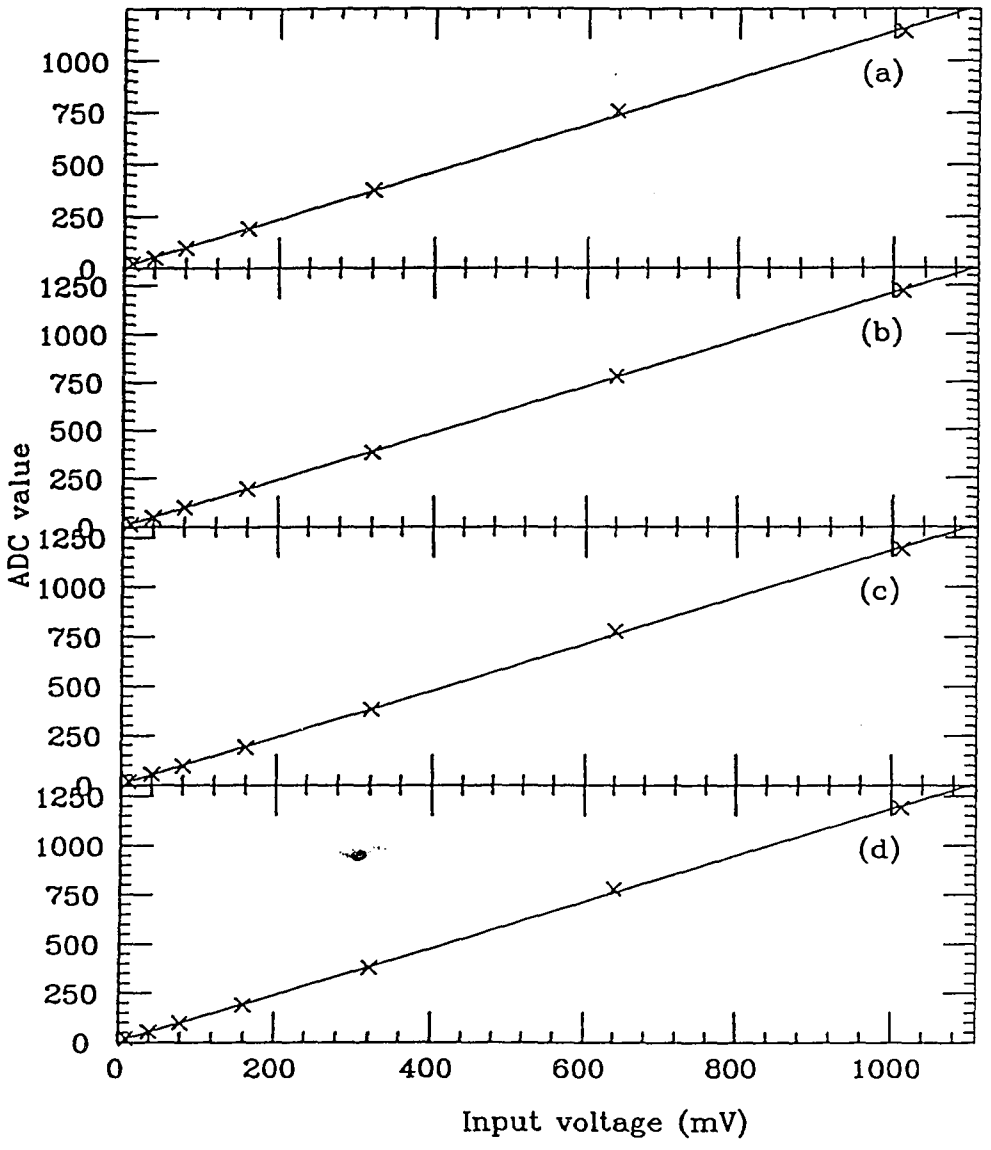

Figure 5.4 ADC Gain curves for 4 channels (from pulser run). Pedestal subtracted ADC values versus input pulse height in millivolts

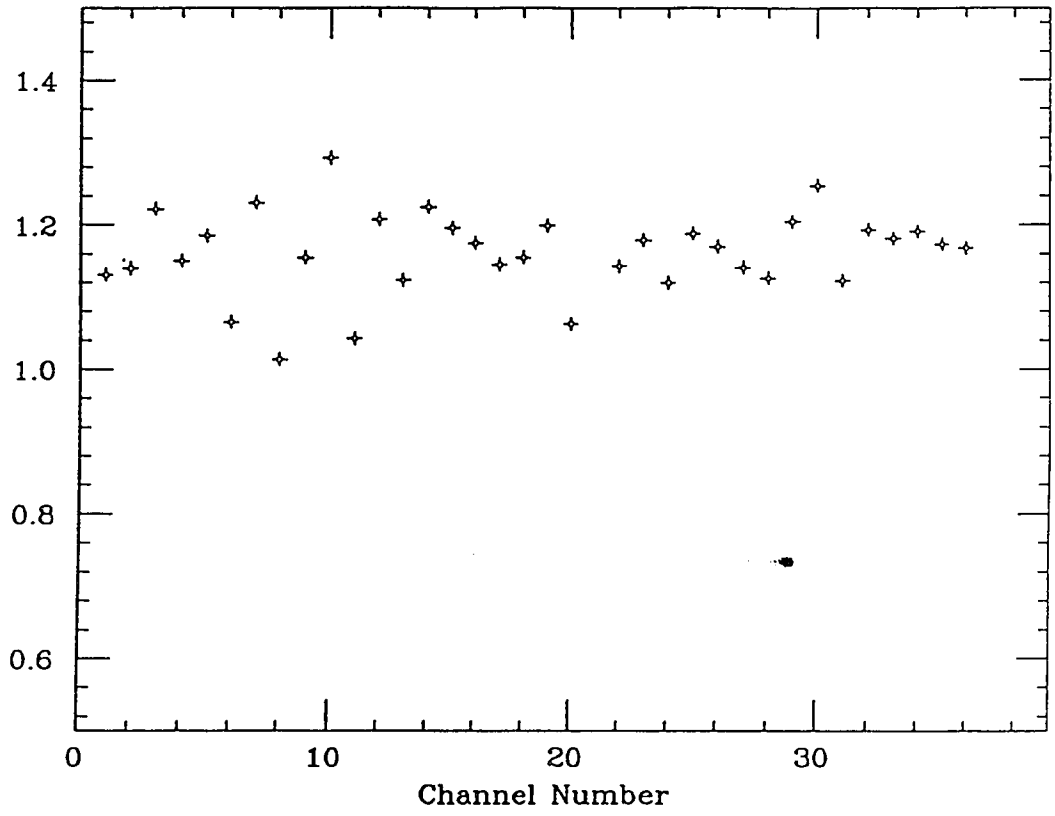

Figure 5.5 Gain of each channel. ADC counts/mV vs. channel number

latches was not sufficient for our purposes. To this end, we installed the 'Camerini ambush'. All of the 620 discriminators in the anode to TDC stop chain were replaced by 623B vetoable discriminators. The ambush consists of an inhibit signal sent to the veto input of the 623Bs. The inhibit is lifted 10 ns before the TDC start is generated by the trigger logic.

5.4 Data Acquisition

The experiment is under the control of a Digital Equipment Corp. LSI 11/73 computer. The operating system is RSX-11M and the data acquisition program used is a modified version of the MULTI system developed at Fermi Lab. Upon generation of an event trigger an interrupt is sent the computer telling it to initiate a reading of the CAMAC modules (containing the TDC and ADC information) as well as the event time.

We have established four different types of triggers. Two normal telescope triggers, one for each aperture, an event where both apertures generate a trigger simultaneously, and an environmental event (see below).

The environmental event is used to monitor the status of the hardware and the background light levels. Here we read out tube voltages via scanning ADC modules, individual tube firing rates via scalers, and tube currents via scanning ADCs. The singles rates of the tubes give us a reliable estimate of the background light levels and therefore the expected trigger rate from random light.

5.4.1 Event Time Determination

In order to perform periodic analysis of fast pulsars it is necessary to have very accurate timing over the time interval that data is being analyzed. In this regard we are rather fortunate to be close to the Lunar Ranging Experiment operated by the University of Hawaii. They are equipped with a cesium beam clock which is constantly corrected by the GPS satellite network. We get a $1MHz$ and a $1Hz$ signal from them which we use to drive a modified Datum clock. This time standard is accurate to within $2\mu s$ at any given time and drifting is less then $10^{-4}\mu s s^{-1}$.

5.5 Calibration Procedures

Here we describe the procedure used to calibrate the telescope. The most important part of the calibration is the timing between the various channels. Timing differences arise from unequal cable lengths and differences amongst individual phototubes and amplifiers. We will show that the differences are stable over long periods of time and can be corrected to give us a relative timing accuracy, between channels, of $\sim .8ns$. In order to determine the number of photoelectrons emitted from the photocathode we must determine the pedestal and the gain of each ADC.

5.5.1 Timing Calibration

To perform with the timing calibration we require a set of events where all hit tubes where hit at the same time (to within the accuracy of our final calibrations). Before selecting such a set of events one must be aware of two important effects: 'trigger slewing' and 'ADC slewing'; both of which introduce a systematic bias to the recorded TDC times. Once these effects are understood and eliminated, we can proceed with the timing calibration.

Trigger Slewing

Since the output from the multiplicity logic unit (MLU) is proportional to the multiplicity of the event (the number of participating channels), and the rise time of the MLU is independent of the multiplicity, an event with a large multiplicity will exceed the MLU discriminator level sooner then a low multiplicity event. The TDCs will receive their start pulses sooner for a higher multiplicity event, translating into larger TDC readings for high multiplicity events. Figure 5.6 clearly shows the effect. Plotted are uncalibrated TDC distributions for various event multiplicities. As the multiplicity of the event is increased, the center of the distribution is shifted to later times. By demanding that events have a multiplicity of fifteen or greater, differences in trigger times between events is made negligible. One can see that between a multiplicity of 15 and 17 the location of the peak shifts by less then $.5ns$.

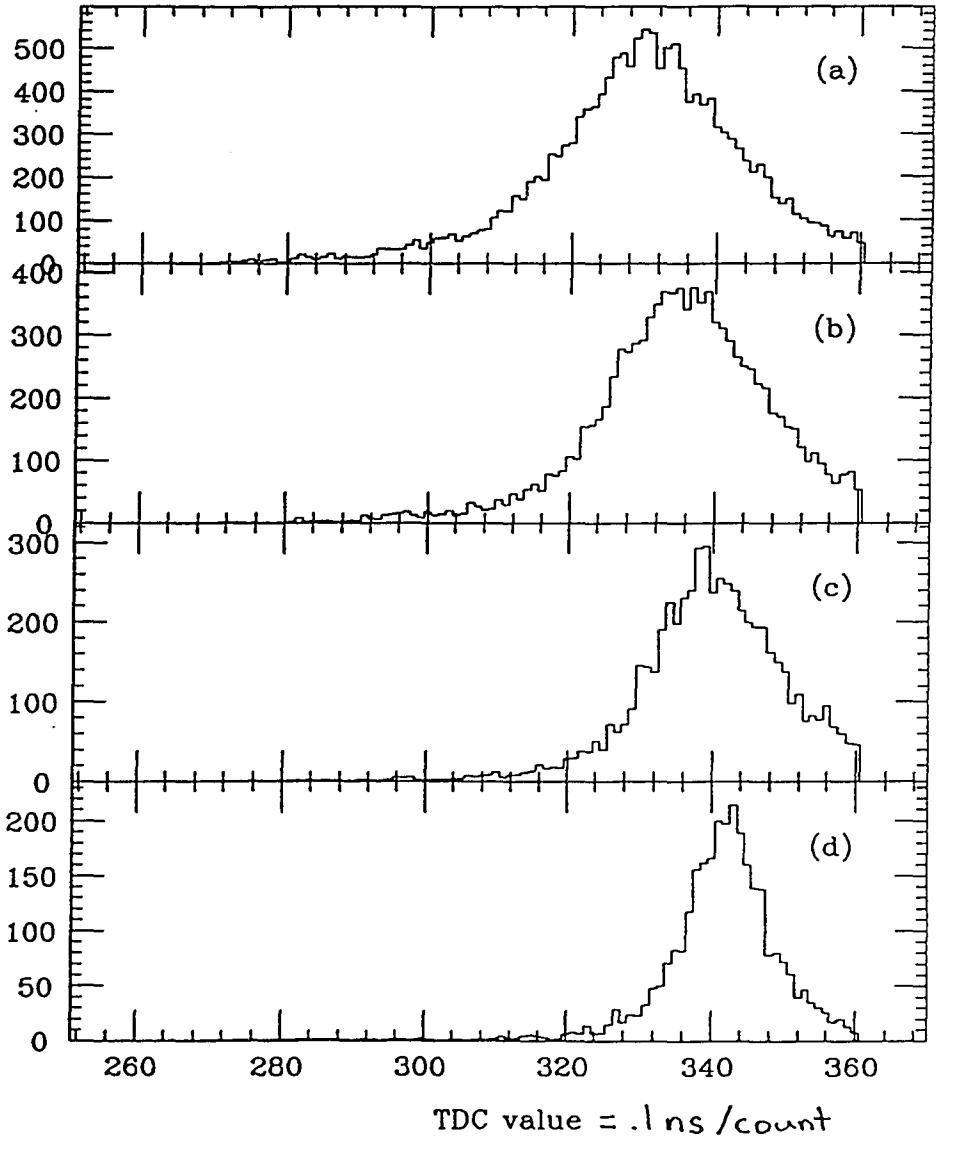

Figure 5.6 Trigger slewing. Shown are uncalibrated timing distributions for channel 3. (a). multiplicity 10, (b). multiplicity 12, (c). multiplicity 15, and (d). multiplicity 18

ADC Slewing

While trigger slewing is a global characteristic of each event (all channels are shifted by the same amount), ADC slewing is different for each channel in the event. The greater the number of photo-electrons produced by the phototube, the larger the pulse height into the discriminator, and the sooner a **stop** pulse will be sent to the TDC unit (see Figure 5.7). Plotted are TDC distributions for a fixed event multiplicity, 10, but for different ranges of ADC values.

By demanding an ADC value of 500 or greater we can eliminate any ADC slewing. We do this for calibration purposes. There is also the question of whether or not to apply ADC slewing corrections to each event used in the analysis. From Figure 5.7 we see that the maximum error introduced by ignoring the slewing corrections is $\sim .4ns$. We see below that this does not add appreciably to our total timing uncertainty, and so choose not to preform such a correction on a channel by channel basis for each event.

Procedure

Having removed all systematic bias from our event samples we are left to find a suitable set of 'equal time' events (i.e. events where all PMT pulses arise from photons which strike the photocathodes of all channels simultaneously). There is a linear relation between event multiplicity (number of channels receiving hits above threshold) and the local photon density. As the photon

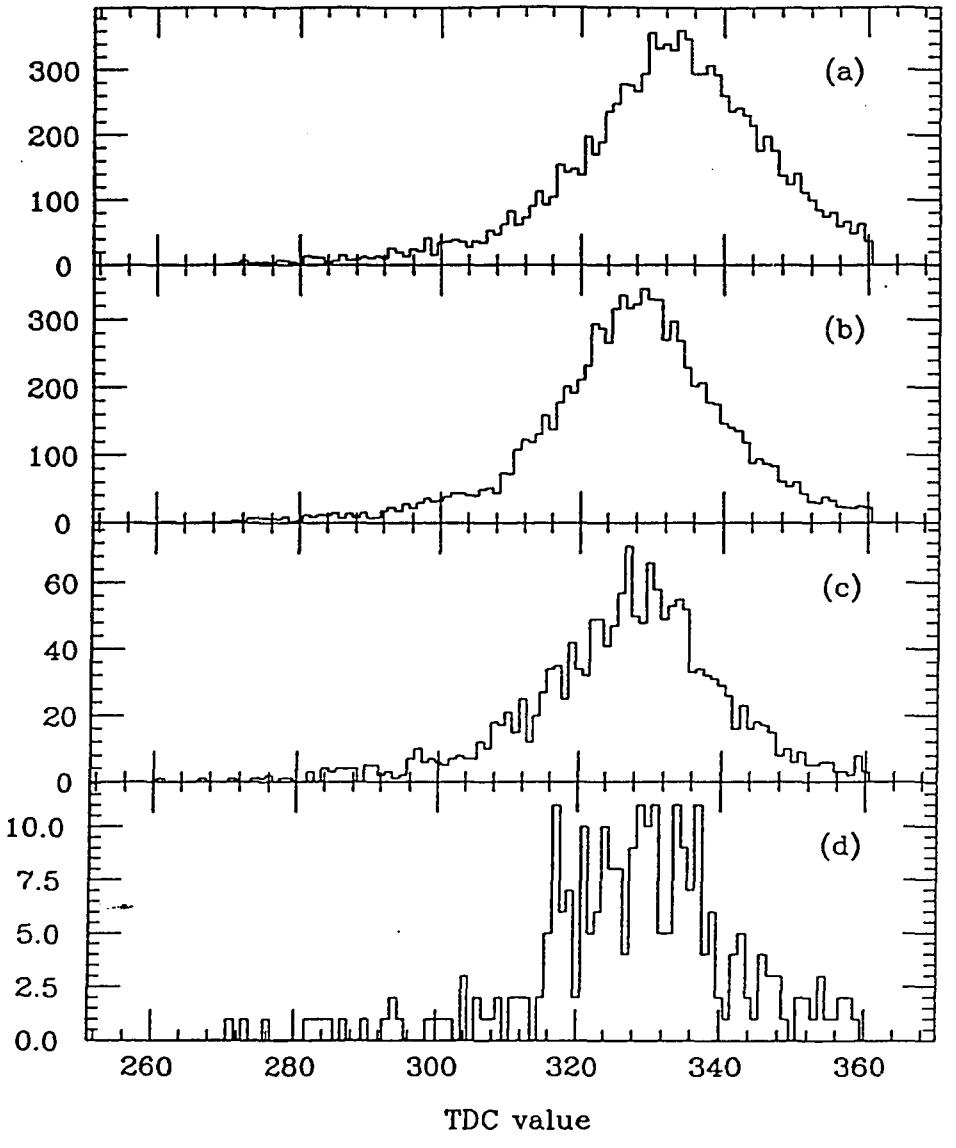

Figure 5.7 ADC slewing. Shown are uncalibrated timing distributions for channel 3, for an event multiplicity 10. (a). ADC range 0-200, (b). ADC range 200-300, (c). ADC range 300-400, and (d). ADC range 400-600

density increases it becomes more probable that all discriminated signals arise from photons contained within the first fraction of the shower front, $\sim$ few tenths of a nanosecond (see Figure 4.6). So in high multiplicity events, we have an isochronous surface with which to calibrate the TDCs.

Calibrations are performed on a monthly basis. All runs from each month being used in the calibration. For each channel a histogram of TDC times is made. In order for a TDC value to be entered into the histogram we require that: (1) the event multiplicity must be greater then or equal to fifteen (for trigger slewing), and (2) the ADC value associated with the channel must be greater than 600 (ADC slewing). After all histograms (one for each channel) are made, they are scanned by computer and the most probable value is selected. The difference between this most probable value and 330 TDC counts is stored in the calibration file.

Accuracy of TDC Calibration

There are 3 main contributions to the inaccuracy of our timing calibrations. First is the inherent 'jitter' of the phototubes, roughly $.6ns$. The next uncertainty arises from the manner in which our trigger is formed. It will be recalled that the seventh tube to be 'hit' initiates the trigger. Therefore all TDC times are times relative to this seventh tube. When performing calibrations we ignored this and therefore made an average calibration over timing differences between all possible triggering tubes.

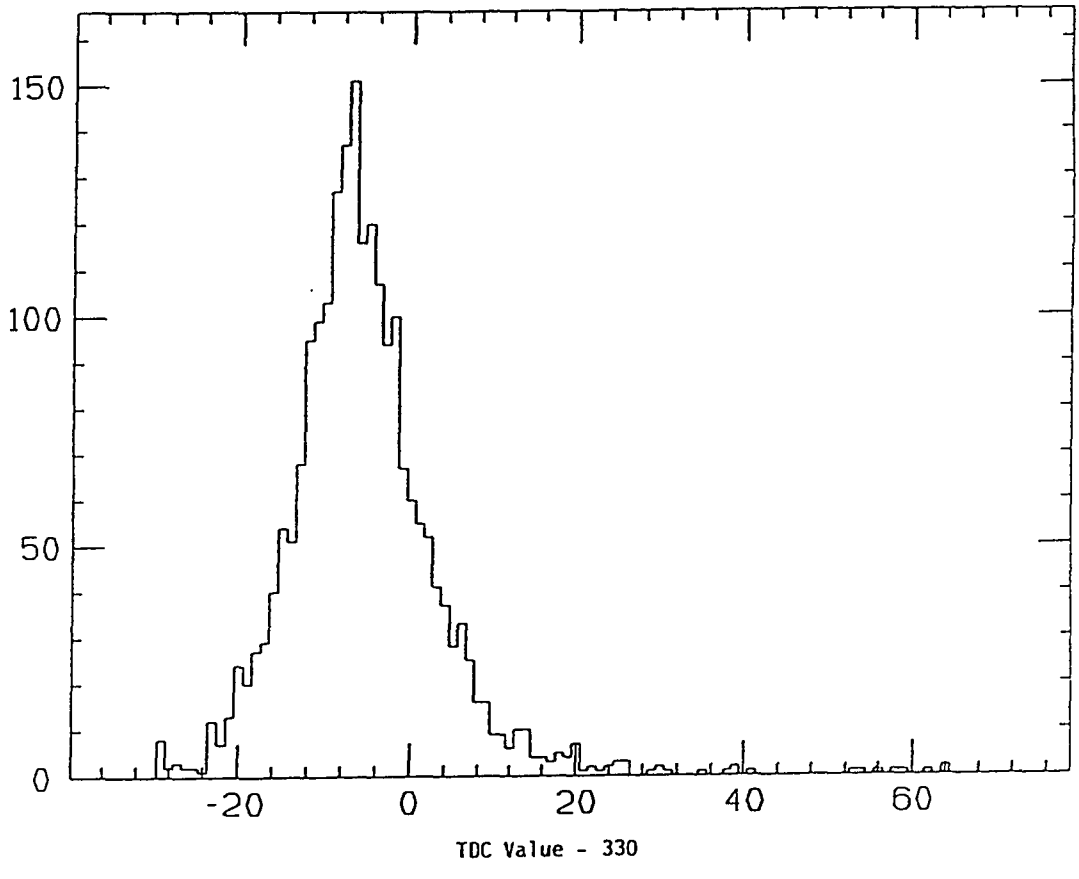

Figure 5.8 Timing histogram for channel 3

Since all timing differences are fixed, if all 18 tubes are hit at the same time (by the leading edge of the shower) the same tube, the seventh fastest channel, will will always be the channel that initiates the trigger. So by looking at the width of the TDC distributions made for events with a multiplicity of 17 and comparing that to the width of the same distributions made with 18-fold events we can estimate the uncertainty associated with not knowing which tube initiated the trigger.

From an examination of Figure 5.9 we estimate that this introduces $\sim$ $.4ns$ uncertainty in the TDC arrival times.

Adding all timing errors in quadrature ($.6ns$ jitter, $.4ns$ neglect of ADC slewing, and $.4ns$ averaging over trigger initiating tube) we obtain a relative timing error of $\pm.8ns$, in agreement with the r.m.s. deviation seen in Figure 5.8.

5.5.2 ADC Calibration

Pedestal Determination

To determine the pedestal of each ADC channel we require a set of events where no photoelectrons were present in the channel. So if in any event a given channel did not receive a hit (look for TDCs that have 'timed out', so no photoelectron was generated while the ADC gate was enabled), its ADC value is entered into a histogram. Again an entire month's data is scanned and histograms are made for each channel. The histogram is scanned for the

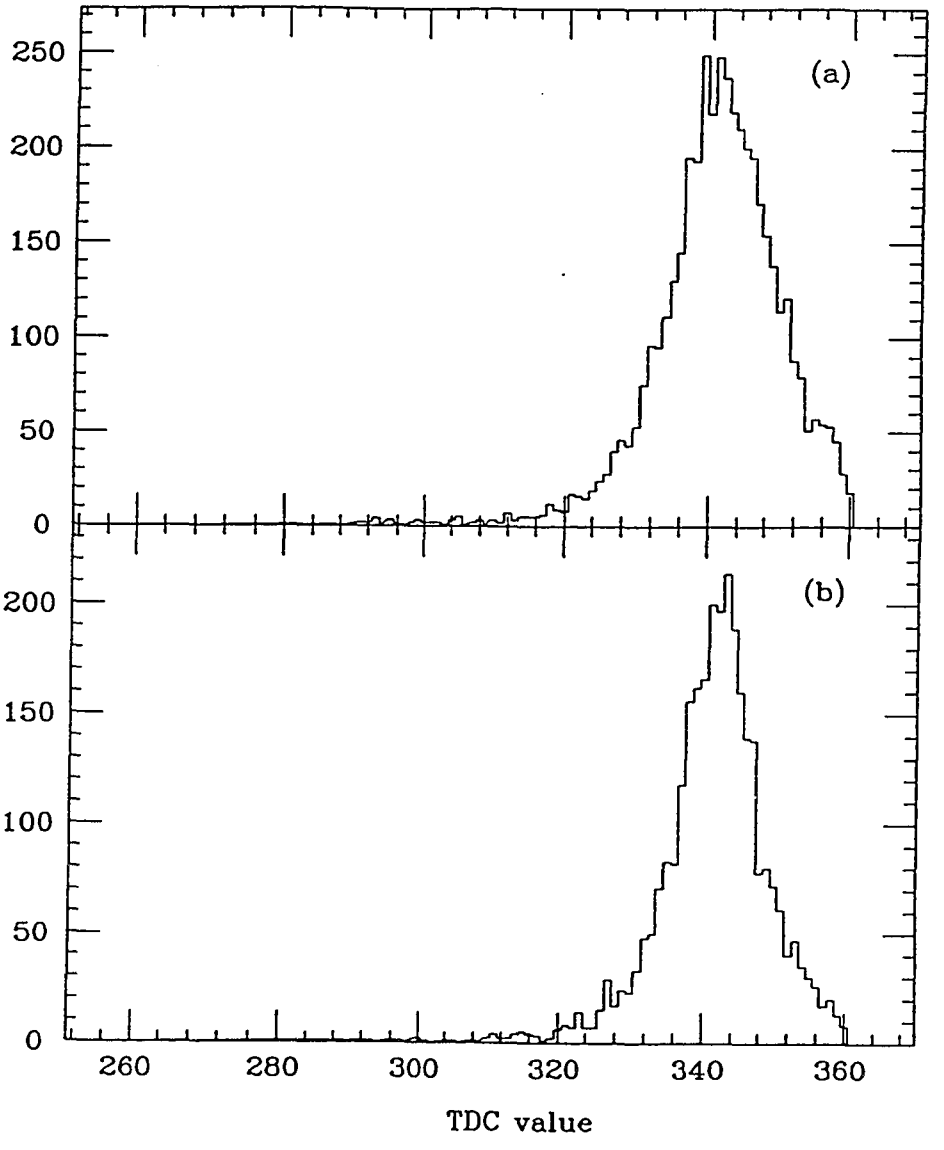

Figure 5.9 Uncalibrated TDC distribution for channel 3 ($ADC > 500$). (a). event multiplicity 17, (b). event multiplicity 18

most probable value and this number is stored in the calibration file as the pedestal for that channel (Figure 5.10).

One PE Determination

To determine the one photo-electron level we need a set of events where the phototube was most probably hit by one photo-electron. Since our singles rates are $\sim 2MHz$, and the hardware trigger window is $\sim 7ns$, there is $\sim 1.4\%$ chance for a hit due to random light to contain two or more photo-electrons. Any channels hit on the non-triggering aperture are due to random skylight and therefore are representative of one photoelectron hits. Again a histogram of the ADC values of all such events is created for each channel and the most probable value of this histogram is stored as the one PE value for that channel (Figure 5.11).

5.6 Stability of Calibrations

As a check on the system, calibrations are also preformed on a run by run basis. The calibration constants from each run are compared to the monthly values. If any calibration constant differs from its monthly average by more than 3 standard deviations it is flagged for further inspection. Any channel which proves to have a problem is removed from the analysis. In addition the values of the run by run calibration constants are plotted as a function of run number. If there has been a hardware change (replaced amplifier, etc.)

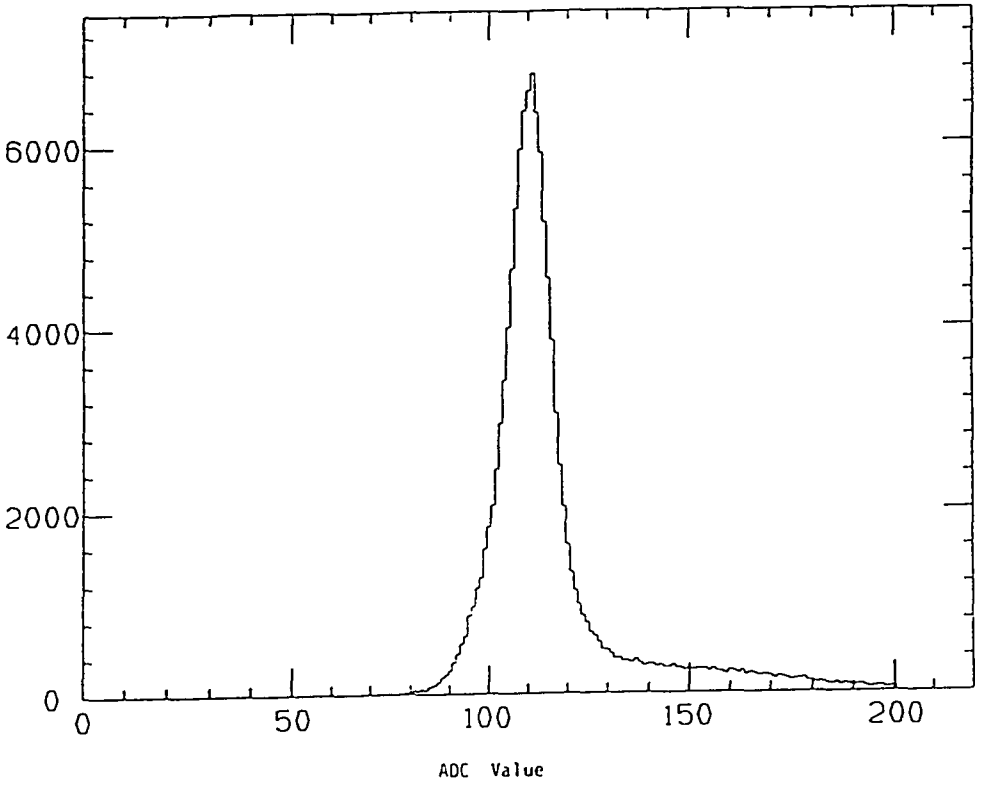

Figure 5.10 Pedestal histogram for channel 3

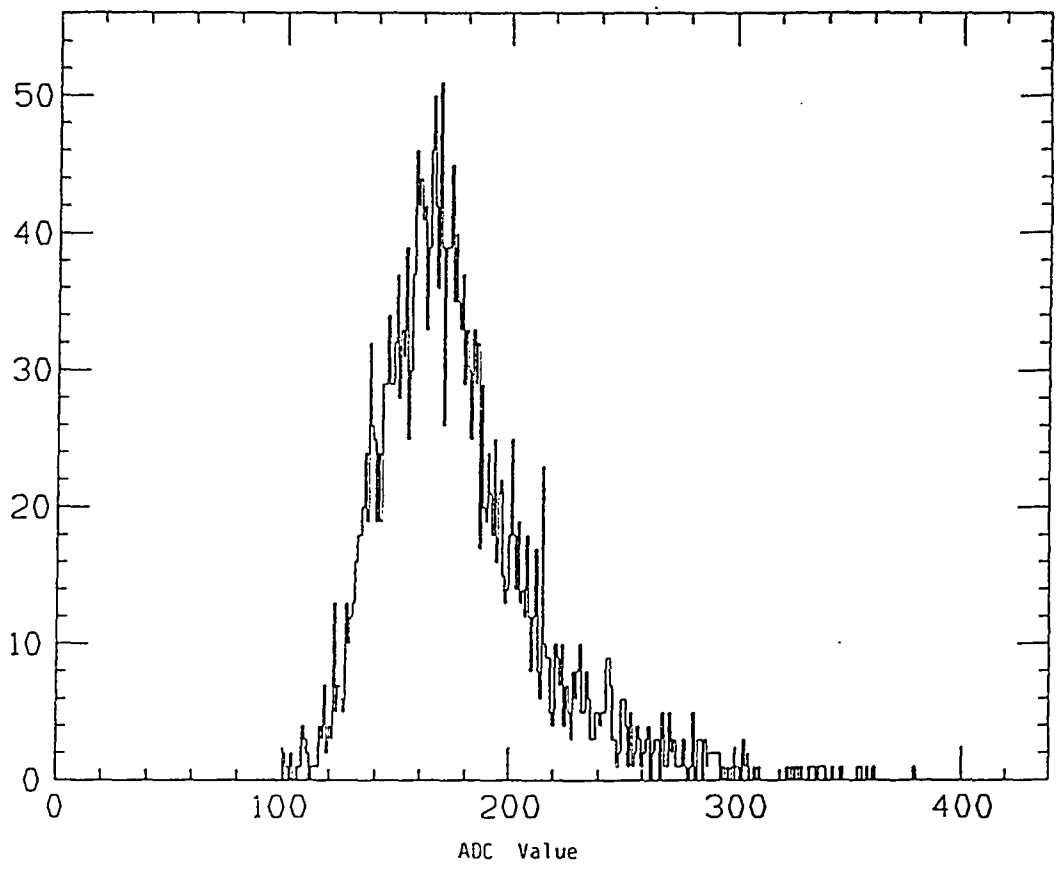

Figure 5.11 One PE histogram for channel 3

the calibration constants will change and the dark period is broken up into segments where all calibration constants are stable.

To examine the long term stability of the electronics, we plot the calibration constants over the entire period that data was taken on Cygnus X–3 (Figure 5.12). Except for changes due to known hardware problems there was very little change in system parameters over the entire 4 months. All channels were operative for the first 2 months of the period. In September tube channel 21 had the amplifier in the cannister burn out, a replacement was not installed until the beginning of the November run. Then at the start of the November run channel 4 was lost and midway through the dark period channel 35. In Figure 5.12 we see the value of all three calibration constants versus day number in the year. Shown are two channels that had no problems during the entire time and one channel (21) which had its amplifier replaced. Note that after the replacement of the amplifier the timing calibration for this channel changed significantly. Aside from such hardware replacements the system is seen to be very stable.

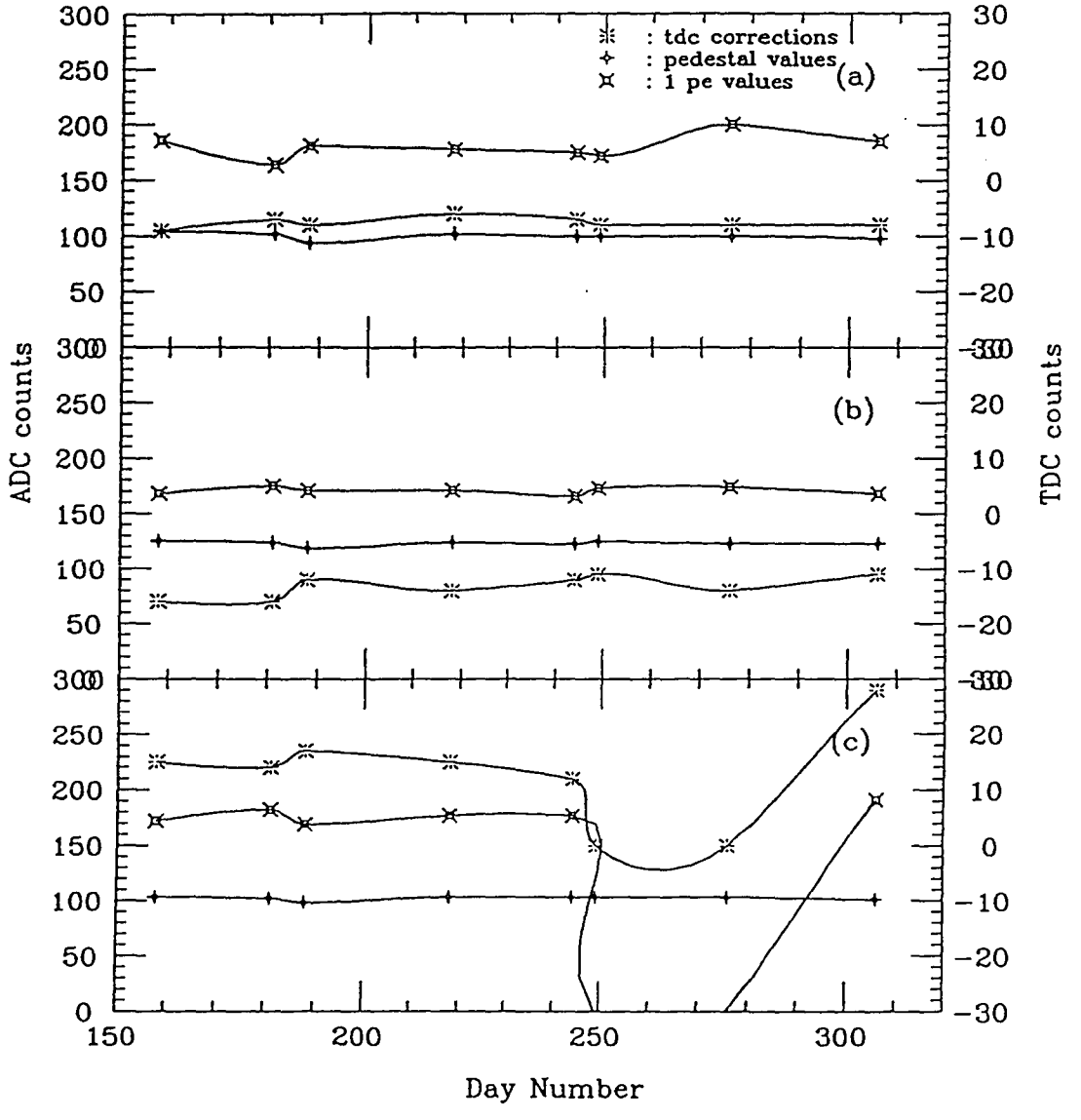

Figure 5.12 The stability of the calibrations. Shown are the calibration constants vs. day number in the year. a. channel 1 b. channel 12 c. channel 21

Chapter 6

Search for an Excess I: Technique

6.1 Introduction

The two apertures of the HGRT provide the capability of simultaneously monitoring source and background regions of the sky. While giving us strict control over the quality of the data, this feature necessitates the development of a different form of analysis than that usually found in air Čerenkov experiments. In most experiments one monitors the source region for a fixed interval of time and range of zenith angles, returns to the initial zenith angle and monitors the background for the same amount of time and range of zenith angles. One then compares the number of events collected in the two data sets and using standard statistical techniques (Li and Ma 1983) searches for excesses. Since the two apertures of the HGRT are at different zenith angles, this method is inappropriate for this experiment. Below we propose a

technique suitable for this experiment, and develop the tools necessary for its implementation.

6.2 Physical Operation

There are two modes of operation for the HGRT. In the first mode known as 'track normal', one aperture is pointed at the suspected source region of the sky while the other monitors a background region of the sky 3.6° north or south from the source region (depending on which aperture is monitoring the source). The telescope follows both regions across the sky for the entire run (from 2 to 4 hours). Since the response of the two apertures is slightly different, this method is inappropriate when searching for rate excesses.

The second mode of operation is known as the 'track wobble' mode. Again, one of the apertures is pointed at the 'source' while the other monitors the background as the telescope tracks across the sky. Every 720 seconds (in 1986, in 1989 the interval was 900 seconds), the telescope is shifted 3.6° in declination so the other aperture can monitor the source region. Note that the background region monitored by the two apertures is different, being separated by 7.2° in declination. All of the data used in this analysis were taken in the 'track wobble' mode.

6.3 Event Selection

6.3.1 Choice of Multiplicity Cut

Before searching for an excess in the cosmic ray rate from a given direction in the sky, we must ensure that all of the events we select arise from extensive air showers. As pointed out in the last chapter it is possible for random skylight to trigger our telescope. If there are N_{tubes} (18 for 1986, 26 for 1989) firing at a rate ρ (the singles rates as measured by our scalers $\sim$ *few MHz*), and τ the duration of the 'coincidence' window ($\sim$ *few ns*), then (if $\rho\tau \ll 1$), the rate for 'm-fold' random coincidences within the time window τ is:

$$R_m = N_{tubes}\rho \times \sum_{i=m}^{N_{tubes}-1} C_{i-1}^{N_{tubes}-1}(\rho\tau)^{i-1}(1-\rho\tau)^{N_{tubes}-i} \qquad (6.1)$$

When performing a search for an excess count rate we must ensure that the rate from random triggers contributes much less than our minimum detectable S/B. For the dataset of interest the singles rates never exceeded $3MHz$ and our minimum detectable S/B is $\sim 1\%$, corresponding to a trigger rate of roughly $2\times10^{-3}Hz$. A multiplicity of 9 hits within a 5 nanosecond window gives an accidental trigger rate of approximately $3\times10^{-3}Hz$, roughly 1% of the measured cosmic ray rate (and is therefore unacceptable). At a multiplicity of 12 hits within $5ns$, the accidental rate is only $5\times10^{-9}Hz$, well below our minimum detectable S/B. In the following analysis we demand that all events satisfy this multiplicity requirement.

6.3.2 Elimination of Contaminated Data

By examining the scaler records (singles rates in the PMTs) one can monitor the expected rate due to random coincidences. However it is possible for the event rate to change without a consequent change in the single PMT rates. These changes can be caused either by atmospheric fluctuations, which cause the rate of cosmic ray triggers to change, or by coherent light produced locally.

To the east of the telescope lies a lunar ranging station (LURE), sporadically operating a pulsed laser at $5Hz$, with each pulse lasting for 2 picoseconds. The laser light which enters the apertures is backscattered and therefore rather weak. We have obtained lists of firing times from LURE and it is found that the above multiplicity cut (12 hits in 5 ns) eliminates these events.

To the north lies a satellite tracking station operated by the Air Force. They operate several pulsed lasers, whose frequencies and firing times are classified.

To eliminate any changes in the event rate not due to actual changes in the cosmic ray rate we use the Gini test (deJager 1987). This test is a bin free method for testing the time interval distribution (between successive events) for exponentiality. The test is performed on the off source data for each wobble interval (720 or 900 seconds) within the run. If the absolute value of the Gini number exceeds 1.97 (corresponding to a 5% confidence level) the

interval is removed from the run.

We still have to develop a criteria for eliminating entire runs where the atmosphere was not stable enough to provide a reliable measure of the true cosmic ray rate. We defer this until after a discussion of the zenith angle effect.

6.4 Zenith Angle Dependence of Trigger Rate

As the zenith angle increases so does the slant depth (penetrated by the shower) through the atmosphere. This causes the effective area and energy threshold of the telescope to increase with zenith angle, causing the measured cosmic ray trigger rate to decrease with increasing zenith angle. Making a few reasonable assumptions we will derive an expression, good to first order, which describes this dependence. We will be able to use this result to determine the stability of the atmosphere, and to calculate an expected number of cosmic ray events for a given time interval and source location, as well as the error in this expected number. In this manner we can eliminate data taken under unstable conditions, and assign a statistical significance to any observed rate excesses.

Previous attempts by our group to parametrize the zenith angle dependence of the rate have relied upon expansions in Legendre polynomials (Slane 1988 and Szentgyorgi 1986). It is found that one must use an entire month's data to obtain reasonable fits with this approach. Due to nightly variations in the atmosphere (moisture content, etc.) this approach is felt to be

inadequate, especially when searching for 'bursts'. It is found that small atmospheric changes may mask or mimic a burst. The Legendre expansion proved to be poorly constrained and inadequate when fitting only a few hours of data. Since the fit is to be used for interpolation it is important to have a correct expression for the curvature of the zenith angle function. In the function derived below there are two free parameters: the rate at zenith, and the curvature of the zenith angle function. Rieke (1969) has obtained an expression similar to that found below. In the same paper he notes the inadequacy of the, then standard, $\cos^n \theta$ fits.

6.4.1 The Assumptions

We start by making some simplifying assumptions.

- The primary cosmic ray background is isotropic.
- The primary cosmic ray rate is a function of energy and can be parametrized as $I_{cr}(E) = I_{cr}(E_0)(E/E_0)^{-\gamma}$, where γ is the cosmic ray differential spectral index, 2.6
- The number of photons produced by a primary cosmic ray is proportional to the energy of the cosmic ray: $n_\gamma = P_f \times E$, where P_f is the production efficiency for photons in our wave band.

- All of the light from an extensive air shower originates at shower maximum.
- The effective area over which our telescope will produce a trigger as a function of energy can be parameterized as $Area = C(E/E_0)^{\alpha}$.
- The density of the earth's atmosphere falls exponentially with height above sea level: $\rho(h) = \rho_0 e^{-h/h_0}$, where $h_0 = 8.434\ km$ is the scale height of the atmosphere and $\rho_0 = .001205\ g/cc$ is the density of air at sea level
- The earth is flat. (Good for $\theta < 85°$

6.4.2 Method

In general the observed count rate of cosmic rays is

$$R = \int_{E_{th}}^{\infty} A(E) I_0 (E/E_0)^{-\gamma} dE \tag{6.2}$$

where $A(E)$ is the area subtended by our aperture at shower max and E_{th} is our energy threshold. From this it is a simple matter to write an expression for the rate at any given zenith angle.

$$R(\theta) = \int_{E_{th}(\theta)}^{\infty} A(\theta, E) I_0 (E/E_0)^{-\gamma} dE \tag{6.3}$$

Writing $A(\theta, E) = g(\theta)f(E)$, where $g(\theta)$ represents the geometry and $f(E)$ parametrizes the energy dependence of our target area, assumed to be of the form $C(E/E_0)^{\alpha}$.

Taking the ratio of the rate at a given zenith angle to that at zenith we have:

$$\frac{R(\theta)}{R(0)} = \frac{g(\theta)}{g(0)} \times \left(\frac{E_{th}(\theta)}{E_{th}(0)}\right)^{-(\gamma'-1)} \tag{6.4}$$

Where $\gamma' = \gamma - \alpha$. If $d(\theta)$ is the distance to shower maximum for a given zenith angle θ then:

$$\frac{g(\theta)}{g(0)} = \left(\frac{d(\theta)}{d(0)}\right)^2 \tag{6.5}$$

Changing Distance to Shower Maximum The quantity which dictates the height of shower maximum is the amount of material traversed by the shower from the top of the atmosphere, the thickness t. With an exponential atmosphere we have:

$$t(d) = \rho_0 \int_{d\cos\theta}^{\infty} e^{-h/h_0} \frac{dh}{\cos\theta} \tag{6.6}$$

For primaries of the same energy this quantity is independent of zenith angle. Therefore:

$$\frac{d(\theta)}{d(0)} = \sec\theta\left(1 - \frac{h_0}{d(0)}\ln\cos\theta\right) \tag{6.7}$$

Where $d(0) \simeq 5km$ is the distance from our telescope to shower maximum at zenith. See Figure 6.1 for an explanation of the geometry.

Changing Energy Threshold The changing distance to shower maximum effects the photon density on the ground in two ways. First is the simple geometric divergence of the beam of photons, assumed to be a point source originating from shower maximum. Second is the attenuation of the Čerenkov light by atmospheric absorption and scattering. It is the second effect which enables us to determine the 'seeing'.

The photon density on the ground can be written as:

$$\rho_\gamma(\theta, E) = \frac{n_\gamma(E)}{\pi\beta d(\theta)^2}(1 + t(\theta)/t(0))^{-a}e^{-\lambda t(\theta)} \tag{6.8}$$

Where $a = .574$, and $t(0)$ will be taken to be the thickness between shower maximum and the observatory at zenith, and β is the opening angle of the shower of photons. The term $(1 + t(\theta)/t_0)^{-a}$ is empirical and represents an averaging of the attenuation over the frequency range of interest to us (Learned 1981). Notice that the geometric term depends on the distance to shower maximum, while the attenuation depends on the thickness to shower maximum.

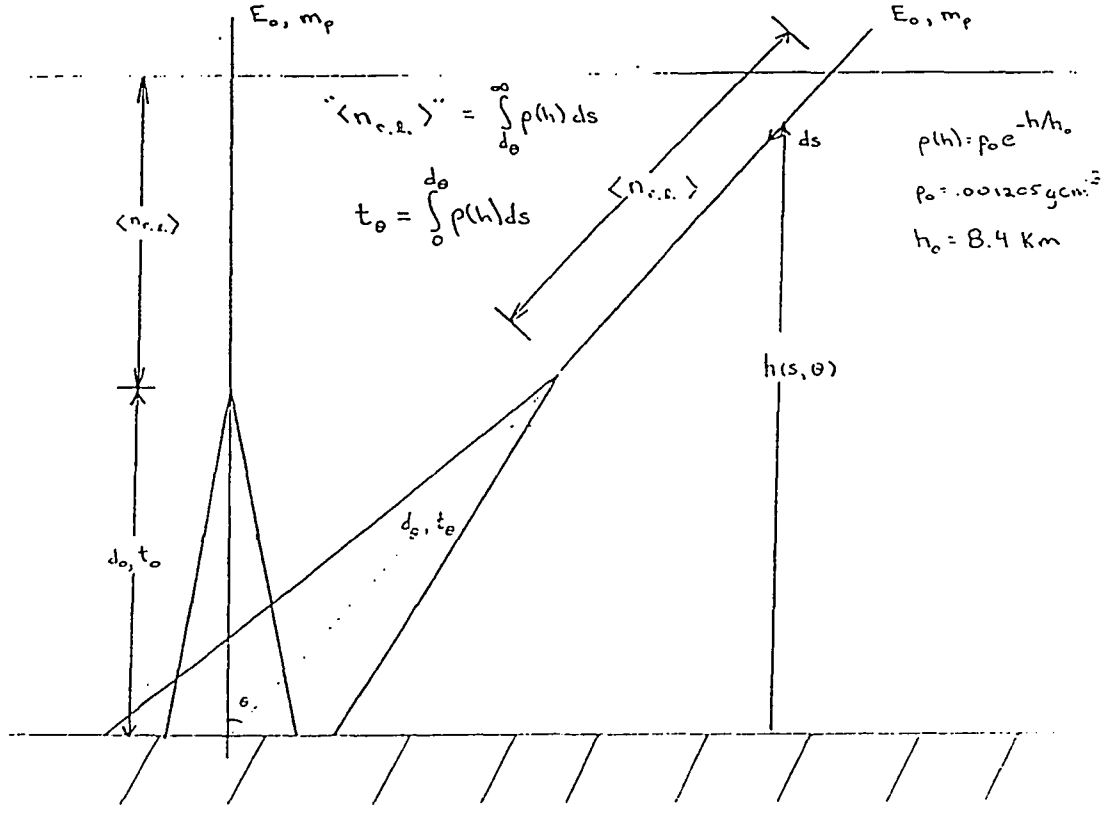

Figure 6.1 Geometry of change in distance to shower maximum with zenith angle. $< n_{r.l.} >$ is the average number of radiation lengths to shower maximum for a proton primary of energy E_0. The quotes in the expression denote that the units are wrong, this should be converted to a thickness of material, gcm^{-2}, for the equality to be strict.

$$t(d) = \rho_0 \int_{H_{obs}}^{d\cos\theta} e^{-h/h_0} \frac{dh}{\cos\theta} \tag{6.9}$$

$$= \frac{\rho_0 h_0}{\cos\theta} \left(e^{-H_{obs}/h_0} - e^{-d\cos\theta/h_0} \right) \tag{6.10}$$

Where $H_{obs} = 3km$, is the altitude of the observatory.

Substituting for d and taking the ratio of the thickness at some zenith angle to the thickness at zenith:

$$\frac{t(\theta)}{t(0)} = \sec\theta \left\{ \frac{1 - \cos\theta e^{-(d(0)-H_{obs})/h_0}}{1 - e^{-(d(0)-H_{obs})/h_0}} \right\} \tag{6.11}$$

To obtain the ratio of the energy threshold at an angle θ to that at zenith we require the photon density on the ground to be independent of angle (i.e. $\rho_\gamma(\theta, E'_{th}) = \rho_\gamma(0, E_{th})$). Resulting in:

$$\frac{E_{th}(\theta)}{E_{th}(0)} = \left(\frac{d(\theta)}{d(0)} \right)^2 \left(\frac{2}{1 + t(\theta)/t(0)} \right)^{-a} e^{\lambda t(0)(t(\theta)/t(0)-1)} \tag{6.12}$$

6.4.3 The Result

Putting everything together we have:

$$\frac{R(\theta)}{R(0)} = \left(\frac{d(\theta)}{d(0)} \right)^{4-2\gamma'} \left(\frac{2}{1 + t(\theta)/t(0)} \right)^{a(\gamma'-1)} e^{-\lambda t(0)(t(\theta)/t(0)-1)(\gamma'-1)} \tag{6.13}$$

$$\tag{6.14}$$

Where $d(\theta)/d(0)$ and $t(\theta)/t(0)$ are given in equations 7 and 11.

The above expression is plotted in Figure 6.2 for various values of the attenuation coefficient λ, in the figure γ' was taken to be 2.2, corresponding to $\alpha = .4$ (i.e. $Area \propto E^{.4}$).

6.4.4 Determination of λt_0

Results of extinction measurements performed on Mauna Kea are given in Table 6.1 and Figure 6.3 (Beland et. al. 1988). The coefficients are in units of magnitudes per airmass. In these units the transmission is $T = e^{-.4\alpha \sec\theta}$.

Wavelength nm	Extinction, α Magnitude/airmass	Wavelength nm	Extinction, α Magnitude/airmass
310	1.37	380	0.30
320	0.82	390	0.27
330	0.57	400	0.25
340	0.51	425	0.21
350	0.42	450	0.17
360	0.37	475	0.14
370	0.33	500	0.13

Table 6.1 Extinction Curve at Mauna Kea

Where θ is the zenith angle. These numbers must be adjusted for the difference in altitude between Mauna Kea and Haleakala.

$$t(\text{Mauna Kea}) = \rho_0 \int_{H_{MK}}^{\infty} e^{-h/h_0} dh \tag{6.15}$$

$$= 615 g/cm^2 \tag{6.16}$$

$$and \tag{6.17}$$

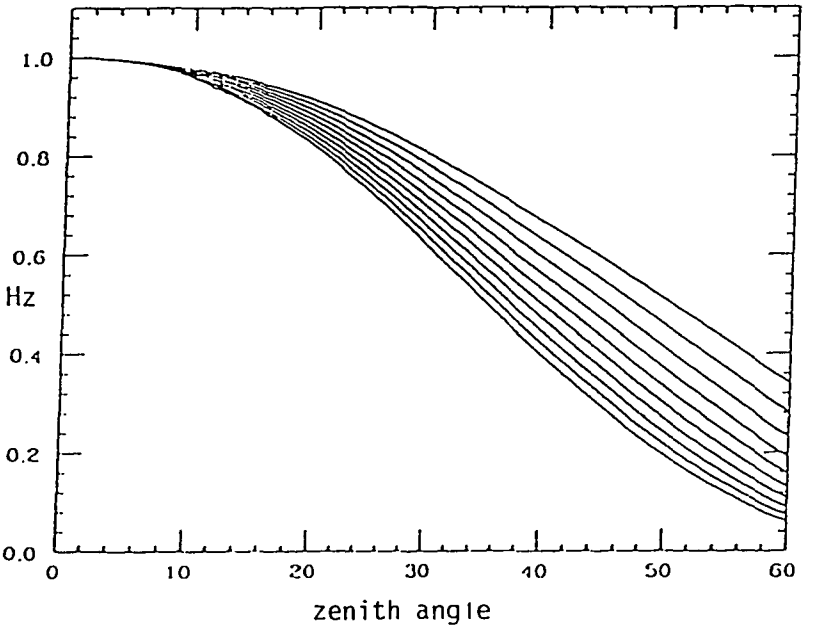

Figure 6.2 Rate as a function of zenith angle, theoretical formula. $\gamma' = 2.2$, $\lambda t_0 = .1$ to 1.0 in steps of .1

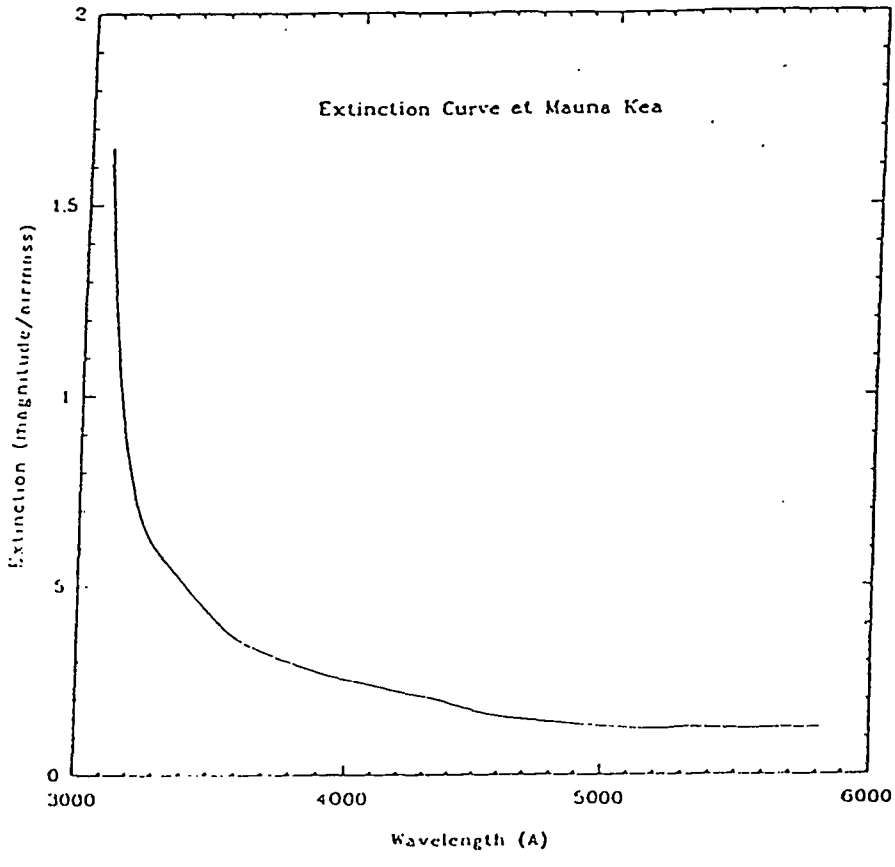

Figure 6.3 Extinction Curve at Mauna Kea: from Beland et al

$$t(\text{Haleakala}) = \rho_0 \int_{H_{Hale}}^{d_0=8km} e^{-h/h_0} dh \quad (6.18)$$

$$= 318 g/cm^2 \quad (6.19)$$

The attenuation is a strong (exponential) function of the wavelength in this region of the spectrum. Figure 4.8 shows the spectral response of our telescope. By choosing a frequency in the middle of our acceptance band, and utilizing the empirical formula given above, one can minimize any error induced by the frequency dependence of the absorption. In practice any error in the determination of the attenuation length can be absorbed by the choice of γ'. Using 370 nm as the mean wavelength of light accepted by the telescope we find a value of .33 for the attenuation coefficient. This leads to an absorption length of:

$$\lambda t(0) = .4 \times .33 \times \frac{t(\text{Haleakala})}{t(\text{Mauna Kea})} \quad (6.20)$$

$$= .07 \text{ attenuation lengths from shower max} \quad (6.21)$$

6.4.5 Determination of γ'

As noted in chapter 4 (Figure 4.9) the effective area of the telescope increases with primary energy. This has the effect of lowering the spectral index measured by the telescope.

As a first pass run by run fits are performed on all of the data. In these fits λt_0 was fixed to .07 while γ' and the rate at zenith, R_0, were allowed to vary. Then, an average value of γ' was determined for each set of runs. The results for a multiplicity cut of 9 hits in $5ns$ are shown below in Table 6.2. The 'groups' represent different hardware configurations, usually different dead electronics channels. In the first group the aperture size was 1/2° (full angle), while in the remaining groups the aperture was 3/4° (full angle).

Group	$< \gamma_A >$	σ_A	$< \gamma_B >$	σ_B
I	2.19	.19	2.22	.16
II	2.21	.18	2.20	.16
III	2.23	.24	2.22	.31
IV	2.05	.40	2.02	.28
Total	2.197	.220	2.201	.208

Table 6.2 Average Measured Spectral Indices by Aperture and Grouping. All sources, multiplicity cut of 9 hits in 5 ns.

Figure 6.4 shows the distribution of γ' over the entire year. Figure 6.5 is the same as Figure 6.4 except that a multiplicity cut of 12 hits in $5ns$ was used and only data taken on Cygnus X–3 was included. The group of runs with low values of γ' where found to be taken under poor atmospheric

conditions. All of the data are consistent with a value of $\gamma' = 2.2$. Even for Group IV the most probable value of γ' was 2.2, but runs taken under adverse seeing conditions brought the average value down to 2.0. For the remainder of the analysis γ' will be fixed to 2.2. To judge any systematic errors induced induced by fixing γ', we will vary γ' by one standard deviation and observe the effects on the analysis.

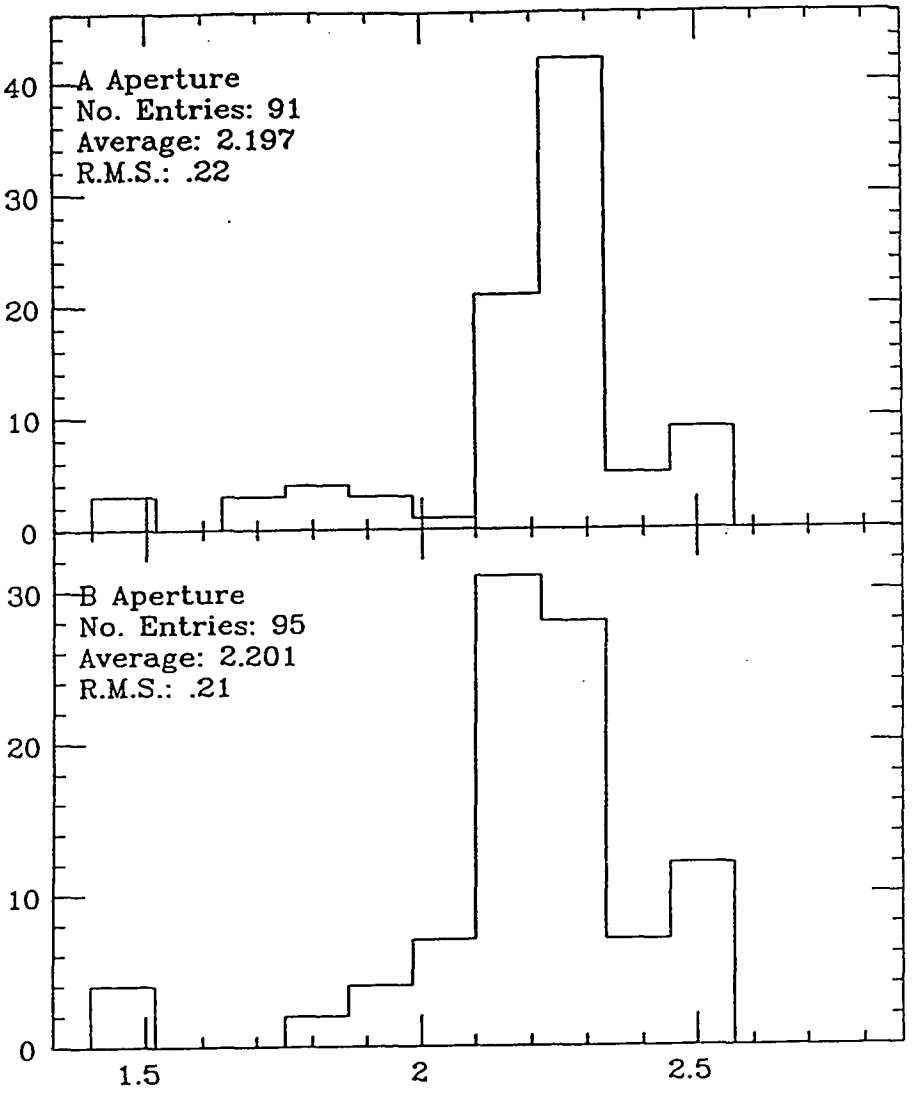

Figure 6.4 Distribution of γ. All data, multiplicity cut of 9 in 5. a.) A Aperture b.) B Aperture

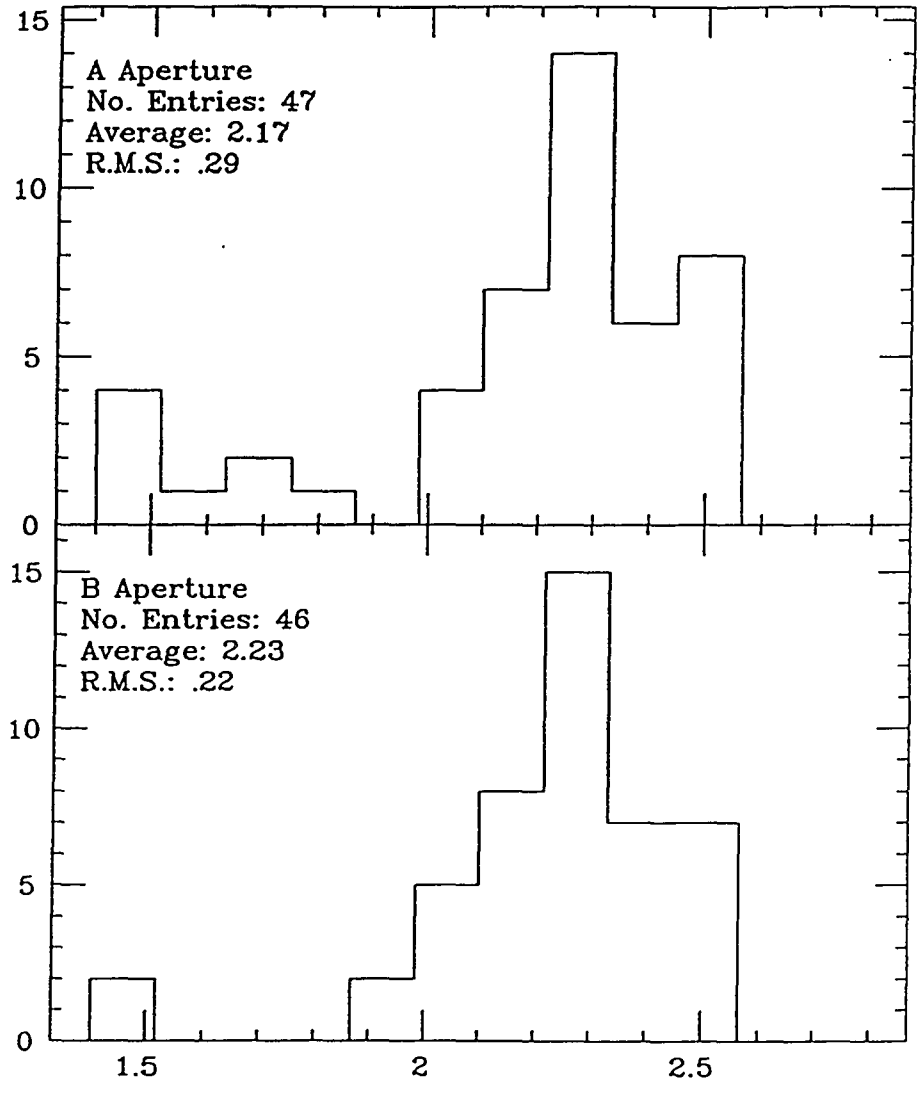

Figure 6.5 Distribution of γ. All Cygnus data, multiplicity cut of 12 in 5. a.) A Aperture b.) B Aperture

6.4.6 Run Selection

To determine the stability of the atmosphere during a given run we perform a fit of the off source data to the above zenith angle function. If the goodness of fit, as determined by the χ^2 probability, is better than 10% (in both apertures) we keep the run. Otherwise the run is excluded from the analysis. If a run was too short, fewer than three degrees of freedom in the fit, it was likewise excluded from the analysis. Figures 6.6 and 6.7 give examples of a good run and a bad run.

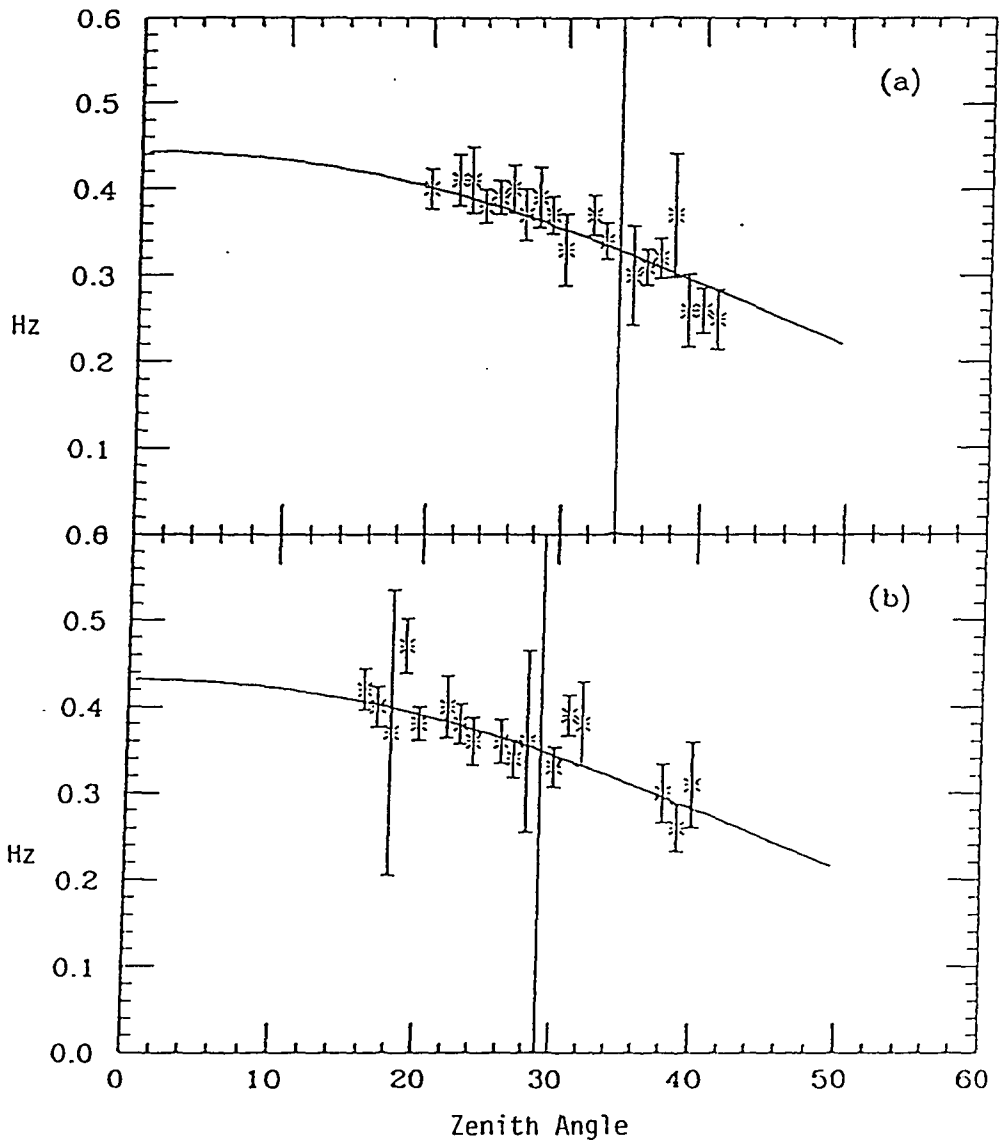

Figure 6.6 Zenith angle fit and data from a good run (no. 816). (a) A aperture (probability 98%), (b) B aperture (51%)

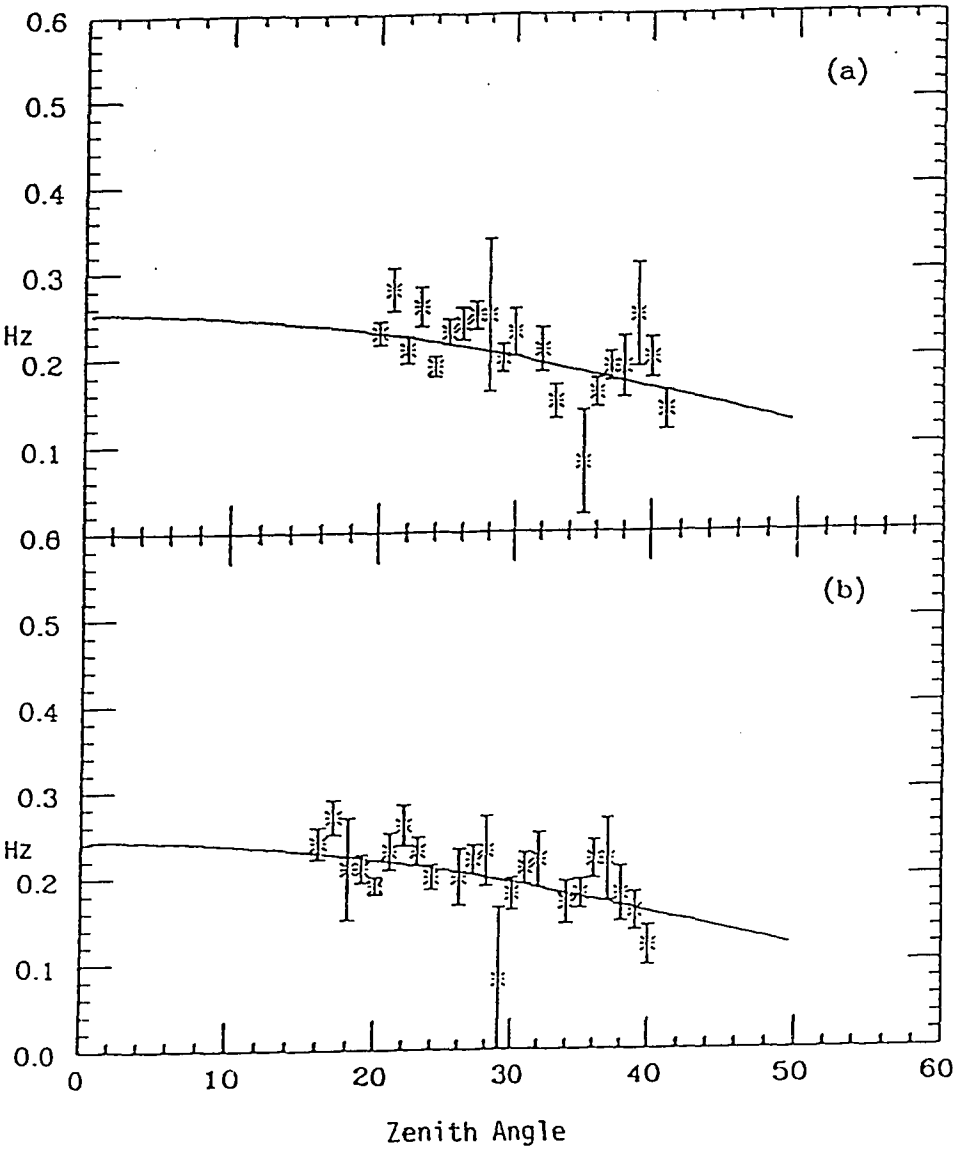

Figure 6.7 Zenith angle fit and data froma rejected run (no. 851). (a) A aperture probability (0.8%), (b) B aperture (5.0%)

6.4.7 Check on the Choice of γ'

After eliminating the runs taken under adverse atmospheric conditions we can check the legitimacy of our choice of γ' by examining the fit residuals for various values of γ' (Figures 6.8-6.13). In Figure 6.8 we show the residuals as a function of zenith angle for $\gamma' < 2.2$ (1.8, and 2.0), in Figure 6.9 for $\gamma' = 2.2$, and in Figure 6.10 for $\gamma' > 2.2$ (2.4, and 2.6). Figures 6.11-6.13 show the distribution of residuals for the above choices of γ'.

In all cases the distribution of residuals is consistent with Gaussian statistics. However, examination of the residuals versus zenith angle reveals a systematic bias for all choices of γ' except 2.2, the value originally determined. For values of $\gamma' < 2.2$ we see a tendency to underestimate the rate for zenith angles less than 30° and to overestimate it for larger zenith angles. While for values of $\gamma' > 2.2$ we see the opposite trend (overestimate the rate for $\theta < 30$ and underestimate for $\theta > 30$). *Since the orbital period of Cygnus is nearly a multiple of the sidereal day, one must ensure that no such systematic bias is present in the rate estimation when performing a search for emission at the orbital period.*

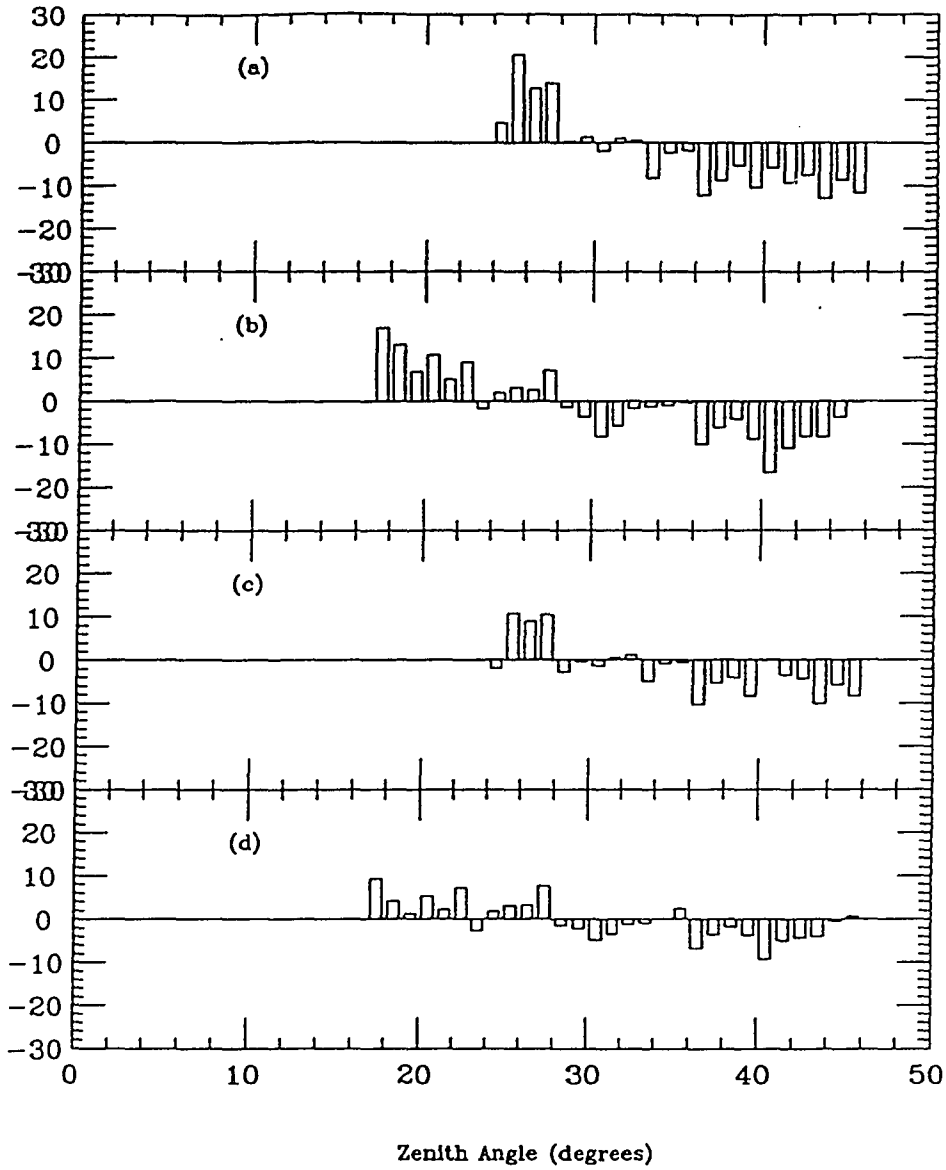

Figure 6.8 Fit residuals vs. zenith angle. (a) $\gamma' = 1.8$ A aperture, (b) $\gamma' = 1.8$ B aperture, (c) $\gamma' = 2.0$ A aperture, and (d) $\gamma' = 2.0$ B aperture

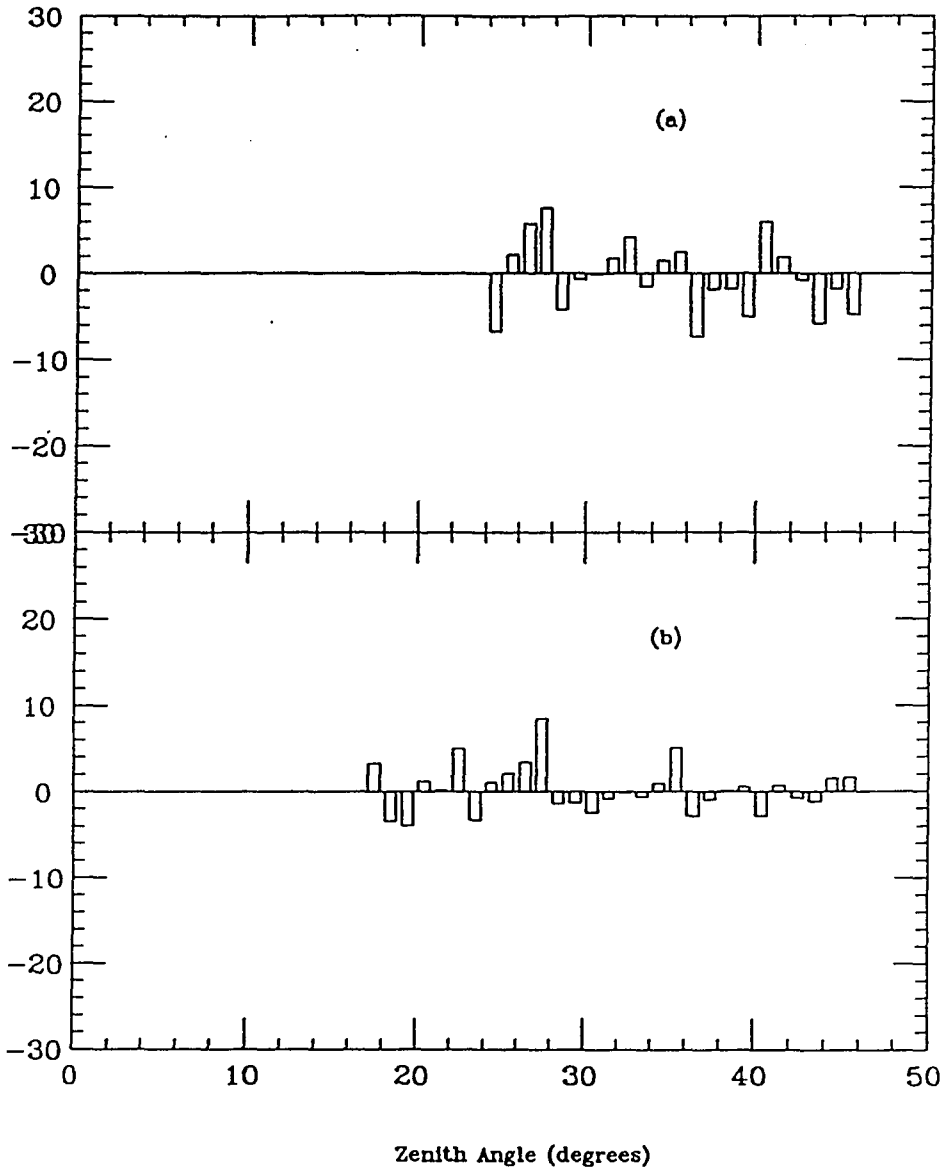

Figure 6.9 Fit residuals vs. zenith angle. (a) $\gamma' = 2.2$ A aperture, (b) $\gamma' = 2.2$ B aperture

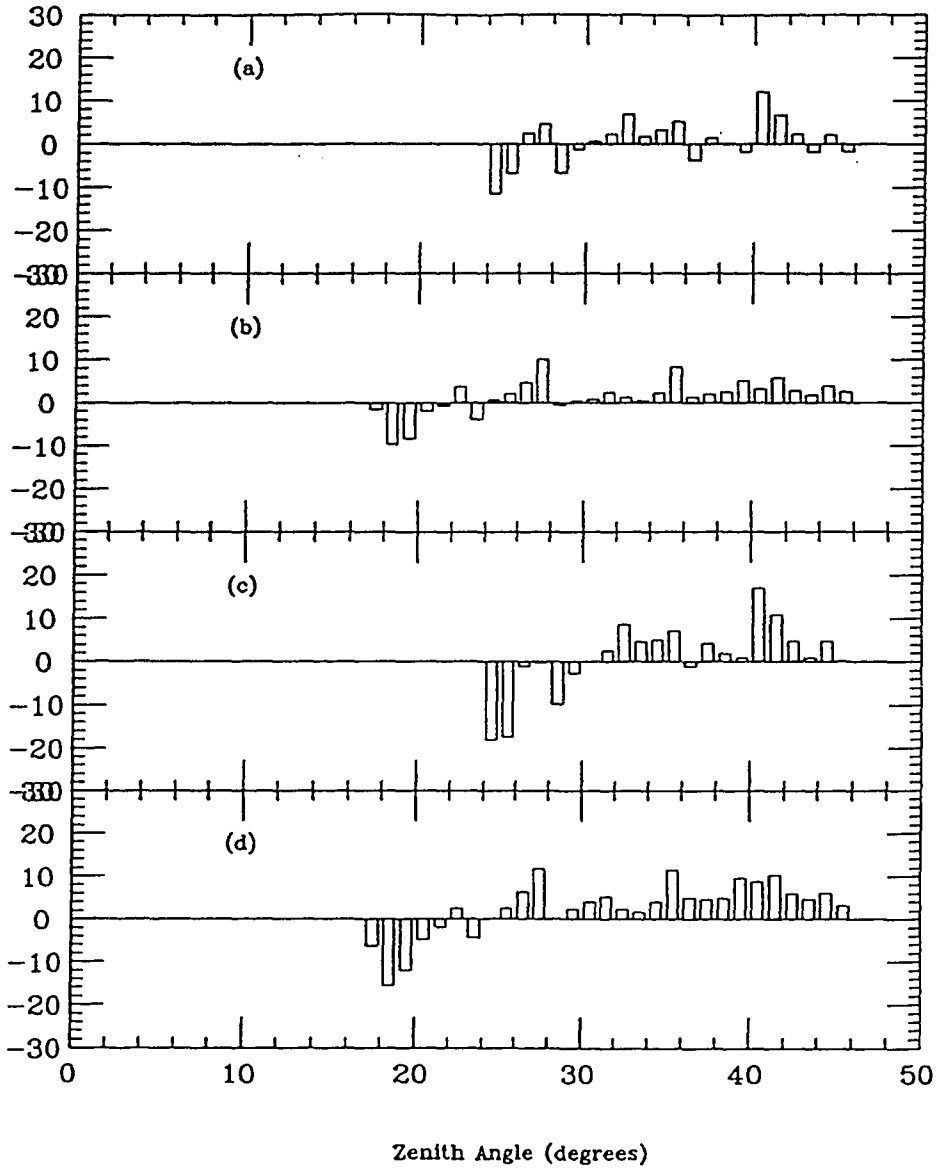

Figure 6.10 Fit residuals vs. zenith angle. (a) $\gamma' = 2.4$ A aperture, (b) $\gamma' = 2.4$ B aperture, (c) $\gamma' = 2.6$ A aperture, and (d) $\gamma' = 2.6$ B aperture

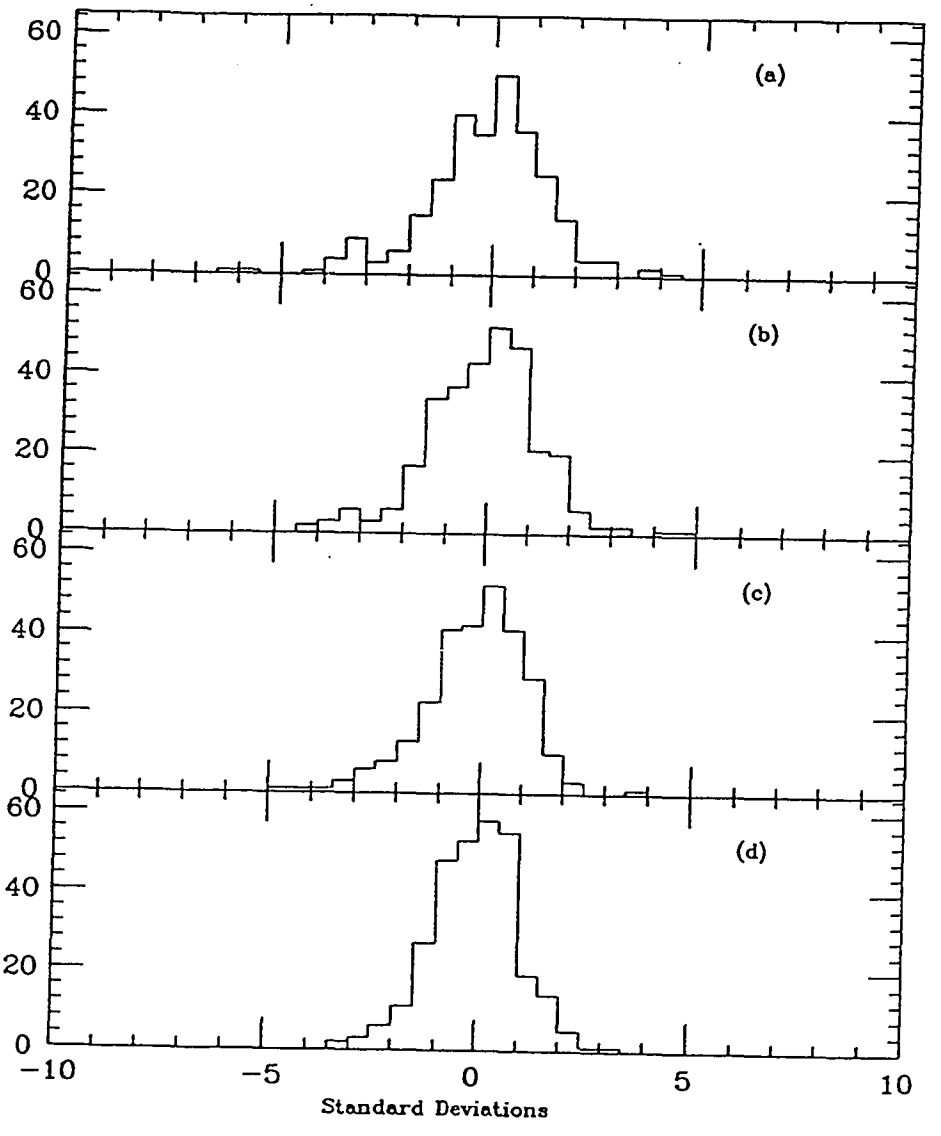

Figure 6.11 Distribution of fit residuals. (a) $\gamma' = 1.8$ A aperture, (b) $\gamma' = 1.8$ B aperture, (c) $\gamma' = 2.0$ A aperture, and (d) $\gamma' = 2.0$ B aperture

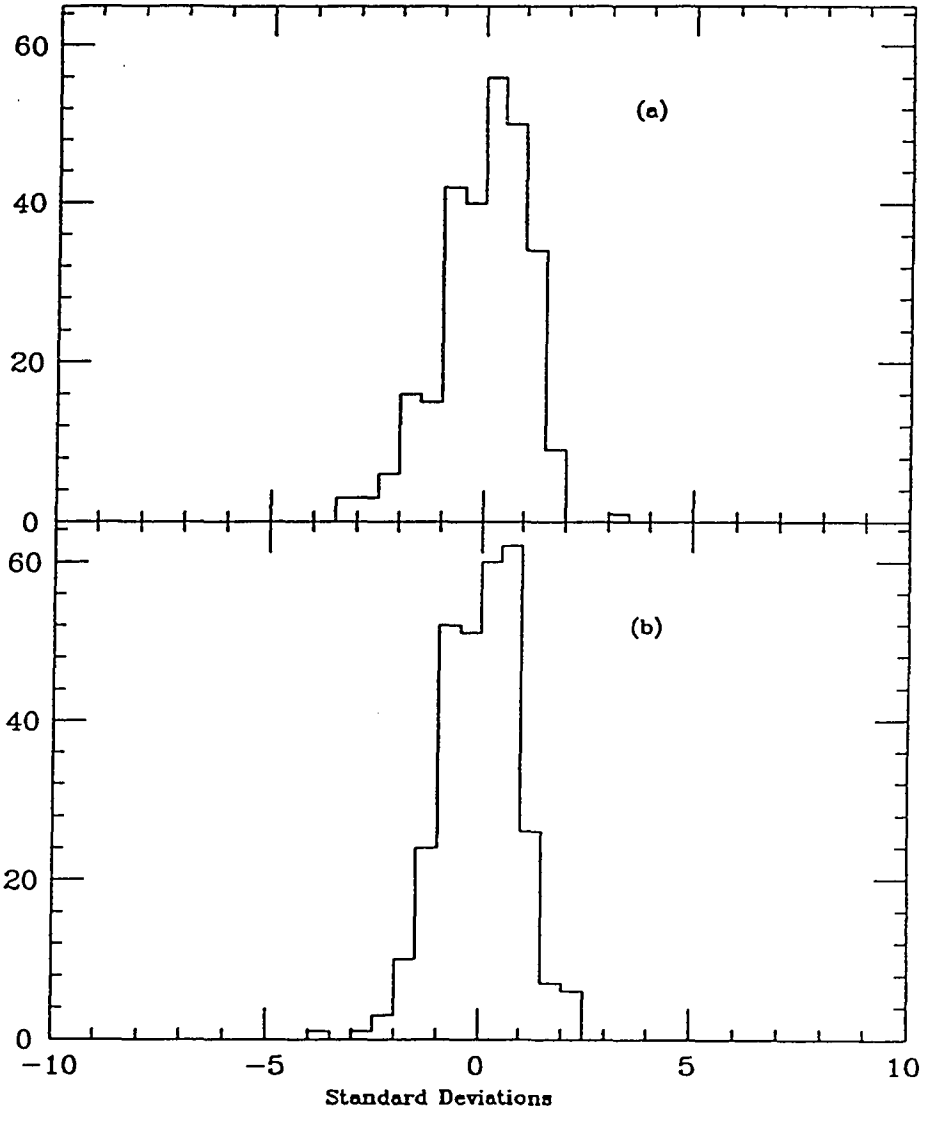

Figure 6.12 Distribution of fit residuals. (a) $\gamma' = 2.2$ A aperture, (b) $\gamma' = 2.2$ B aperture

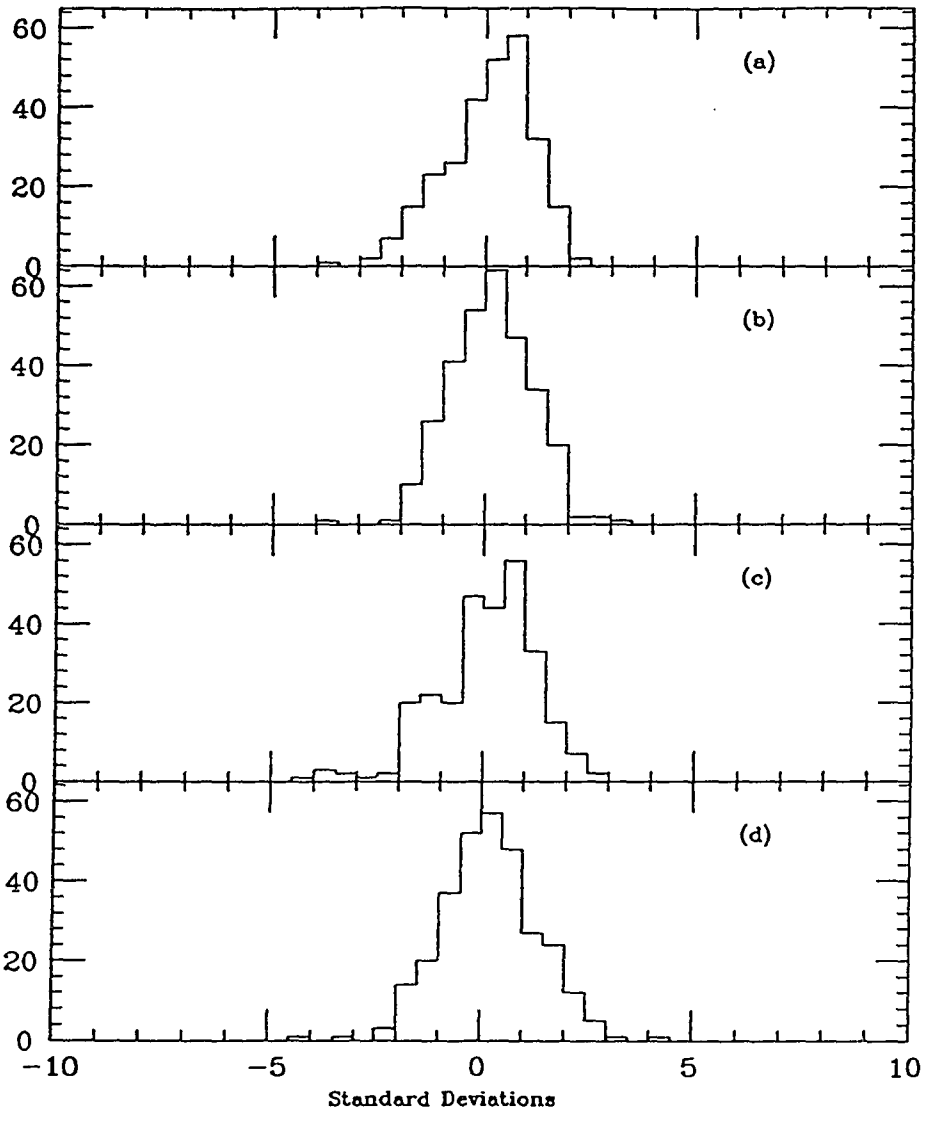

Figure 6.13 Distributrion of fit residuals. (a) $\gamma' = 2.4$ A aperture, (b) $\gamma' = 2.4$ B aperture, (c) $\gamma' = 2.6$ A aperture, and (d) $\gamma' = 2.6$ B aperture

6.5 Analysis Technique

6.5.1 The Expected Number of Events

For each run we fit the off source data to the above rate versus zenith angle function and find the rate at zenith, R_0, for each run. The data from each aperture are fit separately. To find the expected number of events in the on source aperture the rate function is integrated over the livetime and zenith angle of the aperture.

$$N_{exp} = \int_{t_0}^{t_0+T} R(\theta(t))dt \tag{6.22}$$

Where T is an arbitrary time interval. In practice a numerical integration is performed using the event times and zenith angles (determined from the actual position of the telescope as given by the optical encoders) as an integration grid. By using all events to form the grid (not just those satisfying the multiplicity criteria), one minimizes the distance between grid points and therefore minimizes any integration error.

6.5.2 The Error in the Expected Number of Events

To find the error in the expected number of events we integrate the least square error in the rate function over the livetime and zenith angles of the on source aperture.

$$\Delta N_{exp} = \int_{t_0}^{t_0+T} \Delta R(\theta(t))dt \quad (6.23)$$

$$= \int_{t_0}^{t_0+T} \Delta R_0 \times f(\theta(t))dt \quad (6.24)$$

This error grows linearly with time. In Figure 6.14 we show the time development of the error in the expected number over one run; for comparison we also plot $\sqrt{N_{exp}}$, the normal error. Because of the linear growth with time one would like to make the 'correlation' time (the time over which the same fit is used to calculate the expected number of events) as short as possible. However, one needs a reasonable amount of data to keep the fit errors under control. Figure 6.15 is a histogram of the ratio of fit errors to normal errors at the end of each run. One can see that the two errors are nearly equal. It has been found that increasing the length of time used to generate the fit, by performing a monthly fit, only reduces the fit error, ΔR_0, by $\sqrt{(T)}$. So performing nightly, or run by run, fits minimizes the fitting error.

There is an additional error due to the uncertainty in our choice of γ'. Over a single wobble interval this error is negligible. In the next chapter we will show that even for the D.C. analysis this error is negligible.

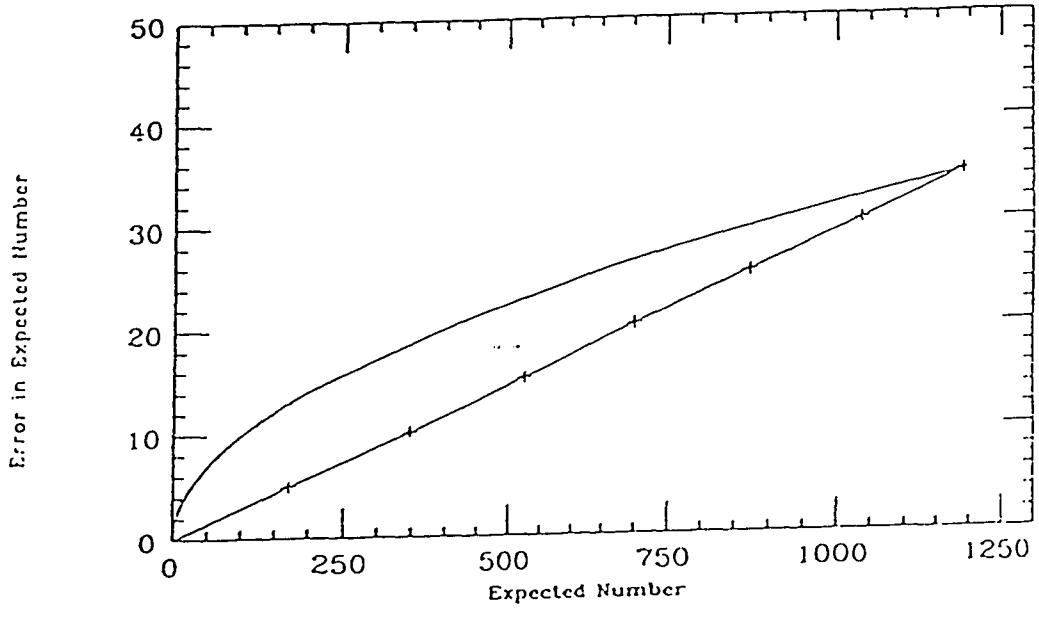

Figure 6.14 Time development of fit error (straight line) and normal error (curve) over a run.

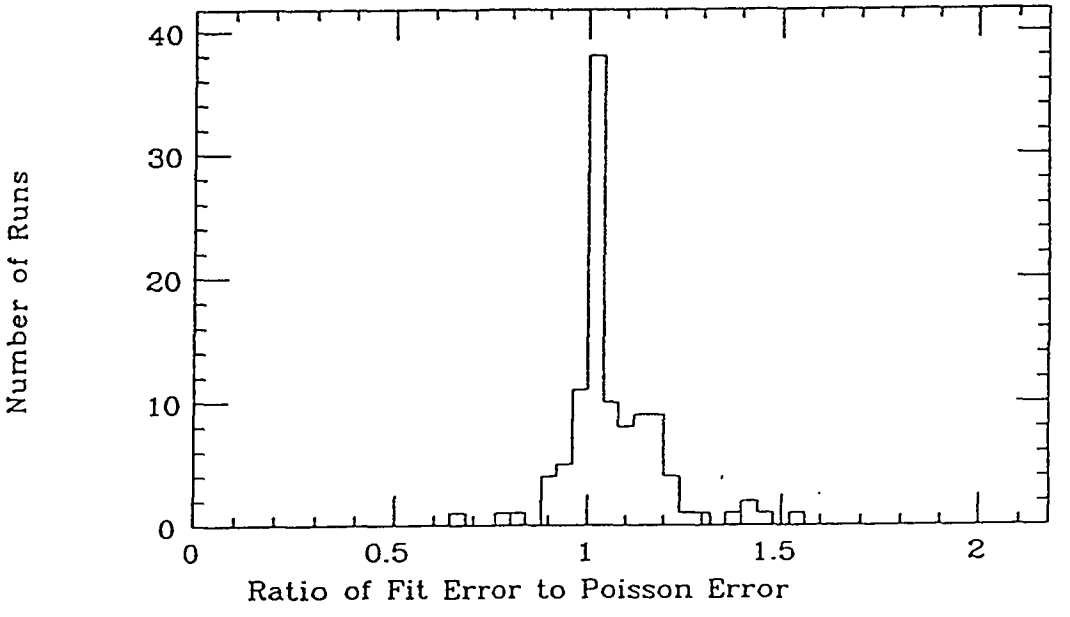

Figure 6.15 Histogram of ratio of fit error to normal error at end of each run. For all Cygnus runs

Chapter 7

Search for an Excess: Results

7.1 Introduction

In this chapter we apply the methods of the previous chapter to search for rate enhancements from the direction of Cygnus X–3. We examine two seasons of data. The first season spanned 1986 June 6 to October 31. The second, 1989 June 9 to August 10. The latter is of particular interest, as Cygnus X–3 underwent two large radio outbursts ($\sim 20Jy$) in 1989, the first on June 3 and the second on July 21. We perform the search over three timescales. First looking for short, $\sim 12min$, bursts, then performing a D.C. analysis, and finally we search for pulsed emission at the $4.79hr$ x-ray period.

7.2 1986 Data Set

Between June 6 and October 31 of 1986, the Haleakala Gamma Ray Telescope logged a total of 120 hours on the X–ray binary source Cygnus X–3. After rejecting runs based on the goodness of the zenith angle fits (see last chapter) we were left with 61 hours of data. Table 7.1 lists the start and end times of the runs used in the analysis.

We used the following rejection criteria:

- Event multiplicity greater than 12 hits in $5ns$.
- Zenith angle of both apertures less then 45°.
- Absolute value of Gini number in off source aperture less then 1.97 over wobble interval.
- Goodness of off source zenith angle fit greater then 10% for both apertures.

Run no.	Day no.	UTC Start(seconds since midnight)	UTC End
764	157	46024.99	49621.85
772	162	49281.52	52254.74
778	164	47922.25	52160.75
781	165	47336.50	52006.60
833	210	24130.79	39714.41
837	211	32091.57	42758.88
838	212	23636.18	29790.50
839	212	30126.68	44614.66
842	213	34437.57	51643.75
845	214	35129.07	44656.84
855	217	30305.16	46771.72
858	218	30925.80	43655.73
860	219	28043.40	33003.64
861	219	33777.35	46217.58
869	241	23318.62	28432.77
870	241	28695.41	42796.82
874	244	22465.65	35958.32
875	244	36371.77	40427.02
878	245	27142.63	32685.64
880	246	22608.80	31610.19
881	246	37744.28	42039.77
888	249	22685.43	39305.31
897	269	21305.69	34951.74
899	273	24252.11	29774.48
931	302	19528.70	29323.32
934	303	19267.15	31597.02
937	304	18635.52	21752.18

Table 7.1 List of runs used in analysis of 1986 data.

7.2.1 Results of Burst Search

Figure 7.1 shows the distribution of excesses from all intervals passing our selection criteria, (i.e. entire run yielded acceptable zenith angle fit, and gini no. for off source aperture less than 1.97 for the interval). The excesses are plotted in units of the total error, $\sqrt{N_{exp} + (\Delta N_{exp})^2}$. The distributions have been fit to a Gaussian using the CERN routine HFITGA. Shown on the plots are the results of the fit, both data sets result in good fits. The width of the on source distribution is as expected (r.m.s. = 1); however, the off source distribution is narrower then one would expect. This is due to the fact that we have already eliminated nonstatistical off source wobble intervals with the Gini test. Though the mean of the on source distribution is inconsistent with zero at the 3σ level, there is no evidence of bursting on these timescales (720 seconds).

The two largest excesses occurred during runs 869 (3.4 σ beginning at UT 29 August $6^{hr}42^{min}$ and lasting for 720 seconds) and 855 (3.2 σ beginning at UT 5 August $9^{hr}54^{min}$ also lasting 720 seconds), corresponding to a chance probability of 8% (two intervals greater than 3.2σ with 301 trials).

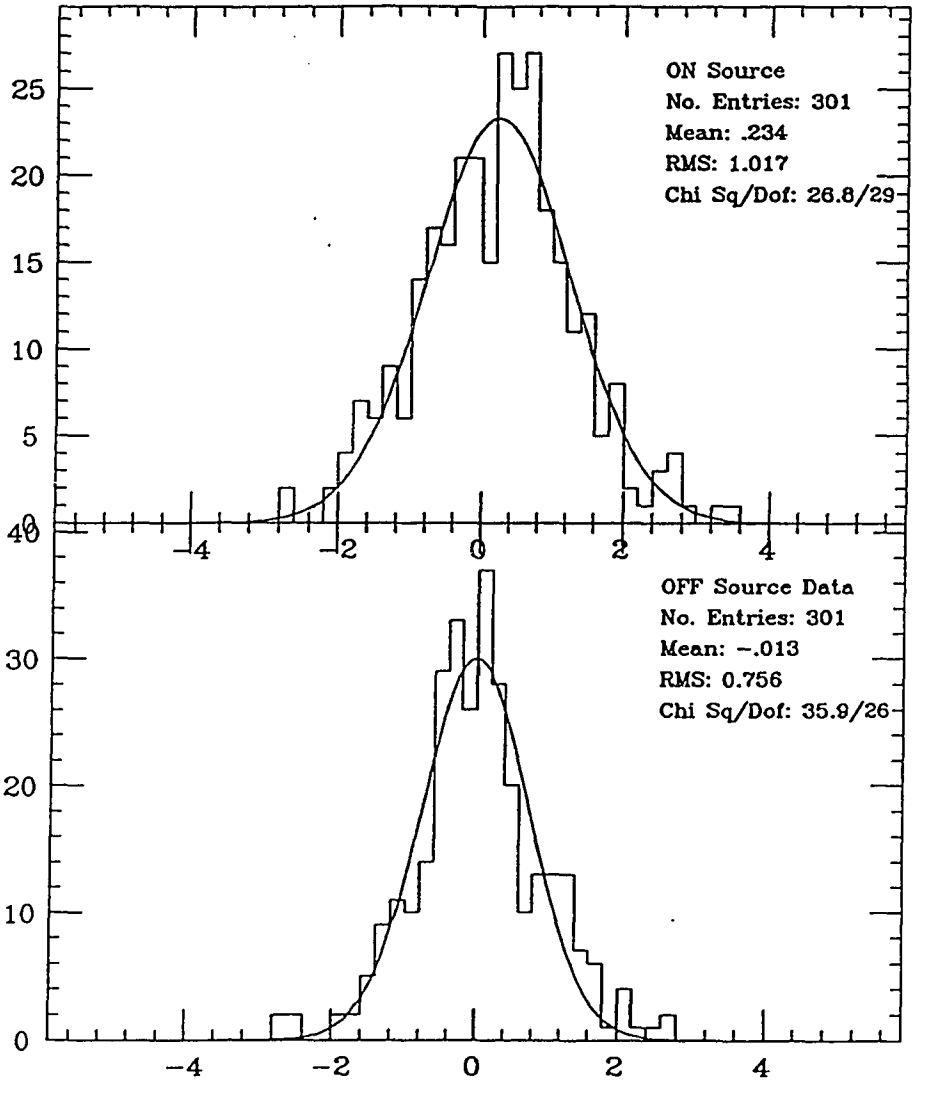

Figure 7.1 Distribution of excesses. Smooth curve is result of a Gaussian fit to the distribution. Parameters given are from HFITGA.

7.2.2 Results of D.C. Analysis

In the previous section we saw that the mean of the distribution of on source excesses was inconsistent with zero. This is an indication of a systematically higher rate in the ON source aperture, albeit a very small one. To find the true significance of the result we perform a D.C. analysis. In Figures 7.2-7.4 we plot the integrated excess as a function of interval number, the error bars shown are the total errors (i.e. statistical and fit errors). Table 7.2 gives the final results by aperture.

Aperture	N_{exp}	ΔN_{exp}	N_{count}	Excess
A ON	23475.9	164.8	23866	390.1
A OFF	23849.5	164.7	24035	185.5
B ON	23358.9	165.5	23868	509.1
B OFF	22826.7	159.4	22888	61.3
A+B ON	46834.8	233.5	47734	899.2
A+B OFF	46676.2	229.2	46923	246.8

Table 7.2 Results of 1986 D.C. analysis.

Examination of the off source excess in Figures 7.2-7.4 shows evidence for a systematic underestimation of the rate, leading to a small overall excess in the off source data. Since this data was used to construct the distributions from which the rate determination was made, there should be no such excess. This systematic bias is caused by non-Gaussian fluctuations in the event rate, probably due to atmospheric phenomenon. Figure 6.12 shows that the fit residuals are not symmetric about zero, there being more deficits than

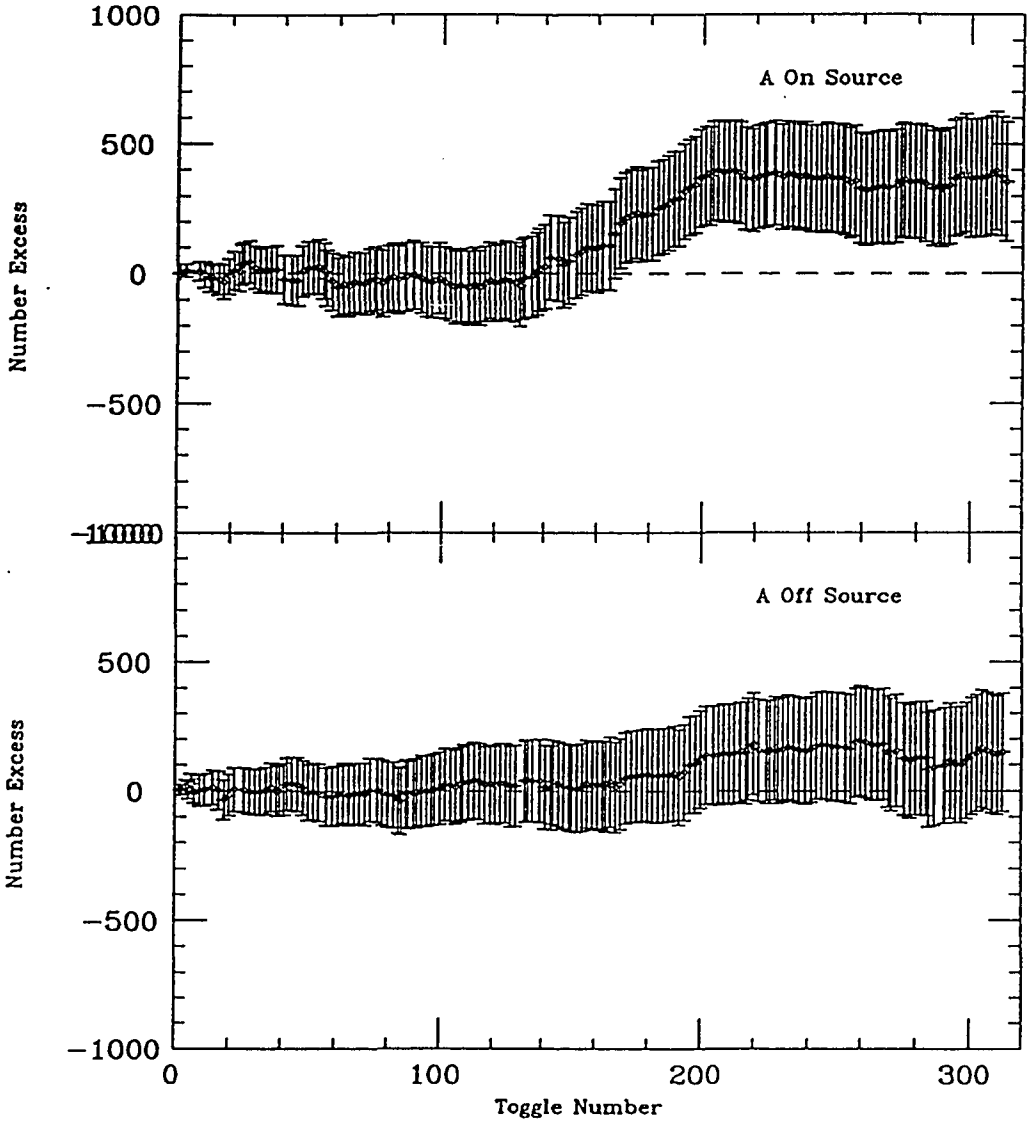

Figure 7.2 Integrated excess versus interval number. A aperture

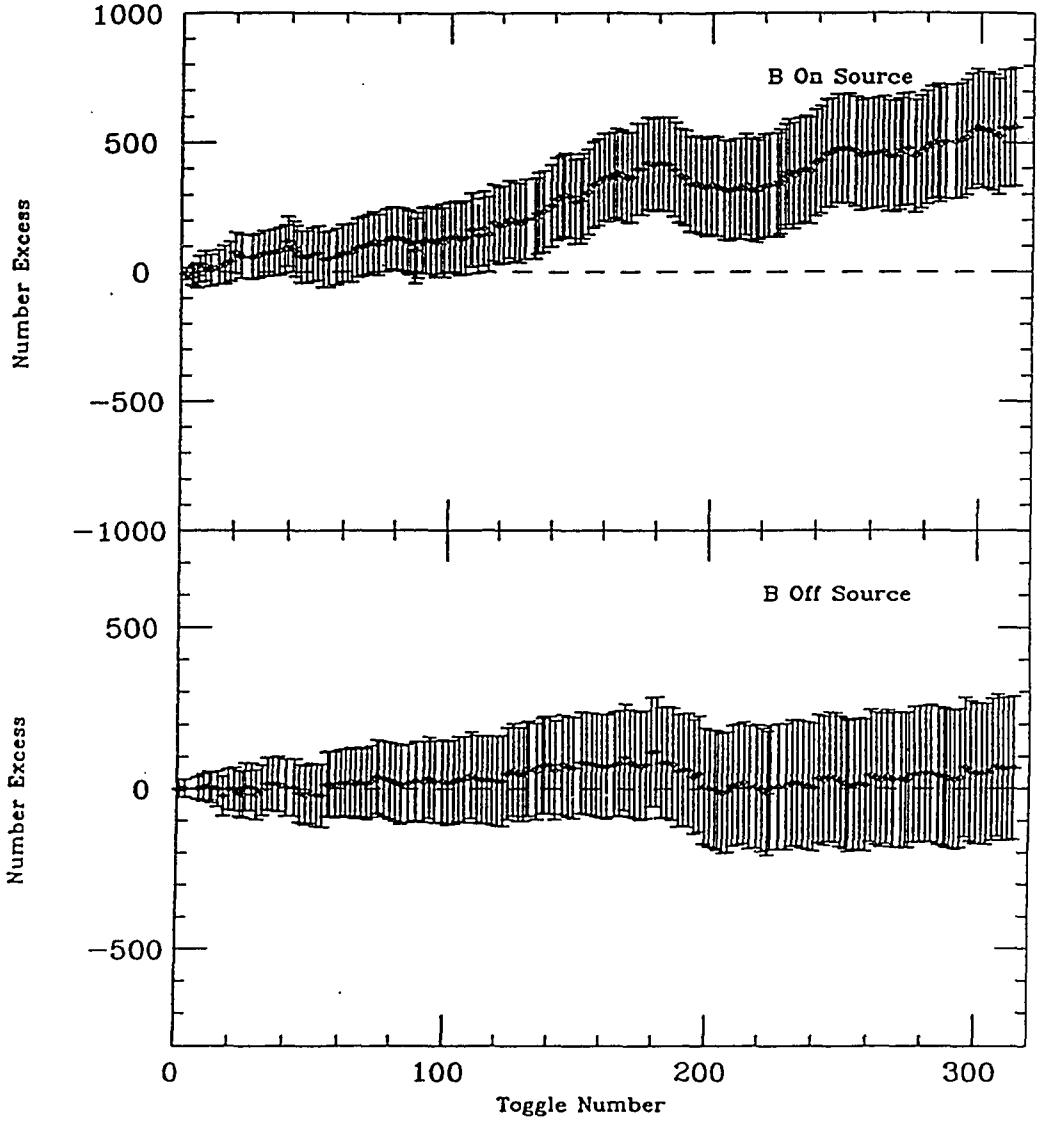

Figure 7.3 Integrated excess versus interval number. B aperture

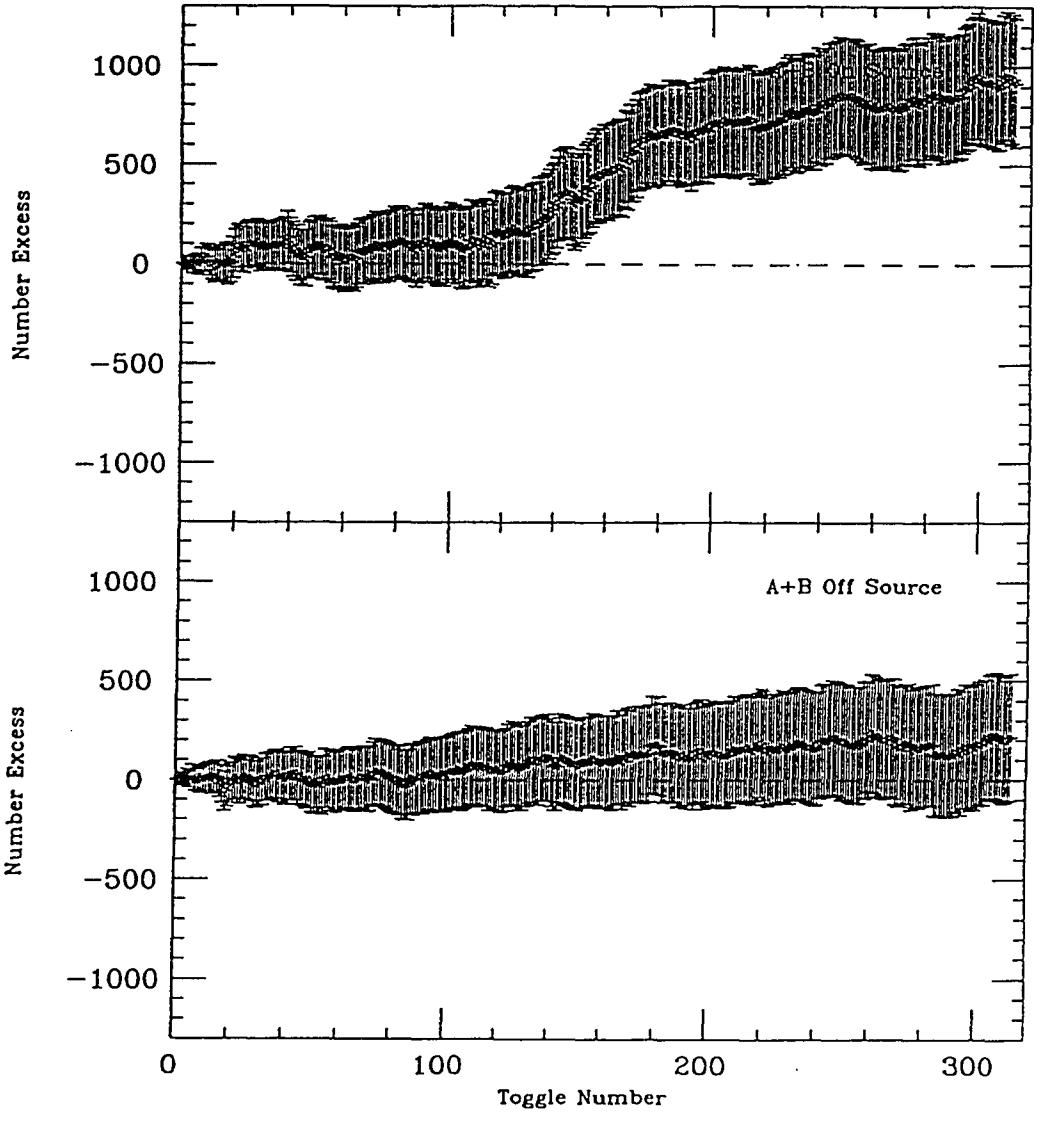

Figure 7.4 Integrated excess versus interval number. A+B aperture

excesses. This has the effect of dragging our estimation of the rate below its true value, and thereby leads to the measured systematic excess. To correct for this bias we simply add the off source excess to the expected number of on source events, so $N'_{exp} = N_{exp} + 246.8 = 47,081.6$, and the true excess is 652.4 events, significant at the 2σ level.

Effect of Choice of γ When computing the fit error we only considered the error in the fitted rate at zenith. We now look into the effect of changing the curvature of the rate function. To this end we have repeated the analysis for different values of γ'. Figure 7.5 shows the final significance of the result, for different values of γ', plotted in units of $\sqrt{N_{exp} + \Delta N^2_{exp}}$. Not only is the final result insensitive to our choice of γ', but $\gamma' = 2.2$ is seen to be at a broad minimum in the excess. The dashed vertical lines mark the one standard deviation limits on γ'.

Final Significance of Result Between June 3 and October 31 of 1986, with a livetime of 221,465.3 seconds, we observed an excess of $652.4 \pm 233.5^{fit} \pm 217.0^{stat}$ events (significant at the 2.0σ level, chance probability 2.3%). This excess is roughly 1.4% of the background cosmic ray rate and corresponds to a time averaged flux of $(5.89 \pm 2.88) \times 10^{-11} \gamma'^{s} / cm^2 / sec$ above 300 Gev (assuming a sensitive area of $5 \times 10^7 cm^2$, Figure 4.9). There is an additional 50% uncertainty in the flux estimation due to the uncertainty in our detection area.

Discussion of Results Examination of Figure 7.4 indicates that the measured excess was not caused by a truly D.C. signal. Essentially all of the excess arises between intervals 120 and 180. In Figure 7.6 we plot the excess received in a given run versus the day number of the run. We see that the excess arises from data taken between days 217 and 250. In Table 7.3 we list

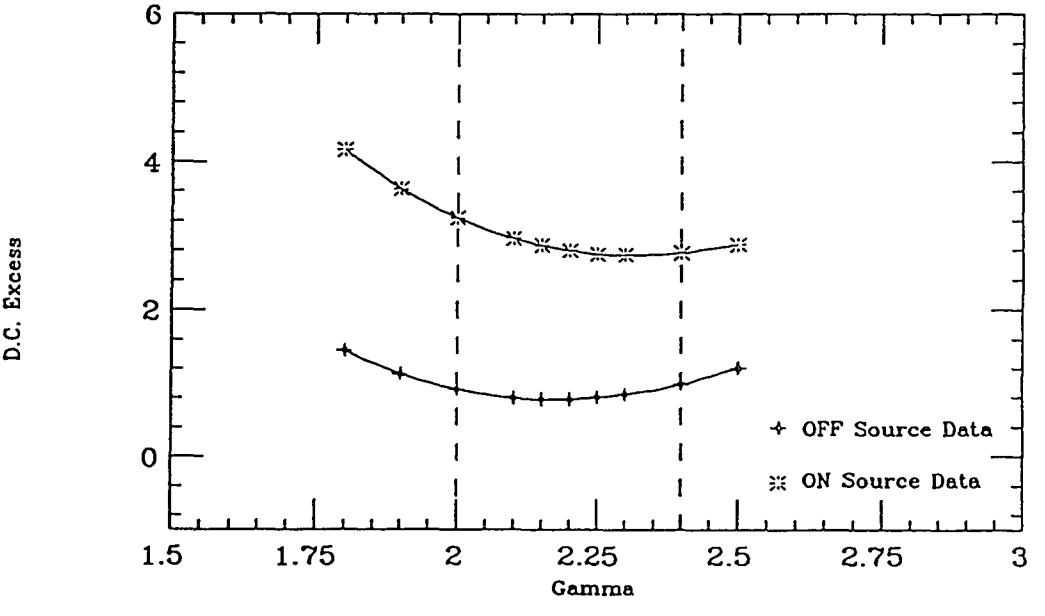

Figure 7.5 Excess versus γ' used in fitting procedure. See above for definition of units.

the runs in this interval and their associated excess. The excess is mostly due to three runs: 858, 861, and 869. The total excess from these three runs is 486. $\pm$ 106. events, significant at the 4.6σ level. We randomly chose three runs from a pool of 27; this corresponds to 2,925 trials, and a chance probability, after trials, of .6% (2.5σ). The total livetime in these three runs was $2.9 \times 10^4 s = 8.06 hrs$, yielding a flux of $(3.3 \pm .72) \times 10^{-10} \gamma's cm^{-2} s^{-1}$ above $300 GeV$.

Run no.	Day no.	Phase Start	Phase End	Excess ON	Excess Off
855	217	.576	.512	37.0 $\pm$ 84.0	13.4 $\pm$ 84.0
858	218	.618	.337	197.0 $\pm$ 67.7	6.3 $\pm$ 66.3
860	219	.458	.737	-27.0 $\pm$ 47.6	10.0 $\pm$ 47.6
861	219	.791	.504	165.0 $\pm$ 66.5	13.0 $\pm$ 65.9
869	241	.358	.637	124.0 $\pm$ 46.5	37.8 $\pm$ 46.3
870	241	.668	.412	55.0 $\pm$ 69.9	7.0 $\pm$ 70.0
874	244	.333	.093	55.5 $\pm$ 84.0	-5.0 $\pm$ 84.3
875	244	.136	.352	-5.0 $\pm$ 41.4	23.0 $\pm$ 41.2
878	245	.612	.924	-39.0 $\pm$ 49.6	-5.5 $\pm$ 48.5
880	246	.356	.855	58.1 $\pm$ 59.4	9.4 $\pm$ 59.4
881	246	.231	.389	20.0 $\pm$ 28.8	1.1 $\pm$ 27.4
888	249	.382	.342	88.8 $\pm$ 80.2	29.0 $\pm$ 80.1

Table 7.3 Runs and excess between day 217 and 250 (1986).

We note that on days 219 and 241 we also had runs with no significant excess, implying that the source is highly variable on timescales of hours. This is to be expected in the beam dump models discussed in chapter 2. We also note that the GREX array at Haverah Park obtained their largest excess from Cygnus X–3 in 1986 on days 242 and 243 (see section 3.6.2).

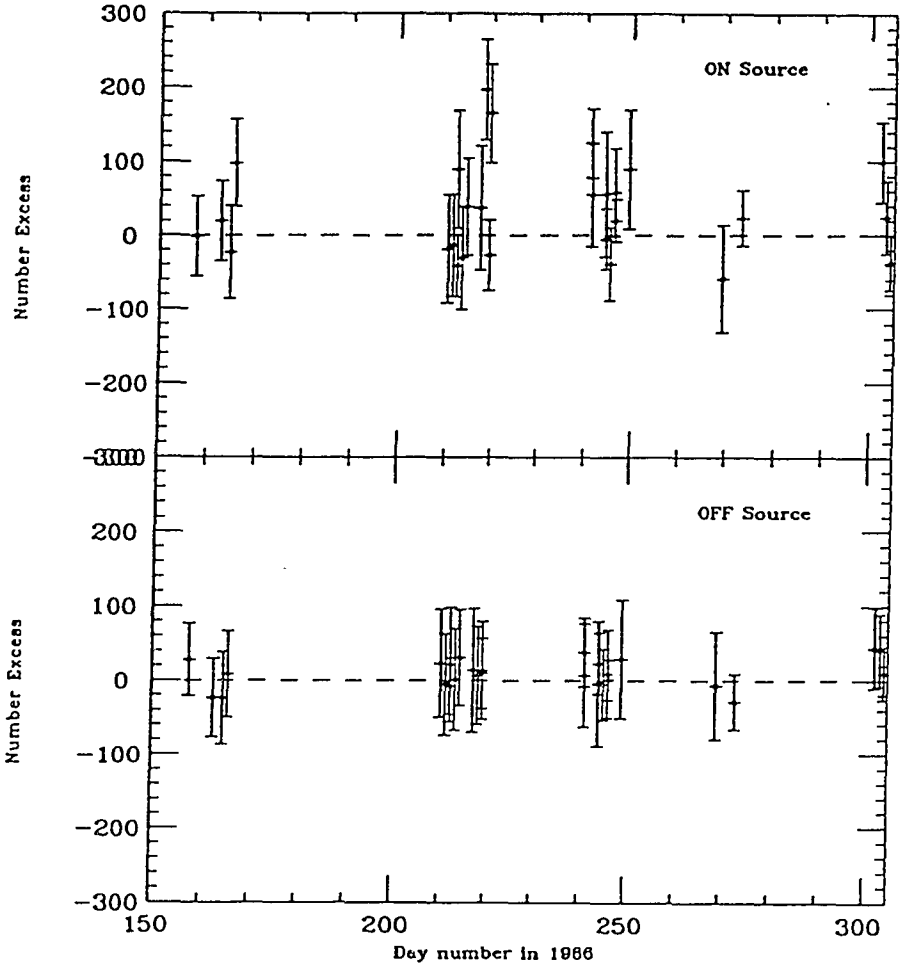

Figure 7.6 Excess by run versus day number in year (1986).

Figure 7.7 shows the radio flux from Cygnus X–3 as measured by the Green Bank radio telescope at 11cm for 1986 (Waltmann private communication). Brackets on the bottom show times where we have data, and the vertical lines mark the period when we observed an excess from Cygnus. The correlation is suggestive of high energy activity preceeding and following the increase in radio intensity though lack of data during the radio active period (due to the moon), makes it impossible to make any claims. In the next section we examine this interval in more detail looking for correlations with orbital phase.

7.2.3 Search for Emission Pulsed at X-Ray Period

In the previous section we saw evidence (of low statistical significance) for steady emission from Cygnus X–3. By itself this is not a strong enough signal to claim a detection of gamma rays from Cygnus X–3. However, if the emission is correlated with a preferred orbital phase the credibility of the signal would be enhanced. Here we search for such a correlation. First we will examine the subset of data that corresponds to the time of enhanced emission, and then the entire data set.

Method The technique is similar to that used in the D.C. analysis. Since we can not directly compare the on source data to the off source data (because of the different zenith angles of the apertures) we use the techniques of the previous chapter to construct 'expected' phase plots for the data sets. To

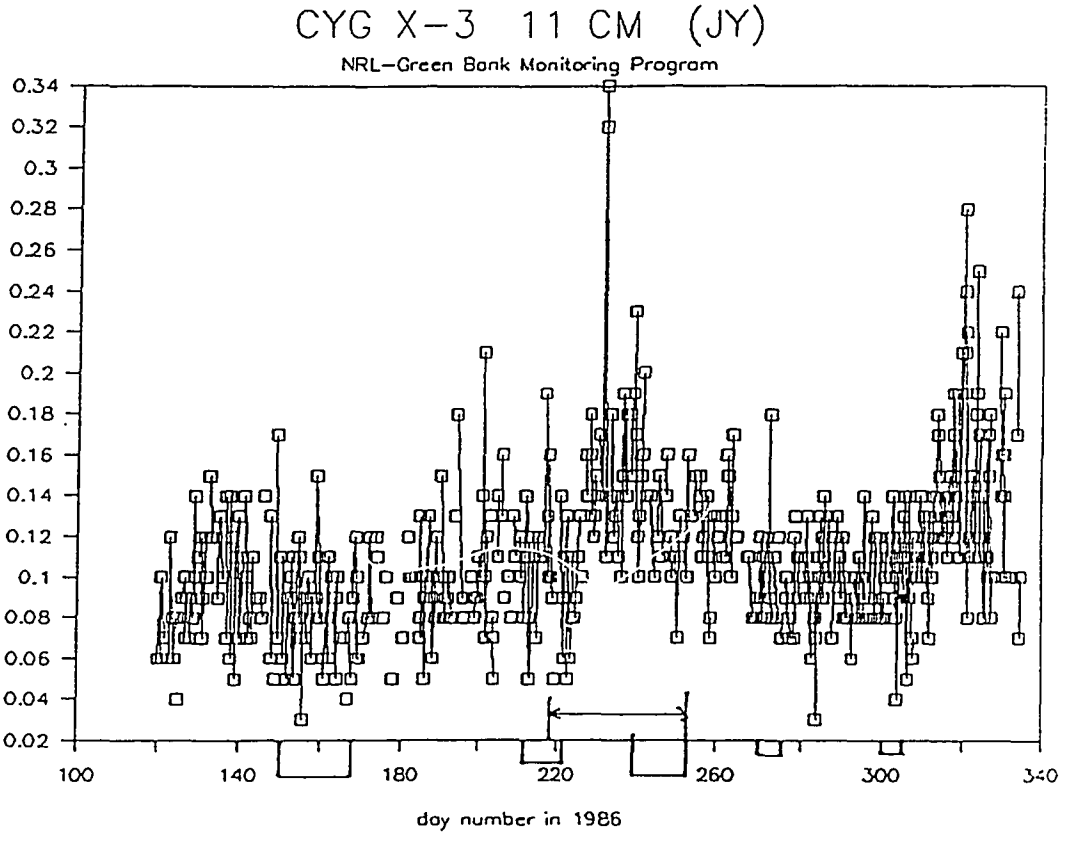

Figure 7.7 Radio flux from Cygnus X–3 vs. day number (1986). Waltmann 1989

construct these we take the time difference between two consecutive events, multiply it by the rate, as given by the fitted function, and enter this number (the expected number of events) into the appropriate bin of the phase plot. If the two events are in the same phase bin we enter the expected number in that bin. If they split a bin, we split the expected number between the two bins according to how much time was spent in each of the bins.

Errors in Expected Number As for the case in the D.C. analysis we have fit errors as well as the Gaussian errors to worry about. We handle these errors in the same manner. Just as we created 'expected' phase plots above by integrating the rate, we construct 'error' phase plots by integrating the error in the rate and entering ΔN_{exp} into the appropriate phase bin.

Results From Time of Increasing D.C. Excess We first use only those runs which occurred during the time that our D.C. excess (Figure 7.4) was increasing. Table 7.3 lists the runs used. Figure 7.8 shows the expected number of events in the on and off source data versus orbital phase, giving our phase coverage. In Figure 7.9 we show the number excess versus phase bin. We have corrected the excess in each phase bin (according to how much time was spent in that phase bin) to remove the D.C. excess.

There appears to be no correlation between excess and orbital phase. The excesses at phase 0.50 and 0.93 are only 2σ above the mean excess, no more significant than the two negative fluctuations seen at phases 0.55 and 0.64.

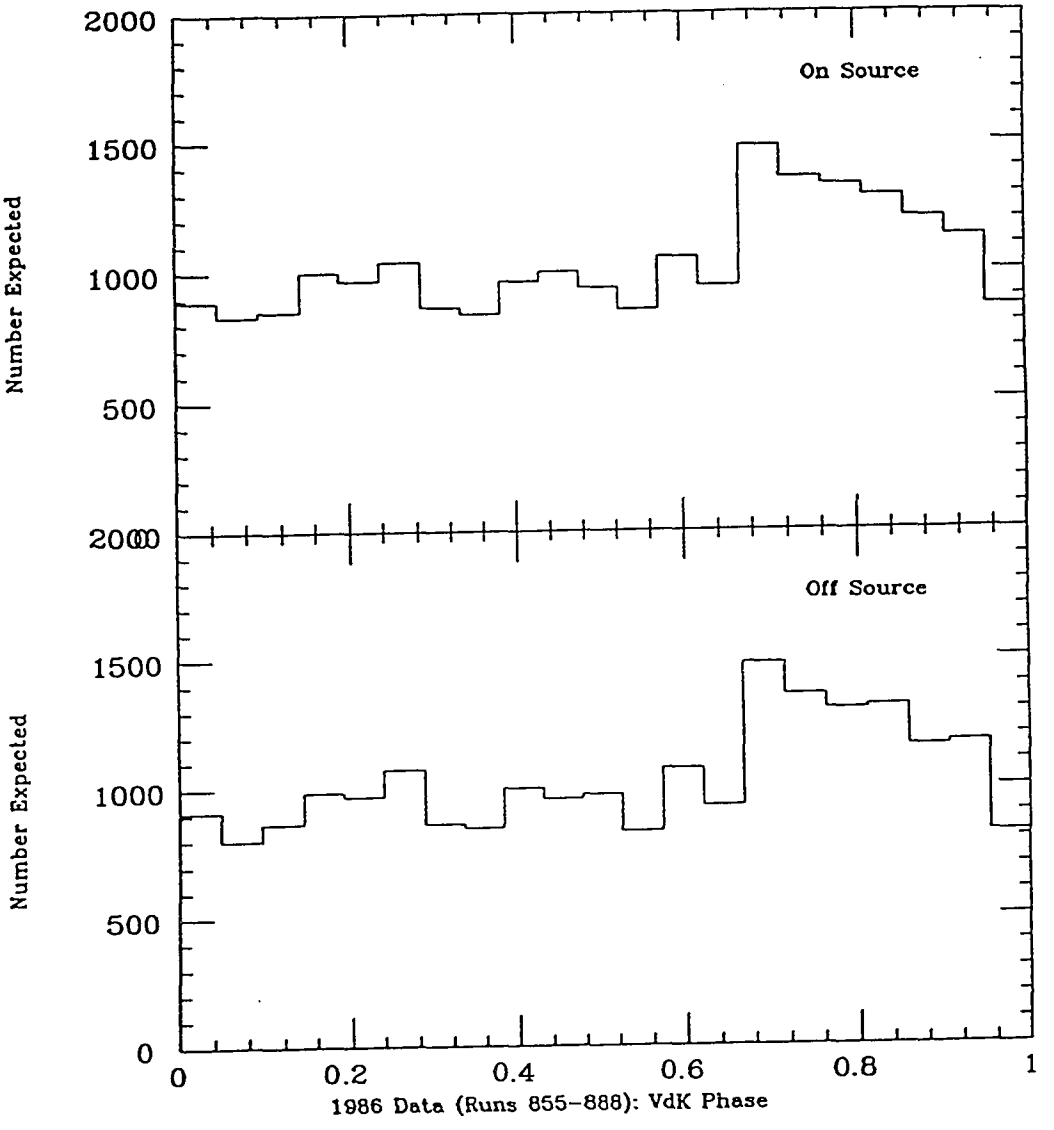

Figure 7.8 Expected number of events vs. orbital phase, day 217-250. (VdK 1988 quadratic ephemeris). (a) ON Source, (b) OFF Source

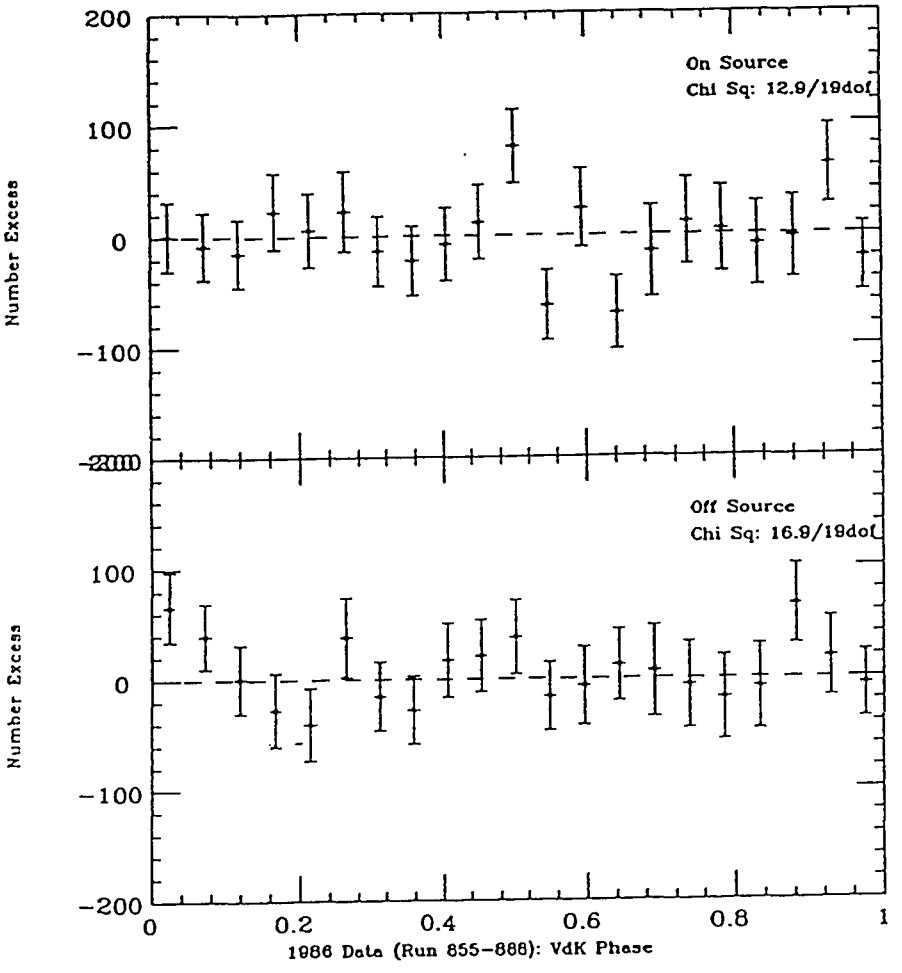

Figure 7.9 Excess number of events (corrected for D.C. excess and phase coverage) vs. orbital phase, day 217-250. (VdK 1988 quadratic ephemeris). (a) ON Source, (b) OFF Source

Orbital Analysis of Entire Data Set Next we perform the same analysis as above on our entire data set. In Figure 7.10 we show our phase coverage of Cygnus (expected number of events versus orbital phase). And in Figure 7.11 we show the excess versus orbital phase. Once we account for the D.C. excess, the most significant deviation is a negative fluctuation at phase 0.64. Though there is some evidence for a broad, double peaked light curve, with peaks at phase 0.26 and 0.93, it is not statistically significant.

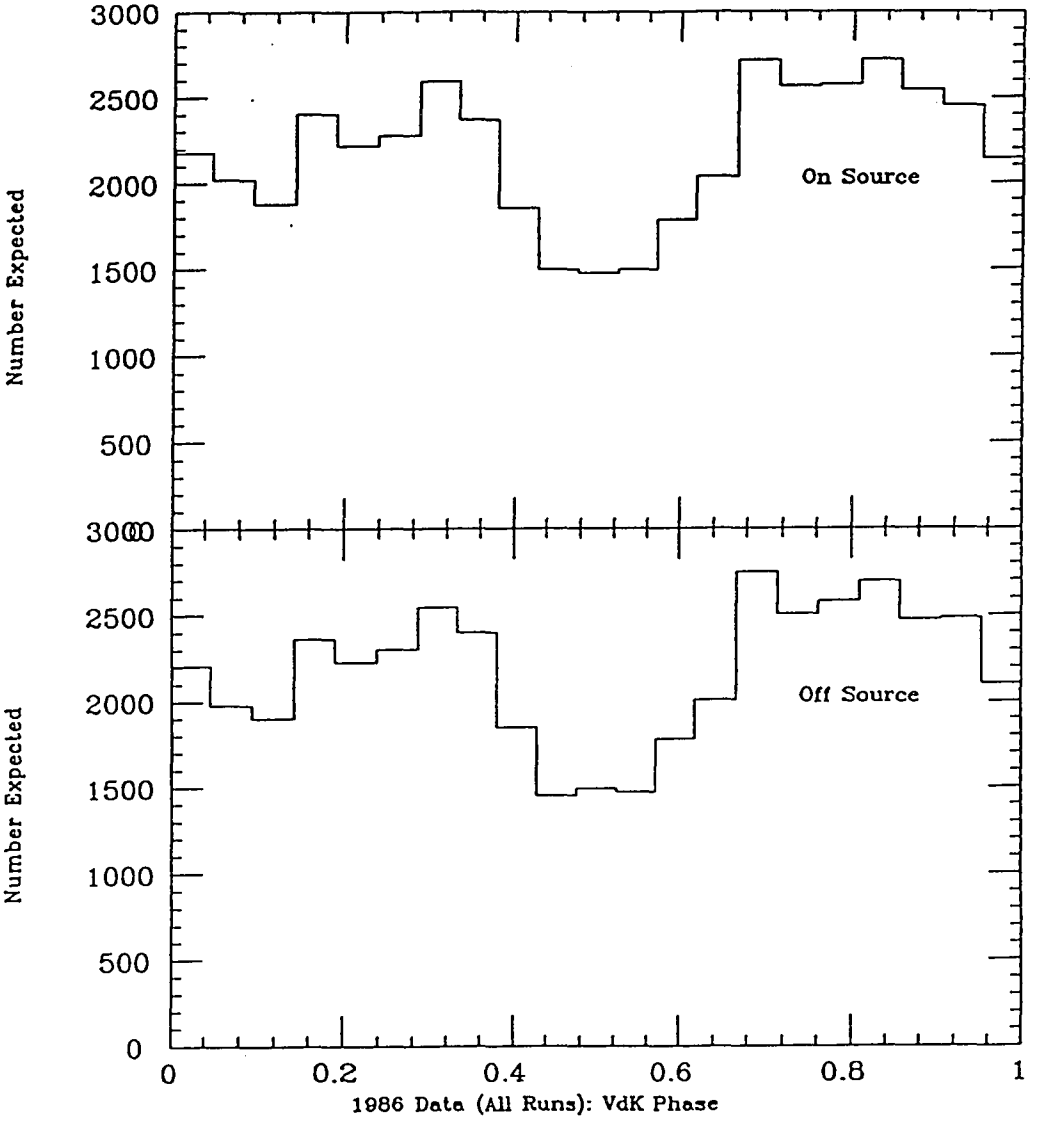

Figure 7.10 Expected number of events vs. orbital phase, all data. (a) ON Source, (b) OFF Source

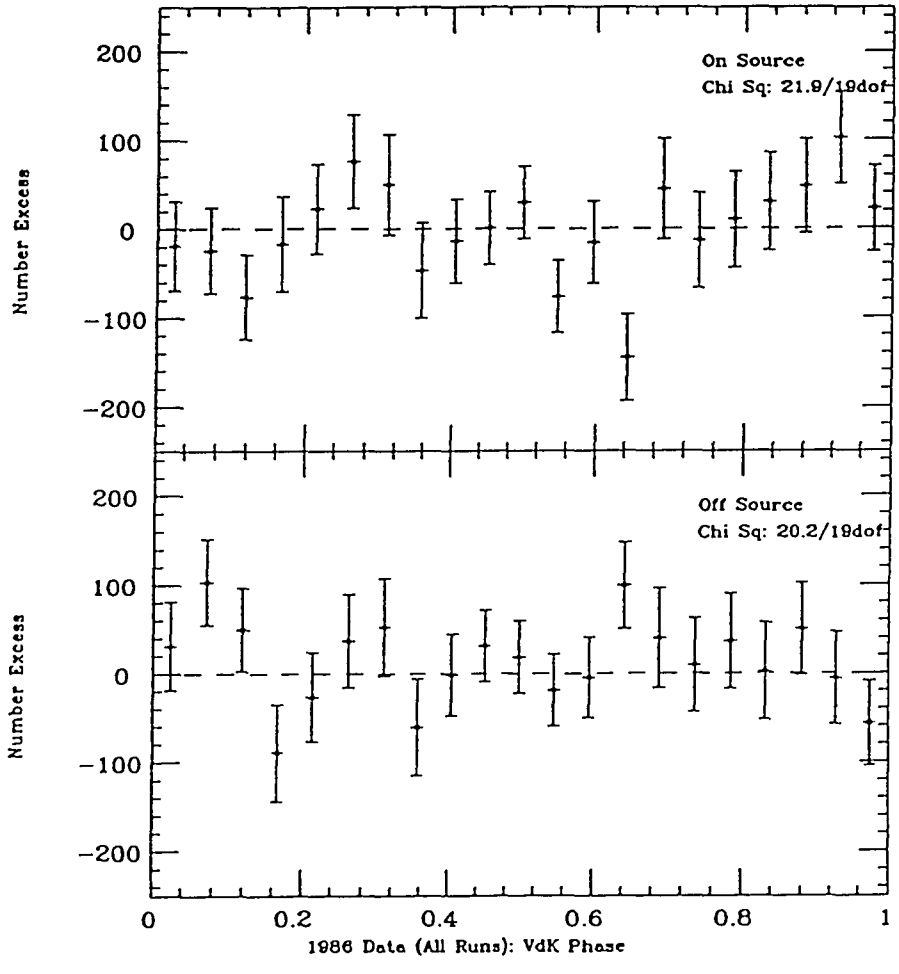

Figure 7.11 Excess number of events (corrected for D.C. excess and phase coverage) vs. orbital phase, all data. (a) ON Source, (b) OFF Source

7.3 1989 Data Set

During the summer of 1989 there were two large flaring events from Cygnus X–3, the first occurred on June 3 and the second on July 21, (Figure 7.12). The Haleakala telescope logged $76.5 hrs$ of high quality data between 1989 June 9 and August 10. We search this data for evidence of bursting on a timescale of $900s$, and for a D.C. excess over the entire interval.

7.3.1 Modifications to the Telescope

In 1988 the telescope underwent substantial modifications aimed at improving the optics and simplifying the alignment of the system. The six large mirrors were replaced by 26 smaller ($.5m^2$ each) mirrors, enabling us to place one phototube at the focus of each mirror and retain our 1 pe discrimination. Previously, with the larger mirrors, the light level at the focus was too high, forcing us to place three phototubes back from the focal plane, making alignment difficult.

The new telescope began taking data in March of 1989 and has been working reliably ever since. All of the analysis techniques developed for the old telescope are easily modified for the new instrument. We estimate the effective area to be $7500m^2$, and the energy threshold to be $100GeV$. Before proceeding we need to reexamine our choice of multiplicity cut and our choice for the effective spectral index used in the zenith angle fit.

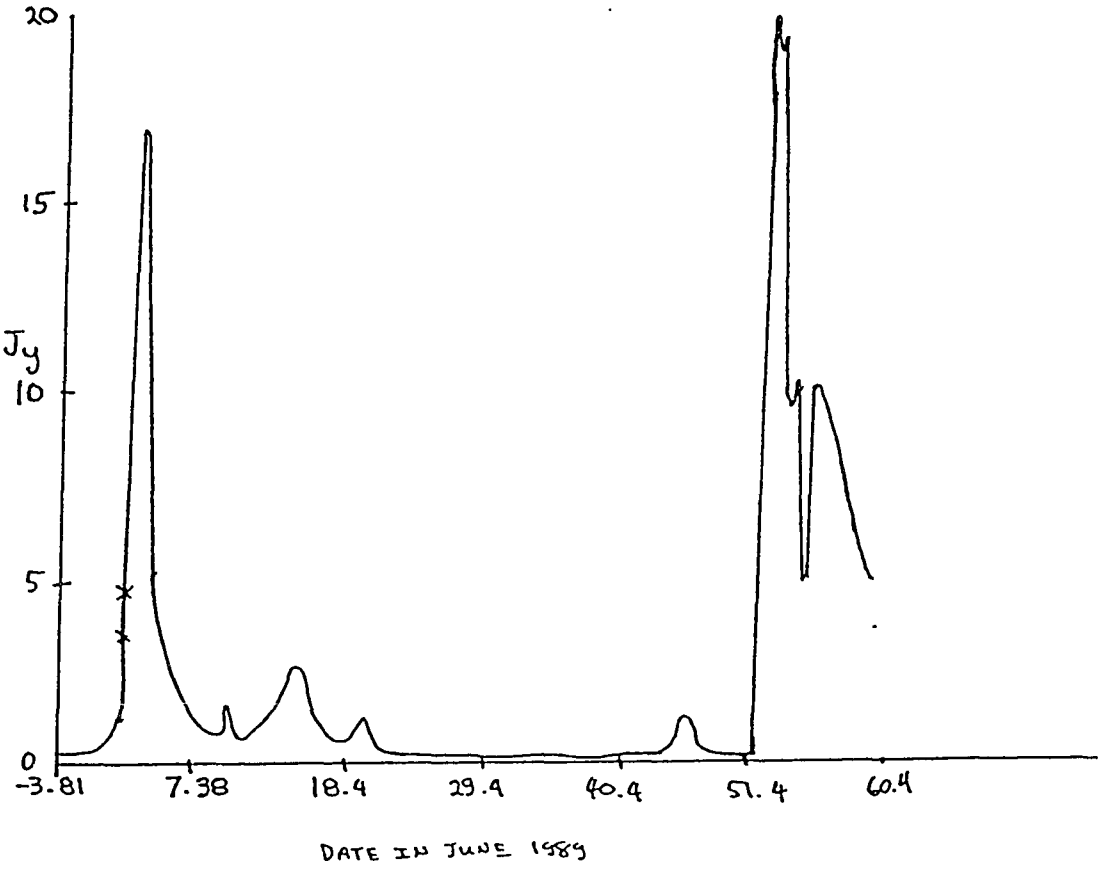

Figure 7.12 1989 Radio outburst from Cygnus X–3. 11 cm. Adapted from Johnston 1989.

Multiplicity Cut With the new telescope we have different singles rates and a different number of tubes participating in the trigger logic. We expect that we may have to adapt our multiplicity cut for the new configuration. Figure 7.13 shows the random trigger rate as a function of multiplicity demanded in a $5ns$ window for various singles rates. With the smaller mirrors the maximum observed singles rates are $2.5MHz$, and a more typical value is $1.5MHz$. With a multiplicity of 12 hits in $5ns$ our random trigger rate is $\sim 10^{-5.5}$ times the cosmic ray trigger rate ($\sim .7Hz$), perfectly acceptable for this analysis.

Zenith Angle Fitting Once again we make two passes through the data. On the first pass we let both R_0 and γ' vary. Figure 7.14 shows the distribution of γ' for each aperture. For both apertures the average γ' is 2.3 ± 0.2. On the second pass we set $\gamma' = 2.3$, perform the fits and reject runs if χ^2 probability of the fit was $< 10\%$. Figure 7.15 gives the data and fitted function for run 1647, and Table 7.4 lists the runs used in the analysis.

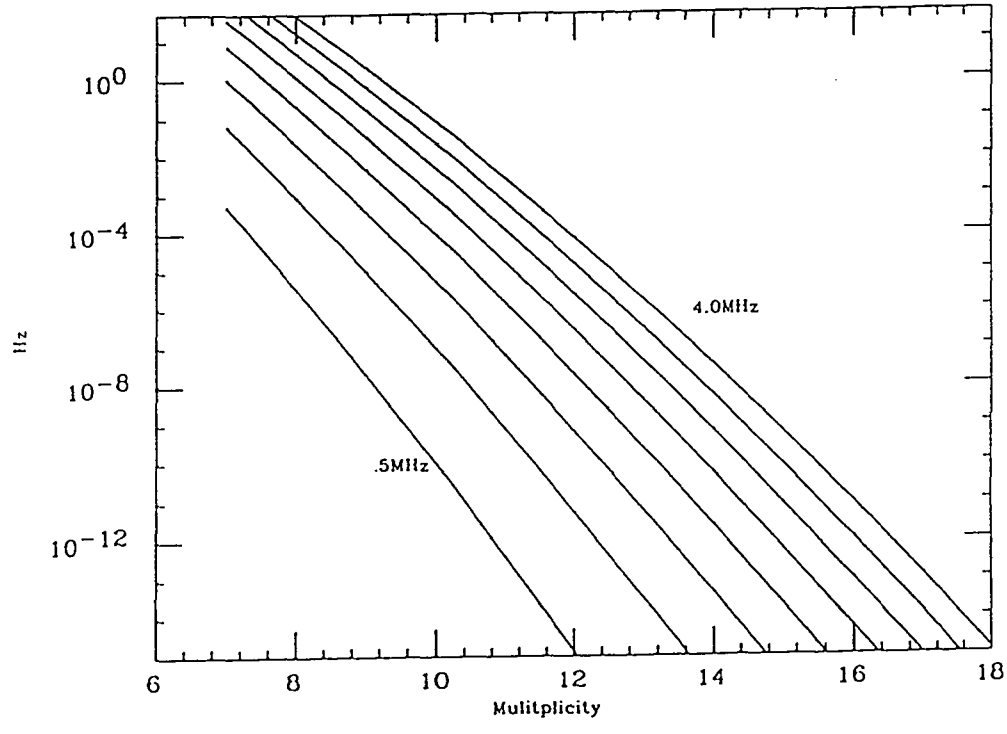

Figure 7.13 Random trigger rate versus multiplicity demanded in $5ns$ window.

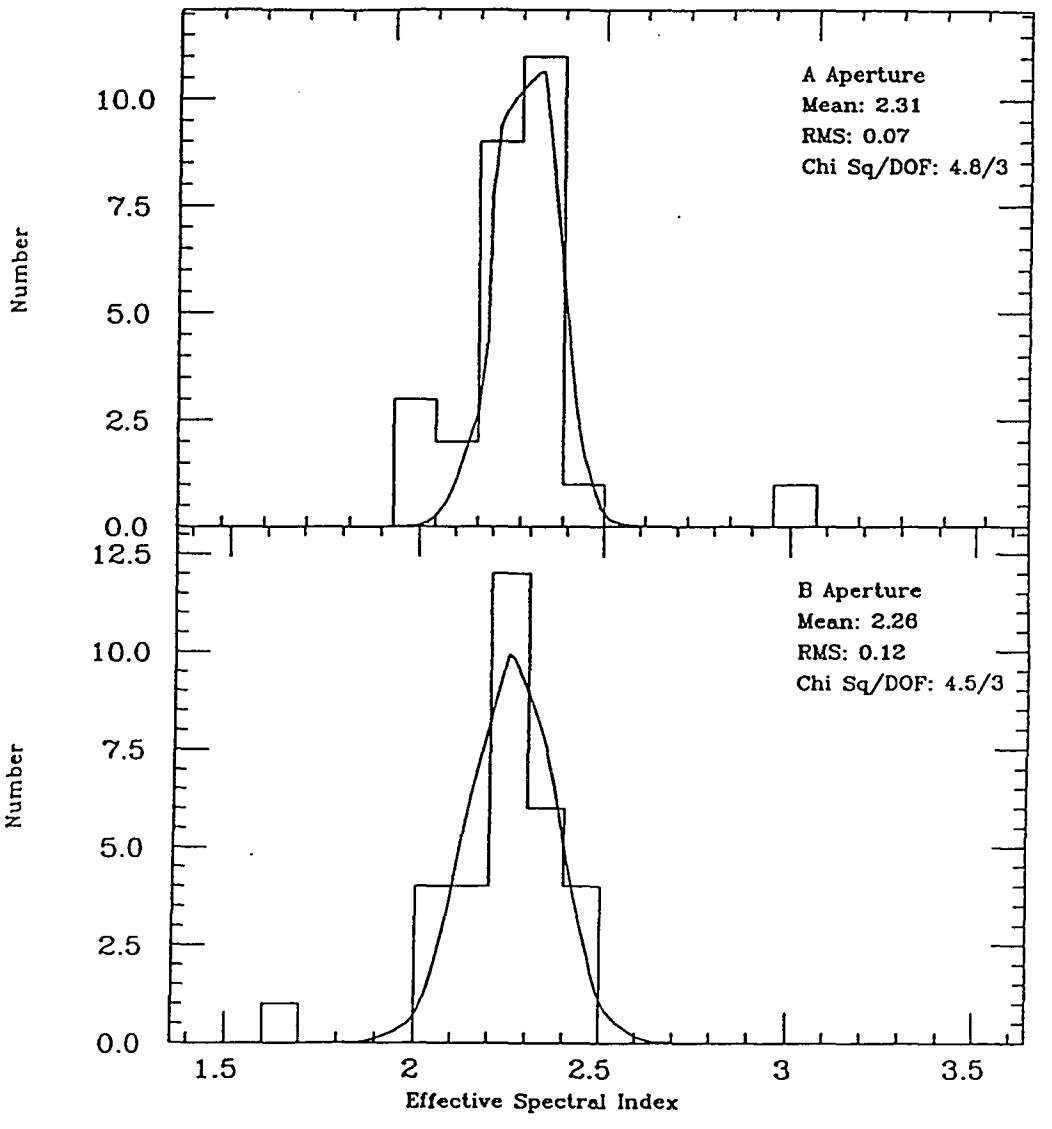

Figure 7.14 Distribution of γ'. All 1989 Cygnus runs. Multiplicity cut of 12 hits in $5ns$. a.) A Aperture b.) B Aperture

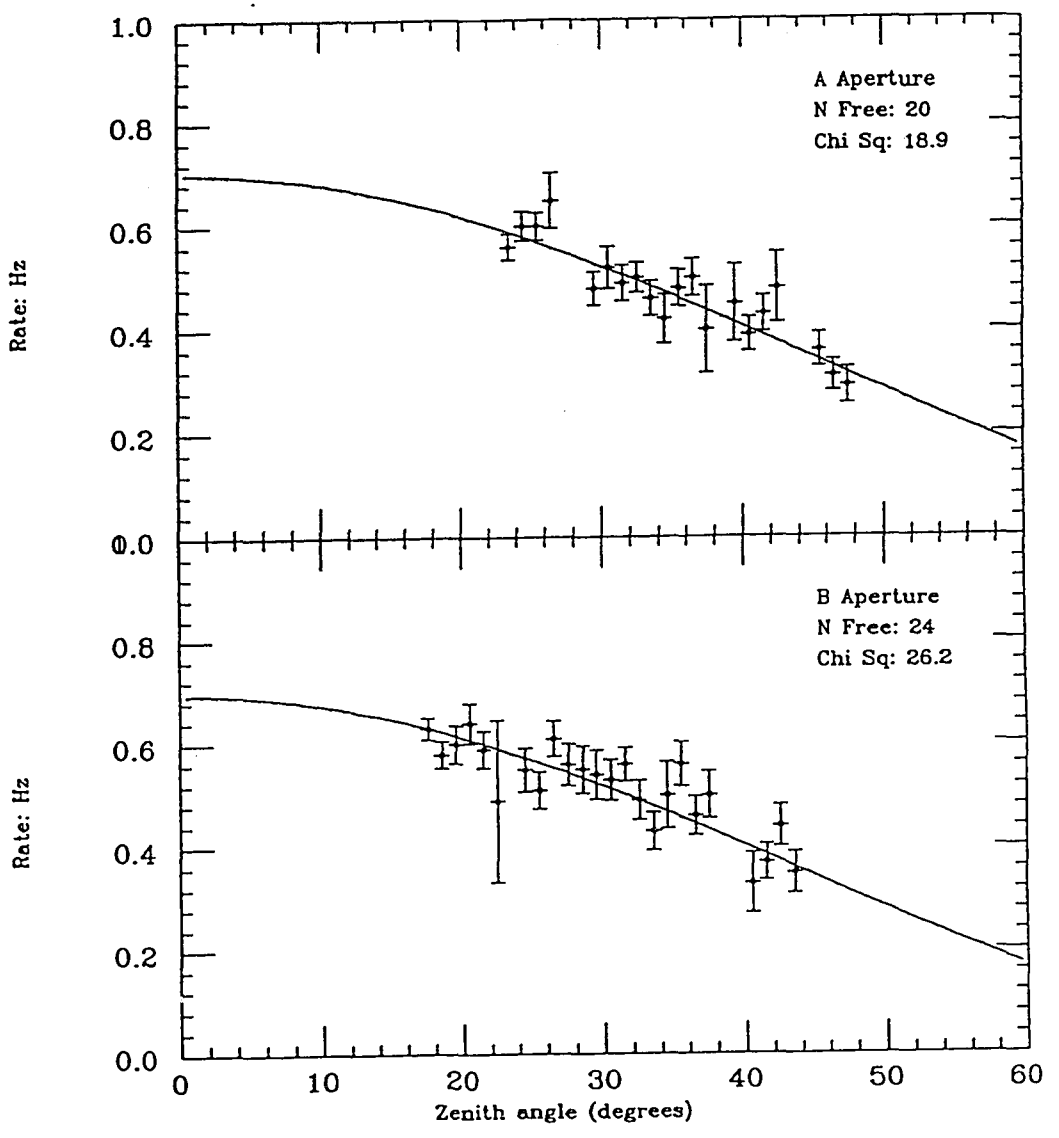

Figure 7.15 Rate as a function of zenith angle from run 1647. Curve is fitted function and points are data. Multiplicity cut of 12 hits in $5ns$. (a) A Aperture, (b) B Aperture

Run no.	Day no.	Start Time (UT)	Duration (seconds)
1629	161	10:34:56	14747.67
1631	162	11:40:33	10921.30
1637	177	9:15:48	7380.03
1639	178	9:02:52	17310.31
1645	180	11:36:25	11250.39
1647	181	8:59:54	20549.23
1651	183	8:56:34	16461.32
1655	184	9:45:21	15503.67
1659	188	9:04:47	20561.73
1666	193	10:25:25	15787.05
1667	205	8:57:07	2902.89
1668	206	7:01:30	14513.72
1672	208	8:12:10	21716.64
1677	211	8:01:45	9230.13
1679	212	8:09:45	17326.29
1682	213	10:03:46	9677.24
1686	215	7:44:44	18059.34
1690	216	10:16:13	2614.63
1691	216	11:24:59	5293.92
1698	218	10:33:07	8517.57
1700	220	9:00:47	9953.81
1703	221	7:57:06	17971.16

Table 7.4 List of Cygnus runs used in 1989 analysis.

7.3.2 Burst Search

The 'wobble' intervals were $900s$ in 1989. We proceed exactly as we did for the 1986 analysis. Figure 7.16 below shows the results.

The largest excess occurred during run 1647, 1989 June 29 $11^{hr}19^{min}36^{sec}$ UT. During this interval we received 633 cosmic ray events when we expected 540.1 ± 9.1 ($S/B = 17\%$), significant at the $(633 - 540.1)/\sqrt{540.1 + 9.1^2} = 3.73\sigma$ level. Accounting for trials (307 intervals) the chance probability is 2.9% (1.9σ). And the corresponding flux is $2.2 \pm .59 \times 10^{-9}\gamma^s/cm^2/sec$ above $100GeV$. The uncertainty of our target area ($\sim 50\%$) has not been included. The orbital phase of Cygnus was $\phi_{vdK} = .444 \pm .026$. The largest negative deviation is identical in magnitude. We see no evidence for bursts between 1989

7.3.3 D.C. Results from 1989

Table 7.5 gives the results of the D.C. analysis, obtained by summing all of the above intervals. The total livetime was $275,241.8s$ The systematic bias observed in 1986 does not appear to be present in this data set, possibly due to the telescope's improved rejection of off axis showers (arising from the more precise pointing). The excess in the on source aperture was $403.01 \pm 371.3^{stat} \pm 459.66^{fit}$, significant at the 0.68σ level, completely consistent with expectations. We set a flux upper limit (95% C.L.) of $5.7 \times 10^{-11}\gamma's^{-}cm^{-2}$, smaller than the flux measured in 1986.

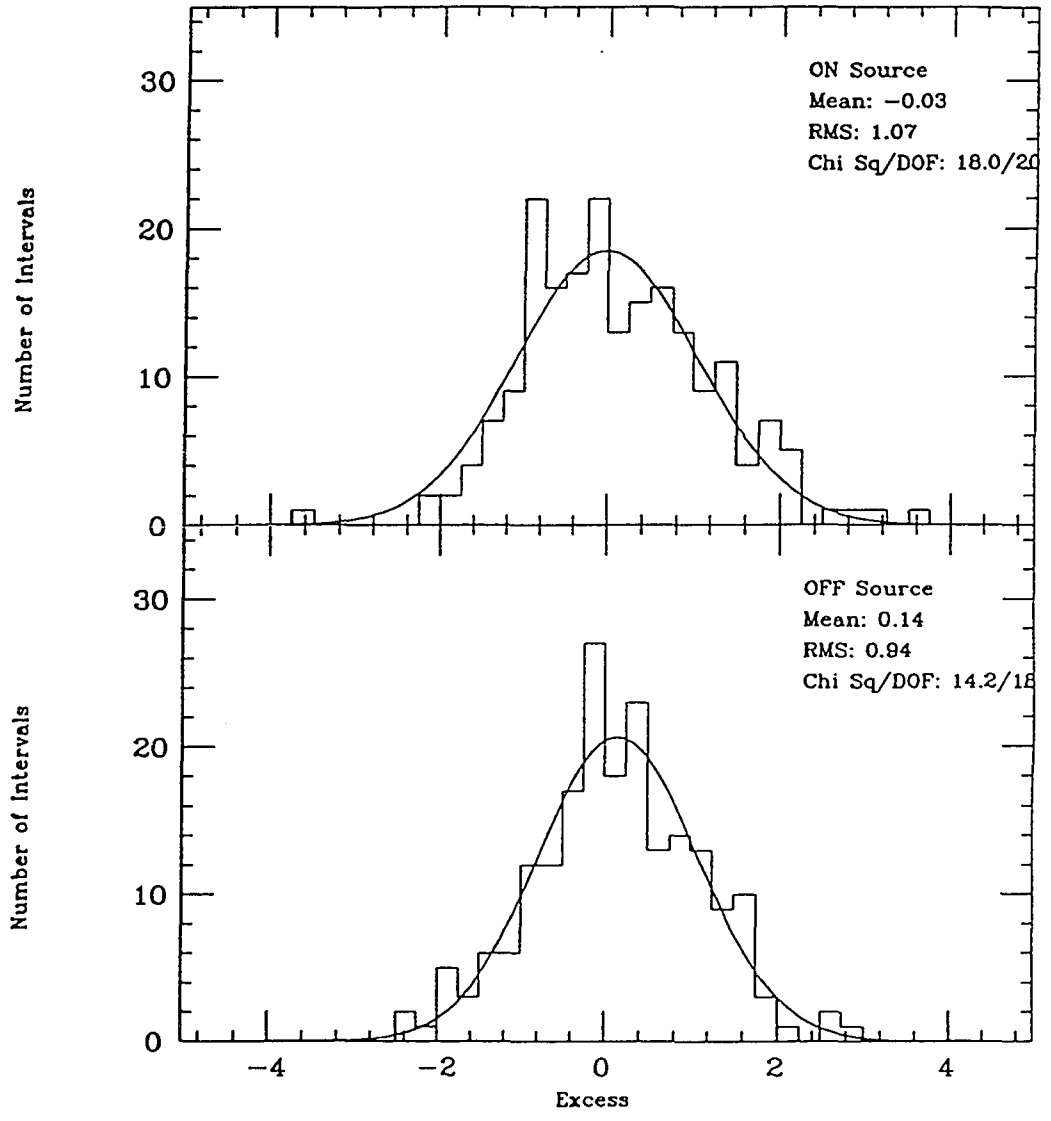

Figure 7.16 Distribution of excesses over 900s intervals. 1989 data.

Aperture	N_{exp}	ΔN_{exp}	N_{count}	Excess
A+B ON	137,871.99	459.66	138,275.	403.01
A+B OFF	137,669.43	456.53	137,700.	0.57

Table 7.5 Results of 1989 D.C. analysis.

7.3.4 Summary of 1989 Results

We have analyzed a total of 76.5 hours of data on Cygnus X–3 around the times of two major radio flares. We have searched 307, 900 second intervals. During one of these intervals, starting on June 29 UT $11^{hr}19^{min}26^{sec}$, we observed an excess of 93 events over a background of 540 events. After accounting for the number of trials this is significant at the 1.9 standard deviation level, consistent with expectations from chance. We note the presence of a deficit of the same magnitude. For the whole data set we set a flux upper limit, 95% C.L., of $5.7 \times 10^{-11}\gamma's^{-1}cm^{-2}$ above $100GeV$.

Chapter 8

Search for a Pulsar in Cygnus X–3

8.1 Introduction

Some models of Cygnus X–3 postulate a rapidly spinning neutron star as the ultimate energy source for the system. Though there has been no evidence for this at lower energies, the Durham collaboration (Chadwick et. al. 1985) claims to have strong evidence of a pulsar with a period of $12.59ms$. To date this claim has not been confirmed by any other group.

Below we carry out a number of searches for the pulsar. The Durham group has given a very restrictive recipe for the search (Brazier et. al. 1990). We first follow their prescription, and search for a signal pulsed at $12.59ms$. Failing in this effort we proceed to search over all Fourier independent frequencies from $1kHz$ to D.C.. To keep the number of trials to a minimum we restrict our general search to intervals with a significant rate excess ($> 3\sigma$).

8.2 1986 Data Base

8.2.1 Search for $12.59ms$ Pulsar

The Durham collaboration has criticized previous attempts by other groups to confirm their detection of a fast pulsar in Cygnus X–3. They claim that many unnecessary trials are being performed, causing the signal to be lost in the noise. Consequently they have published a precise search technique which is designed to minimize the number of trials that one performs (Brazier et. al. 1989).

The Durham Prescription

The claim is that Cygnus emits γ-rays roughly $800s$ after the time of X–ray maximum (orbital phase 0.646 by the parabolic ephemeris of Van der Klis 1988). We restrict our search to $720s$ intervals which contain this orbital phase. The Durham collaboration has also provided an ephemeris for the pulsar, enabling us to restrict the frequency range of our search. This ephemeris (Figure 8.1) predicts pulsations between $12.593ms$ and $12.594ms$ for the dates of interest to us (June-September 1986). The duty cycle claimed is roughly 5%.

Search Method

To search for a periodic signal over a discrete frequency range we employ the discrete Fourier transform (DFT). Much literature has been devoted this

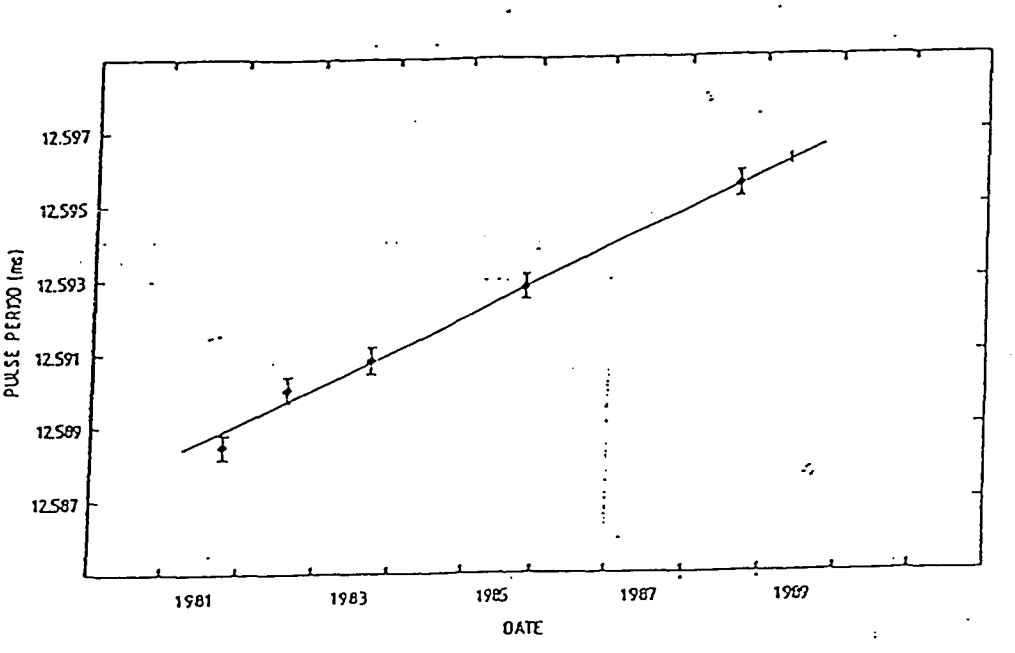

Figure 8.1 Pulsar ephemeris as given by Durham collaboration. (from Brazier et. al. 1989)

topic (see for example Mardia 1972, and Scargle 1982 for a detailed development of the DFT), and here we will simply list the properties of the DFT which we need in this analysis.

Definition of DFT Given a set of N event times, $\{t_i : i = 1, N\}$, one constructs the Rayleigh vector z for a given frequency ω:

$$z(\omega) = \frac{1}{N}\left\{\left(\sum_{i=1}^{N}\sin(\omega t_i)\right)^2 + \left(\sum_{i=1}^{N}\cos(\omega t_i)\right)^2\right\} \qquad (8.1)$$

In frequency space the Fourier independent spacing is given by $\Delta f = 1/T$, where $T = t_N - t_1$. The corresponding spacing in period space is then $\Delta P = P^2/T$ ($P = 1/f$). In practice one usually 'oversamples' (tests frequencies on a finer scale than $1/T$) so as to find the true peak height of any signal. Monte Carlo simulations have shown that a statistical penalty must be paid for this oversampling. In practice one multiplies the number of Fourier independent trials by a factor of three (Middleditch 1976) to arrive at an effective trial factor (in reality this factor is between 2.5 and 3 depending on the degree of oversampling and the number of Fourier periods searched, since this does not appreciably alter the statistical significance of any result we simply take the factor to be 3).

Statistics of DFT If N is large (> 100) then the Rayleigh vector z follows an exponential distribution, $Prob(z \geq Z_0) = e^{-Z_0}$. For smaller event samples

the distribution is modified. The following expression is valid for $N \geq 10$ (Greenwood and Durand 1955):

$$Prob(z \geq Z_0) = e^{-Z_0}\left[1 + \frac{2Z_0 - Z_0^2}{4N} - \frac{24Z_0 - 132Z_0^2 + 76Z_0^3 - 9Z_0^4}{288N^2} - \frac{1440Z_0 + 1440Z_0^2 - 8280Z_0^3 + 4890Z_0^4 - 870Z_0^5 + 45Z_0^6}{17280N^3}\right] \quad (8.2)$$

Rayleigh Power and Rate Excess In general one has an admixture of signal and background events. By rewriting eq. 8.1 one can estimate the expected rate excess for a given Rayleigh power, z, and sample size, $N = N_s + N_b$; where N_s is the number of signal events and N_b is the number of background events. Writing $\sin(\omega t_i) \equiv s_i$ and $\cos(\omega t_i) \equiv c_i$ we have:

$$z(\omega) = \frac{1}{N}\left[\left(\sum_{i=1}^{N_s} s_i + \sum_{i=1}^{N_b} s_i\right)^2 + \left(\sum_{i=1}^{N_s} c_i + \sum_{i=1}^{N_b} c_i\right)^2\right] \quad (8.3)$$

$$= \frac{1}{N}\left[\left(\sum_{i=1}^{N_s} s_i\right)^2 + \left(\sum_{i=1}^{N_b} s_i\right)^2\right] \quad (8.4)$$

$$+\frac{1}{N}\left[\left(\sum_{i=1}^{N_s} c_i\right)^2 + \left(\sum_{i=1}^{N_b} c_i\right)^2\right] \quad (8.5)$$

$$= \frac{1}{N}\left[\left(\sum_{i=1}^{N_s} s_i\right)^2 + \left(\sum_{i=1}^{N_s} c_i\right)^2 + N_b\right] \quad (8.6)$$

$$\approx \frac{1}{N}\left[\left(\sum_{i=1}^{N_s} s_i\right)^2 + \left(\sum_{i=1}^{N_s} c_i\right)^2 + N\right] \quad (8.7)$$

Where we have assumed $N_b \gg N_s$. To proceed further we need to know

the shape of the lightcurve of the signal. For simplicity we assume a δ function light curve. Then we have:

$$z(\omega) \approx \frac{1}{N}\left[\left(\sum_{i=1}^{N_s} s_i\right)^2 + \left(\sum_{i=1}^{N_s} c_i\right)^2 + N\right] \tag{8.8}$$

$$= \frac{1}{N}\left[N_s^2 + N\right] \tag{8.9}$$

so (8.10)

$$N_s = \sqrt{N(z-1)} \tag{8.11}$$

or (8.12)

$$\sigma_{excess} = \sqrt{z-1} \tag{8.13}$$

Leading to a simple relationship between the average pulsed excess and the measured Rayleigh power, for a δ function light curve (this is an average because we have assumed no fluctuations in the noise vector). For a general light curve one has:

$$\sigma_{excess} = \frac{\sqrt{z-1}}{\epsilon} \tag{8.14}$$

where (8.15)

$$\epsilon = \left\{\left[\int_0^{2\pi} A(\phi)\cos\phi d\phi\right]^2 + \left[\int_0^{2\pi} A(\phi)\sin\phi d\phi\right]^2\right\}^{1/2} \tag{8.16}$$

Where $A(\phi)$ gives the amplitude-phase relation for the lightcurve. The parameter ϵ is a measure of the efficiency with which a given light curve can produce a large Rayleigh power. For $A(\phi) = \cos\phi$, $\epsilon = 1/2$, so one needs

twice the rate excess to achieve the same Rayleigh power as from a δ function lightcurve.

Results of the Search

After the above cuts on orbital phase we were left with 11 intervals, 2.26 hours, to scan. Since each interval is $720s$ long, the Fourier independent period spacing within an interval is $\Delta P = P^2/T = .(0125935)^2/720. = 2.2 \times 10^{-7} seconds$. So each interval corresponds to $.(012594 - .012593)/2.2 \times 10^{-7} = 4.5$ Fourier independent trials, giving us a total of 50 Fourier trials. We over sample each interval by a factor of 10, leaving us with 150 effective trials.

The complete power distribution obtained from all trials is shown in Figure 8.2. Both on and off source are given. Clearly there is no evidence for any pulsed signal in this dataset. In fact the interval with the largest on source power ($z = 7.2$) had no rate excess ($N_{exp} = 154.1 \pm 13.1$ and $N_{meas} = 154$).

8.2.2 Search for Pulsar of Arbitrary Period

Here we expand our search for a pulsar beyond the confines of the Durham hypothesis. We wish to search the entire available frequency range, from $1kHz$ to D.C.. The Rayleigh test is computationally prohibitive, the number of independent periods covered over this range is frequency space being roughly 2×10^6. For the Rayleigh test the required CPU time scales like N^2. A more efficient routine for obtaining the same information is the Fast

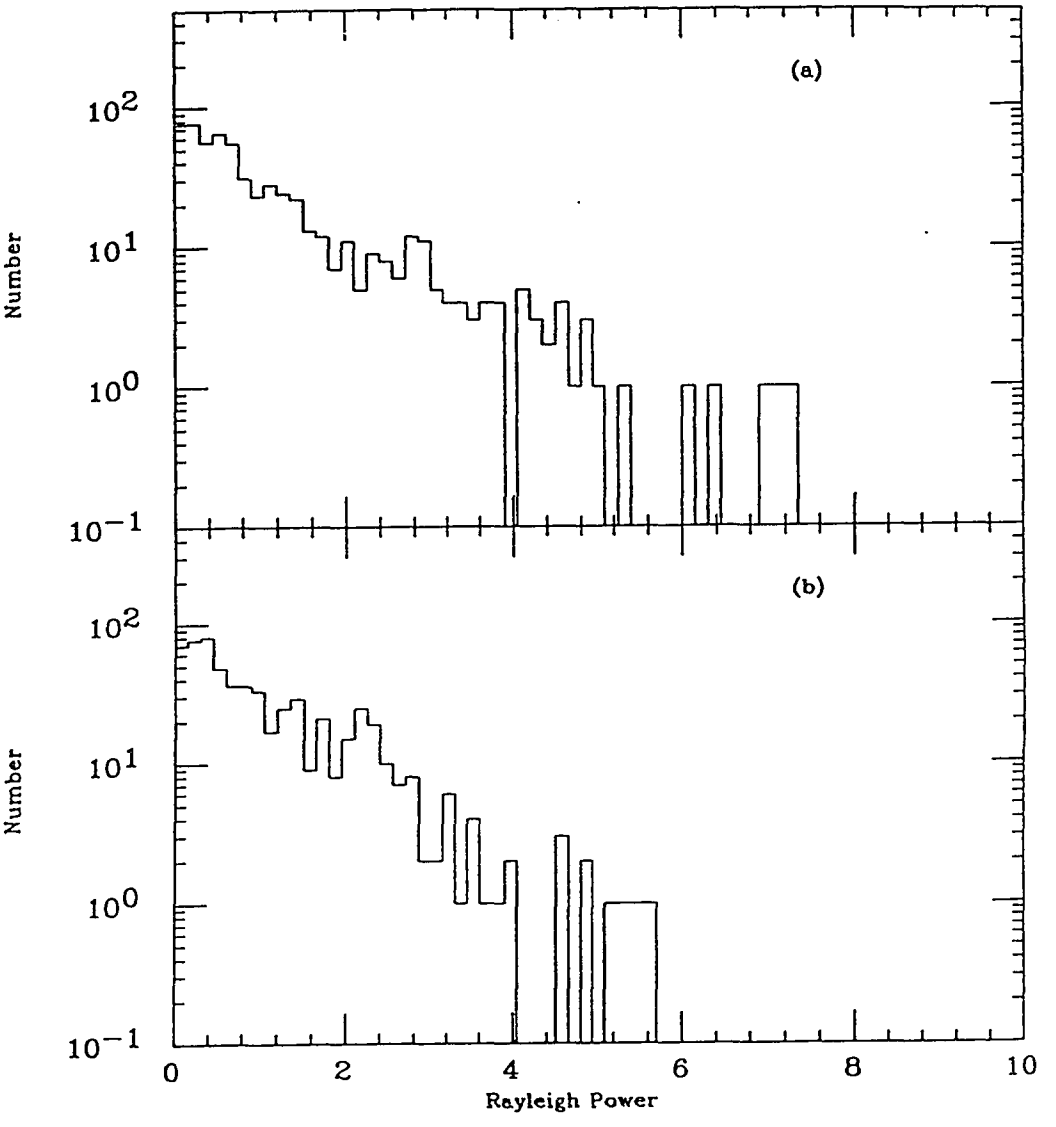

Figure 8.2 Distribution of Rayleigh powers observed from test of the Durham hypothesis. 1986 dataset. (a) On source, (b) OFF source

Fourier Transform or FFT (see for example Press et. al.), which scales like $N \ln N$.

There are 2 million Fourier independent periods in this range of period space, therefore we must severely limit the number of intervals that we examine. We will only examine those intervals with a significant rate excess, $\sigma_{ex} \geq 3.0$. There were two such intervals in the data set. The first occurred during run 855, (day number 217, 36365.–37113. UT seconds past midnight, $\phi_{vdK} = .947 \pm .05$), with a 3.2σ excess, ($N_{exp} = 168. \pm 13.7$ and $N_{meas} = 212$. The other occurred during run 869, (day number 241, 24137.–24885. UT seconds past midnight, $\phi_{orb} = .425 \pm .05$), with a 3.4σ excess, ($N_{exp} = 142. \pm 13.8$ and $N_{meas} = 189$).

Figure 8.3 shows the power distribution from the interval in run 855. Figure 8.4 the power distribution from run 869. Both are as expected from a random background (i.e. an exponential distribution). Table 8.1 lists the twenty largest powers and the frequencies at which they occurred for the 2 intervals.

8.3 1989 Data Set

We performed an FFT of the interval of June 29, 3.7σ (see chapter 7). In Figure 8.5 we show the power spectrum. We see no indication of a pulsed signal. The distributions match those expected from a random background. In Table 8.2 we list the 20 highest powers and their corresponding frequencies.

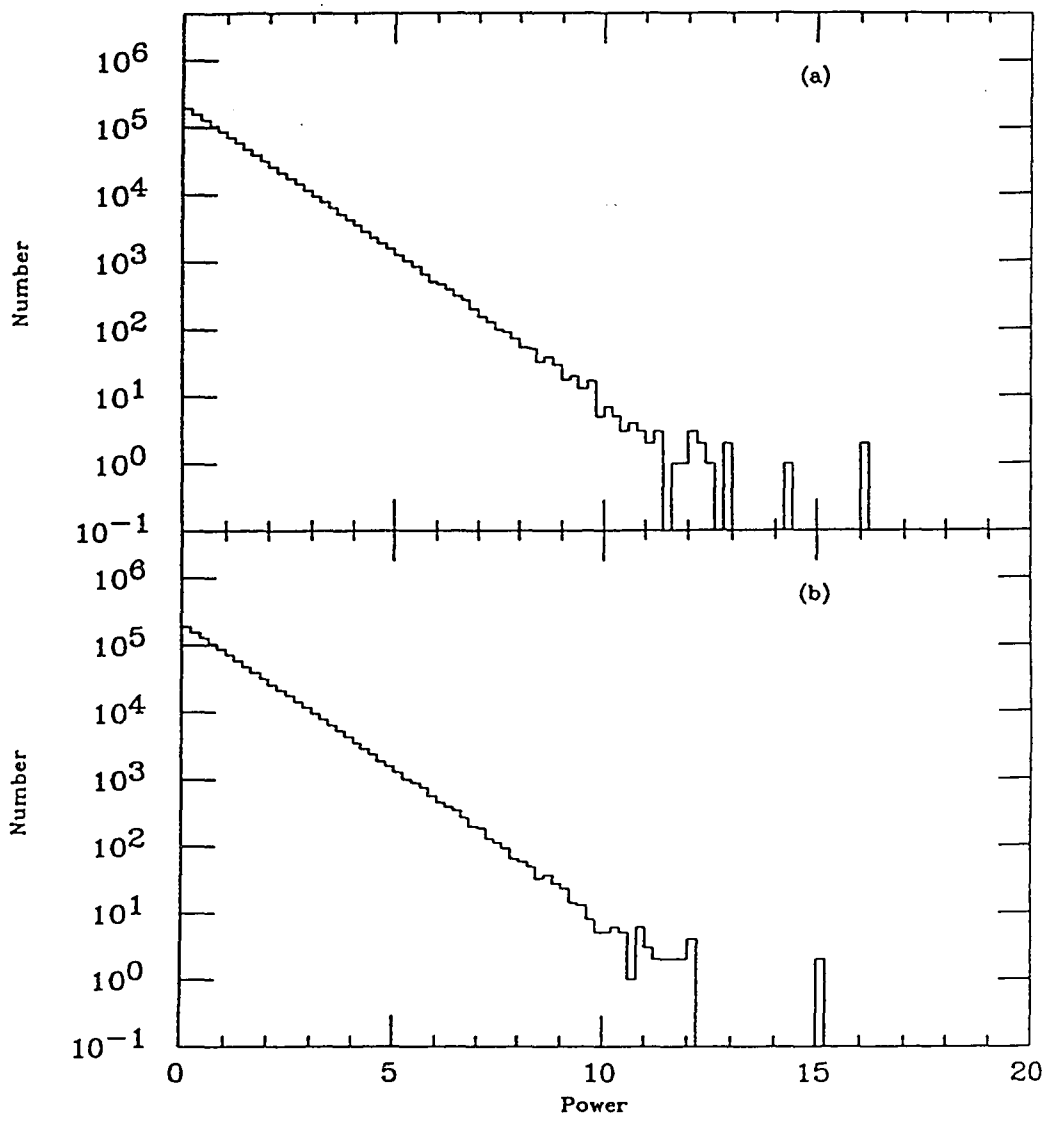

Figure 8.3 Distribution of power observed from FFT. Data from run 855.
(a) On source, (b) OFF source

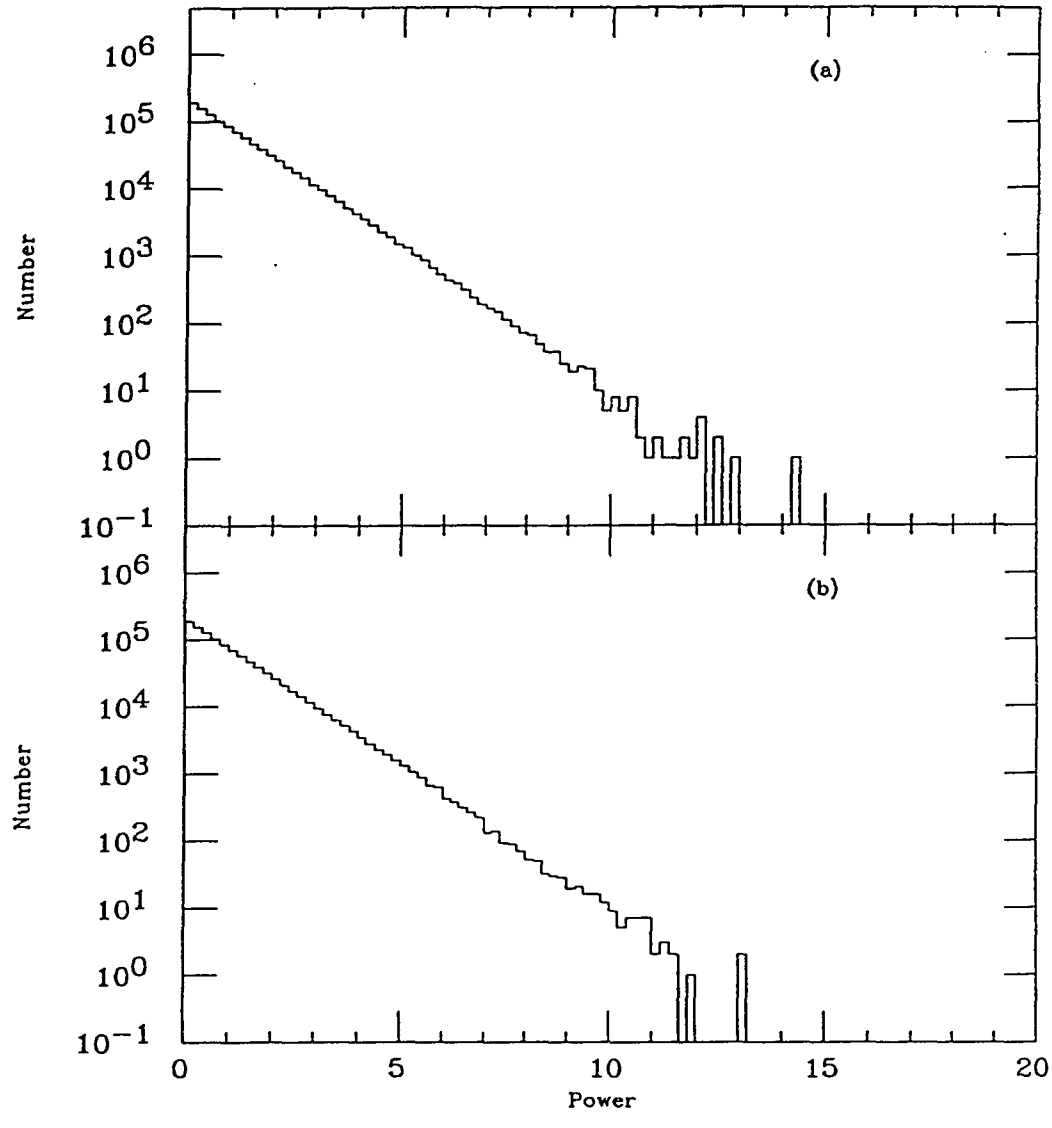

Figure 8.4 Distribution of power observed from FFT. Data from run 869.
(a) On source, (b) OFF source

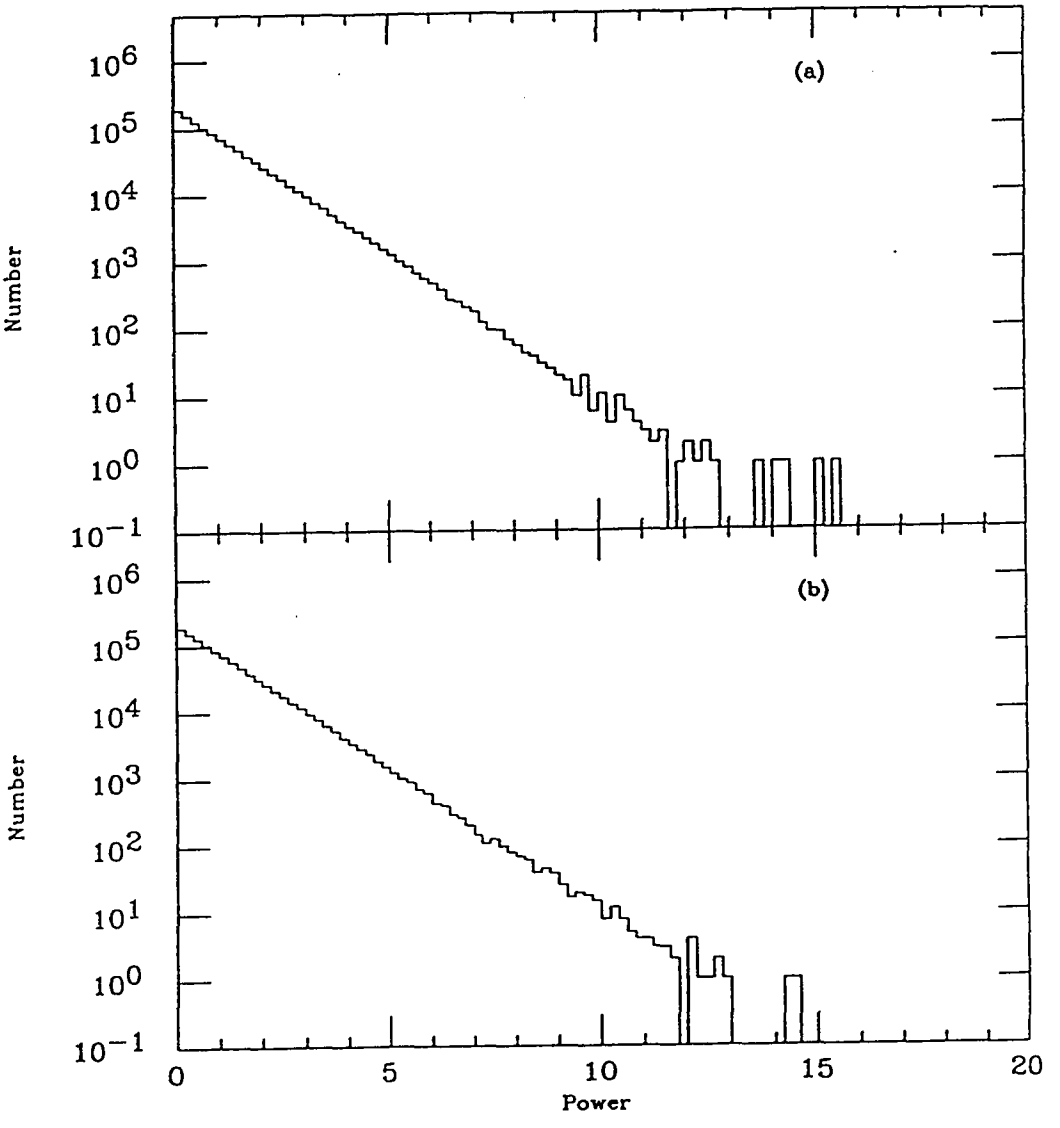

Figure 8.5 Distribution of power observed from FFT. Data from run 1647.
(a) On source, (b) OFF source

8.4 Conclusion

We have tested the 'Durham' hypothesis: a $12.59ms$ pulsar at the heart of Cygnus X–3 only visible for a short time near x-ray maximum. We have found no evidence to support this hypothesis, though with only 11 intervals we are not in contradiction with this result. We have also performed a complete scan in frequency space, from 1000Hz to .001Hz, for the three intervals with significant rate excesses. Two in 1986, and one in 1989, 26 days after the first radio outburst and 23 days before the second. We see no evidence for a pulsed signal in any of these intervals.

RUN 855		Run 869	
Power	Frequency (Hz)	Power	Frequency (Hz)
15.1	156.148	14.3	249.451
15.0	100.306	12.5	41.415
12.1	660.131	12.4	830.903
12.0	769.047	12.1	723.886
12.0	872.994	12.0	41.750
12.0	242.184	12.0	656.711
11.9	455.863	12.0	436.042
11.8	577.631	11.9	254.910
11.7	746.088	11.7	669.495
11.6	678.832	11.6	740.259
11.5	874.501	11.6	608.022
11.4	428.878	11.3	734.916
11.2	652.081	11.2	763.327
11.2	436.211	11.0	80.531
11.0	82.841	10.9	632.761
11.0	832.530	10.6	109.740
11.0	290.175	10.6	177.555
10.9	292.758	10.5	982.229
10.9	131.634	10.5	108.064
10.9	731.464	10.5	484.253

Table 8.1 Top 20 powers from FFT of two 720 second intervals

ON Source		OFF Source	
Power	Frequency (Hz)	Power	Frequency (Hz)
15.5	378.919	14.5	594.247
15.0	58.4917	14.3	813.268
14.0	865.522	12.8	628.108
13.6	727.193	12.7	853.951
12.6	953.296	12.7	842.267
12.4	126.723	12.5	259.193
12.4	460.727	12.2	910.348
12.2	43.687	12.2	176.432
12.0	875.713	12.1	109.590
12.0	276.987	12.1	992.830
11.8	28.887	12.0	766.853
11.5	552.011	11.7	591.105
11.4	627.555	11.6	227.896
11.4	123.326	11.5	360.698
11.3	88.6993	11.4	425.254
11.3	651.137	11.3	7.332
11.1	605.752	11.3	727.514
11.0	222.817	11.2	388.186
11.0	842.771	11.2	776.363
10.9	495.332	11.0	626.540

Table 8.2 Top 20 powers from FFT of 900 second interval in run 1647

Chapter 9

Conclusions

Summary of D.C. Results We obtained a total of 61 hours of data on Cygnus X–3 in 1986, and 76.5 hours in 1989. There was evidence (of low statistical significance, 0.5% after trials) of emission for roughly 8 hours (3 runs in 1986 days 218, 219, and 241) at a flux level of $(3.3 \pm 0.7) \times 10^{-10}\gamma' s cm^{-2}s^{-1}$ above $300GeV$. For the remainder of the dataset, 1986 and 1989, we set a flux upper limit (95% C.L.) of $5.8 \times 10^{-11}\gamma' s cm^{-2}s^{-1}$. Given that we have runs taken on the same days that we observed excesses from Cygnus with no excess, we conclude that if Cygnus X–3 is a source of very high energy gamma rays, it is a sporadic and variable (on the timescale of hours) one. We note that the GREX array at Haverah Park obtained their largest excess of 1986 on days 242 and 243, and the radio flux from Cygnus was at a yearly high between days 217 and 250 of 1986.

Correlation of Emission with Orbital Period We see no statistically significant correlation between γ-ray emission and x-ray phase; in the entire

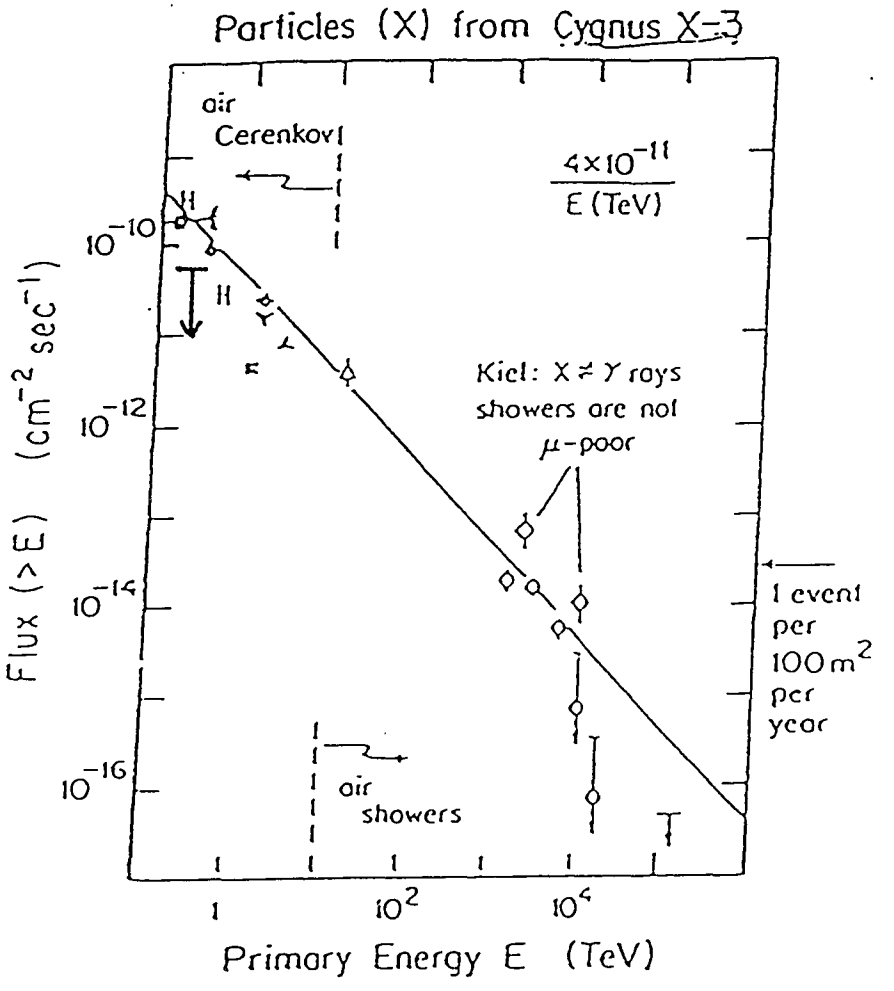

Figure 9.1 Flux from Cygnus X–3 versus Energy. *H* denotes the measurements from this thesis. (adapted from Halzen 1986)

1986 data set and for the limited time where γ-ray activity was evident.

Short Bursts From Cygnus X–3 While we saw evidence for source variability on the timescale of a few hours, we saw no evidence for bursting on $\sim 15min$ timescales.

Pulsar in Cygnus We failed to find any evidence for a VHEGR 'pulsar' in Cygnus X–3, neither the previously reported $12.59ms$ pulsar, nor a pulsar of arbitrary period. Though by itself our lack of confirmation of the $12.59ms$ pulsar is consistent with the published result, taken together with the null results from the Whipple Observatory and the Gulmarg group it becomes difficult to accept the validity of the published result. The absence of a pulsar at all frequencies could be explained by a weak surface magnetic field for the compact object within the system. Implying that accretion may be the ultimate energy source within the system. Though our null result be no means rules out the presence of a pulsar in Cygnus X–3.

Comparison with Previous Haleakala Observations In 1985 we obtained roughly 113 hours of data on Cygnus X–3. This data set showed evidence (of low statistical significance) for low level D.C. emission ($2-3\%$ of the cosmic ray background) from Cygnus X–3. The time averaged flux was measured to be $2-7\times 10^{-11}cm^{-2}s^{-1}$, (Szentgyorgi 1986) in complete agreement with the results of this analysis. No correlation between orbital

phase and γ-ray emission was found in the 1985 data set, and no evidence for the $12.59ms$ pulsar was found. In 1985 there were 45 intervals satisfying the Durham criteria (within $1000s$ of x-ray maximum). Together with the 11 intervals in 1986 we have a total of 56 intervals. With a reported duty cycle of 5%, we should have observed 2 periods of significant pulsar activity. This non-observation is not inconsistent with the the Durham result, though together with the non-observation by the Whipple collaboration (O'Flaherty et. al. 1990) (20 intervals), the world is consistent with the $12.59ms$ pulsar at the 2% level (observe 0, expect 3.8).

Bibliography

Aglietta, M., et. al., 1990, 21^{st} *ICRC*, **Vol. 9**: 388

Arons, J., 1981, in *Origin of Cosmic Rays*, Setti, G., et. al., eds., Reidel, Boston, p. 175

Baltrusaitis, R.M., et. al., 1985, *Ap. J.*, **297**: 145

Baltrusaitis, R.M., et. al., 1987b, *Ap. J.*, **323**: 685

Baltrusaitis, R.M., et. al., 1987b, 20^{th} *ICRC*, **Vol. 1**: 233

Battistoni, G., et. al., 1985, *Phys. Lett. B.*, **155**: 465

Becklin, E.E., et. al., 1974, *Ap. J. Lett.*, **192**: L119

Beland, S., Bouland, O., and Davidge, T., 1988, *CHFT Info. Bull.*, **18**: 16

Bell, A.R. 1978, *MNRAS*, **182**, 147-156

Berezinsky, V.S., 1986, *Phys. Letts. B*, **172**: 423

Berger, C., et. al., 1986, *Phys. Lett. B.*, **174**: 118

Bhat, C.L., et. al., 1990, 21^{st} *ICRC*, **Vol. 2**: 10

Binney, J., and Tremaine, S., 1987, *Galactic Dynamics*, Princeton University Press, Princeton

Bionta, R.M., et. al., 1987, *Phys. Rev. D.*, **36**: 30

Blandford, R.D., 1976, *M.N.R.A.S.*, **176**: 465

Blandford, R., and Eichler, D. 1987, *Phys. Rep.*, **154**, No. 1

Bloomer, S.D., et. al., 1990, 21st *ICRC*, **Vol. 2.**: 39

Bonnet-Bidaud, J.M., and Chardin, G., 1988, *Physics Reports*, **170**, No. 6: 325

Braes, L.L.E., and Miley, G.K., 1972, *Nature*, **237**: 506

Brazier, K.T., et. al., 1990, 21st *ICRC*, **Vol. 2**: 91

Canizares, C.R., et. al., 1973, *Nature Phys. Sci.*, **241**: 28

Cassiday, G.L., et. al., 1989, *Phys. Rev. Lett.*, **62**: 383

Cawley, M.F., et. al., 1985, *Ap. J.*, **296**: 185

Cesarsky, C.J. 1980, *Ann. Rev. Astron. Astrophys.*, **18**: 289

Chadwick, P.M., et. al., 1985, *Nature*, **318**: 642

Chanmugam, G., and Brecher, K., 1985, *Nature*, **313**: 767

Cheng, K.S., Ho, C., and Ruderman, M., 1986a, *Ap. J.*, **300**: 500

Cheng, K.S., Ho, C., and Ruderman, M., 1986b, *Ap. J.*, **300**: 522

Ciampa,D., et. al., 1990, 21st *ICRC*, **Vol. 2**: 35

Clayton, D.D., 1983, *Principles of Stellar Evolution and Nucleosynthesis*, University of Chicago Press, Chicago: pp 186-224

Danaher, S., et. al., 1981, *Nature*, **289**: 568

Davidsen, A., and Ostriker, J.P., 1974, *Ap. J.*, **189**: 331

DeJager, O.C., 1987, *PhD Thesis*, Potchestroom University, S. Africa

Dickey, J.M., 1983, *Ap. J. Lett.*, **273**: L71

Dingus, B.L., et. al., 1990, *Phys. Rev. Lett.*, **60**: 1785

Dothwaite, J.C., et. al., 1983, *Astron. Astrophys.*, **126**: 1

Eichler, D., and Vestrand, W.T., 1984, *Nature*, **307**: 613

Eichler, D., and Vestrand, W.T., 1985, *Nature*, **318**: 345

Elsner, R.F., et. al., 1980, *Ap. J.*, **239**: 335

Faulkner. J., et. al., 1972, *Ap. J. Lett.*, **175**: L79

Fegan, D.J., et. al. 1987, *Very High Energy Gamma Ray Astronomy*, ed. K.E. Turver, D. Reidel, p 111

Fermi, E. 1949, *Phys Rev.*, **75**: 1169

Fichtel, C.E., et. al., 1987, *Ap. J.*, **319**: 362

Friendenreich, H.T., et. al. 1989, *A Study of Hadrons at the Core of Extensive Air Showers and the Elemental Composition of Cosmic Rays at* $10^{15}eV$, UMDCR Preprint 90-024

Gaisser, T.K., and Stecker, F.W., 1986, *Proceedings of the Japan-U.S. Seminar on Cosmic Ray Muon and Neutrino Physics/Astrophysics Using Deep Underground/Underwater Detectors*: p 80

Galper, A.M., et. al., 1987, *JETP Lett.*, **26**: 259

Garcia-Munoz, M., et. al. 1977, *Ap. J.*, **217**: 859

Geldzahler, B.J., et. al., 1983, *Ap. J. Lett.*, **273**: L65

Ghosh, P., and Lamb, F.K., 1978 *Ap. J. Lett*, **223**: L83

Ghosh, P., and Lamb, F.K., 1979a *Ap. J.*, **232**: 259

Ghosh, P., and Lamb, F.K., 1979b *Ap. J.*, **234**: 296

Ghosh, P., et. al., 1981, *Ap. J.*, **251**: 230

Goldreich, P., and Julian, W.H., 1969, *Ap. J.*, **157**: 869

Greenwood, J.A., and Durand, D., 1955, *Ann. Math. Stat.*, **26**: 233

Gregory, P.C. et. al., 1972, *Nature*, **239**: 440

Haines, T.J., et. al., 1990, 21^{st} *ICRC*, **Vol. 2**: 17

Hermsen, W., et. al., 1987, *Astron. Astrophys.*, **175**: 141

Hillas, A.M. 1972, **Cosmic Rays**, Pergamon Press, New York

Hillas, A.M. 1984, **Ann. Rev. Astron. Astrophys., 22**: 425

Hillas, A.M. 1984a, **Nature, 312**: 50

Hillas, A.M., 1987, *Very High Energy Gamma Ray Astronomy*, ed. K.E. Turver, D. Reidel, p. 247

Hjellming, R.M., and Balick, B., 1972, *Nature*, **239**: 443

Holt, S.S., et. al., 1976, *Nature* **260**: 592

Holt, S.S., et. al., 1979, *Ap. J.* **233**: 344

Johns, K., et. al., 1990, 21^{st} *ICRC*, **Vol. 9**: 402

Johnston, K.J. et. al., 1986, *Ap. J.* **309**: 707

Johnston, K.J., 1989, *Private Communication*

Katz, J.I. 1987, **High Energy Astrophysics**, Addison-Wesley, Menlo Park

Kifune, T., et. al., 1986, *Ap. J.*, **301**: 230

Lagage, P.O. and Cesarsky, C.J. 1983, *Astron. Astrophys.*, **125**, 249-257

Lamb, R.C., et. al., 1977, *Ap. J. Lett.*, **212**: L63

Lamb, R.C., et. al., 1982, *Nature*, **296**: 543

Lambert, A., et. al., 1985, 19^{th} *ICRC*, **Vol. 1**: 71

Lawrence, M.A., et. al., 1990, 21^{st} *ICRC*, **Vol. 2**: 67

Leach, R.W., et. al., 1975, *Ap. J.*, **199**: 184

Learned, J.L., 1981, *Hawaii Dumand Commission*, **HDC 81-10**

Li, T.P., and Ma, Y.P., 1983, *Ap. J.*, **272**: 317

Li, T.P., and Wu, M., 1989, *Ap. J.*, **346**: 391

Lloyd-Evans, J., et. al., 1983, *Nature*, **305**: 784

Lloyd-Evans, J., et. al., 1983, *Nature*, **305**: 784

Lovelace, R.V.E., 1976, *Nature*, **262**: 649

Lubow, S.H., and Shu, F.H., 1975, *Ap. J.*, **198**: 383

Lund, N. 1986, in **Cosmic Radiation in Contemporary Astrophysics**, Shapiro, M.M. ed., D. Reidel, Boston, p. 1

Mardia, K.V., 1972, *Statistics of Directional Data*, Academic Press, New York.

Marshak, M.L., et. al., 1985, *Phys. Rev. Lett.*, **54**: 2079

Mason, K.O., et. al., 1976, *Ap. J.*, **207**: 78

Mason, K.O., et. al., 1986, *Ap. J.*, **309**: 700

Manzo, G., et. al., 1978, *Astron. Astrophys.*, **70**: 317

Mauche, C.W., and Gorenstein, P., 1986, *Ap. J.*, **302**: 371

McCray, R.A., and Snow, T.P. 1979, *Ann. Rev. Astron. Astrophys.*, **17**: xxx

McKechnie, S.P., et. al., 1976, *Ap. J. Lett.*, **207**: L151

McKee, C.F., and Ostriker, J.P. 1977, *Ap. J.*, **218**: 148

Michel, F.C. 1982, *Rev. Mod. Phys.*, **54**, No. 1.

Middleditch, J., 1976, *PhD Thesis*, UC Berkeley

Milgrom, M., 1976, *Astron. Astrophys.*, **51**: 215

Molnar, L. A., 1985, PhD Thesis, Harvard University

Molnar, L.A., et. al., 1988a, *Center for Astrophysics*, **Preprint 2664**

Molnar, L.A., et. al., 1988b, *Ap. J.*, **331**: 494

Molnar, L.A., and Mauche, C.W., 1986, *Ap. J.*, **310**: 343

Molteni, D., et. al., 1980, *Astron. Astrophys.*, **87**: 88

Neshpor, Y.I., et. al., 1979, *Astrophys. Space Sci.*, **61**: 349

O'Flaherty, K., et. al., 1990, 21^{st} *ICRC*, **Vol. 2**: 2

Ostriker, J.P., and Gunn, J.E., 1969a, *Phys. Rev. Lett.*, **22**: 728

Ostriker, J.P., and Gunn, J.E., 1969b, *Ap. J.*, **157**: 1395

Oyama, Y., et. al., 1986, *Phys. Rev. Lett.*, **56**: 991

Parsignault, D.R., et. al., 1972, *Nature Phys. Sci.*, **239**: 123

Parsignault, D.R., et. al., 1977, *Ap. J.* **218**: 232

Press, W.H., et. al., 1986, *Numerical Recipes The Art of Scientific Computing*, Cambridge Press, New York

Priedhorsky, W., and Terrel, J., 1986, *Ap. J.*, **301**: 886

Pringle, J.E., 1974, *Nature*, **247**: 21

Resvanis, L., et. al. 1987, *Very High Energy Gamma Ray Astronomy*, ed. K.E. Turver, D. Reidel, p 105

Rieke, G.H., 1969, *PhD Thesis*, Harvard University, Boston, MA

Ruderman, M.A., and Sutherland, P.G., 1975, it Ap. J., **196**: 51

Samorski, M., and Stamm, W., 1983a, *Ap. J. Lett.*, **268**: L17

Samorski, M., and Stamm, W., 1983b, 18^{th} *ICRC*, **Vol.1**: 135

Scargle, J.D. 1982, *Ap. J.*, **263**: 835

Shakura, N.I., and Sunyaev, R.A., 1973, *Astron. & Astrophys.*, **24**: 337

Simpson, J.A. 1983, in **Composition and Origin of Cosmic Rays**, Shapiro, M.M ed., D. Reidel, Boston, p. 1

Slane, P.O., 1988, *PhD Thesis*, University of Wisconsin, Madison

Spencer, R.E. et. al., 1986, *Ap. J.* **309**: 694

Stepanian, A.A., et. al., 1975, *Astrophys. Space Sci.*, **38**: 267

Strom, R.G., et. al., 1988, EXOSAT preprint no. 95

Sturrock, P.A., 1971, *Ap. J.*, **164**: 529

Suda, T., 1989, *Talk presented at University of Hawaii*

Szentgyorgi, A., 1986, *PhD Thesis*, Unversity of Wisconsin, Madison

Takagi, S., 1964, *Lectures on Extensive Air Showers and High Energy Interactions*, Tata Institute of Fundamental Research, Bombay

Tavani, M., Ruderman, M., Shaham, J., 1989, *Ap. J. Lett.*, **342**: L31

Teshima, M., et. al., 1990, 21^{st} *ICRC*, **Vol. 2**: 71

van der Klis, M. and Bonnet-Bidaud, J.M., 1981a, *Astron. Astrophys.*, **95**: L5

van der Klis, M. and Bonnet-Bidaud, J.M., 1981b, *Astron. Astrophys.*, **101**: 299

van der Klis, M. and Bonnet-Bidaud, J.M., 1982, *Astron. Astrophys. Suppl. Ser.*, **50**: 129

van der Klis, M. and Jansen, F.A., 1985, *Nature*, **313**: 768

van der Klis, M. and Jansen, F.A., 1985, *Adv. Space Res.*, Vol. 5, No. 3, p 109

van der Klis, M. and Bonnet-Bidaud, J.M., 1988, *EXOSAT preprint 85*

Van der Laan, H., 1966, *Nature*, **211**: 1131

Vladimirsky, B.M., et. al., 1973, 13^{th} *ICRC*, **Vol. 1**: 456

Waltmann, E., 1989, *Private Communication*

Watson, A.A. 1984, *Adv. Space Res.*, **Vol.** 4, Nos. 2-3, p35

Wdowczyk, J. 1986, in **Cosmic Radiation in Contemporary Astrophysics**, Shapiro, M.M. ed., D. Reidel, Boston, p. 149

Wefel, J.P. 1988 in **Genesis and Propagation of Cosmic Rays**, Shapiro, M.M., and Wefel, J.P. eds., D. Reidel, Boston, p. 1

White, N.E., et. al., 1981, *Ap. J.*, **247**: 994

White, N.E., and Holt, S.S., 1982, *Ap. J.*, **257**: 318

Wiedenbeck, M.E. 1983, in **Composition and Origin of Cosmic Rays**, Shapiro, M.M. ed., D. Reidel, Boston, p. 65

Willingale, R., et. al., 1985, *M.N.R.A.S.*, **215**: 295

Wolfendale, A.W. 1963, **Cosmic Rays**, Philosophical Library Inc., New York

Zeldovich, Ya. B., Ruzmaikin, A.A., and Sokoloff, D.D., 1983, **Magnetic Fields in Astrophysics**, Gordon and Breah, New York